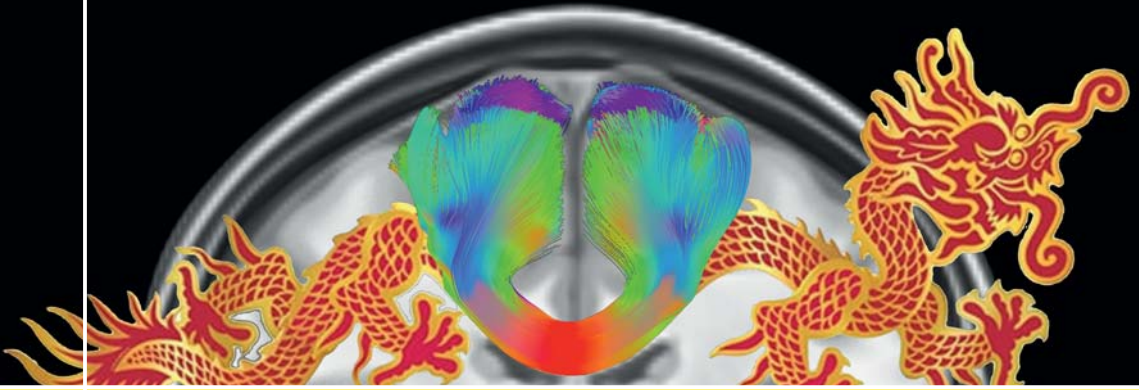


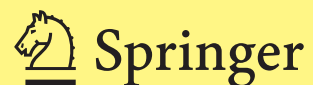
Mathematics and Visualization



Elisenda Bonet-Carne · Jana Hutter ·
Marco Palombo · Marco Pizzolato ·
Farshid Sepehrband · Fan Zhang *Editors*

Computational Diffusion MRI

MICCAI Workshop, Shenzhen, China,
October 2019



Mathematics and Visualization

Series Editors

Hans-Christian Hege, Konrad-Zuse-Zentrum für Informationstechnik Berlin (ZIB),
Berlin, Germany

David Hoffman, Department of Mathematics, Stanford University, Stanford, CA,
USA

Christopher R. Johnson, Scientific Computing and Imaging Institute, Salt Lake
City, UT, USA

Konrad Polthier, AG Mathematical Geometry Processing, Freie Universität Berlin,
Berlin, Germany

The series *Mathematics and Visualization* is intended to further the fruitful relationship between mathematics and visualization. It covers applications of visualization techniques in mathematics, as well as mathematical theory and methods that are used for visualization. In particular, it emphasizes visualization in geometry, topology, and dynamical systems; geometric algorithms; visualization algorithms; visualization environments; computer aided geometric design; computational geometry; image processing; information visualization; and scientific visualization. Three types of books will appear in the series: research monographs, graduate textbooks, and conference proceedings.

More information about this series at <http://www.springer.com/series/4562>


Elisenda Bonet-Carne · Jana Hutter ·
Marco Palombo · Marco Pizzolato ·
Farshid Sepehrband · Fan Zhang
Editors

Computational Diffusion MRI

MICCAI Workshop, Shenzhen, China,
October 2019



Editors

Elisenda Bonet-Carne 
Centre for Medical Imaging and Centre
for Medical Image Computing
University College London
London, UK

BCNatal Fetal Medicine Research Center
Barcelona, Spain

Marco Palombo
Centre for Medical Image Computing
University College London
London, UK

Farshid Sefehrband
Laboratory of Neuro Imaging (LONI)
University of Southern California
Los Angeles, CA, USA

Jana Hutter 
Centre for Medical Engineering
King's College London
London, UK

Marco Pizzolato 
Signal Processing Laboratory (LTS5)
École Polytechnique Fédérale de Lausanne
Lausanne, Switzerland

Fan Zhang
Laboratory of Mathematics in Imaging
Harvard Medical School
Boston, MA, USA

ISSN 1612-3786

ISSN 2197-666X (electronic)

Mathematics and Visualization

ISBN 978-3-030-52892-8

ISBN 978-3-030-52893-5 (eBook)

<https://doi.org/10.1007/978-3-030-52893-5>

Mathematics Subject Classification: 00B25, 00A66, 00A72, 42B35, 60J60, 60J65, 62P10, 65CXX, 65DXX, 65Z05, 68R10, 68T99, 92BXX

© Springer Nature Switzerland AG 2020

This work is subject to copyright. All rights are reserved by the Publisher, whether the whole or part of the material is concerned, specifically the rights of translation, reprinting, reuse of illustrations, recitation, broadcasting, reproduction on microfilms or in any other physical way, and transmission or information storage and retrieval, electronic adaptation, computer software, or by similar or dissimilar methodology now known or hereafter developed.

The use of general descriptive names, registered names, trademarks, service marks, etc. in this publication does not imply, even in the absence of a specific statement, that such names are exempt from the relevant protective laws and regulations and therefore free for general use.

The publisher, the authors and the editors are safe to assume that the advice and information in this book are believed to be true and accurate at the date of publication. Neither the publisher nor the authors or the editors give a warranty, expressed or implied, with respect to the material contained herein or for any errors or omissions that may have been made. The publisher remains neutral with regard to jurisdictional claims in published maps and institutional affiliations.

This Springer imprint is published by the registered company Springer Nature Switzerland AG
The registered company address is: Gewerbestrasse 11, 6330 Cham, Switzerland

Program Committee

Nagesh Adluru	University of Wisconsin-Madison, USA
Manisha Aggarwal	Johns Hopkins University, USA
Dogu Baran Aydogan	University of Southern California, USA
Dafnis Batalle	King's College London, UK
Sylvain Bouix	Harvard Medical School, USA
Ryan Cabeen	University of Southern California, USA
Erick Jorge Canales-Rodríguez	FIDMAG Research Foundation, Spain
Emmanuel Caruyer	IRISA, France
Mara Cercignani	University of Sussex, UK
Jian Cheng	National Institutes of Health, USA
Alessandro Daducci	University of Verona, Italy
Gabriel Girard	EPFL, Switzerland
Francesco Grussu	University College London, UK
Tom Dela Haije	University of Copenhagen, Denmark
Enrico Kaden	University College London, UK
Muge Karaman	University of Illinois at Chicago, USA
Suheyly Cetin Karayumak	Harvard Medical School, USA
Jan Klein	Fraunhofer MEVIS, Germany
Christophe Lenglet	University of Minnesota, USA
Emma Muñoz Moreno	IDIBAPS, Spain
Lipeng Ning	Harvard Medical School, USA
Torben Schneider	Philips Healthcare, UK
Thomas Schultz	University of Bonn, Germany
Filip Szczepankiewicz	Harvard Medical School, USA
Chantal Tax	Cardiff University, UK
Jelle Veraart	Champalimaud Foundation, Portugal
Pew-Thian Yap	University of North Carolina at Chapel Hill, USA

Preface

It is our great pleasure to present the proceedings of the 2019 International Workshop on Computational Diffusion MRI (CDMRI'19) and the main results of the Multi-dimensional Diffusion MRI (MUDI) Challenge. Both were held under the auspices of the International Conference on Medical Image Computing and Computer Assisted Intervention (MICCAI), which took place in Shenzhen, China, on October 17, 2019. CDMRI'19 and MUDI challenges were sponsored by MICCAI, NVIDIA, Wellcome Trust, and MedIAN, and endorsed by the International Society for Magnetic Resonance in Medicine (ISMRM).

This volume presents the latest developments in the highly active and rapidly growing field of diffusion MRI. The reader will find numerous contributions covering a broad range of topics, from the mathematical foundations of the diffusion process and signal generation, to new computational and machine learning methods and estimation techniques for the in vivo recovery of microstructural and connectivity features, as well as combined diffusion-relaxometry acquisitions' techniques. This edition includes invited chapters from high-profile researchers with the specific focus on four advanced topics that are gaining momentum within the diffusion MRI community: (i) diffusion MRI signal acquisition and processing strategies; (ii) machine learning for diffusion MRI; (iii) diffusion MRI outside the brain and clinical applications; and (iv) CDMRI'19 MUDI challenge results on combined diffusion-relaxometry acquisitions. Additionally, the volume also includes contributions in the field of tractography and connectivity mapping, which continue being relevant and popular topics across all editions of CDMRI.

This volume offers the opportunity to share new perspectives on the most recent research challenges for those currently working in the field, but also offering a valuable starting point for anyone interested in learning computational techniques in diffusion MRI. The book includes rigorous mathematical derivations, a large number of rich, full-color visualizations, and clinically relevant results. As such, it will be of interest to researchers and practitioners in the fields of computer science, MRI physics, and applied mathematics.

Each contribution in this volume has been peer-reviewed by multiple members of the international Program Committee. We would like to express our gratitude to

all CDMRI'19 authors and reviewers for ensuring the quality of the presented work and to all the teams who participated in MUDI challenge. We are grateful to the MICCAI 2019 chairs for providing a platform to present and discuss the work collected in this volume, to our sponsors and to ISMRM for the endorsement. We also would like to thank the editors of the Springer book series Mathematics and Visualization as well as Leonie Kunz and Martin Peters (Springer, Heidelberg) for their support to publish this collection as part of their series.

Finally, we express our sincere congratulations to the winners of the prizes that were awarded during CDMRI'19. The prizes were awarded following careful evaluation by a panel of judges, made by the CDMRI'19 and MUDI organizers and by the CDMRI'19 and MUDI keynote speakers.

- Prize for the best CDMRI paper: “Optimized response function estimation for spherical deconvolution”, Tom Dela Haije et al. University of Copenhagen, Denmark.
- Prize for the best CDMRI oral presentation: “A framework to construct a longitudinal DW-MRI infant atlas based on mixed effects modeling of dODF coefficients”, Heejong Kim et al. New York University, USA.
- Prize for the best CDMRI poster presentation: “Diffusion anisotropy identification by short diffusion-diffusion correlation spectroscopy”, Fangrong Zong et al. Institute of Biophysics, Chinese Academy of Sciences, China.
- Prize for the best MUDI method: “Select and Retrieve for Direct Up-sampling network (SARDU-net)”, Francesco Grussu et al. University College London (UCL), UK.
- Prize for the best MUDI team presentation: “Joint RELaxation-Diffusion Imaging Moments (REDIM) to probe neurite microstructure”, Lipeng Ning et al. Harvard Medical School, USA.

Shenzhen, China
October 2019

Elisenda Bonet-Carne, Ph.D.
UCL, UK and BCNatal-FMRC, Spain

Jana Hutter, Ph.D.
KCL, UK

Marco Palombo, Ph.D.
UCL, UK

Marco Pizzolato, Ph.D.
EPFL, Switzerland

Farshid Seppehrband, Ph.D.
USC, USA

Fan Zhang, Ph.D.
Harvard, USA

Contents

Diffusion MRI Signal Acquisition and Processing Strategies	
Connectome 2.0: Cutting-Edge Hardware Ushers in New Opportunities for Computational Diffusion MRI	3
Anastasia Yendiki, Thomas Witzel, and Susie Y. Huang	
Alternative Diffusion Anisotropy Metric from Reduced MRI Acquisitions	13
Santiago Aja-Fernández, Antonio Tristán-Vega, Rodrigo de Luis-García, and Derek K. Jones	
Optimized Response Function Estimation for Spherical Deconvolution	25
Tom Dela Haije and Aasa Feragen	
Optimal Fiber Diffusion Model Restoration	35
Clint Greene, Kate Reville, Cathrin Buetefisch, Ken Rose, and Scott Grafton	
Diffusion Anisotropy Identification by Short Diffusion-Diffusion Correlation Spectroscopy	49
Fangrong Zong, Yan Zhuo, Natasha Spindler, Huabing Liu, and Petrik Galvosas	
Machine Learning for Diffusion MRI	
Current Challenges and Future Directions in Diffusion MRI: From Model- to Data- Driven Analysis	63
Kurt G. Schilling, Baxter Rogers, Adam W. Anderson, and Bennett A. Landman	
Spatial Sparse Estimation of Fiber Orientation Distribution Using Deep Alternating Directions Method of Multipliers Network	79
Ridho Akbar, Yuanjing Feng, Fan Zhang, Jianzhong He, Qingrun Zeng, Lipeng Ning, Carl-Fredrik Westin, and Lauren J. O’Donnell	

Free-Water Correction in Diffusion MRI: A Reliable and Robust Learning Approach	91
Leon Weninger, Simon Koppers, Chuh-Hyoun Na, Kerstin Juetten, and Dorit Merhof	
Convolutional Neural Networks for Fiber Orientation Distribution Enhancement to Improve Single-Shell Diffusion MRI Tractography	101
Oeslle Lucena, Sjoerd B. Vos, Vejay Vakharia, John Duncan, Sebastien Ourselin, and Rachel Sparks	
q-Space Novelty Detection with Variational Autoencoders	113
Aleksei Vasilev, Vladimir Golkov, Marc Meissner, Ilona Lipp, Eleonora Sgarlata, Valentina Tomassini, Derek K. Jones, and Daniel Cremers	
DWI Simulation-Assisted Machine Learning Models for Microstructure Estimation	125
Jonathan Rafael-Patino, Thomas Yu, Victor Delvigne, Muhamed Barakovic, Marco Pizzolato, Gabriel Girard, Derek K. Jones, Erick J. Canales-Rodríguez, and Jean-Philippe Thiran	
Convolutional Neural Network on DTI Data for Sub-cortical Brain Structure Segmentation	135
G. R. Pinheiro, D. S. Carmo, C. Yasuda, R. A. Lotufo, and L. Rittner	
Diffusion MRI Outside the Brain and Clinical Applications	
A Framework to Construct a Longitudinal DW-MRI Infant Atlas Based on Mixed Effects Modeling of dODF Coefficients	149
Heejong Kim, Martin Styner, Joseph Piven, and Guido Gerig	
Investigation of Changes in Anomalous Diffusion Parameters in a Mouse Model of Brain Tumour	161
Qianqian Yang, Simon Puttick, Zara C. Bruce, Bryan W. Day, and Viktor Vegh	
A Network-Based Analysis of the Preterm Adolescent Brain Using PCA and Graph Theory	173
Hassna Irzan, Michael Hütel, Carla Semedo, Helen O'Reilly, Manisha Sahota, Sebastien Ourselin, Neil Marlow, and Andrew Melbourne	
Diffusion MRI Fiber Tractography by Flow Field Formation with Extended Physarum Solver: A Pilot Study with 2D Phantoms	183
Yoshitaka Masutani	

CDMRI’19 MUDI Challenge

**Acquiring and Predicting Multidimensional Diffusion (MUDI) Data:
An Open Challenge 195**

Marco Pizzolato, Marco Palombo, Elisenda Bonet-Carne,
Chantal M. W. Tax, Francesco Grussu, Andrada Ianus, Fabian Bogusz,
Tomasz Pieciak, Lipeng Ning, Hugo Larochelle, Maxime Descoteaux,
Maxime Chamberland, Stefano B. Blumberg, Thomy Mertzanidou,
Daniel C. Alexander, Maryam Afzali, Santiago Aja-Fernández,
Derek K. Jones, Carl-Fredrik Westin, Yogesh Rathi, Steven H. Baete,
Lucilio Cordero-Grande, Thilo Ladner, Paddy J. Sator, Joseph V Hajnal,
Jean-Philippe Thiran, Anthony N. Price, Farshid Sepehrband,
Fan Zhang, and Jana Hutter

Index 209

Diffusion MRI Signal Acquisition and Processing Strategies

Connectome 2.0: Cutting-Edge Hardware Ushers in New Opportunities for Computational Diffusion MRI



Anastasia Yendiki, Thomas Witzel, and Susie Y. Huang

Abstract The first phase of the Human Connectome Project pioneered advances in MRI technology, including ultra-high gradients and accelerated sequences, that have now found their way into commercially available scanners. These technologies have led to a dramatic improvement in the spatial, angular, and diffusion resolution that is feasible in vivo. However, they still fall short of the scale where the microstructural properties of cells in the human brain can be measured accurately. Here we present an overview of the Connectome 2.0 project, which aims to bridge this gap by building the next-generation instrument for imaging microstructure and connectational anatomy in the human brain.

1 Introduction

Less is known about the structure-function relationship in the human brain than in any other organ system. Establishing the cellular composition and the connectational organization of the living human brain is essential for understanding and predicting the functional signals that underlie cognition and behavior. A necessary foundation and enormous challenge for human systems neuroscience is defining the connectome, the complete set of structural connections of the nervous system, on multiple scales: the macro-connections between gray-matter regions, meso-connections between neurons and other cell types, and micro-connections between individual neurons.

This work is supported by NIH/NIBIB award U01-EB026996.

A. Yendiki (✉) · S. Y. Huang

Athinoula A. Martinos Center for Biomedical Imaging, Department of Radiology, Harvard Medical School & Massachusetts General Hospital, Charlestown, MA, USA
e-mail: ayendiki@mgh.harvard.edu

S. Y. Huang

e-mail: susie.huang@mgh.harvard.edu

T. Witzel

Q bio Inc, San Carlos, CA, USA
e-mail: thomas@q.bio

© Springer Nature Switzerland AG 2020

E. Bonet-Carne et al. (eds.), *Computational Diffusion MRI*,

Mathematics and Visualization, https://doi.org/10.1007/978-3-030-52893-5_1

Today, there is no imaging modality that can span this enormous range of size scales in the living human brain. While magnetic resonance imaging (MRI) allows imaging a whole brain with $\sim 1 \text{ mm}^3$ voxels, an electron microscope (EM) can render the connections between individual neurons, axons and dendrites with voxels of less than 100 nm^3 —a range spanning 16 orders of magnitude of volume. The ideal technology for understanding the structural and functional organization of the living human brain would integrate across these scales and would be sensitive to changes across time (e.g., as a result of neural plasticity, development, and pathology) and between individuals.

Towards this goal, the Connectome 2.0 project targets the development of the next-generation human connectomics and microstructure MRI scanner, tailored for inferring cellular size, morphology, and density at unprecedented spatial and diffusion resolution throughout the whole brain, while providing greater sensitivity and imaging speed for structural and functional imaging at multiple scales in living human subjects. This transformative advance in imaging the micro-, meso-, and macroscopic structure of the living human brain builds on the experience of engineering and testing the first human MRI scanner equipped with 300 mT/m gradients, the highest gradient strength achieved for a human scanner to date, which was developed as part of the Human Connectome Project (HCP) [1]. In the following, we describe the planned hardware design of the Connectome 2.0 scanner, and the opportunities that it will usher in for the analysis of microstructure and connectional anatomy in the human brain.

2 Limitations of the Current State of the Art

Diffusion MRI (dMRI) holds the most promise among noninvasive methods for imaging cellular structure of any depth and location in the human brain. Imaging molecular self-diffusion with MRI can probe a multitude of microstructural parameters (e.g., cell size, shape, and packing density) whose cellular scale dimensions ($\sim \mu\text{m}$) are orders of magnitude smaller than the imaged voxel size ($\sim \text{mm}$). However, robust methods for performing dMRI-based microstructural mapping in vivo remained elusive for a long time due to the requirement for fast and strong diffusion-encoding gradients, which limited such experiments to ex vivo and animal studies on small-bore MRI systems. The HCP era marked the availability of ultra-high gradient strengths on human MRI scanners, making such methods practical for the in vivo human brain. Specifically, our original Connectome scanner, featuring a maximum gradient strength (G_{max}) of 300 mT/m and maximum slew rate (SLR_{max}) of 200 T/m/s , enabled in vivo axon diameter mapping with a diffusion resolution limit of $3\text{--}4 \mu\text{m}$ [2, 3].

However, within the technical limits of this initial prototype, resolutions approaching the size of many smaller axons ($\sim 1 \mu\text{m}$ or even less) are not feasible. Furthermore, the pulsed gradient spin echo (PGSE) experiment, which is most commonly used

for dMRI, performs best in evaluating macroscopically anisotropic diffusion arising from well-oriented structures, such as fiber bundles in white matter. The sensitivity of PGSE to compartment size and morphology decreases with increasing heterogeneity of the tissue microenvironment and is thus highly limited in capturing the structural diversity of cells in the brain. Alternative and complementary diffusion encoding approaches have thus been proposed to access the micron to sub-micron length scale with sufficient sensitivity in the complex microenvironment of the human brain. These approaches require not only higher G_{\max} but also higher slew rates to expand the range of gradient waveforms that can be played out for in vivo human microstructural imaging.

3 The Connectome 2.0

Equipped with the lessons on advanced gradient design learned from our initial HCP experience, we are now in a position to redesign the gradient system of the Connectome scanner in full and to enable ultra-fast slew rate as well as ultra-high gradient strength. This advance represents a great technical challenge that is necessary for implementing state-of-the-art diffusion encoding strategies robustly in vivo and gaining sensitivity to the actual range of cellular sizes and morphologies in the human brain. Specifically, the goals of the Connectome 2.0 project are to (1) nearly double the current G_{\max} to 500 mT/m and triple the SLR_{\max} to 600 T/m/s; (2) push the limits of the RF receive coils and gradient characterization to enable maximum sensitivity and real-time eddy current corrected dMRI acquisitions; (3) combine this hardware with pulse-sequence advances to reach for the highest diffusion and spatial resolution ever achieved in vivo; and (4) calibrate the measurements obtained from this next-generation instrument through systematic validation of diffusion microstructural metrics *ex vivo*.

The targeted gradient performance boost will be accomplished by taking advantage of next-generation gradient amplifiers, with 33% increased power compared to those used on the original Connectome scanner, as well as a newly designed head-only gradient coil with improved efficiency and optimized peripheral nerve stimulation (PNS) characteristics.

Increasing the diffusion resolution to approach the typical size of cells and axons in the brain requires shortening the diffusion times with higher slew rates, while making sure that high q -values can still be attained, thereby requiring high G_{\max} . Currently, PNS is the limiting factor of the maximum usable slew rate for a given gradient waveform with a given peak gradient strength. Therefore, maximizing PNS thresholds is critical for the design of the new gradient. To this end, we have access to novel simulation tools for accurate prediction of stimulation thresholds, combining realistic whole-body human nerve models with electric field simulation in a realistic multi-tissue human body model [4].

Since the original design of the Connectome scanner over nine years ago, magnetic field cameras have become available commercially that will allow us to monitor and to correct for the eddy currents that arise due to interactions between the gradient coil and magnet. Dynamic field monitoring and state-of-the-art image reconstruction techniques that incorporate the monitored field data will be critical for enhancing image quality and precision of the acquired diffusion measurements [5]. Importantly, monitoring and correcting for eddy current artifacts on the hardware level would obviate the need for extensive post-processing, thus avoiding unnecessary degradation of image resolution.

Quantitative dMRI requires long-term signal stability beyond that required of typical clinical MRI systems. With the goal of achieving precision of diffusion measurements similar to that of pre-clinical (animal) research MRI devices, the new scanner will feature a high-stability RF transmit system and constant temperature control of tissue specimens for ex vivo imaging, which will be key for our validation studies. A major design change associated with revamping the scanner to allow for the increased slew rates is omission of the RF shield typically laminated to the inside of the gradient coil and replacement of the body transmit coil with a new local head-only transmit coil.

As part of the HCP, a custom 64-channel receive-array coil was developed for the original Connectome scanner, enabling the highest-SNR, accelerated human brain imaging at 3 T to date [6]. Building on this experience, the Connectome 2.0 effort involves the construction of a 72-channel, extended field-of-view coil for in vivo imaging in the new system. The new coil will combine the sensitivity of the 64-channel head-only coil and coverage of the 64-channel head-neck array [7] that was also built for the original Connectome scanner to enable maximum sensitivity imaging of the whole brain in vivo. An integrated, 16-channel, clip-on field camera will allow monitoring the B_0 and gradient fields simultaneously with the dMRI acquisition.

A 64-channel array coil for imaging whole ex vivo human brains in the new system is also planned, following the design of a recently developed 48-channel array coil for ex vivo imaging in the original Connectome scanner [8]. This design involves a human brain-shaped coil geometry, allowing all coil elements to be adjacent to the ex vivo brain for optimal sensitivity. Placing the entire setup in a sealed box with a controlled-temperature air supply will ensure the temperature stability that is critical for the accuracy and reproducibility of diffusion measurements during very long ex vivo scans.

The aforementioned hardware advances will be combined with recent developments in dMRI pulse sequence design to enable sub-mm spatial resolution with whole-brain coverage in vivo. Due to SNR limitations, even the highest-performing systems used in the HCP have only been able to achieve 1.25–1.5 mm isotropic resolution with parallel imaging and simultaneous multi-slice/multi-band techniques [1]. Since then, a simultaneous multi-slab method, combining a novel, “slice-dithered” RF slab encoding scheme (gSlider-SMS) [9] with blipped-controlled aliasing has been shown to enable SNR-efficient, whole-brain diffusion microstructural imaging at 650 μm isotropic resolution. This approach can acquire data from 10–15 imaging

slices across 2–3 thin slabs simultaneously. We will deploy this approach on the Connectome 2.0 system to achieve sub-mm spatial resolution with a variety of diffusion encoding schemes.

4 Opportunities for Computational Diffusion MRI

The unprecedented dMRI acquisitions enabled by the Connectome 2.0 project open up exciting new opportunities for image reconstruction and analysis research. Here we focus on two areas of interest, microstructural modeling and connectional anatomy.

4.1 Microstructural Modeling

With the advent of higher gradient strengths for in vivo dMRI, we anticipate an expansion in the range and depth of diffusion-encoding experiments that can be performed for inferring cellular structure and connectivity within and between cortical regions. The major benefits of $G_{\max} = 500$ mT/m and $\text{SLR}_{\max} = 600$ T/m/s for dMRI are: (1) decreasing the diffusion time Δ needed to achieve the same diffusion-encoding gradient area, and (2) shortening TE, thereby reducing signal losses from T_2 processes. Figure 1 shows the minimum TE simulated for a standard PGSE experiment as a function of b -value for different maximum gradient strengths. The minimum TE is shown for a gradient strength of 80, 300, and 500 mT/m. The largest reduction in TE and Δ occurs for high b -values. The SNR scales exponentially with TE and should thus improve considerably for the next-generation Connectome scanner. The effect of shortening the diffusion time is particularly advantageous for probing tissue microstructure, as shorter diffusion times are expected to sharpen features in the spin probability distribution function. The near-doubling of G_{\max} to 500 mT/m will also act synergistically with shorter Δ to increase sensitivity to small compartment sizes.

We will take advantage of these new capabilities by using a suite of pulse sequences with different types of diffusion encoding for inferring the size, shape, and orientation distribution of neurons, glial cells, dendrites, and axons in the complex micro-environment of the human brain. Below, we describe several key sequences in this dMRI suite and the explicit benefits that the new gradient system will bring to bear on these measurements. The overall goal is to achieve unprecedented diffusion resolution for exquisite characterization of cortical, subcortical, and white-matter microstructure.

The conventional PGSE sequence performs best in evaluating macroscopically anisotropic diffusion arising from well-oriented structures, such as parallel fibers in white-matter bundles, and has been used for quantifying axon diameter and density through approaches such as AxCaliber [10]. However, the diffusion resolution of PGSE, even with $G_{\max} = 300$ mT/m, is only ~ 3 μm [11]. This is larger than the

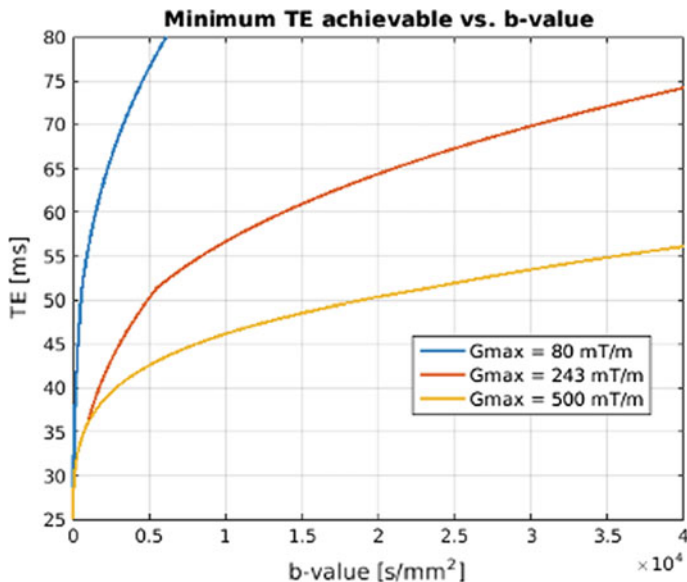


Fig. 1 Minimum TE obtained for PGSE as a function of b -value for different gradient strengths

actual diameter of most axons in the brain ($\sim 1 \mu\text{m}$ or less) [12]. The proposed gradient system, with near-doubling of G_{max} to 500 mT/m and tripling of SLR_{max} to 600 T/m/s, will enable us to increase the resolution limit of axon diameter estimation by PGSE by nearly two times through the synergistic effect of increased sensitivity to small compartment sizes with shorter duration diffusion-encoding gradients and increased SNR with shorter effective TE. These improvements will enable us to estimate axon diameters approaching $1 \mu\text{m}$ with better differentiation and less noise in the estimates (Fig. 2). The increase in resolution is crucial to making the distinction between large and small axonal fiber populations, such as axons projecting from motor and prefrontal cortex, respectively, which fall exactly in the range of $1\text{--}2 \mu\text{m}$ and are just barely discernible with the current generation gradient system.

In reality, the orientation of cells and axons varies across the brain, and even the most homogeneous areas of white matter, e.g., corpus callosum, still show some dispersion at the voxel level. Oscillating gradient spin echo (OGSE) is an experimentally viable alternative to PGSE, with higher sensitivity to cellular and axonal size in the presence of orientation dispersion. Due to the inverse relationship of diffusion time with gradient oscillation frequency, OGSE can achieve short effective diffusion times (~ 1 ms), whereas in PGSE the diffusion time is limited to > 10 ms by the duration of the 180 refocusing pulse. So far, OGSE has been largely limited to small-bore systems due to the fast slew rates needed to maximize the diffusion-encoding gradient area. Figure 2 (bottom panel) shows that in the case of dispersed fibers, the maximum sensitivity for small diameter axons is achieved for OGSE rather than PGSE. In this scenario, OGSE is beneficial because it yields high sensitivity at modest b -value. The

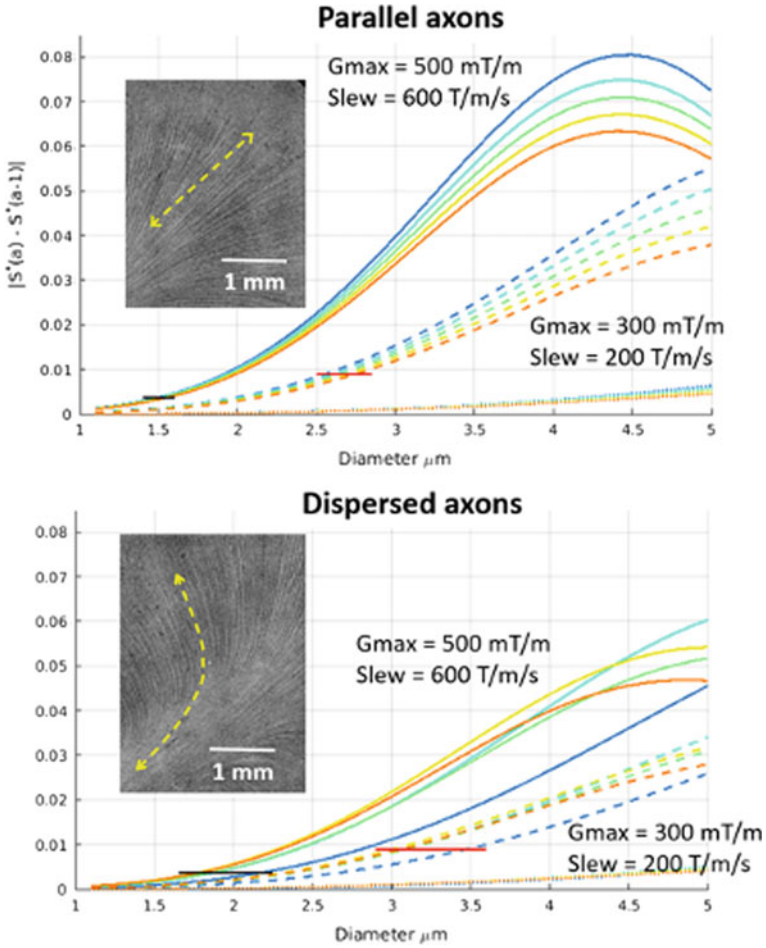


Fig. 2 Resolution limit of PGSE (blue) and OGSE (other colors) for the Connectome 2.0 (solid lines) versus the first-generation scanner (dashed line) in **(TOP)** parallel cylinders and **(BOTTOM)** dispersed cylinders mimicking axons (inset: optical images of axons in human temporal lobe)

lower b -value retains signal sensitivity in the cases of unknown fiber direction and/or dispersion by avoiding excessive signal attenuation due to freely diffusing water [13]. This is particularly advantageous for systems with high-performance gradients, as the area under the diffusion-encoding gradient for OGSE increases with high slew rate. Our redesigned gradient system with stronger G_{max} and increased SLR_{max} will enable OGSE to achieve higher sensitivity to small-diameter cells/axons compared to the current system.

The cortex is challenging to image with dMRI, as it appears isotropic at the macroscopic scale, but is actually composed of highly anisotropic structures on the meso- to microscopic scale. These structures (dendrites, axons, and other neural/glial pro-

cesses) are oriented in a random fashion and intermixed with neuronal and glial cell bodies in gray matter. Gaining sensitivity to these microscopically anisotropic, but macroscopically isotropic, domains in gray matter requires two or more diffusion-encoding periods through a double (or higher-order) pulsed field gradient (DPFG) sequence. The DPFG and related sequences are well-established in materials science but have not been practically implemented in humans due to limited gradient strength and low SNR resulting from multiple diffusion-encoding periods on conventional scanners. The availability of ultra-high G_{\max} would enable DPFG to be performed in vivo with better SNR than ever before, allowing us to gain sensitivity to microscopically oriented domains in gray matter, which we have begun to uncover with diffusion orientation using PGSE [14] but remain incompletely characterized with single pulsed field gradients. The relevant metrics derived from these experiments could serve as a sensitive probe of laminar architecture by distinguishing areas with different microscopic anisotropy (e.g., randomly arranged spheres representative of cell bodies) or compartment shape anisotropy (e.g., randomly oriented ellipsoids representative of neural/glial processes).

4.2 *Connectional Anatomy*

Refining the reconstructions of connectional anatomy that we can obtain from individual, rather than group-averaged, dMRI data is crucial, as neuroimaging studies are currently shifting from group-level comparisons to subject-level prediction [15]. This shift, which is attempting to harness the recent advances in machine learning, will only be as successful as the data quality of individual scans allows. The data collected on our current Connectome scanner has allowed us to reproduce detailed topographies of smaller axon bundles within the large pathways of the human brain, which had been demonstrated previously in non-human primates with anatomical tracer studies [16]. These topographies cannot be identified in the conventional human dMRI scans that had been commonplace before the HCP era. The ability to do this in pathways that have a topographic organization, such as the internal capsule or the corpus callosum, is an advance with neuroscientific and clinical significance. Localizing microstructural alterations to a specific “lane” within a large white-matter highway provides a critical link between the alteration and the cortical or subcortical regions that it is likely to affect, thus facilitating comparison and integration with functional data.

However, even at the 1.5 mm resolution of our MGH-USC HCP data, some of the aforementioned topographies are difficult to resolve within a tightly packed pathway like the internal capsule (see [16]). Furthermore, our recent validation studies in *post mortem* human white-matter samples, which undergo both dMRI and polarization-sensitive optical coherence tomography scans, suggest that reducing the dMRI voxel size from 2 mm to 1 mm affords a substantial improvement in the accuracy of the estimated orientations [17]. Thus the improvements in spatial resolution and SNR that we expect from the Connectome 2.0, owing to the combination of higher gra-

dient strengths and accelerated acquisition methods discussed above, will be critical for dMRI-based connectional anatomy to take the leap from mapping highways to mapping lanes.

Furthermore, the advanced diffusion encoding schemes that are planned for the Connectome 2.0 (see previous section) may provide more information on the geometry of axon bundles, beyond what is available in conventional PGSE data. Ultimately, however, improvements in data acquisition alone will not be sufficient for improving the accuracy of dMRI tractography. The current analytical paradigm relies on a data reduction step, which consists in the reconstruction of peaks, sticks, or a continuous distribution thereof. This step introduces ambiguity that would persist even if we could achieve infinite SNR and infinitesimal angular resolution. When processing the sort of dMRI data that had been commonplace until recently, there is a rationale for such data reduction approaches. However, as the data that we can acquire are set to improve drastically in the next few years, we must be mindful of whether such analysis techniques are still the best way forward. We expect that the Connectome 2.0 will provide the impetus for rethinking this paradigm in fundamental ways.

5 Validation

Validation of microstructural metrics derived from dMRI will be an essential part of the Connectome 2.0 effort, as these metrics represent indirect inferences on cellular/axonal size and morphology. To this end, we will obtain gold-standard measurements with micro-computed tomography (CT) and EM. Micro-CT, in particular, serves as a crucial tool for bridging scales, as it combines the contrast of gold-standard EM with cellular scale resolution that is within the range of the finest diffusion length scales we can interrogate ($\sim 500\text{ nm}$ – $1\mu\text{m}$), but with a much larger field of view ($\sim\text{cm}$) than EM.

6 Conclusion

The Connectome 2.0 project aims to develop the next-generation MRI scanner for interrogating the wiring of the human brain across the macro-, meso-, and microscale. The ability to collect such measurements *in vivo* over the entire human brain promises to be the next leap towards understanding how segregated and distributed function is affected by structural changes in cortical, subcortical, and white-matter regions, across behaviors thought to modify brain structure and connectivity in health and disease.

References

1. Setsompop, K., et al.: Pushing the limits of in vivo diffusion MRI for the human connectome project. *Neuroimage* **80**, 220–33 (2013)
2. Huang, S.Y., et al.: The impact of gradient strength on in vivo diffusion MRI estimates of axon diameter. *Neuroimage* **106**, 464–72 (2015)
3. Huang, S.Y., et al.: High-gradient diffusion MRI reveals distinct estimates of axon diameter index within different white matter tracts in the in vivo human brain. *Brain Struct. Funct.* **225**(4), 1277–1291 (2020)
4. Davids, M., et al.: Predicting magnetostimulation thresholds in the peripheral nervous system using realistic body models. *Sci. Rep.* **7**(1), 5316 (2017)
5. Wilm, B.J., et al.: Higher order reconstruction for MRI in the presence of spatiotemporal field perturbations. *Magn. Reson. Med.* **65**(6), 1690–701 (2011)
6. Keil, B., et al.: A 64-channel 3T array coil for accelerated brain MRI. *Magn. Reson. Med.* **70**(1), 248–58 (2013)
7. Keil, B. et al.: A 64-channel array coil for 3T head/neck/C-spine imaging. In: *Proceedings of the International Society for Magnetic Resonance in Medicine*, p. 160 (2011)
8. Scholz, A. et al.: A 48-channel ex vivo brain array coil for diffusion-weighted MRI at 3T. In: *Proceedings of the International Society for Magnetic Resonance in Medicine*, p. 1494 (2019)
9. Setsompop, K., et al.: High-resolution in vivo diffusion imaging of the human brain with generalized slice dithered enhanced resolution: Simultaneous multislice (gSlider-SMS). *Magn. Reson. Med.* **79**(1), 141–151 (2018)
10. Assaf, Y., et al.: AxCaliber: a method for measuring axon diameter distribution from diffusion MRI. *Magn. Reson. Med.* **59**(6), 1347–1354 (2008)
11. Nilsson, M., et al.: Resolution limit of cylinder diameter estimation by diffusion MRI: the impact of gradient waveform and orientation dispersion. *NMR Biomed.* **30**(7), (2017)
12. Waxman, S.G., et al.: *The Axon: Structure. Function and Pathophysiology*. Oxford University Press, New York (1995)
13. Drobnjak, I., et al.: PGSE, OGSE, and sensitivity to axon diameter in diffusion MRI: insight from a simulation study. *Magn. Reson. Med.* **75**(2), 688–700 (2016)
14. McNab, J.A., et al.: Surface based analysis of diffusion orientation for identifying architectonic domains in the in vivo human cortex. *Neuroimage* **69**, 87–100 (2013)
15. Gabrieli, J.D.E., et al.: Prediction as a humanitarian and pragmatic contribution from human cognitive neuroscience. *Neuron* **85**(1), 11–26 (2015)
16. Safadi, Z., et al.: Functional segmentation of the anterior limb of the internal capsule: linking white matter abnormalities to specific connections. *J. Neurosci.* **38**(8), 2106–17 (2018)
17. Jones, R.J., et al.: Insight into the fundamental trade-offs of diffusion MRI from polarization-sensitive optical coherence tomography in ex vivo human brain. *NeuroImage* **214**, 116704 (2020)

Alternative Diffusion Anisotropy Metric from Reduced MRI Acquisitions



Santiago Aja-Fernández, Antonio Tristán-Vega, Rodrigo de Luis-García, and Derek K. Jones

Abstract A novel diffusion anisotropy metric is presented. It is based on dissimilarity between the acquired diffusion signal and its isotropic equivalent. Using the inner product of signals, a closed form expression is obtained, which allows its computation using spherical harmonics from a reduced set of acquired data, compatible with most popular diffusion MRI acquisition protocols. Results show that the proposed metric (1) is able to discriminate among different microstructure scenarios; (2) shows a robust behaviour in clinical studies.

1 Introduction

The term Diffusion Magnetic Resonance Imaging (DMRI) refers to a set of diverse imaging techniques that, applied to brain studies, provide useful information about the organization and connectivity of the white matter. The most relevant feature of DMRI is its ability to measure orientational variance in the different tissues, i.e. anisotropy. Nowadays, the most common way to estimate the anisotropy is via the popular diffusion tensor (DT) approach [6]. DT-MRI brought to light one of the most common problems in DMRI techniques: in order to carry out clinical studies, the information given by the selected diffusion analysis method must be translated into some scalar measures that describe different features of the diffusion within every voxel. That way, metrics like the Fractional Anisotropy (FA) were defined with the DT as a starting point [18]. Despite the strong limitations the underlying Gaussian assumption imposes on the diffusion model, the FA is still widely used in clinical studies involving DMRI.

However, the diffusion mechanisms cannot be accurately described by DT-MRI because of the oversimplified Gaussian fitting. Accordingly, more evolved techniques

S. Aja-Fernández (✉) · A. Tristán-Vega · R. de Luis-García
Laboratorio de Procesado de Imagen (LPI), E.T.S. Ingenieros de Telecomunicación,
Universidad de Valladolid, Valladolid, Spain
e-mail: sanaja@tel.uva.es

S. Aja-Fernández · D. K. Jones
CUBRIC, Cardiff University, Cardiff, UK

with more degrees-of-freedom naturally arose, such as High Angular Resolution Diffusion Imaging (HARDI) [14, 17] or Diffusion Kurtosis Imaging [11]. The trend over the last decade has consisted in acquiring a large number of diffusion-weighted images distributed over several shells (i.e. with several gradient strengths) and with moderate-to-high b-values to estimate more advanced diffusion descriptors, as the Ensemble Average Diffusion Propagator (EAP) [13].

Regardless of the method selected to describe diffusion, practical applications often use only a reduced set of scalar measures derived from it. Most of these measures are devoted to quantifying different aspects of anisotropy or diffusion directionality, like the Kurtosis Fractional Anisotropy (KFA) [11], the Propagator Anisotropy (PA) [13] or the Generalized Anisotropy (GA) [15]. These alternative anisotropy measures have shown, under certain constraints, higher tissue contrast than the FA in white matter [4].

Nonetheless, these measures have also some drawbacks. For example, both PA and KFA require large amounts of data to be effectively estimated, which involves long scanning times. This issue has slowed down a widespread clinical adoption of such measures. Others, like the GA, have shown a great sensibility to changes in the acquisition parameters, such as the number of gradients, the SNR, the b-value or the resolution [1].

The present paper proposes a novel diffusion anisotropy metric based on the *distance* from the actual diffusion signal to its isotropic equivalent. We achieve a closed-form expression that allows its estimation from a reduced amount of diffusion-weighted signals, even from a single shell, compatible with acquisition protocols commonly used for DTI and HARDI and therefore applicable to data acquired within the clinical domain. The new metric is extensively tested against other anisotropy-based indices to check its capability to detect different configurations and its performance in the analysis of clinical data. The full implementation of the proposed methods may be downloaded for Matlab from <http://www.lpi.tel.uva.es/AMURA>.

2 Theory

2.1 The Diffusion Signal

The EAP, $P(\mathbf{R})$, is the three dimensional Probability Density Function (PDF) of the water molecules inside a voxel moving an effective distance \mathbf{R} in an effective time τ . It is related to the normalized magnitude image provided by the MRI scanner, $E(\mathbf{q})$, by the Fourier transform [8]:

$$P(\mathbf{R}|\tau) = \mathfrak{F}\{|E(\mathbf{q})|\}(\mathbf{R}). \quad (1)$$

With the purpose of obtaining a closed-form analytical solution from a reduced number of acquired images, a model of the diffusion behaviour must be adopted. The

most common techniques rely on the assumption of a Gaussian diffusion profile and a steady state regime of the diffusion process that yields the well-known Diffusion Tensor (DT) approach. Alternatively, a more general expression for $E(\mathbf{q})$ can be used [14]:

$$E(\mathbf{q}) = \exp(-4\pi^2\tau q_0^2 D(\mathbf{q})) = \exp(-b \cdot D(\mathbf{q})), \quad (2)$$

where the positive function $D(\mathbf{q}) = D(q_0, \theta, \phi)$ is the *diffusivity signal*, also known as the Apparent Diffusion Coefficient (ADC), $b = 4\pi^2\tau\|\mathbf{q}\|^2$ is the b-value, τ is the effective diffusion time and $q_0 = \|\mathbf{q}\|$ and θ, ϕ are the angular coordinates in the spherical system. According to [5], in the mammalian brain, this monoexponential model is predominant for values of b up to 2000 s/mm² and it can be extended to higher values if appropriate multicompartment models of diffusion are used.

2.2 Inner Product and Propagator Anisotropy

Let $S_1(\mathbf{q})$ and $S_2(\mathbf{q})$ be two generic signals defined over a common signal space \mathcal{Q} . The inner product is defined as [10]:

$$\langle S_1(\mathbf{q}), S_2(\mathbf{q}) \rangle = \int_{\mathbb{R}^3} S_1(\mathbf{q}) S_2^*(\mathbf{q}) d\mathbf{q}. \quad (3)$$

We can accordingly define the norm of a signal as

$$\|S(\mathbf{q})\| = \langle S(\mathbf{q}), S(\mathbf{q}) \rangle^{1/2} = \left(\int_{\mathbb{R}^3} |S(\mathbf{q})|^2 d\mathbf{q} \right)^{1/2}. \quad (4)$$

The *similarity* of two signals is measured as the cosine of the angle:

$$\cos(\angle[S_1(\mathbf{q}), S_2(\mathbf{q})]) = \cos\theta_{S_1, S_2} = \frac{\langle S_1(\mathbf{q}), S_2(\mathbf{q}) \rangle}{\|S_1(\mathbf{q})\| \cdot \|S_2(\mathbf{q})\|}. \quad (5)$$

This property is exploited in [13] to define the so-called Propagator Anisotropy (PA), which can be seen as a quantification of how much the propagator diverges from an isotropic one.

2.3 Diffusion Anisotropy

In order to use a limited amount of acquisitions to estimate the anisotropy, we assume a prior model that assures that it can be estimated using data collected over one single shell. To that end, we have to consider that the diffusion $D(\mathbf{q})$ does not depend on the radial component, i.e. $D(\mathbf{q}) = D(\theta, \phi)$, so that Eq. (2) becomes:

$$E(\mathbf{q}) = E(q_0, \theta, \phi) = \exp(-4\pi^2 \tau q_0^2 D(\theta, \phi)). \quad (6)$$

Note that, although $D(\mathbf{q})$ no longer depends on q_0 , $E(\mathbf{q})$ does. This assumption, although restrictive, is used to define certain diffusion modalities in HARDI [9, 14], where only one shell is usually acquired. This simplification was initially intended to overcome the limitations of the DT by allowing the diffusion to be evaluated across many orientations, as opposed to the single orientation described by the DT.

In what follows, we define a new anisotropy metric restricting the result in Eq. (3) to the mono-exponential model in Eq. (6). The inner product of two ADCs now becomes:

$$\langle D_1(\mathbf{q}), D_2(\mathbf{q}) \rangle = \int_S D_1(\mathbf{q}) D_2^*(\mathbf{q}) d\mathbf{q}, \quad (7)$$

where S stands for the unit-sphere whose radius is defined by \mathbf{q} . Since the magnitude-reconstructed diffusion-weighted MR signal is always a real signal (and so is the ADC), $D_2^*(\mathbf{q}) = D_2(\mathbf{q})$. For estimating its anisotropy, the diffusion $D(\mathbf{q})$ is projected over the isotropic equivalent signal D_{AV} , defined as:

$$D_{AV} = \frac{1}{4\pi} \int_S D(\theta, \phi) dS. \quad (8)$$

Since isotropic diffusion, by definition, does not depend on the angles θ and ϕ , and since we are also assuming that our signals do not depend on the radial component either, D_{AV} becomes a constant value. Therefore, the inner product reduces to:

$$\langle D(\mathbf{q}), D_{AV}(\mathbf{q}) \rangle = D_{AV} \int_S D(\theta, \phi) dS. \quad (9)$$

At the same time, the norms can be written as

$$\|D(\mathbf{q})\|^2 = \int_S D^2(\theta, \phi) dS, \quad \|D_{AV}\|^2 = 4\pi D_{AV}^2. \quad (10)$$

The *Diffusion Anisotropy* (DiA) is defined as the sine of the angle:

$$\text{DiA} = \sin(\angle[D(\theta, \phi), D_{AV}]) = \sqrt{1 - \frac{[\int_S D(\theta, \phi) dS]^2}{4\pi \cdot \int_S D^2(\theta, \phi) dS}} \quad (11)$$

$$= \sqrt{\frac{\int_S D^2(\theta, \phi) dS - \frac{1}{4\pi} [\int_S D(\theta, \phi) dS]^2}{\int_S D^2(\theta, \phi) dS}}. \quad (12)$$

Note that the dependence with D_{AV} disappears. The DiA, as expressed in Eq. (12), resembles the structure of the FA, which can be seen as the square root of the variance

of the eigenvectors of the DT divided by their second-order moment. In order to increase the dynamic range of the metric, we can use the transformation proposed in [13] for the PA:

$$\gamma(t, \epsilon) = \frac{t^{3\epsilon}}{1 - 3t^\epsilon + 3t^{2\epsilon}}, \quad (13)$$

where $\epsilon = 0.4$. This way, the DiA can be alternatively defined as:

$$\text{DiA}\gamma = \gamma(\sin(\angle[D(\theta, \phi), D_{AV}]), \epsilon). \quad (14)$$

2.4 Practical Implementation

The newly defined DiA relies on the calculation of the integral of the diffusion signal over the surface of the unit sphere S . In practice, such an integral has to be estimated from sampled data, for which we use a Spherical Harmonics (SH) decomposition, where the zero-th coefficient is defined as $C_{0,0}\{H(\theta, \phi)\} = \frac{1}{\sqrt{4\pi}} \int_S H(\theta, \phi) dS$. It follows:

$$\text{DiA} = \left(\max \left\{ 1 - \frac{1}{\sqrt{4\pi}} \frac{C_{0,0}^2\{D(\theta, \phi)\}}{C_{0,0}\{D^2(\theta, \phi)\}}, 0 \right\} \right)^{1/2}. \quad (15)$$

This implementation can be seen as a generalization of the Coefficient of Variation of the Diffusion (CVD) defined in [1] as a robust alternative for the FA. Nonetheless, the CVD requires that the samples of the ADC were to be uniformly distributed over the sphere. This issue is circumvented in DiA by the use of SH.

3 Experiments and Results

For the following experiments, DiA and GA are implemented using SH expansions of even orders up to 6 in all cases, with a Tikhonov regularization parameter $\lambda = 0.006$. PA is calculated using the DIPY toolbox with anisotropic basis and radial order 6 [13]. Two different real data sets are used for the experiments:

1. Human Connectome Project (HCP)¹: we consider volume MGH1007 acquired in a Siemens 3T Connectome scanner with 4 different shells at $b = [1000, 3000, 5000, 10000]$ s/mm², with [64, 64, 128, 256] gradient directions each, in-plane resolution 1.5 mm, and slice thickness was 1.5 mm. The acquisition included 40 different baselines.

¹<https://ida.loni.usc.edu/login.jsp>.

- Public Parkinson's disease (PPD) database²: acquired in the Cyclotron Research Centre, University of Liège. It consists of 53 subjects in a Parkinson's disease (PD) study: 27 PD patients and 26 age, sex, and education-matched control subjects. Data were acquired on a Siemens 3T Magnetom scanner. Images were acquired with a twice-refocused spin-echo sequence with EPI readout at two b-values ($b = [1000, 2500] \text{ s/mm}^2$) along 120 encoding gradients that were uniformly distributed in space and 22 baseline images, were acquired. Acquisition parameters are TR = 6800 ms, TE = 91 ms. More information can be found in [19].

3.1 Visual Results

First, a visual comparison of the metrics is done using 3 axial slices (42, 52, 65) from the HCP volume. DiA and DiA_γ are calculated using a single shell for two different values, $b = [1000, 3000] \text{ s/mm}^2$. For the sake of comparison, we have also calculated FA and GA at $b = 1000 \text{ s/mm}^2$ and PA using all the available information (4 shells). Results are shown in Fig. 1. All the metrics show a similar look, highlighting those anisotropic areas inside of the white matter. DiA , as expected, shows little contrast, a fact that is corrected by DiA_γ . However, it is not the visual aspect what we are interested in, but the ability to discriminate differences inside the white matter.

To better understand the relation of the proposed metrics with the FA, in Fig. 2 we have created the 2D histograms (using a 100×100 grid for the bins) for each pair of metrics. The higher density of points is represented in red. Note that, although most points are distributed along a straight line, FA and DiA are not measuring the same features, since a dispersion of values can also be seen. For a better understanding of this *dispersion of values*, we also show the values of FA and DiA_γ for those voxels corresponding to the FA in the range [0.3–0.5]. Note that DiA_γ , as expected, shows a greater range of values that provides a wider range in certain regions.

3.2 Discrimination Analysis

In order to test the specificity of DiA to microstructure differences, a simulation is carried out. For the sake of simplicity, two compartment models with and without free-water compartment are considered. The intra-cellular compartment is modelled by a Cylinder $C_y(d, \theta, \phi, R)$ [2] and the extra-cellular is modelled by Zeppelin $Z_p(d_{\parallel}, d_{\perp}, \theta, \phi)$ or ball $B_I(d)$ [7]. In those cases in which $d = 3000 \mu\text{m}^2/\text{s}$, the isotropic ball corresponds to the free water. Five different voxel configurations are designed, with parameters tuned to yield the same FA = 0.6260 at $b = 1000 \text{ s/mm}^2$, see Table 1.

²https://www.nitrc.org/frs/?group_id=835.

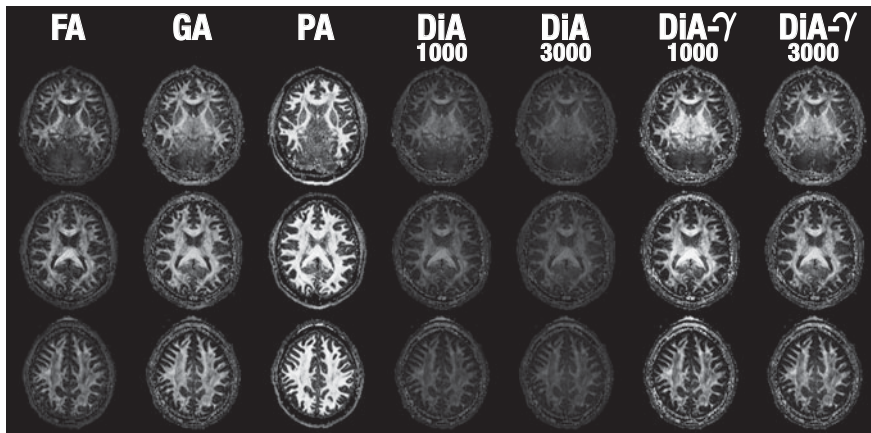


Fig. 1 Visual comparison of the diffusion anisotropy metrics using axial slices 42, 52 and 65 of the MGH1007 volume from HCP. FA and GA are calculated using $b = 1000$ s/mm², DiA and DiA γ using $b = [1000, 3000]$ s/mm² and PA using 4 shells (1000, 3000, 5000 and 10000 s/mm²)

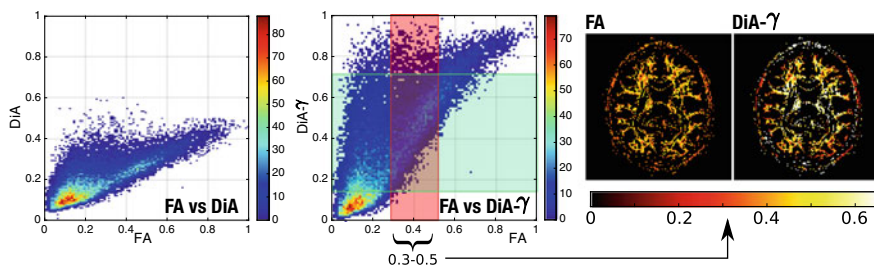


Fig. 2 2D histogram of FA (with $b = 1000$ s/mm²) compared to DiA and DiA γ (for $b = 3000$ s/mm²). The values of FA and DiA γ for those voxels with $FA \in [0.3-0.5]$ are also shown

In order to simulate the signal, we consider the following sampling scheme: 24 gradient directions uniformly distributed in each shell, 1 baseline, 4 different shells at $b = [1001, 2019, 3000, 4000]$ s/mm², $\Delta = 32.2$ ms, $\delta = 27.7$ ms and $|G| = [28.3, 40, 48.77, 56.30]$ mT/m. In order to statistically analyse the results, we corrupt the data with Rician noise with SNR = 40 in the baseline and carry out 30 realizations with the same parameters.

We calculate the PA using all available shells. The GA, DiA, and DiA γ are computed for each shell separately. In order to test the ability to discriminate the different configurations, a multiple comparison test is carried out over each of the metrics. Results can be found in Table 2.

In none of the cases was the FA able to discriminate between voxels, as expected, due to the design of the experiment. Similarly, at $b = 1000$ s/mm², GA, DiA and DiA γ are also unable to discriminate between voxels. However, as the b -value is increased, the ability of DiA and DiA γ to discriminate between voxels improves,

Table 1 Multicompartment voxels used in the simulation. The distribution and parameters of the models are set so that they have the same FA at $b = 1000 \text{ s/mm}^2$

Visual representation	Parameters
$V_1 = \frac{2}{3} \text{ (cylinder)} + \frac{1}{3} \text{ (sphere)}$	$V_1 = \frac{2}{3} C_y(800, 0, 0, 1) + \frac{1}{3} B_I(1854)$
$V_2 = \frac{2}{9} \text{ (cylinder)} + \frac{6}{9} \text{ (rod)} + \frac{1}{9} \text{ (sphere)}$	$V_2 = \frac{2}{9} C_y(1370, 0, 0, 1) + \frac{6}{9} Z_p(1359, 500, 0, 0) + \frac{1}{9} B_I(3000)$
$V_3 = \frac{5}{6} \text{ (rod)} + \frac{1}{6} \text{ (sphere)}$	$V_3 = \frac{5}{6} Z_p(2000, 500, 0, 0) + \frac{1}{6} B_I(3000)$
$V_4 = \text{ (rod)}$	$V_4 = Z_p(1589, 500, \pi/2, 0)$
$V_5 = \left\{ \begin{array}{l} \frac{2}{9} \text{ (cylinder)} + \frac{2}{9} \text{ (rod)} + \frac{1}{9} \text{ (sphere)} \\ \frac{2}{9} \text{ (cylinder)} + \frac{2}{9} \text{ (rod)} + \frac{1}{9} \text{ (sphere)} \end{array} \right.$	$V_5 = \frac{2}{9} C_y(2000, 0, 0, 1) + \frac{2}{9} Z_p(1906, 500, 0, 0) + \frac{2}{9} C_y(2000, \frac{\pi}{4}, 0, 1) + \frac{2}{9} Z_p(1906, 500, \frac{\pi}{4}, 0) + \frac{1}{9} B_I(3000)$

detecting most differences. PA shows also a robust behaviour, but note that it is calculated using 4 shells at the same time, which implies that it uses much more information than the other metrics (at the cost of requiring lengthy acquisitions).

All in all, we can say that DiA shows an ability to discriminate among different multi-compartment configurations for very different microstructural paradigms.

3.3 Validation with Clinical Data

Next, we intend to test the clinical potential of the new metrics, for which we have explored the PPD database. Parkinson disease is known to affect the substantia nigra or the gray matter more than white matter. However, significant differences have also been reported in several white matter regions such as the corpus callosum (CC), the corticospinal tract, or the fornix [3]. Since the aim of this experiment is testing the capability of the proposed metrics to probe the micro-structural properties of the white matter, we have accordingly focused on commonly-studied white matter tracts.

FA is calculated as a reference value using MRTRIX³ with the data at $b = 1000 \text{ s/mm}^2$. The FA maps of all the volumes are warped to a common template using the standard TBSS pipeline [16]. The same transformation is applied to all the metrics considered for the experiment (DiA, DiA γ , PA and GA). Two different analysis are considered:

³www.mrtrix.org.

Table 2 Multiple comparison test between 5 voxels with different microstructure (30 realizations). The p -values represent the probability that the metrics measured on different voxels have identical means. Values that does not show statistical significance above 99% (i.e. $p > 0.01$) are highlighted

	V_1-V_2	V_1-V_3	V_1-V_4	V_1-V_5	V_2-V_3	V_2-V_4	V_2-V_5	V_3-V_4	V_3-V_5	V_4-V_5
FA	1.00	1.00	0.99	0.99	1.00	0.99	0.99	0.99	0.99	1.00
PA	< 0.01	< 0.01	< 0.01	< 0.01	< 0.01	< 0.01	0.90	< 0.01	< 0.01	< 0.01
GA (1k)	0.96	1.00	0.82	0.60	0.95	0.99	0.97	0.80	0.57	0.99
GA (2k)	< 0.01	< 0.01	< 0.01	< 0.01	< 0.01	< 0.01	< 0.01	0.02	< 0.01	< 0.01
GA (3k)	< 0.01	< 0.01	< 0.01	< 0.01	< 0.01	< 0.01	< 0.01	< 0.01	0.09	< 0.01
GA (4k)	< 0.01	< 0.01	< 0.01	< 0.01	< 0.01	< 0.01	< 0.01	< 0.01	< 0.01	< 0.01
DiA- γ (1k)	0.72	0.97	0.91	0.95	0.24	0.14	0.20	0.99	1.00	1.00
DiA- γ (2k)	< 0.01	< 0.01	< 0.01	< 0.01	< 0.01	< 0.01	< 0.01	0.71	< 0.01	< 0.01
DiA- γ (3k)	< 0.01	< 0.01	< 0.01	< 0.01	< 0.01	< 0.01	< 0.01	< 0.01	< 0.01	< 0.01
DiA- γ (4k)	< 0.01	< 0.01	< 0.01	< 0.01	< 0.01	< 0.01	< 0.01	< 0.01	0.99	< 0.01
DiA (1k)	0.68	0.98	0.88	0.89	0.27	0.10	0.11	0.99	0.99	1.00
DiA (2k)	< 0.01	< 0.01	< 0.01	< 0.01	< 0.01	< 0.01	< 0.01	0.80	< 0.01	< 0.01
DiA (3k)	< 0.01	< 0.01	< 0.01	< 0.01	< 0.01	< 0.01	< 0.01	< 0.01	< 0.01	< 0.01
DiA (4k)	< 0.01	< 0.01	< 0.01	< 0.01	< 0.01	< 0.01	< 0.01	< 0.01	0.99	< 0.01

1. A voxelwise cross-subject analysis using the FA skeleton with the randomise tool from the FSL toolbox (which performs a nonparametric permutation inference over the data) with 500 realizations. Those voxels with < 0.01 are highlighted in Fig. 3. In blue, those points where the considered metric decreases in the PD with respect to the controls, in red where it increases.
2. A region of interest oriented analysis. 46 different white matter regions of interest are identified on the subjects using the JHU WM atlas [12]. For the sake of robustness, only the 21 regions larger than 2500 voxels are considered. The average value of the different measures inside each ROI is calculated using the `fslstats` tool from the FSL toolbox. Effect sizes were estimated using the Cohen's d . Results are depicted in Fig 4.

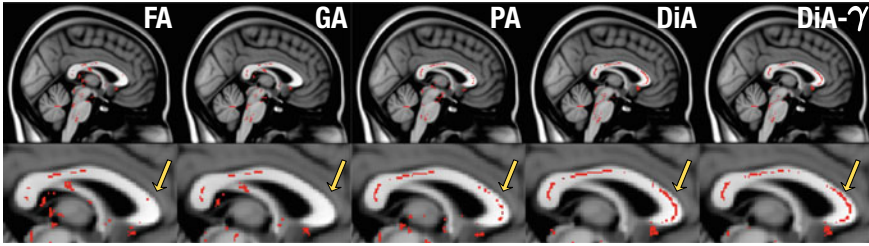


Fig. 3 Significant differences found by statistical test for the Parkinson database, using a voxelwise analysis over the FA skeleton for the different considered metrics (sagittal view). In color, the differences with statistical significance above 99% (< 0.01). In red, those points where the considered metric decreases in the PD with respect to the controls

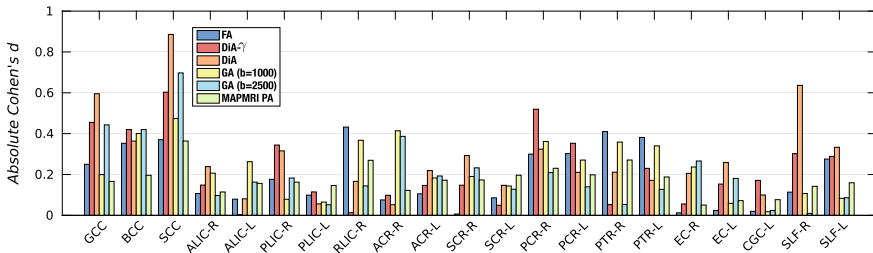


Fig. 4 Absolute value of effect sizes (Absolute Cohen's d) for the Parkinson data base. Labels are obtained from the JHU WM atlas. Only regions with more than 2500 voxels are considered

Since the aim of this experiment is testing the capability of the proposed measures to probe the micro-structural properties of the white matter, we have accordingly focused on the CC, where previous studies have reported relevant differences between PD and healthy controls. If we focus on this area in a sagittal plane, see Fig. 3, we can see that the FA only finds some isolated voxels with statistically significant differences. PA finds some extra voxels, but it cannot show its true potential due to the small b -values considered (higher b -values should result in more accurate EAP estimates). GA at $b = 2500$ s/mm² shows a behaviour very similar to the FA. On the other hand, only DiA and DiA γ find differences in the Genu of the CC (GCC), at the same time that they find more continuous values at the Splenium.

In the region-of-interest analysis, it is precisely in the same area (GCC, BCC and SCC) that the different measures show the greatest values of Cohen's d , see Fig. 4. Once again, DiA and DiA γ show larger effect sizes in most of the ROIs, with exception of the BCC, where all the metrics show low values. In addition, DiA shows a value of d greater than 0.6 in the superior longitudinal fasciculus (SLF-R), where the other measures show very low values. According to the analysis carried out in [19] for the same database, some differences can be found precisely in that ROI. The high value of DiA γ in the posterior corona radiata (PCR-R) is also reflected in that study.

4 Discussion and Conclusions

Two new diffusion anisotropy metrics have been presented, DiA and DiA γ , the latter being a gamma correction to adapt the dynamic range of the former. These measures are based on the projection of the diffusivity signal over its isotropic equivalent in order to quantify how much the ADC differs from a sphere. This way, we obtain a new approach to measure anisotropy from diffusion imaging.

The results we report point to a proper behavior of DiA for group analysis. In particular, the preliminary results of DiA over clinical data sets seems encouraging. DiA and DiA γ both showed a vast discrimination power, well above the FA in the experiments with both synthetic and real data, and partially better than PA. When tested over real data, DiA detects more patient-control differences in some areas of the brain (like the GCC and SCC) than the other anisotropy measures. Of course, since we do not have a gold-standard there is always the risk of false-positives, but results are consistent with other finding in the PD literature. In addition, synthetic experiments provide confidence in these results, since DiA shows the capability to differentiate configurations that the FA do not have.

Acknowledgements This work was supported by Ministerio de Ciencia e Innovación of Spain with research grants RTI2018-094569-B-I00 and PRX18/00253 (Estancias de profesores e investigadores senior en centros extranjeros).

The authors acknowledge Rutger H.J. Fick for providing his personal implementation of the MAP-MRI to estimate the PA. The authors are also grateful to Maryam Afzali from Cardiff University Brain Research Imaging Center for interesting discussion about MAP-MRI model and the multi-chamber experiment.

Data collection and sharing for this work was provided by (1) the *Human Connectome Project* (HCP; Principal Investigators: Bruce Rosen, M.D., Ph.D., Arthur W. Toga, Ph.D., Van J. Weeden, MD). HCP funding was provided by the National Institute of Dental and Craniofacial Research (NIDCR), the National Institute of Mental Health (NIMH), and the National Institute of Neurological Disorders and Stroke (NINDS). HCP data are disseminated by the Laboratory of Neuro Imaging at the University of Southern California; (2) the *High-quality diffusion-weighted imaging of Parkinson's disease* data base, Cyclotron Research Centre, University of Liège.

References

1. Aja-Fernández, S., Pieciak, T., Tristán-Vega, A., Vegas-Sánchez-Ferrero, G., Molina, V., de Luis-García, R.: Scalar diffusion-MRI measures invariant to acquisition parameters: a first step towards imaging biomarkers. *Magn. Reson. Imag.* **54**, 194–213 (2018)
2. Alexander, D.C.: A general framework for experiment design in diffusion MRI and its application in measuring direct tissue-microstructure features. *Magn. Reson. Med.* **60**(2), 439–448 (2008)
3. Atkinson-Clement, C., Pinto, S., Eusebio, A., Coulon, O.: Diffusion tensor imaging in Parkinson's disease: review and meta-analysis. *Neuroimage: Clin.* **16**, 98–110 (2017)
4. Avram, A.V., Sarlls, J.E., Barnett, A.S., Özarlan, E., Thomas, C., Irfanoglu, M.O., Hutchinson, E., Pierpaoli, C., Basser, P.J.: Clinical feasibility of using mean apparent propagator (MAP) MRI to characterize brain tissue microstructure. *NeuroImage* **127**, 422–434 (2016)

5. Basser, P.J.: Relationships between diffusion tensor and q-space MRI. *Magn. Reson. Med.* **47**(2), 392–397 (2002)
6. Basser, P., Pierpaoli, C.: Microstructural features measured using diffusion tensor imaging. *J. Magn. Reson. B* **111**(3), 209–219 (1996)
7. Behrens, T.E., Woolrich, M.W., Jenkinson, M., Johansen-Berg, H., Nunes, R.G., Clare, S., Matthews, P.M., Brady, J.M., Smith, S.M.: Characterization and propagation of uncertainty in diffusion-weighted MR imaging. *Magn. Reson. Med.* **50**(5), 1077–1088 (2003)
8. Callaghan, P., Eccles, C., Xia, Y.: Nmr microscopy of dynamic displacements: k-space and q-space imaging. *J. Phys. E: Sci. Instrum.* **21**(8), 820–822 (1988)
9. Descoteaux, M., Angelino, E., Fitzgibbons, S., Deriche, R.: Apparent diffusion profile estimation from high angular resolution diffusion images: estimation and applications. *Magn. Reson. Med.* **56**(2), 395–410 (2006)
10. Gallager, R.G.: Principles of Digital Communication. Cambridge University Press Cambridge, Cambridge, UK (2008)
11. Hansen, B., Jespersen, S.N.: Kurtosis fractional anisotropy, its contrast and estimation by proxy. *Sci. Rep.* **6**, 23999 (2016)
12. Mori, S., Wakana, S., Van Zijl, P.C., Nagae-Poetscher, L.: MRI Atlas of Human White Matter. Elsevier (2005)
13. Özarslan, E., Koay, C.G., Shepherd, T.M., Komlosh, M.E., Irfanoğlu, M.O., Pierpaoli, C., Basser, P.J.: Mean apparent propagator (MAP) MRI: a novel diffusion imaging method for mapping tissue microstructure. *NeuroImage* **78**, 16–32 (2013)
14. Özarslan, E., Sepherd, T.M., Vemuri, B.C., Blackband, S.J., Mareci, T.H.: Resolution of complex tissue microarchitecture using the Diffusion Orientation Transform (DOT). *NeuroImage* **31**, 1086–1103 (2006)
15. Özarslan, E., Vemuri, B.C., Mareci, T.H.: Generalized scalar measures for diffusion MRI using trace, variance, and entropy. *Magn. Reson. Med.* **53**(4), 866–876 (2005)
16. Smith, S.M., Jenkinson, M., Johansen-Berg, H., Rueckert, D., Nichols, T.E., Mackay, C.E., Watkins, K.E., Ciccarelli, O., Cader, M.Z., Matthews, P.M., et al.: Tract-based spatial statistics: voxelwise analysis of multi-subject diffusion data. *Neuroimage* **31**(4), 1487–1505 (2006)
17. Tuch, D.S., Reese, T.G., Wiegell, M.R., Wedeen, V.J.: Diffusion MRI of complex neural architecture. *Neuron* **40**, 885–895 (2003)
18. Westin, C.F., Maier, S.E., Mamata, H., Nabavi, A., Jolesz, F.A., Kikinis, R.: Processing and visualization for diffusion tensor MRI. *Med. Image Anal.* **6**(2), 93–108 (2002)
19. Ziegler, E., Rouillard, M., André, E., Coolen, T., Stender, J., Balteau, E., Phillips, C., Garraux, G.: Mapping track density changes in nigrostriatal and extranigral pathways in Parkinson's disease. *Neuroimage* **99**, 498–508 (2014)

Optimized Response Function Estimation for Spherical Deconvolution



Tom Dela Haije  and Aasa Feragen 

Abstract Constrained spherical deconvolution (CSD) is the most widely used algorithm to estimate fiber orientations for tractography in diffusion-weighted magnetic resonance imaging. CSD models the diffusion-weighted signal as the convolution of a fiber orientation distribution function and a “single fiber response function”, representing the signal profile of a population of aligned fibers. The performance of CSD relies crucially on the robust and accurate estimation of this response function, which is typically done by aligning and averaging a set of noisy, rotated single fiber signals. We show that errors in the alignment step of this procedure lead to an observable bias, and introduce an alternative algorithm based on rotational invariants that entirely avoids the problematic alignment step. The corresponding estimator is proven to be unbiased and consistent, which is verified experimentally.

1 Introduction

Constrained spherical deconvolution (CSD) [7] is the most widely used algorithm to estimate fiber orientation distribution functions (fODFs) for the purpose of tractography. CSD estimates fODFs by deconvolving the signal with a *response function* representing the signal profile of a population of aligned fibers, which is typically estimated from the data. As CSD is an ill-posed problem, its performance in real-world scenarios relies crucially on the accurate and robust estimation of this response function.

T. Dela Haije (✉) · A. Feragen
Department of Computer Science, University of Copenhagen, Copenhagen, Denmark
e-mail: tom@di.ku.dk

A. Feragen
e-mail: afhar@dtu.dk

A. Feragen
Department of Applied Mathematics and Computer Science, Technical University of Denmark, Lyngby, Denmark

Current response function estimation methods consist of two steps. In the first step one selects from the diffusion-weighted data a set of so-called “single fiber voxels”, which are voxels where—according to some heuristic—the underlying tissue is expected to consist mainly of aligned fibrous structures. For the purpose of our discussion, we view the signal from these single fiber voxels simply as rotated, noisy manifestations of a true underlying axially symmetric response function. These single fiber voxels are used in the second step to estimate the actual response function, where the unknown rotations and noise terms are factored out as much as possible. A number of issues in the first step can be addressed using recursive calibration methods as described by Tax et al. [6], where the estimated response function is used to recursively prune the set of single fiber voxels. In this paper, we reconsider the second step in the response function estimation procedure.

The second step of the response function estimation procedure assumes that a set of single fiber voxels has been found in step one. First addressing the issue of unknown rotations between signals from different voxels, state-of-the-art response function estimation algorithms [6–8] all proceed by (robustly) estimating the orientation of the maximum for each single fiber voxel. The *true* orientations of the maxima can trivially be used to factor out the rotations in the acquired signals, and so, in direct analogy, the *estimated* orientations of the maxima are used to approximately align the noisy single fiber signals. Following this rotational alignment, the voxel-wise data is averaged to obtain a response function estimate. Averaging is either done by first estimating spherical harmonic (SH) expansion coefficients and averaging the corresponding coefficients [6], or by first aggregating the rotationally aligned data from all single fiber voxels and then estimating the SH coefficients [7, 8]. In either case, we obtain an estimate of the underlying response function in the SH basis.

Contributions. This work addresses the problem that the estimation of the true orientation of a signal from noisy measurements is an entirely ill-posed problem even in the ideal case of a *known* response function [1], leading to a significant bias in the final response function estimate. The issue extends to recursive methods, where a biased response function negatively impacts the single fiber voxel identification process, which in turn affects all subsequent response function estimation steps. We show that this bias is already evident under noise conditions that are typical for high quality acquisitions, and can in practice be observed even in the absence of noise. The bias thus cannot be removed by improving the data quality. Instead we propose an alternative response function estimation procedure using *rotational invariants*, inspired by recent work in mathematical biology [2]. Because this new method does not require any explicit alignment, the resulting estimator for the response function can be proven to be unbiased, while a simpler implementation gives it the added benefit of being faster to compute.

2 Methods

2.1 Invariant-based Response Function Estimation

Assume that we have already identified a set of n single fiber voxels in a given data set, providing samples of the noisy and rotated functions $f^i = r \circ (R^i)^{-1} + \varepsilon^i$ corresponding to the desired response function $r: S^2 \rightarrow \mathbb{R}$. Here R^i represents the unknown rotation associated to f^i , $\varepsilon^i: S^2 \rightarrow \mathbb{R}$ represents symmetric, independent, and identically distributed noise, and the index $i = 1, \dots, n$ specifies an element in the set of single fiber voxels. If the R^i were known, we could simply use the aligned average $\frac{1}{n} \sum_{i=1}^n f^i \circ R^i$ as an estimator for r :

$$\mathbb{E}\left(\frac{1}{n} \sum_{i=1}^n f^i \circ R^i\right) = \frac{1}{n} \sum_{i=1}^n \mathbb{E}(r + \varepsilon^i \circ R^i) = r. \quad (1)$$

However, R^i is not known, and estimation of r by means of estimates of R^i as done in all currently available methods, has been proven to have limited potential in the related case of image alignment [1]. We therefore propose using rotational invariants of f^i as estimators for the corresponding invariants of r , from which we can then reconstruct r .

To this end, we approximate f^i and r in a (truncated) SH basis, where we have for any $f \in L_2(S^2, \mathbb{C})$ that $f \approx \sum_{l=0}^L \sum_{m=-l}^l f_{l,m} Y_{l,m}$ with $Y_{l,m}$ the spherical harmonic of frequency l and order m and $f_{l,m} \in \mathbb{C}$. This expansion converges uniformly for $L \rightarrow \infty$, but the maximum order L is practically limited by the number of acquired samples of each f^i . For the unknown response function r we have that $r_{l,m} = 0$ for $m \neq 0$ by axial symmetry, and thus $r_{l,0} \in \mathbb{R}$ because both r and $Y_{l,0}$ are real-valued. We then compute the rotationally invariant quantities

$$I_l^k(f) = \sum_{m_1, \dots, m_k} f_{l,m_1} \cdots f_{l,m_k} \int_{S^2} Y_{l,m_1} \cdots Y_{l,m_k} d\mu \quad (2)$$

$$= \sum_{m_1, \dots, m_k} A_{l,m_1 \cdots m_k} f_{l,m_1} \cdots f_{l,m_k}, \quad (3)$$

with $d\mu$ the standard Lebesgue measure on the sphere. (Rotational invariance follows from the standard result that a rotation of a function f effectively rotates each degree l part $f_l = \sum_{m=-l}^l f_{l,m} Y_{l,m}$ of its expansion independently, combined with the trivial rotational invariance of the spherical integration of f_l .)

The integrals $A_{l,m_1 \cdots m_k}$ are analytically computable; the first three are given by

$$A_{l,m_1} = \sqrt{4\pi} \delta_l \delta_{m_1}, \quad (4)$$

$$A_{l,m_1 m_2} = \delta_{m_1 - m_2}, \quad (5)$$

$$A_{l,m_1 m_2 m_3} = \sqrt{\frac{(2l+1)^3}{4\pi}} \begin{pmatrix} l & l & l \\ 0 & 0 & 0 \end{pmatrix} \begin{pmatrix} l & l & l \\ m_1 & m_2 & m_3 \end{pmatrix}, \quad (6)$$

where the bracketed expressions are the Wigner 3- j symbols. It follows immediately that if we can determine the invariant $I_0^1(r) = \sqrt{4\pi} r_{0,0}$, then the first coefficient $r_{0,0}$ can be trivially reconstructed, while $I_l^1(r) = 0$ for $l > 0$ and is thus uninformative. For $k = 2$ we find $I_l^2(r) = (r_{l,0})^2$, which gives us the absolute value of $r_{l,0}$ but leaves its sign as an unknown. Finally, we have that $I_l^3(r) = A_{l,000} (r_{l,0})^3$, and since $A_{l,000} \neq 0$ we can directly recover the coefficients $r_{l,0}$ from $I_l^3(r)$. Based on these ideas, we remark that we can reconstruct the coefficients $r_{l,0}$ of the response function r from the invariants of f^i as follows.

Proposition 1 *The sample mean invariants $\frac{1}{n} \sum_{i=1}^n I_0^1(f^i)$ and $\frac{1}{n} \sum_{i=1}^n I_l^3(f^i)$ are consistent and unbiased estimators of the invariants $I_0^1(r)$ and $I_l^3(r)$ (for $l > 0$). That is, $\mathbb{E}(\frac{1}{n} \sum_{i=1}^n I_0^1(f^i)) = I_0^1(r)$, $\mathbb{E}(\frac{1}{n} \sum_{i=1}^n I_l^3(f^i)) = I_l^3(r)$ (for $l > 0$), $\text{plim}_{n \rightarrow \infty} \frac{1}{n} \sum_{i=1}^n I_0^1(f^i) = I_0^1(r)$, and $\text{plim}_{n \rightarrow \infty} \frac{1}{n} \sum_{i=1}^n I_l^3(f^i) = I_l^3(r)$ (for $l > 0$), where plim denotes convergence in probability.*

Proof Note first that the coefficients $\varepsilon_{l,m}$ of the noise ε are obtained by projection onto the (complex conjugate) spherical harmonic $Y_{l,m}^*$, i.e., by multiplying with $Y_{l,m}^*$ and integrating over the sphere. Switching the order of integration we then find that the expectation $\mathbb{E}(\varepsilon) = 0$ implies that $\mathbb{E}(\varepsilon_{l,m}) = 0$, so that $f_l = (r \circ R^{-1} + \varepsilon)_l = (r_l + \varepsilon_l \circ R) \circ R^{-1} = (r_l + \varepsilon'_l) \circ R^{-1}$ for some noise term $\varepsilon'_l \sim \varepsilon$, i.e., that satisfies the same properties as ε . Given that for each frequency l , the invariant I_l^3 is thus of the form

$$I_l^3(f) = \int_{S^2} (f_l)^3 d\mu = \int_{S^2} (r_l + \varepsilon)^3 d\mu, \quad (7)$$

we have for $l > 0$ that

$$\mathbb{E}(I_l^3(f)) = I_l^3(r) + 3 \underbrace{\int_{S^2} \mathbb{E}(\varepsilon) r_l^2 d\mu}_{=0} + 3 \underbrace{\int_{S^2} \mathbb{E}(\varepsilon^2) r_l d\mu}_{=0} + \underbrace{\int_{S^2} \mathbb{E}(\varepsilon^3) d\mu}_{=0} \quad (8)$$

where $\mathbb{E}(\varepsilon) = \mathbb{E}(\varepsilon^3) = 0$ by symmetry, and $\int_{S^2} \mathbb{E}(\varepsilon^2) r_l d\mu = \mathbb{E}(\varepsilon^2) \int_{S^2} r_l d\mu = 0$ as the last integral is 0 for $l \neq 0$ by Eq. (4). Unbiasedness follows then by direct computation, and consistency follows from the strong law of large numbers. The arguments for I_0^1 are analogous. \square

Based on the foregoing discussion, we can now define the following estimator for the non-zero coefficients of r :

$$\hat{r}_{l,0} = \begin{cases} \frac{1}{n\sqrt{4\pi}} \sum_{i=1}^n I_0^1(f^i) & l = 0 \\ \sqrt[3]{\frac{1}{nA_{000}'} \sum_{i=1}^n I_l^3(f^i)} & l > 0 \end{cases}. \quad (9)$$

By Proposition 1 and continuity of the cube root, the resulting estimator $\hat{r} = \sum_{l=0}^L \hat{r}_{l,0} Y_{l,0}$ is a consistent and unbiased estimator for r .

2.2 Implementation

We implemented invariant-based response function estimation based on Eq. (9) in DiPy [4] for the case of a given set of single fiber voxels, as well as for the case where recursive pruning is desirable. The latter was done by adapting the recursive scheme of Tax et al. [6] implemented in DiPy, where we replaced the alignment and averaging step with our invariant-based response function estimation. We compare the invariant-based response function estimation to the DiPy implementation of the recursive response function estimation by Tax et al. [6], as well as to the MRtrix [9] implementation of the recursive algorithm by Tournier et al. [8]. We henceforth refer to these as the `Tax` and `Tournier` methods, respectively.

To separate the effects of errors in the single fiber population identification steps from errors in the actual response function estimation, we first perform experiments by terminating all three recursive methods after their first iteration—effectively using only the single fiber signals provided in the initialization. This is referred to as “iteration 0” in the experiments below. Next, we compare the three methods with recursion using their default settings. All signals are represented by $L = 10$ SH expansions, and response functions are computed up to $l = 8$.

3 Experiments and Results

Signal Alignment and Averaging. We aim to document a bias in existing approaches, as well as illustrate consistency and unbiasedness of the invariant-based approach. To this end we generate four synthetic data sets from a ground-truth (GT) response function, based on a single high-FA voxel sampled from a Human Connectome Project (HCP) [3] subject, rounded to give the non-zero SH coefficients (3800, −1600, 700, −300, 100). A noiseless data set is obtained by applying up to 2000 random rotations to the GT response function and then sampling the result according to the $b = 3 \text{ ms}/\mu\text{m}^2$ shell in the HCP acquisition scheme. Noisy data sets are similarly obtained by applying random rotations before sampling, followed by the addition of normally distributed noise corresponding to the designated SNR with $\sigma = 3800/\text{SNR}$. The data sets are re-generated 25 times to estimate precision.

As seen in Fig. 1, both the `Tax` and `Tournier` algorithms converge to incorrect SH coefficients for all considered noise levels. The observed errors can be

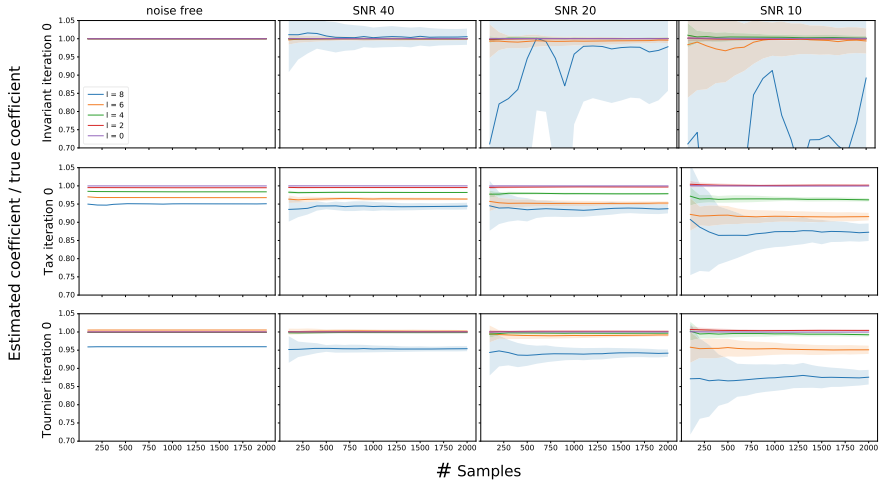


Fig. 1 Convergence of different response function estimation methods on synthetic data sets with different numbers of single fiber voxels. The error bars represent the standard deviation over 25 sampled data sets. Both standard methods, *Tax* and *Tournier*, have a clear and significant bias at all noise levels

significant—in the SNR 10 case, which is not unreasonable for real data, the errors are around 5 and 15% for the $l = 6$ and $l = 8$ coefficients respectively. The invariant method on the other hand converges to the true SH coefficients, although convergence is slower than in the other methods. We do not observe convergence for the $l = 8$ coefficients in the SNR cases 20 and 10, and even by aggregating all 25 data sets and obtaining a data set with 50,000 single fiber voxels, we only observe additional convergence for an SNR of 20, see Fig. 2. This observation is consistent with [5], which suggests that the “sample size” needed to recover an underlying signal generally scales as SNR^{-3} . Note that the *Tax* and *Tournier* methods do not improve even with these large numbers of single fiber voxels. Finally, we note that the biases observed in Fig. 1 exceed the standard deviation in the invariant-based estimates at a typical number of 1000 samples in almost all cases.

Effect of Single Fiber Voxel Selection. As modern response function estimation algorithms include a recursive selection procedure for single fiber voxels, we repeat the experiment of Fig. 1 using recursive response function estimation. The recursive *Tax* and recursive invariant-based algorithms both failed to estimate a response function in the SNR 10 and 20 cases. This was caused by the (identical) single fiber population selection procedures used in these methods, which in this example discarded all single fiber voxels in the most noisy data sets after a few iterations. The recursive *Tournier* method always retained a certain minimum number of single fiber voxels, and so did still produce response function. The results are shown in Fig. 3, and show comparable behavior as seen in Fig. 1. Comparing for example the SNR 40 results for the invariant-based method between Figs. 1 and 3, we do note

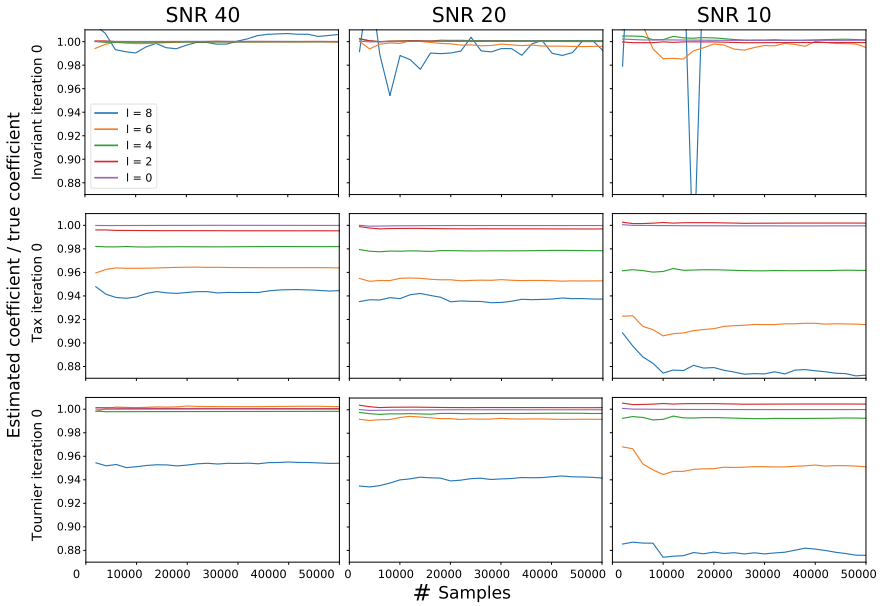


Fig. 2 Convergence of the SH coefficients in the response function estimation of a GT response function based on on 50,000 noisy, randomly rotated observations of the GT

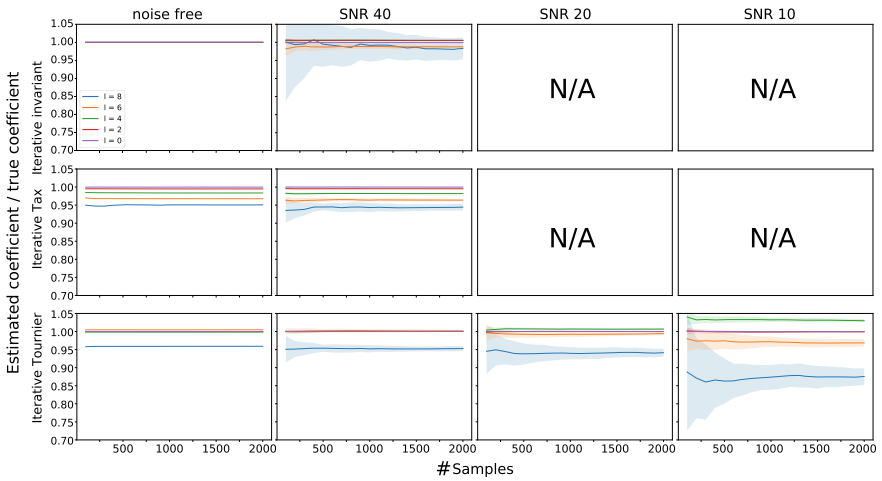


Fig. 3 Results for the recursive response function estimation algorithms on the data from Fig. 1. Note how the bias at higher l persists, and that in this example the biased single fiber selection criteria used in the recursive approach actually has a negative effect on the otherwise unbiased invariant-based method

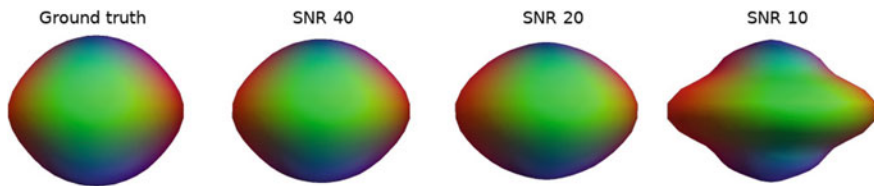


Fig. 4 From left to right: A fat ground truth response function, as well as its reconstructions estimated by the recursive `Tournier` algorithm [8] from 2000 randomly rotated noisy GT response functions

that the recursive selection procedure introduces a (smaller) secondary bias in the SH coefficients. In the non-invariant-based methods this secondary bias is also present, but is obscured by the larger bias introduced by the alignment errors.

Low Quality Data. The secondary bias observed in the previous experiment is caused by selection pressures in recursive methods that emphasize “flat” response functions. As response functions obtained from real data are indeed expected to be flat, this bias is typically small and in fact appears to have a beneficial effect on the precision of the response function estimation (only similar-looking signals are selected in the recursive single fiber voxel identification procedure). However, this apparent improvement in the precision actually conceals the valuable information provided by the uncertainty in the estimate. In the presented artificial data experiments there does not seem to be any justification for including the (apparently reliable) $l = 8$ coefficient for example. At the same time the introduced bias is unpredictable, although we found that in low SNR cases and for “fat” response functions the effect of this bias is much more pronounced, as shown in Fig. 4: increased noise levels lead to increasingly flat, but less correct, estimated response functions. This bias was observed in all considered recursive methods.

Effect on fODF Peaks and Tractography in Real Data. Finally, we aim to show that different response function estimation algorithms produce different fODFs and peak angles on real data, and that they could therefore have a potentially significant impact on e.g. tractography. Using the $b = 3 \text{ ms}/\mu\text{m}^2$ shell of a single HCP [3] subject, we compute the recursive invariant-based, `Tax` and `Tournier` response functions. Using MRtrix we then apply CSD, followed by a peak estimation method. Figure 5 shows histograms over the voxel-wise peak angle differences as well as the estimated fODFs for the three different algorithms in the centrum semiovale region. Although the visual differences in the glyph plots are small, there are significant differences in the peak angles, especially relative to the expected uncertainty in CSD peak angles of 5 degrees. Because the uncertainty in the peak angle is caused in part by the reported biases, Fig. 5 suggests that our method could improve the accuracy in the peak estimation by 20–40%. Furthermore, errors in many commonly used tractography methods accumulate over distance, so even small improvements in the local orientation estimates could have a noticeable impact on longer tracts.

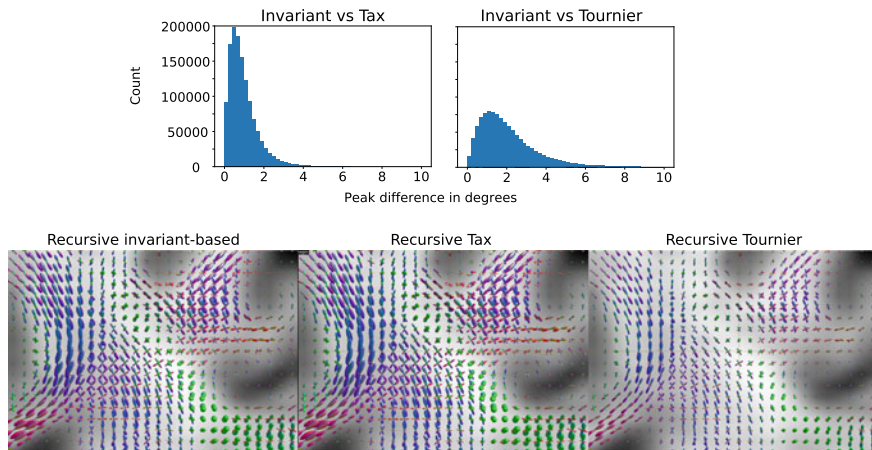


Fig. 5 Top: Histograms over fODF peak angle differences. Bottom: Resulting fODFs visualized in the centrum semiovale region

4 Discussion and Conclusion

We have shown that existing state-of-the-art response function estimation algorithms have a significant bias that cannot be removed by adding more data. We have identified two sources of this bias: (1) errors in the rotational alignment step of these methods due to incorrectly estimated maxima, and (2) biases in the single fiber voxel identification procedure prominently visible in recursive methods. To the best of our knowledge, these biases have not been reported or investigated in other works.

In this paper we have not considered the second source of bias, and we note that the challenging problem of single fiber voxel identification remains an important topic for future work. In response to the first source of bias, we have proposed an alternative response function estimator based on rotational invariants, which is unbiased and consistent assuming a population of single fiber voxels has been reliably determined. The method is straightforward to implement and can be incorporated into any recursive response function estimation algorithm. Finally, the invariant-based method does not rely on computationally costly function maximization and rotation steps, making it generally faster than available alternatives.

Acknowledgments The authors would like to thank ID for discussions related to this work. This research was supported by the Centre for Stochastic Geometry and Advanced Bioimaging and by a block stipendium, both funded by the Villum Foundation. Data were provided in part by the Human Connectome Project, WU-Minn Consortium (Principal Investigators: David Van Essen and Kamil Ugurbil; 1U54MH091657) funded by the 16 NIH Institutes and Centers that support the NIH Blueprint for Neuroscience Research; and by the McDonnell Center for Systems Neuroscience at Washington University.

References

1. Aguerrebere, C., Delbracio, M., Bartesaghi, A., Sapiro, G.: Fundamental limits in multi-image alignment. *IEEE Trans. Signal Proc.* **64**(21), 5707–5722 (2016)
2. Bendory, T., Boumal, N., Ma, C., Zhao, Z., Singer, A.: Bispectrum inversion with application to multireference alignment. *IEEE Trans. Signal Proc.* **66**(4), 1037–1050 (2018)
3. Essen, D.C.V., Smith, S.M., Barch, D.M., Behrens, T.E., Yacoub, E., Ugurbil, K.: The WU-Minn human connectome project: an overview. *NeuroImage* **80**, 62–79 (2013)
4. Garyfallidis, E., Brett, M., Amirbekian, B., Rokem, A., Van Der Walt, S., Descoteaux, M., Nimmo-Smith, I.: Dipy, a library for the analysis of diffusion MRI data. *Frontiers Neuroinform.* **8**, 8 (2014)
5. Perry, A., Weed, J., Bandeira, A.S., Rigollet, P., Singer, A.: The sample complexity of multi-reference alignment. *CoRR* (2017). [arXiv:abs/1707.00943](https://arxiv.org/abs/1707.00943)
6. Tax, C.M., Jeurissen, B., Vos, S.B., Viergever, M.A., Leemans, A.: Recursive calibration of the fiber response function for spherical deconvolution of diffusion MRI data. *NeuroImage* **86**, 67–80 (2014)
7. Tournier, J.D., Calamante, F., Connelly, A.: Robust determination of the fibre orientation distribution in diffusion MRI: Non-negativity constrained super-resolved spherical deconvolution. *NeuroImage* **35**(4), 1459–1472 (2007)
8. Tournier, J.D., Calamante, F., Connelly, A.: Determination of the appropriate b -value and number of gradient directions for high-angular-resolution diffusion-weighted imaging. *NMR Biomed.* **26**(12), 1775–1786 (2013)
9. Tournier, J.D., Calamante, F., Connelly, A.: MRtrix: diffusion tractography in crossing fiber regions. *Int. J. Imaging Syst. Technol.* **22**(1), 53–66 (2012)

Optimal Fiber Diffusion Model Restoration



Clint Greene, Kate Revill, Cathrin Bueteifisch, Ken Rose, and Scott Grafton

Abstract Assessing the effects of white matter (WM) lesions on structural connectivity as measured by diffusion MRI (dMRI) is invaluable for understanding structure-function relationships. These WM lesions have many etiologies that ultimately lead to attenuation of the anisotropic signature in dMRI signals. Attenuation can produce inaccurate reconstructions of the underlying model of the fiber population. In this paper, we combine methods from image inpainting and estimation theory to develop a novel approach for restoring the fiber model in small to moderate sized WM lesions. Our approach begins by taking healthy reconstructed WM fiber models at the boundary of the lesion and filling in lesioned voxels with their optimal affine estimate moving iteratively in a fast-marching method style until the fiber models in the lesion are restored. We demonstrate with in-vivo simulations on diffusion tensors (DTs) and fiber orientation distributions (FODs) that our approach offers superior performance over multiple restoration approaches. We restore lesioned fiber models in three stroke patients suffering hemiparesis from damaged corticospinal tracts (CST). We show that our method restores diffusivities, anisotropy and orientation of lesioned DTs as well as the amplitudes and orientations of fiber populations in lesioned FODs enhancing tractography and enabling more accurate characterization of lesion connectivity and changes in tissue microstructure in patient populations.

1 Introduction

Diffusion-weighted magnetic resonance imaging (DW-MRI) techniques have been successfully used to non-invasively explore fiber bundle architectures in the brain. These techniques are sensitive to the diffusion of water molecules enabling the characterization of the orientation of bundles of myelinated axons when the water is

C. Greene (✉) · K. Rose · S. Grafton
University of California, Santa Barbara, CA, USA
e-mail: clint@ece.ucsb.edu

K. Revill · C. Bueteifisch
Emory University, Atlanta, Georgia

© Springer Nature Switzerland AG 2020
E. Bonet-Carne et al. (eds.), *Computational Diffusion MRI*,
Mathematics and Visualization, https://doi.org/10.1007/978-3-030-52893-5_4

restricted to diffusion along the long axis of the axons. However, due to pathological injury processes such as gliosis, demyelination, and necrosis, the structural integrity of the axons is compromised, and water is no longer restricted to diffusing along the long axis. These macro and microstructural changes attenuate the anisotropic signature in dMRI signals [1]. Consequently, it remains challenging to accurately characterize the change in tissue microstructure and the connectivity within lesioned white matter areas which are crucial for studying disconnection syndromes.

Clinical researchers typically measure changes in tissue microstructure by comparing the measurements in the lesion ROI with measurements in healthy tissue from the left-right flipped ROI [2]. Using microstructure measurements from the contralateral side as a model for the original properties is not the most accurate approach because the brain is not symmetric and where it is symmetric, e.g. CST, the tissue measurements are not identical and are less similar to restored tissue measurements. With regards to mapping lesion connectivity, one strategy clinical researchers use is to project the patient's lesion into a normal database of streamlines to approximate the degree of disruption by the lesion to normative [3]. However, this strategy produces a generic estimate of the patient's lost connectivity, without any characterization of patient specific disrupted connectivity. Other researchers simply track through the lesioned area to map the lesion's connectivity [4]. However, tracking through lesioned areas is known to affect streamline reconstruction and structural networks [5, 6].

Another strategy for characterizing lesion connectivity and changes in microstructure is to restore or inpaint the lesioned fiber diffusion model. This has the advantage of more closely preserving the patient's native connectivity structure. Prior work has primarily focused on inpainting multiple sclerosis (MS) and tumor lesions in T1 and T2 weighted images to improve registration accuracy to a template [7, 8]. Recently, a method has been developed to restore fiber orientation distributions (FODs) in MS lesions [9]. They combine diffusion based inpainting and FOD reconstruction in a single step. But they only assessed their performance on an unrealistic simulated lesion of 9 voxels, so it is unclear how it would perform in-vivo. Moreover, its only capable of restoring FODs.

Although a method exists for restoring FODs, a solution that can restore multiple fiber diffusion models, is needed for multiple reasons. The ability to restore diffusion tensors would be beneficial since diffusion tensor imaging (DTI) remains the most popular technique used by clinical researchers for characterizing changes in tissue microstructure and connectivity in lesioned WM tissue. Furthermore, many clinical diffusion datasets in wide use can be reconstructed in myriad ways and contain lesions from the myriad etiologies of WM injury such as white matter hyperintensities in the Rotterdam Study and the Human Connectome Project (HCP) Lifespan study [10, 11]. Since there is a great need in clinical research to improve prediction outcomes, the ability of researchers to restore the fiber diffusion models of their choice in a lesion would make such an approach more accessible and have the potential to improve these predictions through improved anatomical delineation of lesion disrupted connectivity and measurement of changes in tissue microstructure.

In this paper, we describe a novel approach that combines methods from diffusion-based image inpainting and estimation theory for restoring fiber diffusion models in WM lesions. Our approach begins by taking healthy WM fiber models at the boundary of the lesion and filling in lesioned voxels with their optimal affine estimate moving iteratively in a fast-marching method style until the fiber models in the lesion are restored. By leveraging estimation theory, we can minimize the mean squared error (MSE) of fiber models within the lesion, restoring their original shapes and orientations. We demonstrate with realistic in-vivo simulations on diffusion tensors and fiber orientation distributions that our approach offers superior performance over multiple inpainting approaches. Further we restore diffusion tensors and FODs in lesions in three stroke patients suffering hemiparesis and demonstrate that the shape and orientation of the fiber models and the ability to map the lesions connectivity are recovered.

2 Methods

2.1 Diffusion Imaging Data

The S500 dataset containing 500 subjects was collected from the Washington University-Minnesota Consortium Human Connectome Project [11]. Further analysis was restricted to 210 subjects without familial relation. The diffusion volumes were collected with a spatial resolution 1.25 mm^3 , using three shells at $b = 1000$, 2000 , and 3000 s/mm^2 with 90 diffusion directions/shell.

Diffusion volumes were collected for three stroke patients with unilateral motor impairment at Emory University using the HCP Lifespan protocol with a spatial resolution of 1.5 mm^3 , using two shells at $b = 1500$ and 3000 s/mm^2 with 46 diffusion directions per shell and 7 b0s. All datasets were corrected for geometric, eddy current, and motion distortions using the HCP Pipeline scripts.

The diffusion tensors were reconstructed from the diffusion weighted volumes collected with $b = 1000 \text{ s/mm}^2$ with weighted least squares in Dipy for the HCP dataset and $b = 1500 \text{ s/mm}^2$ for the stroke dataset [12]. Fiber orientation distributions we reconstructed using constrained spherical deconvolution (CSD) in MRtrix with $b = 3000 \text{ s/mm}^2$ and $l_{max} = 8$ for both datasets [12, 13]. The response function was estimated using the recursive Tax algorithm [14].

2.2 Model Estimation

Suppose there is a lesioned fiber diffusion model \mathbf{L} lying at the boundary of the lesion and healthy WM tissue. If the model is a diffusion tensor then there are only 6 unique elements of \mathbf{L} that need to be estimated i.e. D_{xx} , D_{yy} , D_{zz} , D_{xy} , D_{xz} , and D_{yz}

because diffusion tensors are positive semi-definite matrices. Similarly, if a more complex spherical deconvolution model is used then at each lesioned voxel the FOD is represented by a real-valued spherical harmonic coefficient vector, F , containing $(l_{max} + 1) \times (l_{max} + 2) / 2$ elements that need to be estimated. Consider that L has N observed healthy or restored neighboring models, $H_1, H_2, \dots, H_N \in \mathcal{W}$, the white matter mask. Each unknown element, Y_i e.g. D_{xx} or F_i , is treated as a random variable. The collection of matching neighbor elements forms a random vector $X = [X_1, X_2, \dots, X_N]$. Then each unknown element Y_i can be estimated from the known neighboring elements of H_i using an optimal affine estimator.

We seek an affine estimator $\hat{Y} = a_0 + \sum_{i=1}^N a_i X_i$ such that the MSE e.g. $\varepsilon^2 = E \left[(Y - \hat{Y})^2 \right]$ is minimized. To minimize this expression, we differentiate it with respect to a_i . Differentiating $E \left[(Y - a_0 + \sum_{i=1}^N a_i X_i)^2 \right]$ with respect to a_0 and setting it to 0 we find that $a_0 = \mu_Y - \sum_{i=1}^N a_i \mu_{X_i}$ from which it follows that $\hat{Y} = \mu_Y + \sum_{i=1}^N a_i (X - \mu_{X_i})$. Letting $\tilde{Y} = Y - \mu_Y$ and $\tilde{X} = X - \mu_X$ we can rewrite our MSE criterion as $E \left[(\tilde{Y} - \sum_{i=1}^N a_i \tilde{X}_i)^2 \right]$.

By differentiating this with respect to the coefficients and setting the result to 0 produces: $E \left[(\tilde{Y} - \sum_{i=1}^N a_i \tilde{X}_i) \tilde{X}_j \right] = 0 \quad j = 1, 2, \dots, N$ which can be rewritten as $E \left[\tilde{X}_j \tilde{Y} \right] = \sum_{i=1}^N E \left[a_i \tilde{X}_i \tilde{X}_j \right]$. These sets of equations can be expressed in matrix form as $R_{XY} = (R_{XX}) a$ where R_{XY} is the cross-correlation vector and R_{XX} is the auto-correlation matrix and a is the coefficient vector. We obtain the optimal coefficients: $a = (R_{XX})^{-1} R_{XY}$.

From this solution it is possible to produce the optimal affine estimate of elements of L : $L_i = a_1 L_i^{\tilde{H}_1} + a_2 L_i^{\tilde{H}_2} + \dots + a_N L_i^{\tilde{H}_N} + \mu_{Y_i}$, where $\tilde{H}_i = H_i - \mu_{X_i}(1)$.

By taking the affine combination of the neighboring healthy elements. Since Y and X are approximately Gaussian, the optimal affine estimate excellently approximates the optimal MMSE estimate of Y . However, to construct an optimal affine estimator at each voxel a distribution of fiber diffusion models must exist at every voxel in the patient.

2.3 Distribution of Fiber Models

A fiber model distribution at every voxel in the patient can be constructed through spatial normalization. Custom fiber diffusion model templates are constructed using DTI-TK for tensors and FOD Reorientation and ANTs for FODs [15–17]. After the templates are constructed, we spatially normalize the patients reconstructed tensors or FODs into its respective custom HCP template using cost-function masking. We then combine the estimated deformation fields to the template for the patients and the HCP subjects to warp a subset of tensor or FOD data from the HCP subjects that corresponds to voxels in the patients lesion and healthy voxels at the boundary.

2.4 Model Inpainting

We use a diffusion based inpainting algorithm where the lesion region is filled from its border to the center inspired from [18]. At each iteration, rather than taking a simple average of the known neighboring models, we estimate the unknown model \mathbf{L} by taking the affine combination of its healthy neighbors where the coefficients are estimated from the optimal affine estimator in Eq. (1). Note that an optimal affine estimator is constructed for each element of the fiber diffusion model for each voxel in the lesion region.

while the lesion region is not empty:

for all $\mathbf{L} \in \partial\Omega$:

for all $y \in \mathbf{L}(y)$:

$$y = a_1 L_i^{\tilde{H}_1} + a_2 L_i^{\tilde{H}_2} + \dots + a_N L_i^{\tilde{H}_N} + \mu_{Y_y}$$

$$\Omega = \Omega / \partial\Omega$$

where $\tilde{H}_i = H_i - \mu_{X_y} \in \bar{\Omega} \cap \mathcal{W}$ and $y \in [L_1, L_2, \dots, L_N]$, \mathbf{L} is the model to inpaint, Ω is the lesion region, $\bar{\Omega}$ its complement (the voxels outside Ω), $\partial\Omega$ its border (voxels of Ω having one of its 6 cube neighbors in $\bar{\Omega}$).

3 Results

3.1 Simulation In-Vivo

We demonstrate the efficacy of our approach by simulating a lesion within a healthy HCP subject that is not part of the model distribution. The lesion was created by adding Rician noise to a cuboidal region consisting of 1035 voxels (129 cm³) until the SNR = 3. The lesioned voxels are then inpainted with a baseline approach and our optimal approach. For our baseline, we use the same diffusion based inpainting algorithm as used in the optimal estimation where the inpainted model is estimated by simply taking an average of its neighbors [18]. The results of inpainting the tensors (top) and FODs (bottom) with both approaches is shown in Fig. 1 within the transparent border.

Column C shows the ground truth reconstructed tensors (top) and FODs (bottom). The baseline approach is shown in column B and our optimal approach is shown in column D. At first glance, the baseline approach appears to provide a reasonable restoration of the tensors but upon closer inspection many tensors have different anisotropy (shape) and orientation (color) relative to the ground truth tensors. For

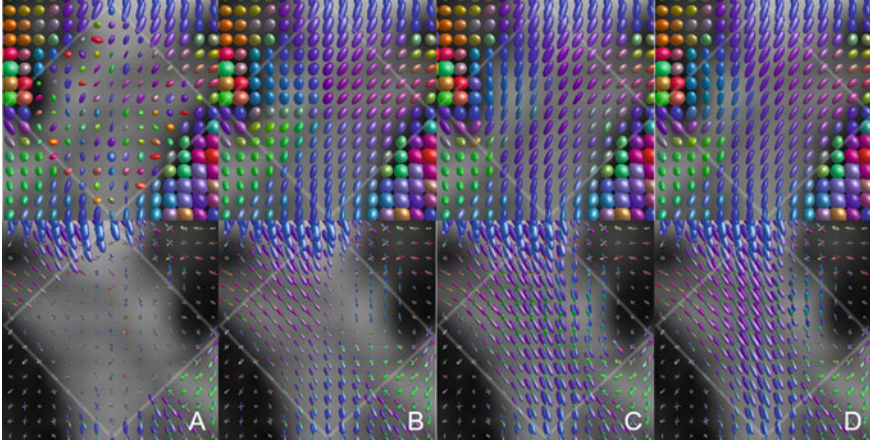


Fig. 1 In-vivo simulated model restoration: The lesion region is demarcated by the transparent border. Rician noise is added to the original diffusion signal until $\text{SNR} = 3$ producing the tensors (top) and FODs (bottom) in A. The baseline approach in B appears to provide reasonable approximation of normal tensors but upon closer inspection the restored tensors differ in anisotropy and orientation, while for FODs there are large deviations in magnitude and orientation from the ground truth. The ground truth reconstructions are in C. Tensors and FODs restored using our optimal approach are in D. Notice that the tensors and FODs restored using our approach more closely match the ground truth in terms of orientation and shape compared to the baseline

FODs restored using the baseline approach it is immediately clear that they differ in both magnitude and orientation with respect to the ground truth. Our optimal approach more accurately preserves the anisotropy and orientation of the ground truth tensors and the magnitude and orientation of the ground truth FODs.

The mean angular error (MAE) is plotted for the primary fiber direction for tensors on the left and on the right for FODs (solid) from the HCP template mean normalized into the lesion area (green), restored using the baseline approach (orange), and restored using our optimal approach (blue) with respect to the primary fiber direction from the respective ground truth tensors and FODs for lesion sizes varying from 6 voxels to 1035 voxels in Fig. 2. For the smallest lesions, the difference in MAE is negligible for all the approaches and the FODs MAE is less than the tensors MAE. However, as lesion size increases the FODs MAE quickly outpaces the tensors MAE. In general, the template average has the largest MAE while our optimal approach has the smallest as lesion size increase. The MAE for the baseline approach grows more rapidly than our optimal approach for both tensors and FODs and for large lesions the MAE is twice as large compared to our optimal approach. On the right in Fig. 2, the MAE for the second fiber population is plotted as the dotted line and is typically twice as large as the MAE for the primary FOD fiber population. The trends for the angular error in the second fiber population mirror those seen in the primary FOD fiber population. Our optimal approach achieves the smallest MAE.

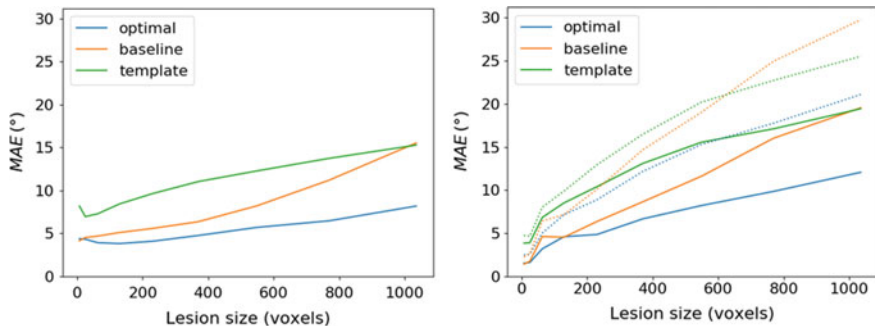


Fig. 2 Analysis of angular error: The MAE is plotted on the left for tensors and on the right for FODs (solid) for the primary fiber direction for varying lesions sizes. The MAE for the smallest lesion sizes is comparable across all approaches and the FODs MAE is smaller than the tensors MAE. However, the FODs MAE quickly outpaces the tensors MAE at larger lesion sizes. The template average (green) has the largest MAE while our optimal approach (blue) as the smallest as lesion size increase. The MAE for the baseline approach (orange) grows more rapidly than our optimal approach for both tensors and FODs. Typically, the baseline approach has a MAE twice as large as of our optimal approach. On the right, the MAE for the second fiber population is plotted as the dotted line. It is typically twice as large as the MAE for primary FOD fiber population. The MAE trend in the secondary fiber population mirrors those seen in the primary FOD fiber population for all restoration approaches. Our optimal approach minimizes the MAE the most compared to the baseline and template approaches

On the top left of Fig. 3, the root mean squared error (RMSE) in fractional anisotropy (FA) with respect to the ground truth is measured for varying lesion sizes. The RMSE starts high and then slowly decreases until its constant with increasing lesion size for the template mean (green). The RMSE of FA values extracted from the flipped ROI in the contralesional area (red) with respect to the original FA values also starts high and then grows slowly with increasing lesion size. For lesion sizes < 200 voxels, the baseline and optimal approach have almost identical trends, but for larger sizes the baseline error grows much faster than for our optimal approach. At large lesion sizes the baseline approach again has an error almost double our optimal approach. For axial diffusivity (AD) on the top right, the template mean and optimal AD RMSEs both grow moderately with increasing lesion size while the RMSE for the baseline and flipped case grow faster. On the bottom row in Fig. 3, the RMSEs for mean diffusivity (MD) and radial diffusivity (RD) are plotted. The MD and RD RMSE for the flipped case grows the fastest with increasing lesion size while the template mean, the baseline, and optimal approaches RMSE grow slowly. Interestingly, there is not much gain in terms of RMSE for MD and RD between the baseline and our optimal approach. In general, our optimal approach has the smallest RMSE and grows the slowest with increasing lesion size while the baseline outperforms the template mean which outperforms the flipped-case for all tissue measures.

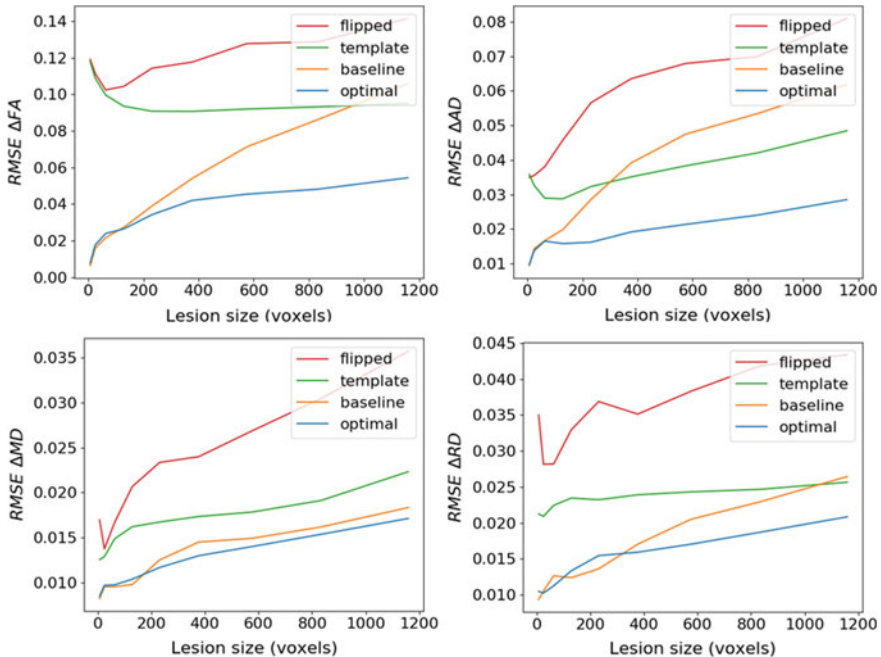


Fig. 3 RMSE of tissue microstructure measurements: On the top left, RMSE FA for the baseline (orange) and our optimal approach (blue) show nearly identical trends for lesion sizes < 200 voxels. The baseline RMSE FA increases more rapidly compared to our optimal approach and is nearly twice as large at larger lesion sizes. For the template mean (green) the RMSE gradually decreases until becoming constant as the lesion size increases. The RMSE of FA values extracted from the flipped ROI in the contralesional area (red) with respect to the original FA values grows slowly with increasing lesion size. On the top right the RMSE for axial diffusivity (AD) is plotted. The template mean and optimal AD RMSEs both grow moderately with increasing lesion size while the RMSE for the baseline and flipped case grow faster. On the bottom row, the RMSEs for mean diffusivity (MD) and radial diffusivity (RD) are plotted. The MD and RD RMSE for the flipped case grows the fastest with increasing lesion size while the template mean, the baseline, and optimal approaches RMSE grow slowly. For MD and RD there is not much gain with our optimal approach over the baseline. In general, our optimal approach has the smallest RMSE and grows the slowest with increasing lesion size for all tissue measures

3.2 Lesion Restoration

The restoration results using our optimal approach are plotted in Fig. 4 for three patients. The lesion region for each patient that undergoes restoration is demarcated in red on the coronal FA slice in column A. The lesioned tensors before and after the restoration are seen in columns B and C in Fig. 4. In column B, the tensors in the lesion area have lost their normal color (orientation) and shape (anisotropy). Notice that the restored tensors in column C have both normal appearing shape and color. The lesioned FODs before and after restoration are plotted in columns

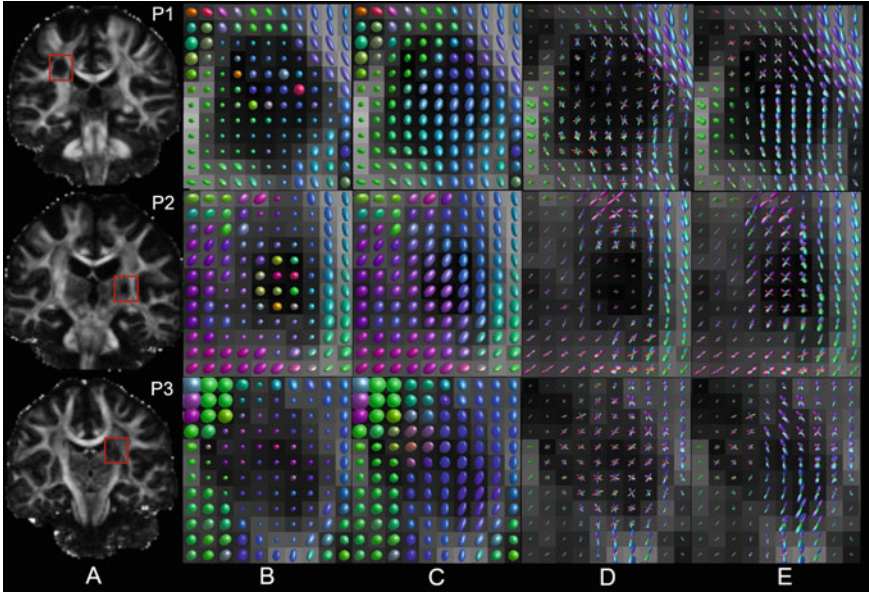


Fig. 4 Restoration results for three stroke patients: The lesion regions where models undergo restoration is demarcated in red in column **A**. The average lesion size is 390 voxels. In column **B** are the tensors before the restoration and afterwards in column **C**. The loss of anisotropy (shape) and proper orientation (color) of healthy white matter tissue in the CST are visible in column **B**. In column **C**, our approach restores the orientations and anisotropy of the tensors to a normal appearance. Similarly, the FODs in the lesion area of column **D** have lost their normal orientation and magnitude. After undergoing restoration using our optimal approach the normal orientation and magnitude of the FODs in the lesion area have been recovered in **E**. The restored tensors (**C**) and FODs (**E**) demonstrate high spatial coherence with their surroundings

D and **E**. In column **D**, the lesioned FODs have lost their normal orientation and magnitude. The orientation and magnitude of FODs in the lesion are recovered after undergoing restoration using our optimal approach. Moreover, the restored tensors and FODs demonstrate high spatial coherence with the surrounding healthy white matter tensors and FODs.

The restoration of scalar tissue microstructure measures AD , MD , and RD are plotted in Fig. 5 for patient 1 on the same coronal plane. In the top row are the measures before the restoration and in the bottom row after the restoration. The lesion area is demarcated in red. Notice that after restoration using our optimal approach that the lesion area has been restored to a normal appearance for all the scalar diffusivities.

To demonstrate the improved mapping of lesion connectivity after fiber model restoration, we perform deterministic tractography before and after restoration on FODs in MRtrix with default settings using the SD_STREAM algorithm from a seed image consisting of two voxels below the lesion area with 1000 seeds per voxel [14]. In Fig. 6, the tractography results before the restoration (top) and after the

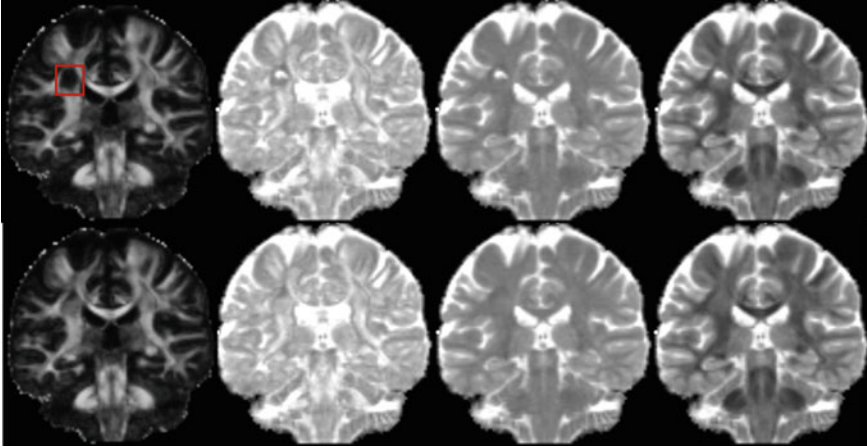


Fig. 5 Coronal view of tissue microstructure measures before (top) and after (bottom) restoration for patient 1: From left to right axial diffusivity, mean diffusivity, and radial diffusivity. The lesion area is demarcated in red. The lesion area has been restored to a normal appearance for all measures

restoration (middle) are displayed on top of the magnified portion of their lesion in the sagittal FA slice which is denoted by the arrow (bottom). In all three patients, once the tracking enters portions of the lesion area it prematurely terminates before the restoration, preventing an accurate mapping of connectivity within the lesion. After the FODs have been restored, tracking through the lesion area becomes feasible enabling a more accurate mapping of the lesions connectivity.

4 Discussion

Using in-vivo simulations and stroke patient data, we demonstrated the ability of our novel approach for accurately restoring both the orientation and magnitude of FODs and the orientation, anisotropy, and tissue microstructure measures of diffusion tensors in WM lesions. Our optimal affine estimator approach offers superior performance over a diffusion based inpainting approach that takes the average of neighboring tensors for inpainting a lesioned area as well as the trivial copy and pasting of tensors or FODs from the normalized HCP tensor or FOD template.

Simple neighbor averaging performs well for very small lesions. However, as the lesion sizes increases, it introduces increased blurring that compounds moving inward. The increased blurring is reflected by the large increases in angular error and error in scalar measures such as FA or AD as the lesion sizes increase. Our optimal approach performs well at restoring tensors and FODs across all lesion sizes with only modest increases in angular error and error in scalar measures as the lesion size increases because as the algorithm moves inward, the fiber diffusion models are

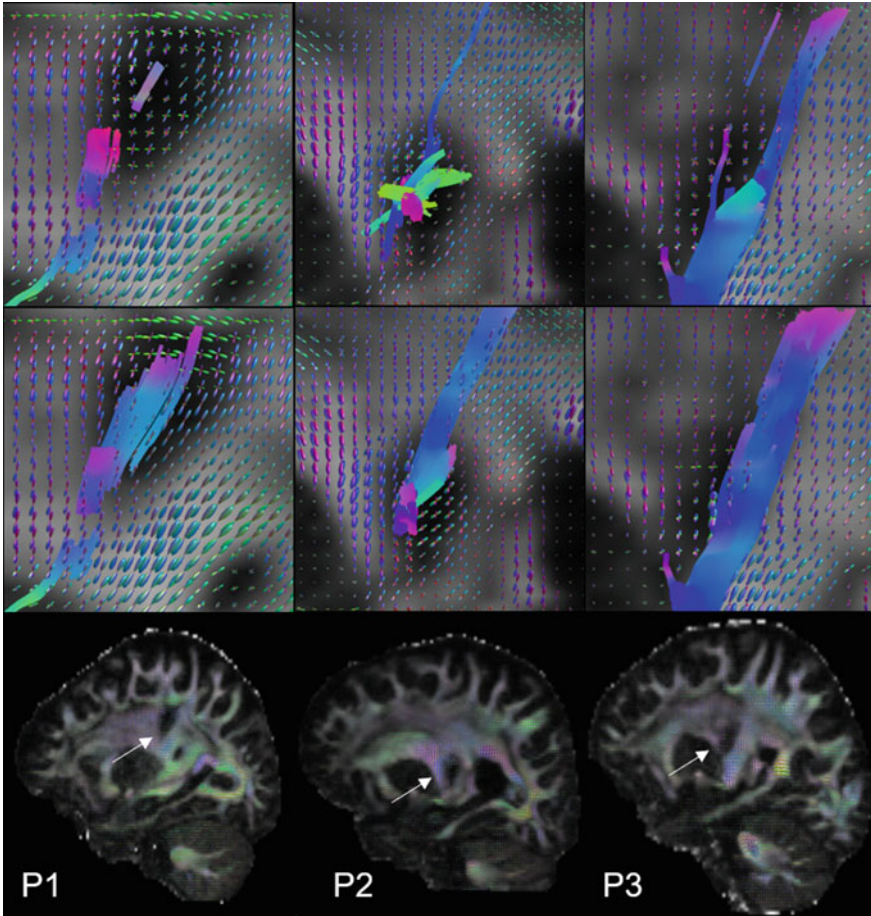


Fig. 6 Deterministic tractography results before (top) and after (middle) restoration: Before the restoration, a portion of all three patients streamlines prematurely terminate once they enter the lesion area, making it difficult to study the patients lesion connectivity. After the restoration, tractography can be performed more accurately because the FODs have been restored, enhancing the tracking and mapping of connectivity in the lesion areas. The results are plotted on top of magnified portion of the lesion area in the sagittal FA slice (bottom)

inpainting with their optimal affine combination of their neighbors such that the MSE is minimized. Consequently, blurring is reduced as the algorithm moves toward the center of the lesion.

Although performance was only measured on simulated cuboidal lesions, our method is applicable to lesions of any shape. Besides lesion size and location, the quality of the restoration depends on the initial healthy fiber diffusion models that are optimally combined to inpaint the first set of models in the lesion area. If the healthy models are corrupted by noise or by proximity to the lesion, it will get propagated

into all subsequent inpainted models. Consequently, we recommend overestimating the lesion mask and carefully defining the white matter mask to ensure all models used in the initial stages are in fact healthy. Moreover, despite only demonstrating the restoration of lesioned diffusion tensors and FODs, orientation distribution functions (ODFs) from QBI could also be restored using our approach by representing them with an orthonormal spherical harmonic basis and using FOD reorientation to build a distribution of ODFs.

Clinicians and researchers could find our approach beneficial for restoring fiber diffusion models in lesioned areas in their clinical diffusion datasets because it not only improves the accuracy of measuring changes in tissue microstructure relative to measurements from the contralesional area but also improves the accuracy of tractography results and the mapping of connectivity from the lesion for improved study of structure-function relationships and outcome prediction. To apply our approach, visit <https://github.com/clintg6/OFDMR>.

References

1. Chiang, C.-W., et al.: Quantifying white matter tract diffusion parameters in the presence of increased extra-fiber cellularity and vasogenic edema. *Neuroimage* **101**, 310–319 (2014)
2. Song, J., et al.: DTI measures track and predict motor function outcomes in stroke rehabilitation utilizing BCI technology. *Frontiers Hum. Neurosci.* **9**, 195 (2015)
3. Greene, Clint., Cieslak, Matt, Grafton, Scott T.: Effect of different spatial normalization approaches on tractography and structural brain networks. *Netw. Neurosci.* **2**(3), 362–380 (2018)
4. Langen, C.D., et al.: Disconnection due to white matter hyperintensities is associated with lower cognitive scores. *Neuroimage* **183**, 745–756 (2018)
5. Theaud, G., et al.: Impact of white-matter hyperintensities on tractography. In: 25th Annual Meeting of the International Society for Magnetic Resonance in Medicine (ISMRM). Honolulu: International Society for Magnetic Resonance in Medicine (2017)
6. Greene, C., Cieslak, M., Grafton, S.T.: Effect of different spatial normalization approaches on tractography and structural brain networks. *Netw. Neurosci.* **2**(3), 362–380 (2018)
7. Sdika, Michal, Pelletier, Daniel: Nonrigid registration of multiple sclerosis brain images using lesion inpainting for morphometry or lesion mapping. *Hum. Brain Mapp.* **30**(4), 1060–1067 (2009)
8. Prados, F., et al.: Fully automated patch-based image restoration: application to pathology inpainting. In: International Workshop on Brainlesion: Glioma, Multiple Sclerosis, Stroke and Traumatic Brain Injuries. Springer, Cham (2016)
9. Sun, W., Amezcua, L., Shi, Y.: FOD restoration for enhanced mapping of white matter lesion connectivity. In: International Conference on Medical Image Computing and Computer-Assisted Intervention. Springer, Cham (2017)
10. Hofman, A., et al.: The Rotterdam study: 2016 objectives and design update. *Eur. J. Epidemiol.* **30**.8, 661–708 (2015)
11. Glasser, M.F., et al.: The minimal preprocessing pipelines for the human connectome project. *Neuroimage* **80**, 105–124 (2013)
12. Tournier, J.-D., Calamante, F., Connelly, A.: Robust determination of the fibre orientation distribution in diffusion MRI: non-negativity constrained super-resolved spherical deconvolution. *Neuroimage* **35**.4, 1459–1472 (2007)
13. Tournier, J.-D., Calamante, F., Connelly, A.: MRtrix: diffusion tractography in crossing fiber regions. *Int. J. Imaging Syst. Technol.* **22**.1, 53–66 (2012)

14. Tax, C.M.W., et al.: Recursive calibration of the fiber response function for spherical deconvolution of diffusion MRI data. *Neuroimage* **86**, 67–80 (2014)
15. Raffelt, D., et al.: Reorientation of fiber orientation distributions using apodized point spread functions. *Magn. Reson. Med.* **67.3**, 844–855 (2012)
16. Zhang, H., et al.: Unbiased white matter atlas construction using diffusion tensor images. In: *International Conference on Medical Image Computing and Computer-assisted Intervention*. Springer, Heidelberg (2007)
17. Avants, B.B., et al.: Symmetric diffeomorphic image registration with cross-correlation: evaluating automated labeling of elderly and neurodegenerative brain. *Med. Image Anal.* **12.1**, 26–41 (2008)
18. Telea, A.: An image inpainting technique based on the fast marching method. *J. Graphi. Tools* **9(1)**, 23–34 (2004)
19. Garyfallidis, E., et al.: Dipy, a library for the analysis of diffusion MRI data. *Frontiers Neuroinform.* **8**, 8 (2014)

Diffusion Anisotropy Identification by Short Diffusion-Diffusion Correlation Spectroscopy



Fangrong Zong, Yan Zhuo, Natasha Spindler, Huabing Liu,
and Petrik Galvosas

Abstract Water diffusion is generally anisotropic in porous media, giving the opportunity to access the microstructure of a substance. Two-dimensional (2D) Diffusion-Diffusion CORrelation Spectroscopy (DDCOSY), which is one kind of multi-dimensional diffusometry (MUD) techniques, was introduced to reveal microscopic anisotropy by tracing molecular displacements in orthogonal spatial directions. As DDCOSY is most applicable to substances with long transverse relaxation times, a short version of DDCOSY (i.e. sDDCOSY) was proposed with two diffusion gradient pairs applied simultaneously. With the increased interest in applying the MUD techniques in more complex media, it should be noted that the non-zero off-diagonal diffusion coefficients may lead to ambiguous correlation results in macroscopically anisotropy systems. In this work, we investigate the behavior of off-diagonal diffusion coefficients and suppress their influences on final correlation maps by altering one pulsed-field-gradient (PFG) direction. Results from Monte-Carlo simulations in a three-dimensional confining domain with a bundle of capillaries orientated by a certain degree verified the correction. Further experiments on different capillary networks demonstrate the ability of the proposed approach to unveil sample microstructure. The proposed sDDCOSY approach allows for applying MUD techniques for both microscopic and macroscopic anisotropic systems, with potentials to combine with imaging encodings.

F. Zong (✉) · Y. Zhuo
Institute of Biophysics, Chinese Academy of Sciences, Beijing, China
e-mail: fangrong.zong@ibp.ac.cn

N. Spindler
Tecan Schweiz AG, Männedorf, Switzerland

H. Liu
Beijing Limecho Technology Co., Ltd, Beijing, China

P. Galvosas
Victoria University of Wellington, Wellington, New Zealand

1 Introduction

Multi-dimensional diffusometry (MUD) techniques have been extensively used in biological and medical sciences to investigate the molecular composition and morphology of a substance under study [1–5]. By applying multiple diffusion-sensitive gradient pairs at different angles/directions, the non-uniformity of molecular diffusivity can be revealed with the aid of numerical analysis algorithms. For instance, the angular double pulsed field gradient (d-PFG) measures the averaged axon diameter in a nervous system [6] and has been applied to detect brain injury [7]. Among these MUD techniques, a diffusion-diffusion correlation spectroscopy (DDCOSY) technique was proposed to map out the portion of spatially dependent diffusion from living plant samples and tumor-bearing mouse brains, resolving local anisotropy without imaging encodings [8, 9]. The DDCOSY approach uses two diffusion encodings at subsequent observation time windows which are most applicable to substances with long transverse relaxation time and ignorable internal magnetic field effect. In tissues with short transverse relaxation times (e.g. the T_2 of the gray matter of the rat brain is less than 90 ms at the magnetic field above 3 T), it may not be advisable to use the conventional DDCOSY techniques to detect tissue microstructure.

A simplified approach to retain signal from short relaxation time components and correlate the diffusions along different directions is to apply two independent PFGs simultaneously, which was proposed in 2011 and named with sDDCOSY [10]. The timing of the sDDCOSY pulse sequence is identical to the single PFG, with half shortening the period of signal loss due to spin relaxation as compared to the conventional DDCOSY pulse sequence. Therefore, a significant improvement of the acquired signal intensity is gained by using the sDDCOSY pulse sequence, which has been demonstrated in isotropic samples with only non-zero diagonal diffusion coefficients (e.g. bulk water and sands). However, when using the original sDDCOSY sequence in samples with non-zero off-diagonal diffusion coefficients, the correlation probability of diffusion coefficients along different directions that is obtained by a common numerical analysis algorithm for two-dimensional NMR correlation experiments (i.e. two-dimensional inverse Laplace transform (2D-ILT) [11]) may not be properly mapped. In previous published work [12], a possible compensation method was proposed, for which we provide an upgrade and more details here.

With the continuously increasing effort in applying MUD techniques in complex porous media, such as combining MUD with imaging encodings (i.e. MUDI), it is therefore essential to bring attention to the off-diagonal effects or any cross terms that may occur in signal acquisition. In this contribution, we start by reviewing the advantages and limitations of sDDCOSY with a MUD example by studying the signal evolution of the sequence, followed by introducing a detailed acquisition and analysis procedure to mitigate the problem. We further demonstrate our approach with Monte-Carlo simulation and experimental data in a bundle of capillaries with various orientation degrees.

2 Theory

2.1 Short Diffusion-Diffusion Correlation Spectroscopy

The DDCOSY pulse sequence allows one to investigate sample microstructure both qualitatively and quantitatively [1, 8, 9]. However, the acquired signal intensity would attenuate due to spin relaxation during the diffusion observation time. For instance, in the DDCOSY spin echo sequence, the factor from a transverse relaxation time (T_2) can be simplified as $\exp(-T_E/T_2)$, where T_E is the echo time. If T_2 of the sample is one-order shorter than T_E , there will be no signal acquired as $\exp(-T_E/T_2) \approx 0$. To overcome this limitation, the common pulse sequence for DDCOSY was shortened where two gradients with different directions are applied instantaneously. An example of the short DDCOSY (sDDCOSY) pulse sequence with spin echo acquisition can be found in the previous work [12]. It correlates the diffusion coefficients (or molecular displacements) at the same time but along different directions. Given certain diffusion gradients applied along different directions, the signal acquisition is identical to a single PFG measurement. In this case, time evolution of the obtained signal would obey similar expression with the single PFG evolution but with two independent diffusion gradients in a narrow gradient pulse approximation,

$$M(\mathbf{q}_1, \mathbf{q}_2) = \sum_{i=1}^N f(\mathbf{D}^i) \exp\left(-\frac{T_E}{T_2}\right) \exp\left[-\Delta(\mathbf{q}_1^T + \mathbf{q}_2^T) \mathbf{D}^i (\mathbf{q}_1 + \mathbf{q}_2)\right], \quad (1)$$

where, $\mathbf{D}^i = [D_{xx}, D_{xy}, D_{xz}; D_{yx}, D_{yy}, D_{yz}; D_{zx}, D_{zy}, D_{zz}]^i$ stands for the symmetric diffusion tensor with six independent elements. $\mathbf{q} = [q_x, q_y, q_z]^T$ with a subscript of 1,2 indicates the two scattering wave vectors with the definition of $q = (2\pi)^{-1} \gamma \delta G_{\text{diff}}$ (γ is the gyromagnetic ratio, $2\pi \times 42.56$ MHz/T for ^1H , δ and G_{diff} are the duration and strength of the diffusion gradient respectively) [13], $f(\mathbf{D}^i)$ is the correlation probability of the i th diffusion tensor at two directions. N is the number of different diffusion environments in the porous space.

To expand Eq. (1) and normalize the magnetization with no gradients applied, one can cancel the effect from transversal relaxation time and write in the tensor form of

$$M_{\text{norm}}(\mathbf{q}_1, \mathbf{q}_2) = \sum_{i=1}^N f(\mathbf{D}^i) \exp\left[-\Delta(\mathbf{q}_1^T \mathbf{D}^i \mathbf{q}_1 + \mathbf{q}_2^T \mathbf{D}^i \mathbf{q}_2 + \mathbf{q}_1^T \mathbf{D}^i \mathbf{q}_2 + \mathbf{q}_2^T \mathbf{D}^i \mathbf{q}_1)\right]. \quad (2)$$

The first two terms in the right bracket contain the influences of diagonal diffusion coefficients while the rest (i.e. the cross or mixing terms) show the additional decay due to the off-diagonal diffusion coefficients.

2.2 Cancellation of the Mixing Term

Given that the two gradients in the sDDCOSY are applied along y and z directions, meaning $\mathbf{q}_1 = [q_y, 0, 0]^T (q_y \geq 0)$ and $\mathbf{q}_2 = [0, q_z, 0]^T (q_z \geq 0)$, further tensor expansion of Eq. (2) would be

$$M_{norm}(q_y, q_z) = \sum_{i=1}^N f(D_{yy}^i, D_{zz}^i) \exp \left[-\Delta(q_y^2 D_{yy}^i + q_z^2 D_{zz}^i + q_y q_z D_{yz}^i + q_y q_z D_{zy}^i) \right]. \quad (3)$$

The first two terms in the right bracket contain the contributions of diagonal diffusion coefficients (D_{yy} and D_{zz}) while the last two terms show the extra decay due to the off-diagonal diffusion coefficients $D_{yz} = D_{zy}$. For isotropic substances, the diffusion tensor of bulk samples contains non-zero diagonal and zero off-diagonal elements, thus the mixing term is zero. In this case, Eq. (3) becomes

$$M_{norm}(q_y, q_z) = \sum_{i=1}^N f(D_{yy}^i, D_{zz}^i) \exp \left[-\Delta(q_y^2 D_{yy}^i + q_z^2 D_{zz}^i) \right], \quad (4)$$

where, $f(D_{yy}^i, D_{zz}^i)$ is the diffusion correlation probability along y and z directions in the i th diffusion tensor environments. Because q_y and q_z are two independent variables, the acquired signal is a 2D matrix. Each elements in the matrix is obtained from a summation of N diffusion components at a particular set of (q_y, q_z) . Therefore, one can thus use a well-known numerical processing toolbox, 2D-ILT [11, 14], to obtain a D - D correlation map from the 2D signal through a constraint optimization approach [15]:

$$\hat{f} = \underset{f \geq 0}{\operatorname{argmin}} \|M - K_1 f K_2\|^2 + \rho \|f\|^2, \quad (5)$$

where \hat{f} is an estimated 2D distribution function holding the joint correlation probability of D_{yy} and D_{zz} , and the $\|\cdot\|$ is the Frobenius norm of the matrix. K_1 and K_2 are the kernel functions constituted from the first two exponential factors in Eq. (3), with $K_1 = \exp(-\Delta q_y^2 D_{yy})$ and $K_2 = \exp(-\Delta q_z^2 D_{zz})$. In this inversion step, D_{yy} and D_{zz} are discretized to form a meshgrid and the singular value decomposition method is used to solve this highly ill-posed problem. ρ is the smoothing parameter to suppress the noise and control/improve the stability in the estimated distribution. After processing the acquired signal decay by using Eq. (5), \hat{f} can be distributed in a correlation map referred to as a D - D map.

However, for macroscopically anisotropic samples (i.e. D_{yz} may not equal to 0), the mixing term in Eq. (3) will start contributing to the signal decay, thus it may return the biased D - D map if directly processing the obtained signal by using 2D-ILT (which will be visualized in Sect. 4.1). The obtained joint probability of diffusion coefficients along two orthogonal directions will be contaminated by the coupling from the off-diagonal diffusion coefficients.

Here, we propose to add an additional set of sDDCOSY data to erase out the contamination from the off-diagonal diffusion coefficients. Firstly, (3) can be rewritten as

$$M_{norm1}(q_y, q_z) = \sum_{i=1}^N f(D_{yy}^i, D_{zz}^i) \exp[-\Delta(q_y^2 D_{yy}^i + q_z^2 D_{zz}^i)] \exp(2q_y q_z D_{yz}^i \Delta). \quad (6)$$

Another sDDCOSY sequence but with alternating direction of the second pair ($\mathbf{q}_2 = [0, 0, -q_z]^T$ ($q_z \geq 0$)) is applied, thus we have

$$M_{norm2}(q_y, -q_z) = \sum_{i=1}^N f(D_{yy}^i, D_{zz}^i) \exp[-\Delta(q_y^2 D_{yy}^i + q_z^2 D_{zz}^i)] \exp(-2q_y q_z D_{yz}^i \Delta). \quad (7)$$

By multiplying Eqs. (6) and (7), it would return

$$M_{norm3} = M_{norm1} \times M_{norm2} = \left[\sum_{i=1}^N f(D_{yy}^i, D_{zz}^i) \exp[-\Delta(q_y^2 D_{yy}^i + q_z^2 D_{zz}^i)] \right]^2. \quad (8)$$

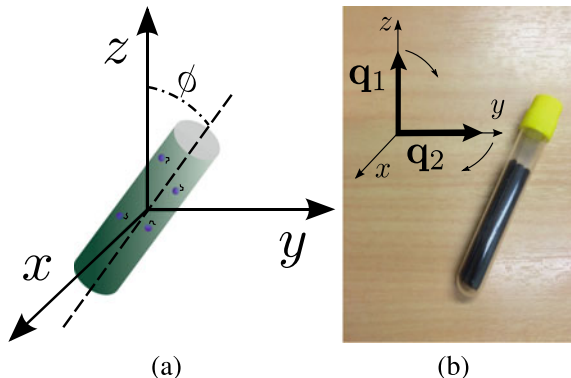
By taking the square root of M_{norm3} , the processed data would follow same evolution as given in Eq. (4). Moreover, the effect from the mixing term will vanish and only the diagonal diffusion coefficient components contribute in the processed data, which guarantees the 2D-ILT output to be the exact D - D correlation probability.

3 Numerical Simulation and Experimental Parameters

In order to verify the proposed approach in canceling the off-diagonal effect when using sDDCOSY in macroscopic anisotropic system (previous studies have demonstrated its application in isotropic samples [10]), the response of water diffusion through fiber networks was modeled using Monte-Carlo simulations [16]. The simulation volumes were defined as cubes of side 2000 μm . The fibers were cylinders of radius $R = 10 \mu\text{m}$ and represented in the simulation by a randomly generated pivot point and fixed directional vector with 30° off from the z -axis.

Particles were allowed to walk randomly through the space as illustrated in Fig. 1a. The number of particles was set to be $N_p = 5000$. Each particle represented the spin-carrying molecules with the diffusion step of $\Delta t = 5 \mu\text{s}$ and the diffusion coefficient of $D_0 = 2 \times 10^{-9} \text{m}^2/\text{s}$. Thus, the length (displacement) step was $\Delta r \approx 0.24 \mu\text{m}$ which is much smaller than R and can be noted as a valid length resolution. The starting position of each molecule was determined by uniformly sampling points within the simulation volume to guarantee that water molecules spread the whole space in the simulated volume. During the random walk simulation, the rule of elastic collision was adopted when the molecule hits the fiber or the simulated volume wall. The total time for one particle to perform the random walk simulation was set $T = 110 \text{ms}$.

Fig. 1 Illustration of **a** the simulated model, with blue dots representing water molecules inside the capillaries and **b** the experimental sample used in this study



At the end of the simulation, the elements of the laboratory-frame diffusion tensor were calculated:

$$D_{ij} = \frac{\langle r_i r_j \rangle}{6T} = \frac{1}{6N_p T} \sum_{n=1}^{N_p} (r_{N_T, n}^i - r_{0, n}^i) (r_{N_T, n}^j - r_{0, n}^j), \quad (9)$$

where $r_{N_T, n}$, and $r_{0, n}$ represent the initial and final positions of the n th particle, respectively.

The phase of the magnetization is accumulated during the random walk as a consequence of the employed radio-frequency pulses and diffusion gradients. According to Sect. 2.2, the simulation is separated into two steps. In the first step, the gradient strengths are set to be linearly incremented from 0 to 0.2 T/m by 16 steps along the independent directions of $[1, 0, 0]$ and $[0, 0, 1]$ which produces the signal M_{norm1} ; whereas in the second step, the gradient strengths are linearly incremented from 0 to 0.2 T/m along the directions of $[1, 0, 0]$ and $[0, 0, -1]$ which forms M_{norm2} .

All experiments were performed on a Bruker Advance 400 MHz NMR spectrometer equipped with a micro-imaging system. It provides a maximum gradient strength $G_{max} = 1.45$ T/m. All the experiments were carried out at ^1H resonance frequency of 399.14 MHz at the temperature of 20 °C. The experiments were firstly performed on water in 20 μm diameter aligned capillaries (z -axis) which are the experimental alternatives to fibers/axons (as shown in Fig. 1b). The environment of water in capillaries is macroscopic anisotropy when the observation time is larger than $R^2/6D_0$. Therefore, in the sDDCOSY experiments, $\Delta = 100$ ms was chosen for capillaries. The gradient duration δ was set to be 2 ms. The gradients were applied using the same strategies as described in Sect. 4.1. A Carr-Purcell-Meiboom-Gill (CPMG) experiment [17, 18] with an echo time of 1 ms and number of 3000 echoes was conducted to calculate T_2 of the bundle of the capillary network.

4 Results

4.1 Simulation Validation

The simulation results of the magnetization evolution in two separated steps are shown in Fig. 2. The horizontal and vertical axes are the employed gradient strengths along y - and z - axis. The intensities quantify the normalized magnetization as defined in Eqs. (6) and (7). It should be noted that the horizontal gradient strengths increase from left to right. As can be seen from Fig. 2a, signal decreases in both directions due to molecular displacements. However, in Fig. 2b, signal increases when G_z is between 0 and 0.75 T/m and G_y is from 0.05 T/m to 0.15 T/m with the opposite direction. Moreover, the decay pattern follows non-orthogonal exponents which means molecular displacements coupling along these two directions and is ascribed to the mixing terms in Eq. 2. Consequently, it is unsuitable to use the 2D ILT algorithm to directly process the datasets shown in Fig. 2.

Nevertheless, if one follows the strategy as stated in Sect. 2.2, the normalized magnetization will be corrected and displayed in Fig. 3a. Strong orthogonality is now present in the signal decay along any directions which meets the requirement of the 2D ILT algorithm in the data processing procedure. The correlated diffusion map is illustrated in Fig. 3b and the discretized size in the map is 100×100 . The horizontal and vertical axes are pre-defined series of possible values of diffusion coefficients along y - and z -axis logarithmically distributed from 10^{-11} to $\times 10^{-8}$ m^2/s . The intensities quantify the joint probability function \hat{f} as defined in Eq. (5). The diagonal line in the map is a reference representing the identical diffusion coefficients of the two directions, thus the peak lying on this line indicates an identical probability of water diffusion in any of the two directions. The peak off the diagonal line shows that different diffusion coefficients dominate in two directions, implying a preferable diffusing pathway in the sample. It can be read from Fig. 3b that the peak positions along y - and z -axis were around 0.5×10^{-9} m^2/s and 3.5×10^{-9} m^2/s .

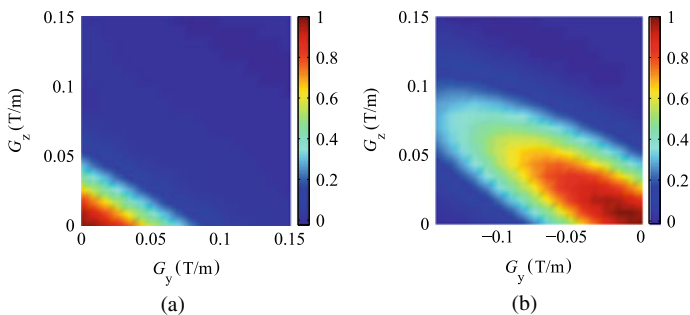


Fig. 2 The simulated signal decay of **a** M_{norm1} and **b** M_{norm2} . The horizontal and vertical axes are the gradient strengths along y - and z - axis. The intensities are the normalized magnetization. It should be noted that the horizontal gradient strengths increase from left to right

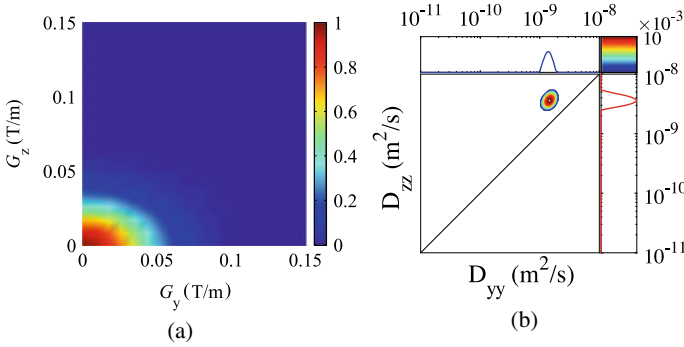


Fig. 3 The corrected signal decay **(a)** and correlation map **(b)** before and after 2D ILT

To validate the results, the diffusion tensor is calculated using Eq. 9 independently. The tensor matrix is

$$\mathbf{D} = \begin{pmatrix} 0.5377 & 0.0068 & 0.0111 \\ 0.0068 & 0.5418 & 0.0139 \\ 0.0111 & 0.0139 & 3.6833 \end{pmatrix} \times 10^{-9} \text{ m}^2/\text{s},$$

from which, one can see that the values of D_{yy} and D_{zz} are consistent with the peak positions from the correlation map given in Fig. 3b.

4.2 Experimental Results

The T_2 distribution of waters in the capillaries calculated from the CPMG dataset is approximately 80 ms, which is comparable to the T_2 value in the gray matter of the rat brain [19]. In these scenarios, it is not advisable to use conventional d-PFG sequence as signal may attenuate to a non-detectable level at the start of acquisition and the sDDCOSY sequence may be a promising candidate to investigate sample microstructure.

Figure 4 shows the experimental results of the capillaries with orientation angles of 30° after applying the proposed strategy. It is observable from the maximal value of the joint probability that the measured signal-to-noise is much less than the simulated dataset, but the correction still works reasonably well on the measured data. Diffusion correlation maps of the experiments correspond very well with the simulation results despite that a broader peak can be found in the experimental map. This is due to a large smoothing parameter ρ (in Eq. 5) automatically selected in the experimental data processing as a result of low signal-to-noise (SNR) ratio. Nevertheless, the aligning degree of peaks on both maps seems to be identical, which may indicate the orientation of the sample.

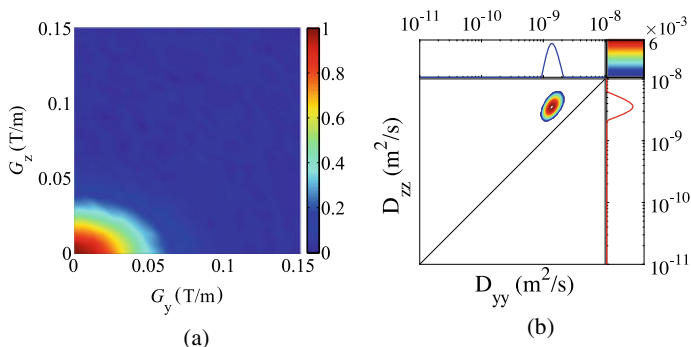


Fig. 4 The corrected signal decay (a) and diffusion correlation map (b) of measured water in the capillaries with orientation angles of 30 degrees

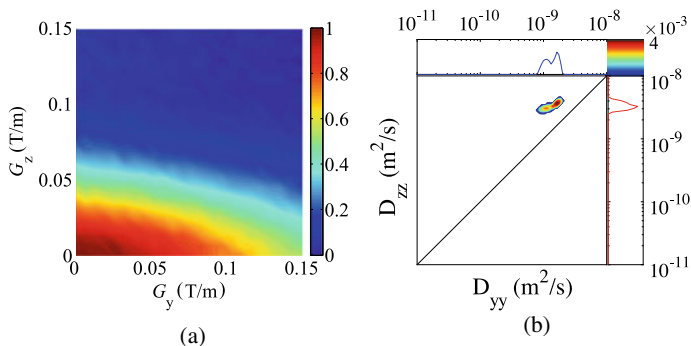


Fig. 5 The corrected signal decay (a) and diffusion correlation map (b) of measured water in mixed capillaries with radii of 20 and 10 μm

Further experiments were conducted by mixing capillaries with two different diameters (20 and 10 μm) in Fig. 1b. As expected, the uncorrected signal decay shows strong off-diagonal effects which is similar to Fig. 2. The corrected 2D datasets and its corresponding D - D map is shown in Fig. 5. The capillaries with the radius of 10 μm created much more restricted environments for water to diffuse, thus leading to much slower decay around y -axis. Correspondingly, the D - D map shows two distinct diffusing environment along y -axis. Nevertheless, this result demonstrates the capability of the modified sDDCOSY approach in a sample with different structural compartments.

5 Conclusions and Discussions

The sDDCOSY sequence is particularly suitable for substances with short transverse relaxation times. For macroscopic anisotropic system, the mixing term in sDDCOSY signal leads to ambiguous diffusion-diffusion correlation maps. A two-step experiment was proposed with one of the diffusion gradient pairs blipped to cancel the effect from the mixing terms of diffusion coefficient along two directions. Based on the results of Monte-Carlo simulations and experiments of the capillary network, their correspondence provides a good demonstration of the proposed approach.

The advantage of the proposed method over single PFG is its capability to reveal local anisotropy (or microscopic anisotropy) that is a common constraint in single PFG measurements. Moreover, as compared to DDCOSY, the sDDCOSY is advantageous in two major aspects. Firstly, there is much less influence from the relaxation effect, which makes sDDCOSY more suitable in denser tissues and materials, and at high fields. Secondly, sDDCOSY correlates the anisotropic diffusion at the same interval without diffusion exchange effects. The downsides of the proposed sDDCOSY is that it fails to resolve the correlation and exchange of diffusion along the same directions since the two PFGs are applied at the same time and have to be on orthogonal directions.

The combination of double PFG and imaging has shown great potential in investigating brain pathology such as traumatic brain injury [7]. As sDDCOSY is one kind of double PFG technique, it is believed that by combining the sDDCOSY and imaging encoding sequence, more detailed microstructure information can be revealed within a voxel. A MADCO scheme [20] can be used to accelerate the total acquisition time of the diffusion-diffusion correlation imaging to be clinically feasible.

In summary, these findings have demonstrated that the sDDCOSY technique is capable of investigating different diffusion environments in porous media, and can be much useful in more broad scenarios (such as ultra-high field where the transverse relaxation time is usually very short) to detect tissue morphology and microstructure.

Acknowledgments This work was supported by the New Zealand Ministry of Business, Innovation, and Employment (Grant E1990) and the Chinese National Major Scientific Equipment R&D Project (Grant ZDYZ2010-2).

References

1. Callaghan, P.T., Komlosh, M.E.: Locally anisotropic motion in a macroscopically isotropic system: displacement correlations measured using double pulsed gradient spin-echo NMR. *Magn. Reson. Chem.* **40**(13), S15–S19 (2002)
2. Callaghan, P.T., Furó, I.: Diffusion-diffusion correlation and exchange as a signature for local order and dynamics. *J. Chem. Phys.* **120**(8), 4032–4038 (2004)
3. Song, Y.Q., Zielinski, L., Ryu, S.: Two-dimensional NMR of diffusion systems. *Phys. Rev. Lett.* **100**(24), 248002 (2008)

4. Bernin, D., Topgaard, D.: NMR diffusion and relaxation correlation methods: new insights in heterogeneous materials. *Current Opin. Colloid Interface Sci.* **18**(3), 166–172 (2013)
5. Paulsen, J.L., Song, Y.Q.: Two-dimensional diffusion time correlation experiment using a single direction gradient. *J. Magn. Reson.* **244**, 6–11 (2014)
6. Komlosh, M.E., Özarlan, E., Lizak, M., Horkayne-Szakaly, I., Freidlin, R.Z., Horkay, F., Basser, P.J.: Mapping average axon diameters in porcine spinal cord white matter and rat corpus callosum using d-PFG MRI. *Neuroimage* **78**, 210–216 (2013)
7. Komlosh, M.E., Benjamini, D., Hutchinson, E.B., King, S., Haber, M., Avram, A.V., Holtzclaw, L.A., Desai, A., Pierpaoli, C., Basser, P.J.: Using double pulsed-field gradient MRI to study tissue microstructure in traumatic brain injury (TBI). *Microporous Mesoporous Mater.* (2017)
8. Qiao, Y., Galvosas, P., Callaghan, P.T.: Diffusion correlation NMR spectroscopic study of anisotropic diffusion of water in plant tissues. *Biophys. J.* **89**(4), 2899–2905 (2005)
9. Zong, F., Ancelet, L.R., Hermans, I.F., Galvosas, P.: Determining mean fractional anisotropy using DDCOSY: preliminary results in biological tissues. *Magn. Reson. Chem.* **55**(5), 498–507 (2017)
10. Spindler, N.: Diffusion and flow investigations in natural porous media by nuclear magnetic resonance. *Schriften des Forschungszentrums Jülich* (2011)
11. Venkataramanan, L., Song, Y.Q., Hürlimann, M.D.: Solving fredholm integrals of the first kind with tensor product structure in 2 and 2.5 dimensions. *IEEE Trans. Signal Process.* **50**(5), 1017–1026 (2002)
12. Zong, F., Spindler, N., Ancelet, L.R., Hermans, I.F., Galvosas, P.: Local and global anisotropy-recent re-implementation of 2D ILT diffusion methods. *Microporous Mesoporous Mater.* **269**, 71–74 (2018)
13. Callaghan, P.T., Eccles, C.D., Xia, Y.: NMR microscopy of dynamic displacements: k -space and q -space imaging. *J. Phys. E* **21**(8), 820–822 (1988)
14. Song, Y.Q., Venkataramanan, L., Hürlimann, M.D., Flaum, M., Frulla, P., Straley, C.: T1–T2 correlation spectra obtained using a fast two-dimensional Laplace inversion. *J. Magn. Reson.* **154**(2), 261–268 (2002)
15. Tikhonov, A.N., Arsenin, V.Y.: *Solutions of Ill-Posed Problems*. V. H. Winson Sons (1977)
16. Fieremans, E., De Deene, Y., Delpitte, S., Ozdemir, M.S., D’Asseler, Y., Vlassenbroeck, J., Deblaere, K., Achten, E., Lemahieu, I.: Simulation and experimental verification of the diffusion in an anisotropic fiber phantom. *J. Magn. Reson.* **190**(2), 189–199 (2008)
17. Carr, H.Y., Purcell, E.M.: Effects of diffusion on free precession in nuclear magnetic resonance experiments. *Phys. Rev.* **94**, 630–638 (1954)
18. Meiboom, S., Gill, D.: Modified spin-echo method for measuring nuclear relaxation times. *Review in Scientific Instrument.* **29**(8), 688 (1958)
19. de Graaf, R.A., Brown, P.B., McIntyre, S., Nixon, T.W., Behar, K.L., Rothman, D.L.: High magnetic field water and metabolite proton t_1 and t_2 relaxation in rat brain in vivo. *Magn. Reson. Med.* **56**(2), 386–394 (2006)
20. Benjamini, D., Basser, P.J.: Use of marginal distributions constrained optimization (MADCO) for accelerated 2D MRI relaxometry and diffusometry. *J. Magn. Reson.* **271**, 40–45 (2016)

Machine Learning for Diffusion MRI

Current Challenges and Future Directions in Diffusion MRI: From Model- to Data- Driven Analysis



Kurt G. Schilling , Baxter Rogers , Adam W. Anderson ,
and Bennett A. Landman 

Abstract Diffusion weighted MRI is a prominent non-invasive modality to probe in vivo tissue micro- and macro-structure and has been widely applied throughout neuro- and body imaging. The promise of micro-scale analyses has been in the creation of *virtual biopsies* that provide information in place of physical histology, while tractography and its related methods offer maps of the neuronal wiring through *virtual dissection*. While both approaches have had strong successes at the group level, specificity and sensitivity at the individual dataset/single subject level have been more elusive. Herein, we reflect on current challenges and potential future directions in the context of a futurist piece. As such, we go beyond the reasonably well-established science to offer hypotheses/postulates/challenges to encourage discussion and exploration. We postulate that there are transformative opportunities available if we complement our perspective of diffusion MRI as a signal that is explained by a tractable biophysical model with one in which data driven machine learning can inform us about detection, localization, and assessment of both normal and abnormal brain tissue in both local (voxels) and global connectivity. Towards this end, this manuscript describes challenges associated with achieving virtual biopsy (i.e., microstructural modeling) and virtual dissection (i.e., fiber tractography) and suggests opportunities to use data-driven techniques to improve modeling geometry, to learn features of the signal that may prove useful as biomarkers, and to harmonize signal, techniques, and datasets to improve tissue characterization.

K. G. Schilling · B. Rogers · A. W. Anderson · B. A. Landman (✉)
Vanderbilt University Medical Center, Nashville, TN 37235, USA
e-mail: bennett.landman@vanderbilt.edu

A. W. Anderson · B. A. Landman
Vanderbilt University, Nashville, TN 37235, USA

1 Introduction

A broad overview of the current literature could be summarized as diffusion weighted magnetic resonance imaging (MRI) offers the ability to probe a wide range of microstructure, connectivity, vascularity, perfusion, and even function parameters. Nearly all of our papers in the past decade have begun with a variant of “diffusion weighted MRI is the only non-invasive modality to ...” We note the enthusiasm in a few seminal papers. Le Bihan et al. succinctly states “diffusion is an ubiquitous process that can be investigated to understand cell physiology and life.” [1] Basser et al. noted, “These imaging parameters characterize diffusion isotropy, diffusion anisotropy, macrostructural similarity, and fiber-tract organization. We call them ‘quantitative’ because each parameter behaves like a quantitative histological or physiological stain.” [2] Similarly, Mori et al. observed “it is now possible to tract the 3D structure of axonal projections” [3]. Their works and others have transformed our understanding of tissue properties in the brain, nervous system, and body throughout the lifespan and in disease.

With over 43 thousand papers on PubMed referencing diffusion and MRI, one might think that the diffusion MRI properties are deeply understood at a fundamental level. While the sensitivity of metrics estimated from diffusion MRI shows broad promise, the specificity has been low and difficult to translate into interpretable biomarkers. One of the early successes (and to date the primary clinical use case) is in detecting acute brain ischemia [4], where the water diffusion drops significantly at a very early stage of ischemic events, providing clinicians the opportunity to provide treatment in a timely manner. While the exact biophysical basis has not been fully clarified, the substantial magnitude and low variance of the signal in the impacted tissue enables clear detection of abnormal and affected tissue.

Meanwhile, diffusion MRI has had wide success in the research literature [5, 6]. The holy grail for diffusion MRI (or any quantitative imaging method for that matter) is application as a quantitative *in vivo* “virtual biopsy” and “virtual fiber dissection.” Related to cancer, diffusion measurements have shown potential in managing patients, with derived diffusion measures capable of approximating tumor cellularity, detecting degree of malignancy, or predicting response to therapy [7, 8]. As a proxy of histology, quantitative diffusion modeling has facilitated investigations of axon and dendritic densities, axon diameter mapping, permeabilities, and cell shape estimation [9], with applications for studying normal brain development, aging, and understanding of a broad range of brain disorders. As a dissection technique, diffusion measurements have been used to map the wiring of the brain in a process called fiber tractography [10], permitting analysis of individual white matter pathways, or of the connectivity as a whole—while also creating beautiful 3D displays that have graced the covers of journals and textbooks. Finally, some novel applications include quantification of blood microcirculation, mapping information flow in white matter, or mapping functional and neuronal activation processes.

Despite these successes, the original promise of non-invasive, quantitative metrics for virtual tissue biopsies and white matter virtual dissections has not been fully realized [11, 12]. Indeed, the metrics are non-invasive. However, several limitations have impeded the realization of diffusion MRI as a true virtual biopsy, including technical limitations, model selection, experimental design, and assumptions or biases in the parameter estimation process. Tractography has also been shown to be limited in its ability to accurately map the anatomy of the brain, suffering from both false positive and false negative results, and variability due to analysis rather than true biological variations. [12, 13] Additionally, misinterpretation (e.g., “fractional anisotropy is a marker of white matter *integrity*”) and overly literal of interpretation (“the number of streamlines connecting two regions is a measure of *connectivity*”) have caused confusion, and possibly over-enthusiasm, about the abilities of these techniques.

We recognize that there are major challenges in both microstructure and fiber tractography modeling. A particular glaring open issue is that we do not yet have the ability to accurately and consistently make single subject inferences – i.e., making diagnosis, prognosis, and predictions – from a single diffusion dataset. It is quite possible that to fully realize the potential of diffusion MRI necessitates a fundamentally sound theory (an understanding of what is biophysically relevant and the relationship to the signal) and ability to estimate parameters from the signal. For this, validation of the precision and specificity of these parameters is necessary and an exact calibration of the scanning machines is required. However, we postulate that there is transformative opportunity available if we complement our perspective of diffusion MRI as a signal that is explained by a tractable biophysical model with one in which data driven machine learning can inform our detection, localization, and assessment of both normal and abnormal brain tissue in both local (voxels) and global connectivity.

Towards this end, this manuscript describes challenges associated with achieving virtual biopsy (i.e., microstructural modeling) and virtual dissection (i.e., fiber tractography). We suggest opportunities to use data-driven techniques to improve tissue modeling geometry, to learn features of the signal that may prove useful as biomarkers, and to harmonize signal, techniques, and datasets to improve tissue characterization. While we attempt to highlight/reference emerging innovation, this manuscript intentionally goes beyond the reasonably well-established science to offer hypotheses/postulates/challenges to encourage discussion and exploration. The opinions expressed herein are those of the authors and are proffered within the spirit of an ongoing discussion.

2 Virtual Biopsy

Mapping tissue microstructure with MRI holds great promise as a noninvasive window into tissue organization at the cellular level. Novikov et al. [14]

Virtual biopsies are widely and enthusiastically discussed in the popular press as new imaging modalities offer the potential for doctors to get the needed information without removing (albeit small) tissues samples from their patients. The potential benefits for medical care in terms of reduced risk, increased information availability, and greater access are easy to tout. However, reflecting on the work of [2], it is exceedingly difficult to generate diffusion MRI-based contrasts that can be considered equivalent to a standard of care histological stain. The set of challenges and opportunities that we consider focus on a pathway toward quantitative adoption of biomarkers from diffusion MRI as articulated by [2].

Voxel-wise Analysis

Consider a situation in which one has a limited sample size of patients, but choose to consider their dataset not as consisting of a few score individuals, but rather tens of millions of virtual brain biopsies. This optimistic perspective is worth striving for from image processing, machine learning, and informatics perspectives. However, to reach this state, we need a deep understanding of acquired resolution, reconstruction statistics, realized versus idealized protocols (i.e., hardware performance), noise structure (i.e., signal to noise ratio, and including spatially varying components), and how these technical factors influence voxel-wise modeling.

The entire modeling sub-field of diffusion MRI research is devoted to modeling tissue architectures and developing “contrasts” from measured signals that are reflective of relevant microstructural/micro-anatomical features as observed across millimetric volumes. As George Box famously wrote, “All models are wrong, but some are useful.” This is never truer given the near infinite complexity for in vivo cellular organization in human tissue aggregated over $\sim 10 \text{ mm}^3$ (a volume containing 0.5 to > 5 million axons [15]). The simple mean diffusivity model, which is the diffusivity averaged over orthogonal directions (the apparent diffusion coefficient), is clinically relevant in ischemia and remains the most widely used metric of diffusion. Perhaps surprisingly, the 3-D generalization of Gaussian diffusion, which approximates free random particle motion is the next most widely used representation as it provides both directional and anisotropy information that can be used to infer contrasts sensitive to white matter changes while providing a framework for fiber tracking. More recently, a plethora of models have explored multiple diffusion environments, sub-voxel orientation structure, and sensitivity to complex compartment geometry. Yet, all of these pale in comparison to what would be seen on a nanometer/micrometer level characterization of the environment (e.g., as seen on confocal or electron microscopy [16–19]). Thus, we conclude clearly non-correct models (or not entirely accurate) provide useful information.

The estimation of parameters themselves are limited by our understanding of the theory. We posit that we are reaching a stage at which explicit modeling of micro-/nano- architecture can be usefully complemented with machine learning approaches to tissue characterization. Simply put from our empirical perspective, non-idealities in hardware, dynamic aspects of anatomy, and spatial considerations render the conventional inverse problem ill-posed and exceptionally complex. To truly understand the relationship between the diffusion signal and any individual

feature of the environment, the physical theory needs to be understood at across three orders of magnitude of spatial scales (micrometer boundaries to millimeter voxels) and eight orders of temporal scales (microsecond particle interactions to minutes of acquisition).

Yet, we do not argue that we are at a theoretical impasse. We propose that rather than following a pathway solely focused on model generation, estimation, and evaluation, we ask whether the data can help identify which parameters to estimate and how to create estimators of model parameters that are robust to imaging/nuisance effects.

First, data analytics and manifold learning techniques can identify areas of variation or drive estimation of parameters. Data driven clustering and manifold learning can be used to derive representations that inspire theoretical models. In particular, identifying trends that are robust to variations in protocol, scanner, and noise will be essential to ensure broad applicability of resulting theory. Much work is yet to be done as it relates to hypothesis generation and data visualization with these complex data structures.

Second, we envision that machine learning will be able to improve our estimation methods to be able to tell the relationship between a signal and a feature. For example, consider the early statistical work on the statistics of diffusion tensor estimation [20–22]. By modeling the non-Gaussian noise distribution and presence of outliers, diffusion tensor estimation could be substantially more robust and less biased in the context of low SNR and artifact laden imaging (e.g., nearly all in vivo studies).

In many situations, both a signal and a truth are known for a limited subset of data. For example, consider: numerical simulations with geometrically determined spin walkers, physical phantoms with mechanical construction, measurement of samples with both MRI and histological imaging, or synthetic datasets derived from exceptionally high SNR/resolution studies. In these situations, supervised machine learning can be used to determine non-linear mapping functions between observable signals and the voxel-wise truth.

There has been much recent progress in supervised data driven methods. Fick et al. assessed the feasibility of estimating axon diameter using random forests trained from co-registered diffusion and histology of the rodent spinal cord [23]. Interestingly, this approach reduced the overestimation biases present in state-of-the-art modeling of axon diameter. Nedjati-Gilani et al. learned random forest mapping between Monte Carlo simulations and permeability and applied these models to multiple sclerosis patients [24]. Again, the estimated models were consistent with expected pathology.

Finally, general purpose deep learning methods are emerging to link diffusion weighted signals to histologically determined models of fiber geometry and orientation, e.g., by Nath et al. [25]. A particular advantage of deep models is that they can leverage semi-supervised data (e.g., learning environments for which truth is known for a portion of the data, but is unknown for another portion) and even conditions where truth might not be paired with observed/observable data (e.g., generative adversarial models). New resources are being developed that will enable greater participation in data driven model learning, e.g., with GPU-driven diffusion simulation architectures [26] and realistic generative tissue models [27].

Voxel-wise Biomarkers

The intent of model driven voxel-wise analyses (as well as the data-driven models described above) is to identify parameters of interest that are associated with specific biological characteristics of the tissue. For example, fractional anisotropy was developed as a representation of local orientation preference in a unitless context while axon diameter metrics specifically seek to estimate the spatial characteristics of the axon within a voxel. When these markers are sensitive/specific to disease states or conditions of interest, a clear narrative can be explained to connect imaging to biology and then to biomarker. Yet, we have seen existing putative biomarkers have largely been shown to be sensitive to changes of interest, but not specific to differences in pathology.

We have seen that data-driven approaches are beginning to complement direct modeling of the relationship between the diffusion signal and microstructural features. To date, these methods still attempt to estimate a characteristic of the tissue that may not capture the complete picture of the microstructure. For example, for a pathologist examining tissue biopsy under a microscope, a discrete value of a volume-wise axon diameter, permeability, or g-ratio may not be clinically useful (although they are certainly relevant in some way).

The core idea that we are advocating is that we can brute-force learn a biomarker from a signal that may or may not be interpretable from a microstructural perspective, but could offer clinical value. For example, it has been shown that measures of tissue variance (i.e., heterogeneity), and auto-correlation of structural boundaries, provide potentially meaningful clinical information – measures which are neither intuitively observable, nor easily quantified, from standard histological slices. [28, 29] We hypothesize that an important future area of exploration is supervised learning on patient data with known conditions in order to learn a biomarker, or feature(s) of the signal that drives useful variation in the actual measured features to best identify differences in individual brains or across populations. This variation could be driven at both local (i.e., a voxel-wise measure) or global (i.e., patterns of these voxel-wise measures) scales, and the “biomarker” could be output as continuous (regression) or binary (classification). Given a generalizable dataset (perhaps the largest obstacle to AI-informed decision making) we envision the use of complex multi-factorial biomarkers in some way, possibly complementing or in parallel with recent advances in modeling [30, 31], resulting in a number which may be hard to intuitively quantify, but is useful clinically.

New advances in regularized machine learning (including random forests and deep learning) have proven remarkably adept at identifying robust and reliable models in a massively underdetermined environment. We are particularly excited about opportunities to integrate anatomical context with local learning (e.g., atlas-based anatomy with deep learning [32]) and integrate patient context (e.g., electronic health record information [33]). These lines of research promise to allow quantitative integration of imaging information within the broader patient context and reduce the distinction between image-based biomarkers and traditional clinical risk factors/biomarkers.

Voxel-wise Harmonization

As we transition toward data driven perspectives on diffusion MRI, we must be cognizant of the lessons learned from the enthusiasm and concerns of Radiomics [34]. High order features (e.g., textures, nonlinear functions of the data) offer the potential to explore what the human eye cannot appreciate. Yet, ensuring stability/generalizability of these features in diffusion MRI across patients, protocols, and scanners is notoriously difficult.

In the context of diffusion MRI, substantial effort has been invested in harmonization across scanners, studies, and patient populations. This problem can be approached from a physics perspective to empirically measure [35] and correct for system performance [36–40]. However, identifying and correcting systemic issues is quite difficult and not amenable to modeling of supposedly isotropic regions (e.g., cerebrospinal fluid [41]).

Statistical modeling approaches have proven reasonably effective at harmonization of scalar and vector values [42, 43]. Fortin et al. have translated mixed effects regression from the genetics community [44] to apply COMBAT to correct site effects while avoiding corruption of main effects [42], which generalize to more complex analysis environments [45]. Meanwhile, Mirzaalian et al. approach inter-scanner harmonization from the perspective of signal normalization [46]. Their method uses rotationally invariant features to normalize signal energy in the spherical harmonic domain. Phantom work is progressing on both isotropic [47], temperature-controlled arrays [41], and biological mimics [48–50].

Again, modern regularized machine learning presents the opportunity to overcome limitations of a priori models. The multi-year CDMRI MUSHAC 2017-2019 challenge presented data from 2 scanners, with 2 different protocols each, and had entrants compete to harmonize and/or enhance the data [51]. Numerous groups have presented dictionary-based and deep learning methods to solve this puzzle [52], including fully convolutional networks or residual networks, most often learning directly from the spherical harmonic representation of the diffusion signal over a sphere, or rotationally invariant features of these functions, rather than learning directly from the diffusion signal [51]. In general, algorithms were successful in harmonizing data across scanners, and enhancing data in both spatial and angular domains, showing improvements in normalized errors between scanners, and improvements over simple linear spatial interpolations.

Signal and tissue modelling of DW-MRI has been aggressively pursued from various classic mathematical perspectives. We are particularly excited about the expansion of signal modeling into semi-supervised machine learning approaches. The family of Siamese networks [53] from computer vision can be adapted to a null space tuning approach [54]. The foundational/corpus idea is to use a core network/model in a supervised manner and stabilize the estimation based on paired unlabeled data (e.g., data for which ground truth is not known and the pairs can be sets of scans that are expected to share similar results, i.e., scan-rescan or “traveling” data). Incorporating paired unlabeled data in a semi-supervised fashion, the core estimator can be augmented with enhanced reproducibility from different sites

even when the true value is unknown for inter-site data [54]. The proposal of semi-supervised deep learning approaches for DW-MRI has unlocked further potential for a host of new methods for tissue and signal modelling of DW-MRI. As with all data-driven methods, we must be cautious of risks associated with overfitting and extrapolating beyond the bounds of the training data. Explainability, especially in the context of outliers and abnormal situations will be critical for bridging the gap between physics-based theory and empirical parameters.

3 Virtual Dissection

Three-dimensional tract reconstruction (tractography) ... allows us to visualize trajectories of specific white matter fiber bundles and has potential to perform quantitative evaluation of properties of individual tracts. This provides exciting opportunities to assess the impact of diseases on specific white matter tracts. Once the location of a tract is defined, its size can be measured. Wakana et al. [55]

One of the most intriguing and elusive promises of diffusion weighted MRI has been to trace individual axons (or fibers or fiber bundles) through the brain. The initially presented formulation of *tractography* traced long range connectivity on a point-by-point “shooting” basis using local definitions of orientation to construct extended line segments known as streamlines. These streamlines exhibit a striking resemblance to brain fibers visualized with freeze-thaw brain white matter dissections [56], showed strong sensitivity for known white matter anatomy [57], and correlated well with disease phenotypes. Yet, we now know that the relationship between computer traced fibers and anatomy is quite a bit more complex and nuanced than digital representations of axon connections. Recently, new terms have emerged to distinguish the process of reconstructing fibers (i.e., tractography) from the broader goal of characterizing white matter structural connectivity. This new field is often presented as tractometry in analogy with brain morphometry being the study of shape [58] (in contrast to the more limited field of brain segmentation, which identifies specific shapes). Tractometry is “a comprehensive assessment of tract-specific microstructural measures.” [59] Yet, as with voxel-wise methods, tractography/tractometry have shown promising sensitivity, but specificity concerns remain [60–63]. We hypothesize that a combination of data driven approaches and anatomical/expert context will allow the field to transition from tractography towards subject specific *virtual dissection*.

Anatomical Modeling

Traditionally, fiber tractography is used to segment specific pathways of interest or to quantify whole brain structural connectivity. For the former, once a white matter bundle of interest is extracted, its properties—geometrical, microstructural, and locational - can be quantified and compared across populations or across time. While the general organization of major pathways of the brain had been described hundreds of

years ago through gross dissection, histological staining, degeneration, and clinico-pathologic correlations studies by the likes of Thomas Willis (1664), Nicolaus Steno (1671), Johann Christian Reil (1809), Karl Burdach (1819), Augustus Waller (1854), and Joseph Dejerine (1895) [64]—and further elucidated through the highly specific investigations of histological tracer studies [65] - there is still tremendous heterogeneity in the nomenclature and presumed organization of many of these structures. For example, confusion due to synonymous names, cross-species differences in bundles, sub-divisions or networks of pathways, may lead to tremendous differences in approaches taken to reproduce these pathways using tractography. Because of this, explicitly modeling the spatial extent of specific white matter bundles using tractography may quickly become problematic.

Towards this end, we suggest that this challenge of subject specific in vivo virtual dissection can be overcome with existing tractography (or streamline generation) algorithms, in combination with highly detailed definitions and descriptions of the pathways. Several studies comparing tractography to neuroanatomical tracers [61, 66–69] have illustrated the high sensitivity of tractography. By highly constraining the tractography process through anatomical limitations of known spatial structures, we hypothesize that we can significantly increase specificity as well. With enough constraints, derived through expert knowledge, on large enough datasets, automated single-subject tractography using “artificial intelligence-captured” constraints may become a possibility. While some progress has been made in using machine-learning/artificial intelligence to improve fiber orientation estimation [70], or to set priors on spatial locations of bundles [71], learning and adapting the propagation of streamlines individually [70] and throughout the bundles, may be a possible future direction.

While there is considerable optimism in future ability to automatically extract fiber pathways of the brain with high anatomical accuracy, challenges will certainly exist in the context of non-healthy or atypical individuals (i.e., the presence of tumors). At present, we do not have significant, validated, models of how pathways (or streamlines) should behave in the presence of affected tissue. We hypothesize that the same “AI-driven” constraints and rules for where pathways start and where they end will not apply in these scenarios. Thus, it remains to be seen how tractography can be applied in this clinical context—Do we need priors on abnormal anatomy, or are they the same as for normal anatomy? Do we actually require anatomical accuracy of the spatial extent of pathways, or does the presence or absence of streamlines indicate clinical utility, or can simple measures of tumors or lesions relative to typical pathways aid in decision making?

Connectivity Biomarkers

As a tool for pathway delineation and connectivity estimation, tractography techniques offer a number of potential biomarkers. Just as “tractometry” [72, 73] has recently emerged as a way to describe the comprehensive assessment of tract-specific measures of the brain, the term structural “connectome” can be used to describe the wiring diagram of the brain. While these quantitative tools have proven useful in studying health, development, and disease, they are open to criticism related to

biases in the streamline process, possible over-interpretation of metrics (i.e., changes in “white matter integrity”), unintuitive interpretation of measures, or the tremendous dimensionality of the datasets and the search for significant differences (i.e., multiple microstructural measures, for every vertex along a streamline, for all streamlines, for all white matter bundles, in every subject).

To date, connectivity driven biomarkers have largely either focused on graph theory/graph-based metrics [74] or on a priori characterization of specific pathways given the combinatoric issues associated with multiple comparison correction. Recently, relatively simple linear principal component analysis of tractometry has shown that a few biologically interpretable components explain the majority of the variation in diffusion measures [75]. Local connectome fingerprints appear to indicate clear patterns of subject-specific features [76]. Following in the vein of data driven voxel-wise analysis, deep methods are starting to be applied to connectivity/tractometry, e.g., in epilepsy [77, 78].

It is perhaps controversial to suggest that biomarkers do not need to be interpretable, but rather just useful. However, starting with data-driven biomarkers that are useful and seeking to understand how they can be interpreted (e.g., [75]) seems to be a promising method to search the extremely large space of potential biomarkers from the high dimensional tractometry/connectometry. As we seek to refine biomarkers, we observe that limiting the number of hypotheses has proven successful with existing techniques to mitigate the curse of dimensionality. Hence, we postulate the inclusion of prior information, population distributions (especially those that perform patient-specific adaptation), and statistical characterizations of second and higher-order statistics will guide the data-driven approaches to learn both useful and meaningful metrics.

Connectivity Harmonization

Just as with virtual biopsies, uncertainties and variations in pathway segmentation and connectivity approaches are influenced by all stages of processing from acquisition (SNR, angular resolution, diffusion weightings), reconstruction (diffusion tensor versus high angular resolution diffusion imaging), and the tractography process itself (deterministic versus probabilistic approaches) [79]. Just as crucial, we argue that to yield consistent, meaningful results within and across studies, it is critical to not only harmonize protocols, but harmonize the language we use to describe anatomy.

Currently, there are two fundamental challenges with harmonization of connectivity analyses. First, there is no consensus for the geometry, trajectory, and connectivity of even the most well studied pathways. Second, even if a consensus on the nomenclature is reached within by the experts working on a given study, it is technically challenging to integrate this information into the tractography/tractometry/connectometry framework. While substantial progress is being made in standardizing language in these contexts, the work is exceptionally difficult, time consuming, and challenging to generalize.

Perhaps optimistically, we postulate that data-driven approaches offer a solution to this problem. A large body of public diffusion datasets has now become available through the Human Connectome Project [80], UK Biobank [81], Pediatric Imaging,

Neurocognition, and Genetics (PING) study [82], etc. These resources offer an opportunity to aggregate consensus definitions in a federated/asynchronous manner so that experts can explore each other's work separated both in space and in time. As with harmonization of virtual biopsies, supervised learning can identify programmatic definitions of consensus definitions and be used to build tractometry "spaces" that provide a common reference framework, as has been done with simple white matter parcellations [83], skeletons [84], or bundle clusters [85]. Moreover, we have the opportunity to use unsupervised machine learning techniques to identify common anatomical patterns that transcend cohort, scanner, study, site, etc. and link these patterns to explainable anatomical features. A grand, big-data challenge will be integrating the diffusion virtual dissections with functional and structural metrics, which are made available with hundreds of millions of potential streamlines.

4 Closing Thoughts

Microstructural imaging relies on a model that relates microscopic features of tissue architecture to MR signals. Alexander et al. [9]

Advances in functional, vascular, and chemical exchange imaging provide exciting complementary information, but do not directly probe the cellular compartmental/organization in a geometric sense. Advancements in diffusion MRI are at the cusp of providing robust single subject inferences in terms of virtual biopsies and white matter tract dissections. Across the key technical areas of these fields (estimation, biomarker creation, and harmonization), we observe rapid innovation and creativity with data driven techniques. We foresee a rapid growth of machine learning studies in the diffusion MRI literature, which will ultimately aid efforts in microstructural modeling and lead to new classes of biomarkers. Indeed, "diffusion weighted MRI is the only non-invasive modality" to shed light on the intra-voxel microarchitecture and extended structural connectivity of tissues. By further developing machine learning techniques, we may find that up to this point we have only seen the 'tip of the iceberg' of information available in diffusion MRI data.

Acknowledgments This work was supported by NIH R01EB017230, NIH R01NS058639, and NIH T32EB001628.

References

1. Le Bihan, D., Iima, M.: Diffusion magnetic resonance imaging: what water tells us about biological tissues. *PLoS Biol.* **13**, e1002203 (2015)
2. Basser, P.J., Pierpaoli, C.: Microstructural and physiological features of tissues elucidated by quantitative-diffusion-tensor MRI. *J. Magn. Reson.* **213**, 560–570 (2011)

3. Mori, S., Crain, B.J., Chacko, V.P., Van Zijl, P.C.: Three-dimensional tracking of axonal projections in the brain by magnetic resonance imaging. *Ann. Neurol. Official J. Am. Neurol. Assoc. Child Neurol. Soc.* **45**, 265–269 (1999)
4. Warach, S., Chien, D., Li, W., Ronthal, M., Edelman, R.: Fast magnetic resonance diffusion-weighted imaging of acute human stroke. *Neurology* **42**, 1717 (1992)
5. Jones, D.K.: *Diffusion MRI: theory, methods, and application*. Oxford University Press, Oxford, New York (2010)
6. Le Bihan, D., Johansen-Berg, H.: Diffusion MRI at 25: exploring brain tissue structure and function. *Neuroimage* **61**, 324–341 (2012)
7. Koh, D.M., Collins, D.J.: Diffusion-weighted MRI in the body: applications and challenges in oncology. *AJR Am. J. Roentgenol.* **188**, 1622–1635 (2007)
8. Nilsson, M., Englund, E., Szczepankiewicz, F., van Westen, D., Sundgren, P.C.: Imaging brain tumour microstructure. *Neuroimage* **182**, 232–250 (2018)
9. Alexander, D.C., Dyrby, T.B., Nilsson, M., Zhang, H.: Imaging brain microstructure with diffusion MRI: practicality and applications. *NMR Biomed.* **32**, e3841 (2019)
10. Mori, S., van Zijl, P.C.: Fiber tracking: principles and strategies—a technical review. *NMR Biomed.* **15**, 468–480 (2002)
11. Jones, D.K., Knösche, T.R., Turner, R.: White matter integrity, fiber count, and other fallacies: the do’s and don’ts of diffusion MRI. *Neuroimage* **73**, 239–254 (2013)
12. Schilling, K.G., Daducci, A., Maier-Hein, K., Poupon, C., Houde, J.C., Nath, V., Anderson, A.W., Landman, B.A., Descoteaux, M.: Challenges in diffusion MRI tractography—lessons learned from international benchmark competitions. *Magn. Reson. Imaging* **57**, 194–209 (2019)
13. Maier-Hein, K.H., Neher, P.F., Houde, J.C., Cote, M.A., Garyfallidis, E., Zhong, J., Chamberland, M., Yeh, F.C., Lin, Y.C., Ji, Q., Reddick, W.E., Glass, J.O., Chen, D.Q., Feng, Y., Gao, C., Wu, Y., Ma, J., He, R., Li, Q., Westin, C.F., Deslauriers-Gauthier, S., Gonzalez, J.O.O., Paquette, M., St-Jean, S., Girard, G., Rheault, F., Sidhu, J., Tax, C.M.W., Guo, F., Mesri, H.Y., David, S., Froeling, M., Heemskerk, A.M., Leemans, A., Bore, A., Pinsard, B., Bedetti, C., Desrosiers, M., Brambati, S., Doyon, J., Sarica, A., Vasta, R., Cerasa, A., Quattrone, A., Yeatman, J., Khan, A.R., Hodges, W., Alexander, S., Romascano, D., Barakovic, M., Auria, A., Esteban, O., Lemkaddem, A., Thiran, J.P., Cetingul, H.E., Odry, B.L., Mailhe, B., Nadar, M.S., Pizzagalli, F., Prasad, G., Villalon-Reina, J.E., Galvis, J., Thompson, P.M., Requejo, F.S., Laguna, P.L., Lacerda, L.M., Barrett, R., Dell’Acqua, F., Catani, M., Petit, L., Caruyer, E., Daducci, A., Dyrby, T.B., Holland-Letz, T., Hilgetag, C.C., Stieltjes, B., Descoteaux, M.: The challenge of mapping the human connectome based on diffusion tractography. *Nat. Commun.* **8**, 1349 (2017)
14. Novikov, D.S., Kiselev, V.G., Jespersen, S.N.: On modeling. *Magn. Reson. Med.* **79**, 3172–3193 (2018)
15. Walhovd, K.B., Johansen-Berg, H., Karadottir, R.T.: Unraveling the secrets of white matter—bridging the gap between cellular, animal and human imaging studies. *Neuroscience* **276**, 2–13 (2014)
16. Schilling, K.G., Janve, V., Gao, Y., Stepniewska, I., Landman, B.A., Anderson, A.W.: Histological validation of diffusion MRI fiber orientation distributions and dispersion. *Neuroimage* **165**, 200–221 (2018)
17. Schilling, K., Janve, V., Gao, Y., Stepniewska, I., Landman, B.A., Anderson, A.W.: Comparison of 3D orientation distribution functions measured with confocal microscopy and diffusion MRI. *Neuroimage* **129**, 185–197 (2016)
18. Salo, R.A., Belevich, I., Manninen, E., Jokitalo, E., Gröhn, O., Sierra, A.: Quantification of anisotropy and orientation in 3D electron microscopy and diffusion tensor imaging in injured rat brain. *Neuroimage* **172**, 404–414 (2018)
19. Kelm, N.D., West, K.L., Carson, R.P., Gochberg, D.F., Ess, K.C., Does, M.D.: Evaluation of diffusion kurtosis imaging in ex vivo hypomyelinated mouse brains. *Neuroimage* **124**, 612–626 (2016)
20. Jones, D.K., Basser, P.J.: Squashing peanuts and smashing pumpkins: how noise distorts diffusion-weighted MR data. *Magn. Reson. Med.* **52**, 979–993 (2004)

21. Chang, L.C., Jones, D.K., Pierpaoli, C.: RESTORE: robust estimation of tensors by outlier rejection. *Magn. Reson. Med.* **53**, 1088–1095 (2005)
22. Jones, D.K., Horsfield, M.A., Simmons, A.: Optimal strategies for measuring diffusion in anisotropic systems by magnetic resonance imaging. *Magn. Reson. Med.* **42**, 515–525 (1999)
23. Fick, R.H.J., Sepasian, N., Pizzolato, M., Ianus, A., Deriche, R.: Assessing the feasibility of estimating axon diameter using diffusion models and machine learning. In: 2017 IEEE 14th International Symposium on Biomedical Imaging (ISBI 2017), pp. 766–769 (Year)
24. Nedjati-Gilani, G.L., Schneider, T., Hall, M.G., Cawley, N., Hill, I., Ciccarelli, O., Drobnyak, I., Wheeler-Kingshott, C.A.G., Alexander, D.C.: Machine learning based compartment models with permeability for white matter microstructure imaging. *NeuroImage* **150**, 119–135 (2017)
25. Nath, V., Schilling, K.G., Parvathaneni, P., Hansen, C.B., Hainline, A.E., Huo, Y., Blaber, J.A., Lyu, I., Janve, V., Gao, Y., Stepniewska, I., Anderson, A.W., Landman, B.A.: Deep learning reveals untapped information for local white-matter fiber reconstruction in diffusion-weighted MRI. *Magn. Reson. Imaging* **62**, 220–227 (2019)
26. Ginsburger, K., Matuschke, F., Poupon, F., Mangin, J.-F., Axer, M., Poupon, C.: MEDUSA: A GPU-based tool to create realistic phantoms of the brain microstructure using tiny spheres. *NeuroImage* **193**, 10–24 (2019)
27. Palombo, M., Alexander, D.C., Zhang, H.: A generative model of realistic brain cells with application to numerical simulation of the diffusion-weighted MR signal. *NeuroImage* **188**, 391–402 (2019)
28. Burcaw, L.M., Fieremans, E., Novikov, D.S.: Mesoscopic structure of neuronal tracts from time-dependent diffusion. *Neuroimage* **114**, 18–37 (2015)
29. Novikov, D.S., Jensen, J.H., Helpert, J.A., Fieremans, E.: Revealing mesoscopic structural universality with diffusion. *Proc. Natl. Acad. Sci. U S A* **111**, 5088–5093 (2014)
30. Szczepankiewicz, F., van Westen, D., Englund, E., Westin, C.-F., Ståhlberg, F., Lätt, J., Sundgren, P.C., Nilsson, M.: The link between diffusion MRI and tumor heterogeneity: Mapping cell eccentricity and density by diffusional variance decomposition (DIVIDE). *NeuroImage* **142**, 522–532 (2016)
31. Chiang, C.-W., Wang, Y., Sun, P., Lin, T.-H., Trinkaus, K., Cross, A.H., Song, S.-K.: Quantifying white matter tract diffusion parameters in the presence of increased extra-fiber cellularity and vasogenic edema. *Neuroimage* **101**, 310–319 (2014)
32. Bermudez, C., Plassard, A.J., Chaganti, S., Huo, Y., Aboud, K.E., Cutting, L.E., Resnick, S.M., Landman, B.A.: Anatomical context improves deep learning on the brain age estimation task. *Magn. Reson. Imaging* (2019)
33. Chaganti, S.: Contextualizing Medical Image Analyses with Electronic Health Histories (2019)
34. Gillies, R.J., Kinahan, P.E., Hricak, H.: Radiomics: images are more than pictures, they are data. *Radiology* **278**, 563–577 (2015)
35. Rogers, B.P., Blaber, J., Welch, E.B., Ding, Z., Anderson, A.W., Landman, B.A.: Stability of Gradient Field Corrections for Quantitative Diffusion MRI. In: Proceedings of SPIE—The International Society for Optical Engineering, p. 10132 (2017)
36. Bammer, R., Markl, M., Barnett, A., Acar, B., Alley, M.T., Pelc, N.J., Glover, G.H., Moseley, M.E.: Analysis and generalized correction of the effect of spatial gradient field distortions in diffusion-weighted imaging. *Magn. Reson. Med.* **50**, 560–569 (2003)
37. Rogers, B.P., Blaber, J., Newton, A.T., Hansen, C.B., Welch, E.B., Anderson, A.W., Luci, J.J., Pierpaoli, C., Landman, B.A.: Phantom-based field maps for gradient nonlinearity correction in diffusion imaging. In: Proceedings of SPIE—The International Society for Optical Engineering, p. 10573 (2018)
38. Tao, A.T., Shu, Y., Tan, E.T., Trzasko, J.D., Tao, S., Reid, R.D., Weavers, P.T., Huston, J., Bernstein, M.A.: Improving apparent diffusion coefficient accuracy on a compact 3T MRI scanner using gradient nonlinearity correction. *J. Magn. Reson. Imaging* **48**, 1498–1507 (2018)
39. Newitt, D.C., Tan, E.T., Wilmes, L.J., Chenevert, T.L., Kornak, J., Marinelli, L., Hylton, N.: Gradient nonlinearity correction to improve apparent diffusion coefficient accuracy and standardization in the american college of radiology imaging network 6698 breast cancer trial. *J. Magn. Reson. Imaging* **42**, 908–919 (2015)

40. Malyarenko, D.I., Ross, B.D., Chenevert, T.L.: Analysis and correction of gradient nonlinearity bias in apparent diffusion coefficient measurements. *Magn. Reson. Med.* **71**, 1312–1323 (2014)
41. Hansen, C.B., Nath, V., Hainline, A.E., Schilling, K.G., Parvathaneni, P., Bayrak, R.G., Blaber, J.A., Irfanoglu, O., Pierpaoli, C., Anderson, A.W., Rogers, B.P., Landman, B.A.: Characterization and correlation of signal drift in diffusion weighted MRI. *Magn. Reson. Imaging* **57**, 133–142 (2019)
42. Fortin, J.P., Parker, D., Tunç, B., Watanabe, T., Elliott, M.A., Ruparel, K., Roalf, D.R., Satterthwaite, T.D., Gur, R.C., Gur, R.E., Schultz, R.T., Verma, R., Shinohara, R.T.: Harmonization of multi-site diffusion tensor imaging data. *Neuroimage* **161**, 149–170 (2017)
43. Fortin, J.P., Cullen, N., Sheline, Y.I., Taylor, W.D., Aselcioglu, I., Cook, P.A., Adams, P., Cooper, C., Fava, M., McGrath, P.J., McInnis, M., Phillips, M.L., Trivedi, M.H., Weissman, M.M., Shinohara, R.T.: Harmonization of cortical thickness measurements across scanners and sites. *Neuroimage* **167**, 104–120 (2018)
44. Johnson, W.E., Li, C., Rabinovic, A.: Adjusting batch effects in microarray expression data using empirical Bayes methods. *Biostatistics* **8**, 118–127 (2007)
45. Parvathaneni, P., Bao, S., Hainline, A., Huo, Y., Schilling, K.G., Kang, H., Williams, O., Woodward, N.D., Resnick, S.M., Zald, D.H.: Harmonization of white and gray matter features in diffusion microarchitecture for cross-sectional studies. In: *Computer Aided Intervention and Diagnostics in Clinical and Medical Images*, pp. 21–29. Springer, Berlin (2019)
46. Mirzaalian, H., Ning, L., Savadjiev, P., Pasternak, O., Bouix, S., Michailovich, O., Grant, G., Marx, C.E., Morey, R.A., Flashman, L.A., George, M.S., McAllister, T.W., Andaluz, N., Shutter, L., Coimbra, R., Zafonte, R.D., Coleman, M.J., Kubicki, M., Westin, C.F., Stein, M.B., Shenton, M.E., Rath, Y.: Inter-site and inter-scanner diffusion MRI data harmonization. *Neuroimage* **135**, 311–323 (2016)
47. Prohl, A.K., Scherrer, B., Tomas-Fernandez, X., Filip-Dhima, R., Kapur, K., Velasco-Annis, C., Clancy, S., Carmody, E., Dean, M., Valle, M., Prabhu, S.P., Peters, J.M., Bebin, E.M., Krueger, D.A., Northrup, H., Wu, J.Y., Sahin, M., Warfield, S.K.: Reproducibility of structural and diffusion tensor imaging in the TACERN multi-center study. *Frontiers Integr. Neurosci.* **13**, 24 (2019)
48. Provenzale, J.M., Taylor, B.A., Wilde, E.A., Boss, M., Schneider, W.: Analysis of variability of fractional anisotropy values at 3T using a novel diffusion tensor imaging phantom. *Neuroradiol J* **31**, 581–586 (2018)
49. Fan, Q., Nummenmaa, A., Wichtmann, B., Witzel, T., Mekkaoui, C., Schneider, W., Wald, L.L., Huang, S.Y.: Validation of diffusion MRI estimates of compartment size and volume fraction in a biomimetic brain phantom using a human MRI scanner with 300 mT/m maximum gradient strength. *Neuroimage* **182**, 469–478 (2018)
50. Fan, Q., Nummenmaa, A., Wichtmann, B., Witzel, T., Mekkaoui, C., Schneider, W., Wald, L.L., Huang, S.Y.: A comprehensive diffusion MRI dataset acquired on the MGH Connectome scanner in a biomimetic brain phantom. *Data Brief* **18**, 334–339 (2018)
51. Tax, C.M., Grussu, F., Kaden, E., Ning, L., Rudrapatna, U., John Evans, C., St-Jean, S., Leemans, A., Koppers, S., Merhof, D., Ghosh, A., Tanno, R., Alexander, D.C., Zappalà, S., Charron, C., Kusmia, S., Linden, D.E., Jones, D.K., Veraart, J.: Cross-scanner and cross-protocol diffusion MRI data harmonisation: a benchmark database and evaluation of algorithms. *Neuroimage* **195**, 285–299 (2019)
52. St-Jean, S., Coupé, P., Descoteaux, M.: Non Local Spatial and Angular Matching: enabling higher spatial resolution diffusion MRI datasets through adaptive denoising. *Med. Image Anal.* **32**, 115–130 (2016)
53. Bromley, J., Guyon, I., LeCun, Y., Säckinger, E., Shah, R.: Signature verification using a “siamese” time delay neural network. In: *Advances in Neural Information Processing Systems*, pp. 737–744 (Year)
54. Nath, V., Parvathaneni, P., Hansen, C.B., Hainline, A.E., Bermudez, C., Remedios, S., Blaber, J.A., Schilling, K.G., Lyu, I., Janve, V.: Inter-scanner harmonization of high angular resolution DW-MRI using null space deep learning. In: *International Conference on Medical Image Computing and Computer-Assisted Intervention*, pp. 193–201. Springer, Berlin (Year)

55. Wakana, S., Caprihan, A., Panzenboeck, M.M., Fallon, J.H., Perry, M., Gollub, R.L., Hua, K., Zhang, J., Jiang, H., Dubey, P.: Reproducibility of quantitative tractography methods applied to cerebral white matter. *Neuroimage* **36**, 630–644 (2007)
56. Koutsarnakis, C., Liakos, F., Kalyvas, A.V., Sakas, D.E., Stranjalis, G.: A laboratory manual for stepwise cerebral white matter fiber dissection. *World Neurosurg.* **84**, 483–493 (2015)
57. Catani, M., De Schotten, M.T.: A diffusion tensor imaging tractography atlas for virtual in vivo dissections. *Cortex* **44**, 1105–1132 (2008)
58. Jones, D.K., Nilsson, M.: Tractometry and the hunt for the missing link: a physicist perspective. *Microstruct. Learn.* **38** (2014)
59. Bells, S., Cercignani, M., Deoni, S., Assaf, Y., Pasternak, O., Evans, C., Leemans, A., Jones, D.: Tractometry—comprehensive multi-modal quantitative assessment of white matter along specific tracts. In: *Proceedings ISMRM (Year)*
60. Schilling, K.G., Nath, V., Hansen, C., Parvathaneni, P., Blaber, J., Gao, Y., Neher, P., Aydogan, D.B., Shi, Y., Ocampo-Pineda, M., Schiavi, S., Daducci, A., Girard, G., Barakovic, M., Rafael-Patino, J., Romascano, D., Rensonnet, G., Pizzolato, M., Bates, A., Fischl, E., Thiran, J.-P., Canales-Rodríguez, E.J., Huang, C., Zhu, H., Zhong, L., Cabeen, R., Toga, A.W., Rheault, F., Theaud, G., Houde, J.-C., Sidhu, J., Chamberland, M., Westin, C.-F., Dyrby, T.B., Verma, R., Rathi, Y., Irfanoglu, M.O., Thomas, C., Pierpaoli, C., Descoteaux, M., Anderson, A.W., Landman, B.A.: Limits to the anatomical accuracy of diffusion tractography using modern approaches. *NeuroImage* (2019)
61. Knösche, T.R., Anwander, A., Liptrot, M., Dyrby, T.B.: Validation of tractography: comparison with manganese tracing. *Hum. Brain Mapp.* **36**, 4116–4134 (2015)
62. Ambrosen, K.S., Eskildsen, S.F., Hinne, M., Krug, K., Lundell, H., Schmidt, M.N., van Gerven, M.A., Mørup, M., Dyrby, T.B.: Validation of structural brain connectivity networks: the impact of scanning parameters. *NeuroImage* 116207 (2019)
63. Thomas, C., Frank, Q.Y., Irfanoglu, M.O., Modi, P., Saleem, K.S., Leopold, D.A., Pierpaoli, C.: Anatomical accuracy of brain connections derived from diffusion MRI tractography is inherently limited. *Proc. Natl. Acad. Sci.* **111**, 16574–16579 (2014)
64. Schmahmann, J., Pandya, D.: *Fiber Pathways of the Brain*. OUP USA (2009)
65. Schmahmann, J.D., Pandya, D.N.: *Fiber Pathways of the Brain*. Oxford University Press, Oxford; New York (2006)
66. Schilling, K.G., Nath, V., Hansen, C., Parvathaneni, P., Blaber, J., Gao, Y., Neher, P., Aydogan, D.B., Shi, Y., Ocampo-Pineda, M., Schiavi, S., Daducci, A., Girard, G., Barakovic, M., Rafael-Patino, J., Romascano, D., Rensonnet, G., Pizzolato, M., Bates, A., Fischl, E., Thiran, J.P., Canales-Rodríguez, E.J., Huang, C., Zhu, H., Zhong, L., Cabeen, R., Toga, A.W., Rheault, F., Theaud, G., Houde, J.C., Sidhu, J., Chamberland, M., Westin, C.F., Dyrby, T.B., Verma, R., Rathi, Y., Irfanoglu, M.O., Thomas, C., Pierpaoli, C., Descoteaux, M., Anderson, A.W., Landman, B.A.: Limits to anatomical accuracy of diffusion tractography using modern approaches. *Neuroimage* **185**, 1–11 (2019)
67. Schilling, K.G., Gao, Y., Stepniewska, I., Janve, V., Landman, B.A., Anderson, A.W.: Anatomical accuracy of standard-practice tractography algorithms in the motor system—a histological validation in the squirrel monkey brain. *Magn. Reson. Imaging* **55**, 7–25 (2019)
68. Thomas, C., Ye, F.Q., Irfanoglu, M.O., Modi, P., Saleem, K.S., Leopold, D.A., Pierpaoli, C.: Anatomical accuracy of brain connections derived from diffusion MRI tractography is inherently limited. *Proc. Natl. Acad. Sci. U S A* **111**, 16574–16579 (2014)
69. Donahue, C.J., Sotiropoulos, S.N., Jbabdi, S., Hernandez-Fernandez, M., Behrens, T.E., Dyrby, T.B., Coalson, T., Kennedy, H., Knoblauch, K., Van Essen, D.C., Glasser, M.F.: Using diffusion tractography to predict cortical connection strength and distance: a quantitative comparison with tracers in the monkey. *J. Neurosci.* **36**, 6758–6770 (2016)
70. De Leener, B., Fonov, V.S., Collins, D.L., Callot, V., Stikov, N., Cohen-Adad, J.: PAM50: unbiased multimodal template of the brainstem and spinal cord aligned with the ICBM152 space. *Neuroimage* **165**, 170–179 (2018)
71. Yendiki, A., Panneck, P., Srinivasan, P., Stevens, A., Zöllei, L., Augustinack, J., Wang, R., Salat, D., Ehrlich, S., Behrens, T., Jbabdi, S., Gollub, R., Fischl, B.: Automated probabilistic

- reconstruction of white-matter pathways in health and disease using an atlas of the underlying anatomy. *Frontiers Neuroinform.* **5**, 23 (2011)
72. Chamberland, M., Raven, E.P., Genc, S., Duffy, K., Descoteaux, M., Parker, G.D., Tax, C.M.W., Jones, D.K.: Dimensionality reduction of diffusion MRI measures for improved tractometry of the human brain. *Neuroimage* **200**, 89–100 (2019)
 73. Rheault, F., Houde, J.C., Descoteaux, M.: Visualization, Interaction and Tractometry: dealing with Millions of Streamlines from Diffusion MRI Tractography. *Frontiers Neuroinform.* **11**, 42 (2017)
 74. Rubinov, M., Sporns, O.: Complex network measures of brain connectivity: uses and interpretations. *Neuroimage* **52**, 1059–1069 (2010)
 75. Chamberland, M., Raven, E.P., Genc, S., Duffy, K., Descoteaux, M., Parker, G.D., Tax, C.M., Jones, D.K.: Dimensionality reduction of diffusion MRI measures for improved tractometry of the human brain. *NeuroImage* (2019)
 76. Yeh, F.-C., Vettel, J.M., Singh, A., Poczos, B., Grafton, S.T., Erickson, K.I., Tseng, W.-Y.I., Verstynen, T.D.: Quantifying differences and similarities in whole-brain white matter architecture using local connectome fingerprints. *PLoS Comput. Biol.* **12**, e1005203 (2016)
 77. Gleichgerrcht, E., Kocher, M., Bonilha, L.: Connectomics and graph theory analyses: novel insights into network abnormalities in epilepsy. *Epilepsia* **56**, 1660–1668 (2015)
 78. Gleichgerrcht, E., Munsell, B., Bhatia, S., Vandergrift III, W.A., Rorden, C., McDonald, C., Edwards, J., Kuzniecky, R., Bonilha, L.: Deep learning applied to whole-brain connectome to determine seizure control after epilepsy surgery. *Epilepsia* **59**, 1643–1654 (2018)
 79. Nath, V., Schilling, K.G., Parvathaneni, P., Huo, Y., Blaber, J.A., Hainline, A.E., Barakovic, M., Romascano, D., Rafael-Patino, J., Frigo, M., Girard, G., Thiran, J.P., Daducci, A., Rowe, M., Rodrigues, P., Prčkovska, V., Aydogan, D.B., Sun, W., Shi, Y., Parker, W.A., Ould Ismail, A.A., Verma, R., Cabeen, R.P., Toga, A.W., Newton, A.T., Wasserthal, J., Neher, P., Maier-Hein, K., Savini, G., Palesi, F., Kaden, E., Wu, Y., He, J., Feng, Y., Paquette, M., Rheault, F., Sidhu, J., Lebel, C., Leemans, A., Descoteaux, M., Dyrby, T.B., Kang, H., Landman, B.A.: Tractography reproducibility challenge with empirical data (TraCED): the 2017 ISMRM diffusion study group challenge. *J. Magn. Reson. Imaging* (2019)
 80. Van Essen, D.C., Ugurbil, K., Auerbach, E., Barch, D., Behrens, T., Bucholz, R., Chang, A., Chen, L., Corbetta, M., Curtiss, S.W.: The Human Connectome Project: a data acquisition perspective. *Neuroimage* **62**, 2222–2231 (2012)
 81. Sudlow, C., Gallacher, J., Allen, N., Beral, V., Burton, P., Danesh, J., Downey, P., Elliott, P., Green, J., Landray, M.: UK biobank: an open access resource for identifying the causes of a wide range of complex diseases of middle and old age. *PLoS Med.* **12**, e1001779 (2015)
 82. Jernigan, T.L., Brown, T.T., Hagler Jr., D.J., Akshoomoff, N., Bartsch, H., Newman, E., Thompson, W.K., Bloss, C.S., Murray, S.S., Schork, N.: The pediatric imaging, neurocognition, and genetics (PING) data repository. *Neuroimage* **124**, 1149–1154 (2016)
 83. Zhang, Y., Zhang, J., Oishi, K., Faria, A.V., Jiang, H., Li, X., Akhter, K., Rosa-Neto, P., Pike, G.B., Evans, A.: Atlas-guided tract reconstruction for automated and comprehensive examination of the white matter anatomy. *Neuroimage* **52**, 1289–1301 (2010)
 84. Smith, S.M., Jenkinson, M., Johansen-Berg, H., Rueckert, D., Nichols, T.E., Mackay, C.E., Watkins, K.E., Ciccarelli, O., Cader, M.Z., Matthews, P.M.: Tract-based spatial statistics: voxelwise analysis of multi-subject diffusion data. *Neuroimage* **31**, 1487–1505 (2006)
 85. Guevara, M., Román, C., Houenou, J., Duclap, D., Poupon, C., Mangin, J.F., Guevara, P.: Reproducibility of superficial white matter tracts using diffusion-weighted imaging tractography. *Neuroimage* **147**, 703–725 (2017)

Spatial Sparse Estimation of Fiber Orientation Distribution Using Deep Alternating Directions Method of Multipliers Network



Ridho Akbar, Yuanjing Feng, Fan Zhang, Jianzhong He, Qingrun Zeng, Lipeng Ning, Carl-Fredrik Westin, and Lauren J. O'Donnell

Abstract Sparse prior information is introduced to improve the accuracy of (FOD) estimation. Spatial continuity is another important aspect of prior information, but it is difficult to directly consider in sparse FODs estimation. First, we proposed a model based on adaptive group-patch and l_1 -norm regularization. Second, in order to solve the FOD estimation problem of complex spherical deconvolution optimization using alternating directions method of multipliers (ADMM), a deep ADMM network is proposed to learn the optimal model parameters from training data. In order to obtain the qualitative and quantitative evaluation of the proposed method and the state-of-the-art constrained spherical deconvolution (CSD): first, ISBI 2013 phantom with known ground truth will be used to evaluate the local accuracy of the fiber configuration. Second, the global impact of FOD accuracy on real brain datasets was assessed using standard tractography and automatic white matter analysis algorithms. Compared with the comparison method, the proposed method has good consistency in sparse fiber reconstruction and fiber continuity.

1 Introduction

To date, diffusion-weighted magnetic resonance imaging (DW-MRI) based on fiber orientation distribution (FOD) has become the key to solving complex fiber configurations, which facilitates the understanding a human brain's fiber connectivity. Extensive research based on high angular resolution diffusion imaging (HARDI) using multi-fiber models (e.g, spherical deconvolution (SD)) has been proposed to over-

R. Akbar · Y. Feng (✉) · J. He · Q. Zeng
Institute of Information Processing and Automation, Zhejiang University of Technology,
Hangzhou, China
e-mail: fyjing@zjut.edu.cn

Y. Feng
Zhejiang Provincial United Key Laboratory of Embedded Systems, Hangzhou, China

F. Zhang · L. Ning · C.-F. Westin · L. J. O'Donnell
Brigham and Women's Hospital, Harvard Medical School, Boston, MA, USA

© Springer Nature Switzerland AG 2020
E. Bonet-Carne et al. (eds.), *Computational Diffusion MRI*,
Mathematics and Visualization, https://doi.org/10.1007/978-3-030-52893-5_7

come single fiber estimation of diffusion tensor imaging (DTI) [1, 2]. Constrained spherical deconvolution (CSD) applies non-negative regularization to reduce spurious fibers [1]. MSMT-CSD is an extended version of CSD that takes into account multiple shells and multiple tissues [3]. Based on the assumption that FOD is a non-negative function, both CSD and MSMT-CSD achieve good accuracy results in fiber estimation [2, 3]. An efficient method for reconstructing sparse fiber is provided by sparse regularization (i.e., l_1 -norm, l_0 -norm) [4–6].

In order to characterize the continuity of the fiber, the spatial consistency of the neighbor information is introduced to smooth the sparse FOD, and the sparse regularization helps to characterize the complex fiber crossing and accelerate the reconstruction time from the dictionary basis [7]. However, the use of spatial prior information in this method does not explicitly exist in minimizing the objective function, which may limit the ability to estimate the actual fiber and its fiber connectivity. Although alternating directions method of multipliers (ADMM) can be used to effectively minimize the objective function [8]. However, the limitation of the dictionary-based model is that after obtaining the learning set, optimization must be performed in each reconstruction of the new data. Lin et al. [9] shows the performance of deep learning based model in estimating FOD by end-to-end learning of inputs and true labels. This method possibly obtains the optimal FOD estimation but requires a lot of data training. You must also consider the large number of actual fibers in the real brain. However, determining the optimal parameters for precise spatial FOD reconstruction is not trivial for ADMM.

The motivation of this study is to reveal the natural properties of continuous fibers in complex fiber configurations by explicitly optimizing model-based FOD estimation. First, we propose a spatial sparse FOD estimation model by incorporating the and simultaneously based on and . The adaptive group-patches uses a combination of Euclidean distance and cosine similarity measures of FODs between adjacent voxels. The FOD sparsity is consistent with the l_1 -norm regularization [4]. In this case, the use of many fiber fragments can result in a very complex cost function. Second, In order to effectively solve these coordinating optimization problems, we enroll the spatial sparse FOD estimation model to the deep alternating directions method of multipliers network (deep ADMM network), efficiently model different terms like data fidelity, regularizations, and all parameters of the network are directly learned end-to-end using L-BFGS algorithm. Each layer contains nodes similar to the subgroups in ADMM so the feedback of network can coordinate the parameters in between the subproblems. The performance of the method will be evaluated using two main criteria: first, the local accuracy of the fiber configuration will be evaluated using ISBI 2013 phantom ground truth and state-of-the-art CSD. Second, the global impact of FOD accuracy on real brain fiber connectivity is evaluated using standard tractography algorithm [10] and an automatic white matter analysis algorithm [11].

2 Methods

2.1 Deconvolution for Diffusion Estimation

Let $S_c(g)$ be the diffusion signal of a voxel c given a magnetic field unit vector $g = \{g_k \in \mathbb{S}^2 | k = 1, 2, \dots, K\}$ where g_k is the k -th direction of the diffusion-encoding gradient on the unit sphere \mathbb{S}^2 , and $S_c(0)$ be the non-DW b0 signal of the voxel c . The signal attenuation in voxel c is expressed as the convolution between the dictionary basis and the fiber orientation distribution.

$$S_c(g) / S_c(0) = R(g, u) \otimes f_c(u|v) = \int_{\mathbb{S}^2} R(g, u) f_c(u|v) du \quad (1)$$

where $S_c(g) / S_c(0) : \mathbb{R}^3 \rightarrow [0, 1]$ is the normalized attenuation signal. $R(g, u)$ is an axisymmetric dictionary basis that represents the diffusion signal attenuation that can be modeled using fixed tensor basis [4]. Our FOD can be calculated in a straightforward manner using the following approximation:

$$f_c(u|v) = \sum_{i=1}^I \sum_{j=1}^J w_{c,j} K(u_i, v_j) \quad (2)$$

where $w_c = \{w_{c,j} | j = 1, 2, \dots, J\}$ is the unknown FOD coefficients. The unit vector $v = \{v_j \in \mathbb{S}^2 | j = 1, 2, \dots, J\}$ is approximated by a uniform discrete point on the hemisphere. The unit vector $u = \{u_i \in \mathbb{S}^2 | i = 1, 2, \dots, I\}$ is approximated by a uniform discrete point on the sphere. $K(u, v)$ is a spherical double-lobe basis function [12].

$$K(u, v) = \sum_{i=1}^I \sum_{j=1}^J \left[\frac{\sin |v_j \cdot u_i^T|}{1 - \varphi \cos^2 (2 \sin |v_j \cdot u_i^T|)} \right]^\tau, (K(u, v) \in [0, 1]) \quad (3)$$

where φ is a parameter to modulate the FOD ($\varphi \in [0.1, 0.9]$). τ is a constant associated with controlling the radial distribution sharpening of the FOD lobes. The spherical double-lobe basis uses a spherical Gaussian kernel to establish a spherical distribution for the overcomplete basis $(v \cdot u^T)$. It recovers each w_c to the recovered FOD $f_c(u|v)$. The FOD coefficients can be estimated by minimizing the following energy

$$E = \sum_{k=1}^K \left(S_c(g_k) / S_c(0) - \sum_{j=1}^J \sum_{i=1}^I w_{c,j} (R(g_k, u_i) K(u_i|v_j)) \right)^2 \quad (4)$$

Given the above overview, we define the vector $y_c = (S_c(g) / S_c(0))^T$ for the signal attenuation associated with the magnetic gradient direction g_k and the b -value b_k in the voxel c . The structural estimate in Eq. 4 can be expressed by the following linear formula

$$y_c = R w_c + \epsilon_c \quad (5)$$

where $R \in \mathbb{R}^{K \times J}$ is a dictionary basis with $R = R(g, v)$, $w_c = (w_{c,1}, \dots, w_{c,J})^T$ consists of an unknown FOD coefficients. ϵ_c is a noise term. Linear system Eq. 5 is typically dominated by noise, and the direct application of least squares [13] results in an estimated spurious fiber orientation distribution. Regularization is a necessary condition to define a unique solution (i.e., non-negative and sparse constraints) that have been proposed for robust estimation of FOD coefficients [1, 6, 14].

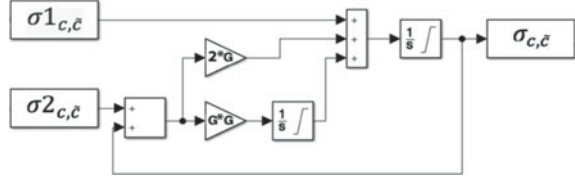
2.2 Sparse Spatial Model Based on Adaptive Group-Patches

The 3D-patches implementation uses a $(3 \times 3 \times 3)$ voxel with 26-neighborhoods. Let $\tilde{c} \in \mathcal{N}_c$ be defined as the voxel neighbor of voxel c . The adjacent success elements are determined by linking the two voxels up to all possible paths of the discrete meshes in the plurality of possible connections c and \tilde{c} , and then by measuring features based on the diffusion intensity.

$$\sigma_{1_{c,\tilde{c}}} = 1 - \frac{|y_c \cdot y_{\tilde{c}}|}{\|y_c\| \cdot \|y_{\tilde{c}}\|}; \sigma_{2_{(c,\tilde{c})}} = 1 - \sqrt{(y_c - y_{\tilde{c}})^2} \quad (6)$$

where y_c and $y_{\tilde{c}}$ are the signal attenuation for c and c 's neighbors. $\frac{|y_c \cdot y_{\tilde{c}}|}{\|y_c\| \cdot \|y_{\tilde{c}}\|}$ is the weight of the Cosine similarity measurement. $\sqrt{(y_c - y_{\tilde{c}})^2}$ is the weight of the Euclidean distance measurement. $\sigma_{1_{c,\tilde{c}}}$ and $\sigma_{2_{c,\tilde{c}}}$ are $\mathcal{N}_c \times 1$ matrices, which are defined as dissimilarity weights of Cosine similarity and Euclidean distance, respectively. $\sigma_{1_{c,\tilde{c}}}$ and $\sigma_{2_{c,\tilde{c}}}$. Dissimilarity weights of $\sigma_{1_{c,\tilde{c}}}$ and $\sigma_{2_{c,\tilde{c}}}$ are not directly used in the model. The idea of a complementary filter is to pass $\sigma_{1_{c,\tilde{c}}}$ through a low pass filter, $\sigma_{2_{c,\tilde{c}}}$ through a high pass filter and combine them to achieve the actual weight of $\sigma_{c,\tilde{c}}$ [15]. The notation G in Fig. 1 is the gain factor of the complementary filter. If G approximate 0, then $\sigma_{c,\tilde{c}}$ will approximate $\sigma_{2_{c,\tilde{c}}}$. In this experiment, we set $G = 1$ based on empirical research to obtain an accurate estimate of the spatial weight in anisotropic region. If $\sigma_{2_{c,\tilde{c}}}$ approximate 0, $\sigma_{c,\tilde{c}}$ will converge to $\sigma_{1_{c,\tilde{c}}}$. The adverse effect of noise could possibly cause the method to miss-estimating the actual fiber orientations. To reduce such an adverse effect, the spatial prior information introduced by spatial weight and coefficient-contrast regularization from the piecewise smoothness of nerve bundles orientation as the results of spatial consistency. We defined a spatial sparse model:

Fig. 1 Block diagram of second-order complementary filter



$$\begin{aligned} & \min_{w_c} \frac{1}{2} \| R w_c - y_c \|_2^2 + \sum_{\tilde{c} \in \mathcal{N}_c} \sigma_{c, \tilde{c}} \| w_{\tilde{c}} - w_c \|_2^2 \\ & + \| P \left(\sum_{\tilde{c} \in \mathcal{N}_c} \sigma_{c, \tilde{c}} w_{\tilde{c}} - w_c \right) \|_2^2 + \lambda \| w_c \|_1, \quad s.t \quad w_c \geq 0 \end{aligned} \quad (7)$$

where \mathcal{N}_c denotes the second-order spatial neighbour of voxel c . $P \in \mathbb{R}^{J \times J}$ is identity matrix. w_c and $w_{\tilde{c}}$ are FOD coefficients for c and c 's neighbors. The regularization parameter σ determines the importance of spatial consistency to the data fitting term, which is the adaptive parameter σ obtained from the neighbor information. The regularization parameter λ encourages sparse spatial FOD coefficients. Equation 7 has four fidelity terms. The first term is to ensure consistency between the spread signal and the reconstructed signal using the dictionary representation. The second term ensures the consistency between the FOD coefficient of voxel c and its neighborhood. The third term encodes the dissimilarity between the FOD coefficients at voxel c and its neighborhood, expressed as a weighted sum of the similarity of the paired FOD coefficients. The fourth term ensures the sparsity of the FOD coefficients.

2.3 Network Architecture

The deep ADMM network built on multiple specific layers uses the spatial sparse model for FOD estimation, and the ADMM optimizer enrolls as a network, as shown in Fig. 2B. The deep ADMM network can learn the corresponding level of feature representation and train the dictionary basis. The reconstructed layer (Eqs. 8 and 9) were derived from Eq. 7 and reformulate an adaptive weight and mixture FOD. Its last layer represents the actual FOD. The convolutional layer (Eq. 10) represents the local spatial filtering operation of the estimated FOD. The nonlinear transformation layer (Eq. 11) was developed using a piecewise linear function, allowing approach to nonlinear data. The multiplier update layer (Eq. 12) performs an update learning rate for each layer.

$$w_c = \arg \min_{w_c} \frac{1}{2} \| R w_c - y_c \|_2^2 \quad (8)$$

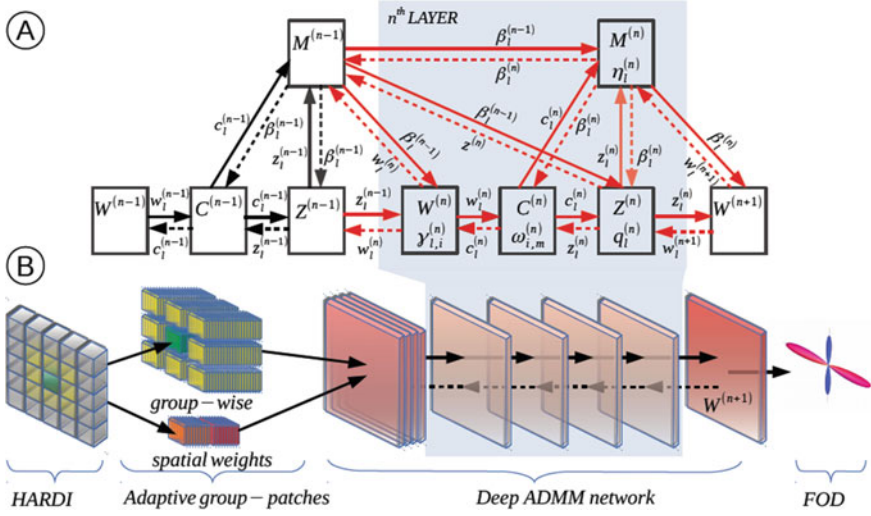


Fig. 2 **A** The deep ADMM network algorithm. **B** FOD reconstruction structure of the proposed method

$$W^{(n)} : \hat{w}_c^{(n)} = F^T \left(P^T P + \sum_{l=1}^L \rho_l F H_l^T H_l F^T + \sum_{\tilde{c} \in \mathcal{N}_c} \sigma_{c, \tilde{c}} (I) + (P^T P) \right)^{-1} \left[+ P w_c + \sum_{l=1}^L \rho_l F H_l^T (z_l^{(n-1)} - \beta_l^{(n-1)}) + \sum_{\tilde{c} \in \mathcal{N}_c} \sigma_{c, \tilde{c}} w_{\tilde{c}} F + \sum_{\tilde{c} \in \mathcal{N}_c} \sigma_{c, \tilde{c}} w_{\tilde{c}} (P^T P) F \right] \quad (9)$$

$$C^{(n)} : c^{(n)} = D_l \hat{w}_c^{(n)} \quad (10)$$

$$Z^{(n)} : z^{(n)} = Q \left(c_l^{(n)} + \beta_l^{(n-1)}; \frac{\lambda_l}{\rho_l} \right) \quad (11)$$

$$M^{(n)} : \beta^{(n)} = \beta_l^{(n-1)} + \eta_l (c_l^{(n)} - z_l^{(n)}) \quad (12)$$

where Q is a piecewise linear function for approach any function. The Q function imposes a l_1 -norm with a parameter $\lambda = \lambda_l, \forall l \in [1, 2, \dots, L]$. I is represented as a undersampled matrix. The parameter η_l is an update rate. \hat{w}_c, z, α are the optimal values to update. $\alpha = \alpha_l$ is Lagrangian multipliers and $\rho = \rho_l$ is penalty parameters. $\beta_l = \alpha_l / \rho_l, \forall l \in [1, 2, \dots, L]$. D_l is a filter matrix, $\forall l \in [1, 2, \dots, L]$. F is equal to $K K^T$ with $J \times J$ matrix, while K is a spherical double-lobe function.

Training: Given a training data pair, the loss function in network training can be calculated as

$$E(\Theta) = \frac{1}{|\Gamma|} \sum_{\hat{w}_c, w_c \in \Gamma} \frac{\|\hat{w}_c - w_c\|_2^2}{\|w_c\|_2^2} \quad (13)$$

where \hat{w}_c is the network output based on the network parameter Θ . Learnable parameters $\Theta = \{\{q_{l,i}^{(n)}\}_{i=1}^{N_c}, D_l^{(n)}, H_l^{(n)}, \rho_l^{(n)}, \eta_l^{(n)}\}_{n=1}^{N_s} \cup \{H_l^{N_s+1}, \rho_l^{N_s+1}\}, (\forall l \in L)$. The gradient of the loss function $E(\Theta)$ according to the parameter Θ is calculated by using backpropagation. *Backpropagation* is necessary to calculate the gradient of the loss function $E(\Theta)$ according to the parameter Θ in the reverse order, as shown by the dotted line in the Fig. 2A.

3 Experiments

The dictionary is based on the diffusion tensor model with main diffusivities $[1.7, 0.2, 0.2] \times 10^{-3} \text{ mm}^2/s$. v is a tessellation scheme, distributed evenly on 321 points on a hemisphere. When solving the coefficient w_c , $v = \{v_j \in \mathbb{S}^2 | j = 1, 2, \dots, J\}$ the down-sampling usually happens on unit sphere, and v is made to be identical to the basis vector u . Furthermore, double-lobes function K constructed fitting up-sampling vectors v its coefficient to obtain the final FOD. u is a symmetric sphere with 642 vertices, which is an array of the 642 FOD values corresponding to the vertices of the sphere. Equation 8 is solved using a non-negative least squares method for each voxel in the selected ROI. The proposed 5 layers (L5) uses ISBI 2013 Phantom's diffusion signal (SNRs 10, 20, 30) and corresponding ground truth fiber for end-to-end training; 20% of the them is used for testing. We used L-BFGS¹ to train the network. The one with the best test score is chosen for FOD reconstruction. H_l and D_l are generated by the discrete cosine transform. The learning parameter $\rho_l = 0.1$, the regularization parameter $\lambda_l = 0.1$. For the CSD² and MSMT-CSD³ algorithms, the SH order is equal to 8, and the FOD sphere uses 642 vertices.

3.1 ISBI 2013 Phantom

We demonstrate the proposed algorithm on the synthetic phantom dataset provided by ISBI 2013⁴ with a b -value of 3000 s/mm^2 and SNRs of 10, 20, 30. We summarize the fiber configuration assessment results of our method and CSD in Table 1 using evaluation metrics as described in [7] over-estimated fiber ratio associated with ground truth (FP), under-estimated fiber ratio associated with ground truth (FN), true-

¹<http://users.iems.northwestern.edu/~nocedal/lbfgsb.html>.

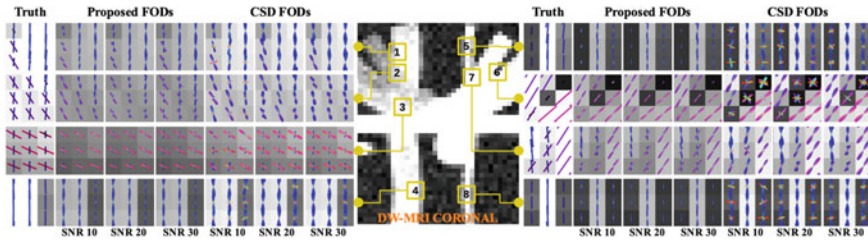
²<http://nipy.org/dipy/>.

³<http://www.mrtrix.org/>.

⁴<http://hardi.epfl.ch/static/events/2013-ISBI>.

Table 1 Quantitative evaluation on the ISBI 2013 fiber estimation challenge

METHOD	SNR	\angle AAE	\angle MAE	FP	FN	SR (%)
CSD/Proposed	10	12.88/ 4.34	7.97/ 3.61	1.09/ 0.11	0.07 /0.10	53.94/ 90.68
CSD/Proposed	20	8.70/ 3.70	5.51/ 3.27	1.14/ 0.04	0.09 /0.10	59.23/ 93.82
CSD/Proposed	30	7.73/ 3.58	4.40/ 3.22	1.11/ 0.03	0.09 /0.10	62.24/ 94.86

**Fig. 3** Qualitative evaluation on the ISBI 2013 fiber estimation challenge

estimated fiber ratio associated with ground truth (SR) in percentages. The mean and median of the angular errors associated with true-estimated fiber (AAE) and (MAE) in degrees.

Our method does a good job of recovering about 90% of the ground truth fiber, producing a very small portion of the spurious fiber, but slightly less fiber than CSD. Qualitative and quantitative evaluation shows that the resulting FODs are in-line with the ground truth phantom. It can be seen from Fig. 3 that our FODs is more robust to SNR changes than the comparison method.

3.2 Real Brain

We further performed FOD reconstruction on human brain datasets, using the model trained on ISBI 2013 phantom. Three HCP⁵ datasets (IDs: 100307, 100610, 101006) were obtained at 1.25 mm isotropic resolution, with diffusion weights of $b = 1000$, 2000 and 3000 mm^2/s applied in 90 directions in each shell. In this scheme, 18 of $b = 0$ mm^2/s images were separated temporally, resulting in a total of 288 diffusion signals. The real brain has no ground truth based on FOD, so we emphasize the qualitative comparison of MSMT-CSD. In addition, we evaluated the effect of FOD estimation accuracy on tractography and connectivity analysis of white matter fiber. *Tractography*: whole brain tractography was performed using eudx deterministic algorithm [10]. A total of 100,000 seed points were placed throughout the brain mask. Streamline was done with a half-cone curvature 45° and a length of 40–200 mm. *An automatic white matter analysis*: fiber clusters based on white matter analysis

⁵<https://www.humanconnectome.org>.

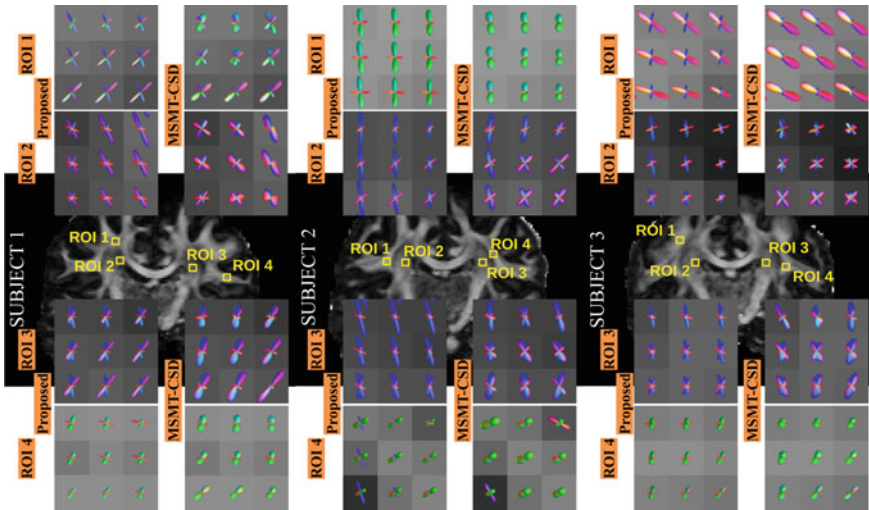


Fig. 4 The FOD visualization of the proposed method and MSMT-CSD on real brain subjects

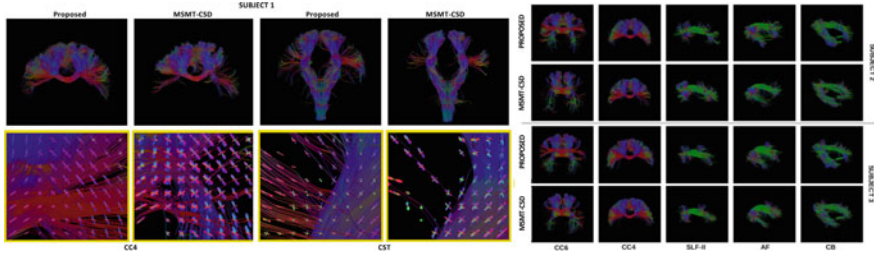


Fig. 5 Qualitative comparison of fiber bundles obtained by the proposed method and MSMT-CSD on real brain datasets

were used to assess fiber connectivity in white matter [11]. Figure 4 shows the FOD visualization of the proposed method and MSMT-CSD on real brain subjects. Visual assessments indicate that the proposed FOD strongly characterizes the spatial connectivity of complex fiber configurations. Figure 5 shows fiber bundle visualization obtained on real brain subjects based on the proposed method and MSMT-CSD. The results show that the proposed method is consistent with the crossing of the internal capsule and corpus callosum, revealing the continuity of the white matter fiber better than the comparison method.

4 Summary and Discussion

We propose a method in which neighbor information of diffusion signals and FOD coefficients is considered in a deep ADMM network to characterize the natural properties of white matter fiber continuity. In this work, we focus on training and testing our methods on simulated phantoms and applying the models trained in simulated phantoms to real brain data. While the results demonstrate the potential of our FOD estimation, we believe that additional high-quality data is required to further progress this area of research. However, this is not the first time that a new method provides better results than CSD and MSMT-CSD in the ISBI 2013 dataset [14]. It was shown that none of the methods outperformed the others in all experimental conditions. More evaluation is still needed, i.e., training by a larger datasets containing multiple subjects, and it will be taken with care.

Acknowledgments The research is supported by National Natural Science Foundation of China [grant number 61703369, 61976190]. Natural Science Foundation of Zhejiang Province [grant number LQ16F030009, LY13F030007]. Major Science and Technology Projects of Wenzhou [grant number ZS2017007].

References

1. Tournier, J.D., Calamante, F., Connelly, A.: Robust determination of the fibre orientation distribution in diffusion MRI: non-negativity constrained super-resolved spherical deconvolution. *NeuroImage* **35**(4), 1459–1472 (2007). <https://doi.org/10.1016/j.neuroimage.2007.02.016>
2. Tournier, J.D., Calamante, F., Gadian, D.G., Connelly, A.: Direct estimation of the fiber orientation density function from diffusion-weighted MRI data using spherical deconvolution. *NeuroImage* **23**(3), 1176–1185 (2004). <https://doi.org/10.1016/j.neuroimage.2004.07.037>
3. Jeurissen, B., Tournier, J.D., Dhollander, T., Connelly, A., Sijbers, J.: Multi-tissue constrained spherical deconvolution for improved analysis of multi-shell diffusion MRI data. *NeuroImage* **103**, 411–426 (2014). <https://doi.org/10.1016/j.neuroimage.2014.07.061>
4. Landman, B.A., Bogovic, J.A., Wan, H., ElShahaby, F.E.Z., Bazin, P.L., Prince, J.L.: Resolution of crossing fibers with constrained compressed sensing using diffusion tensor MRI. *NeuroImage* **59**(3), 2175–2186 (2012). <https://doi.org/10.1016/j.neuroimage.2011.10.011>
5. Daducci, A., Canales-Rodri, E.J., Descoteaux, M., Garyfallidis, E., Gur, Y., Lin, Y.C., Mani, M., Merlet, S., Paquette, M., Ramirez-Manzanares, A., Reisert, M.: Quantitative comparison of reconstruction methods for intra-voxel fiber recovery from diffusion MRI. *IEEE Trans. Med. Imaging* **33**(2), 384–399 (2013). <https://doi.org/10.1109/TMI.2013.2285500>
6. Daducci, A., Van De Ville, D., Thiran, J.P., Wiaux, Y.: Sparse regularization for fiber ODF reconstruction: From the suboptimality of ℓ_2 and ℓ_1 priors to ℓ_0 . *Med. Image Anal.* **18**(6), 820–833 (2014). <https://doi.org/10.1016/j.media.2014.01.011>
7. Auría, A., Daducci, A., Thiran, J.P., Wiaux, Y.: Structured sparsity for spatially coherent fibre orientation estimation in diffusion MRI. *NeuroImage* **115**, 245–255 (2015). <https://doi.org/10.1016/j.neuroimage.2015.04.049>
8. Rathi, Y., Michailovich, O., Laun, F., Setsompop, K., Grant, P.E., Westin, C.F.: Multi-shell diffusion signal recovery from sparse measurements. *Med. Image Anal.* **18**(7), 1143–1156 (2014). <https://doi.org/10.1016/j.media.2014.06.003>

9. Lin, Z., Gong, T., Wang, K., Li, Z., He, H., Tong, Q., Yu, F., Zhong, J.: Fast learning of fiber orientation distribution function for MR tractography using convolutional neural network. *Med. Phys.* (2019). <https://doi.org/10.1002/mp.13555>
10. Garyfallidis, E., Brett, M., Amirbekian, B., Rokem, A., Van Der Walt, S., Descoteaux, M., Nimmo-Smith, I.: Dipy, a library for the analysis of diffusion MRI data. *Frontiers Neuroinform.* **8**, 8 (2014). <https://doi.org/10.3389/fninf.2014.00008>
11. Zhang, F., Wu, Y., Norton, I., Rigolo, L., Rathi, Y., Makris, N., O'Donnell, L.J.: An anatomically curated fiber clustering white matter atlas for consistent white matter tract parcellation across the lifespan. *NeuroImage* **179**, 429–447 (2018). <https://doi.org/10.1016/j.neuroimage.2018.06.027>
12. Wu, Y., Feng, Y., Li, F., Westin, C.F.: Global consistency spatial model for fiber orientation distribution estimation. In: 2015 IEEE 12th International Symposium on Biomedical Imaging (ISBI), pp. 1180–1183. IEEE (2015). <https://doi.org/10.1109/ISBI.2015.7164083>
13. Elden, L.: Algorithms for the regularization of ill-conditioned least squares problems. *BIT Numer. Math.* **17**(2), 134–145 (1977). <https://doi.org/10.1007/BF01932285>
14. Canales-Rodríguez, E.J., Legarreta, J.H., Pizzolato, M., Rensonnet, G., Girard, G., Rafael-Patino, J., Barakovic, M., Romascano, D., Aleman-Gomez, Y., Radua, J., Pomarol-Clotet, E.: Sparse wars: A survey and comparative study of spherical deconvolution algorithms for diffusion MRI. *NeuroImage* **184**, 140–160 (2019). <https://doi.org/10.1016/j.neuroimage.2018.08.071>
15. Kottath, R., Narkhede, P., Kumar, V., Karar, V., Poddar, S.: Multiple model adaptive complementary filter for attitude estimation. *Aerosp. Sci. Technol.* **69**, 574–581 (2017). <https://doi.org/10.1016/j.ast.2017.07.011>

Free-Water Correction in Diffusion MRI: A Reliable and Robust Learning Approach



Leon Weninger, Simon Koppers, Chuh-Hyoun Na, Kerstin Juetten,
and Dorit Merhof

Abstract In clinical settings, diffusion MRI can be used for extracting biomarkers such as fractional anisotropy or for revealing brain connectivity based on fiber tractography. Both are impacted by the free-water partial volume effect that arises at the border of cerebrospinal fluid or in presence of vasogenic edema. Hence, in order to robustly track white matter fibers close to cerebrospinal fluid and in presence of edema, or to extract consistent biomarkers in these cases, the diffusion MRI signal needs to be corrected for partial volume effects. We present a novel method that reproducibly infers plausible free-water volumes across different diffusion MRI acquisition schemes. Based on simulated data closely following the individual characteristics of each measurement, a neural network is trained on synthetic groundtruth data. According to our evaluation, this methodology produces more consistent and more plausible results than previous approaches.

1 Introduction

In regions near cerebrospinal fluid (CSF) or in presence of vasogenic edema, the signal obtained by diffusion-weighted MRI (DWI) stems from both, the free-water (FW) as well as the parenchyma. Thus, in order to analyze the parenchyma in free-water contaminated voxels, first the signal stemming from FW and parenchyma needs to be disentangled.

Several algorithms that directly estimate the FW proportion have been published. Free-water elimination DTI [8] uses a two compartment model, in which the diffusivity of one compartment (the FW compartment) is fixed to a predefined isotropic diffusion. The diffusion tensor properties of the other compartment are variable, as well as the volume fraction of both compartments. With at least two different spher-

L. Weninger (✉) · S. Koppers · D. Merhof
Institute of Imaging & Computer Vision, RWTH Aachen University, Aachen, Germany
e-mail: leon.weninger@lfb.rwth-aachen.de

C.-H. Na · K. Juetten
Department of Neurosurgery, University Hospital RWTH Aachen, 52074 Aachen, Germany

© Springer Nature Switzerland AG 2020
E. Bonet-Carne et al. (eds.), *Computational Diffusion MRI*,
Mathematics and Visualization, https://doi.org/10.1007/978-3-030-52893-5_8

ical shells, i.e. acquisitions with at least two different non-zero b-values, this model can be fitted to the data. If only one shell is acquired, the same model can be fit using spatial regularization [11]. An adaption of diffusion kurtosis imaging to include FW elimination has also been presented recently [2]. A first deep-learning based FW elimination technique was presented at MICCAI 2018. Molina-Romero et al. [10] used completely synthetic diffusion data, on which they trained a neural network to estimate the tissue compartment fraction. For the synthetic data generation, water is modeled as a predefined isotropic gaussian diffusion, and the diffusion behavior of tissue is modeled as a random uniform distribution. Based on these two descriptions and a tissue volume fraction, synthetic diffusion weighted signals can be generated, and the FW volume fraction predicted. This technique also works independent of the number of b-value shells and is 55x faster than previous approaches. Further, recent advanced diffusion models (e.g. multi-shell multi-tissue CSD [9], DIAMOND [12]), mostly requiring multi-shell acquisitions, also include an isotropic FW compartment in their models. The presented approaches either rely on multi-shell acquisitions, which are often not available for clinical applications, or, according to our evaluation, seem to produce inconsistent results with unrealistic free-water fractions.

We propose a novel approach, that determines the FW volume fraction using a neural network (NN) trained on data directly generated from individual DWI data. Relying on diffusion measurements from regions with known tissue microstructure, such as the corpus callosum (CC), the brain’s ventricular system or cortical gray matter, voxels with known tissue properties can be extracted. From these voxels, a synthetic dataset with up to three random fiber compartments and a groundtruth FW volume fraction can be composed. Hence, such a dataset should closely follow the characteristics of FW contaminated voxels. A similar synthetic data generation technique has been successfully used to predict fiber directions [13]. Finally, a NN trained on this data can be used to correctly infer the FW volume fraction of the whole brain. This paper makes the following contributions:

- Creation of synthetic yet plausible data of FW contaminated diffusion signals
- A fast and accurate method for determining FW compartments in DWI, that can be applied to single shell diffusion data
- Thorough comparison with current methods
- An application to clinical data

2 Image Data

Data from the Human Connectome Project (HCP) [6] is used, which provides high-resolution multi-shell DWI data. Three spherical shells ($b = 1000, 2000$ and 3000 s/mm^2) with 90 gradient directions each were acquired in an isotropic resolution of 1.25 mm. From this database, the 100 unrelated subjects release was selected.

As a FW volume fraction groundtruth is not available for human brains, we also rely on a synthetic dataset for evaluation. In this dataset, the same gradient scheme as

used in the HCP data was employed. Single-fiber white matter diffusion is simulated as a prolate diffusion tensor with a major eigenvalue of $1.7 \times 10^{-3} \text{ mm}^2/\text{s}$ and two perpendicular eigenvalues of $0.3 \times 10^{-3} \text{ mm}^2/\text{s}$. CSF is modeled as an isotropic diffusion tensor with eigenvalues of $3 \times 10^{-3} \text{ mm}^2/\text{s}$, and GM as an isotropic diffusion tensor with eigenvalues of $0.5 \times 10^{-3} \text{ mm}^2/\text{s}$. Using up to three randomly selected and rotated WM fibers, a CSF and/or GM compartment, 1,000,000 voxels for which the water compartment proportion is known were obtained. Finally, Rician noise was added with an SNR of 20.

For DWI data of brain tumor patients, we rely on an in-house database. This database includes DWI-acquisitions ($b = 1000 \text{ s/mm}^2$ single-shell, 64 gradient directions, isotropic voxel size of 2.4 mm) next to T1- and T2-FLAIR images of 28 patients. The diffusion data was corrected for susceptibility induced- and eddy current distortions with the tools “topup” and “Eddy” from FSL [14]. The use of this data was approved by a local ethics committee, and the patients gave written consent.

3 Methods

Data extraction and signal generation From a registered T1-image, typical CSF- and gray matter (GM) voxels are extracted using an eroded Fast segmentation [16] mask. Diffusion tensors are fitted for each b-value shell to these voxels. Using these voxels, the mean diffusion of CSF and the mean diffusion of GM is obtained. These values are then used for the generation of the synthetic training data.

However, a single diffusion tensor is not enough to model the diffusion signal of white matter of the whole brain, as diffusion depends on microstructural parameters. Corresponding to the generation of a single-fiber response function in CSD [15], single-fiber white matter (WM) voxels are extracted from voxels within the corpus callosum with a fractional anisotropy (FA) greater than a predefined threshold ($FA > 0.7$). In contrast to CSD, we keep all extracted single-fiber WM voxels, and fit prolate diffusion tensors for each voxel and each shell (e.g. three diffusion tensors for a three-shell acquisition such as the HCP diffusion sequence) independently. Thus, a variety of diffusion tensors representing different white matter microstructures is obtained.

By superposition of up to three randomly sampled- and rotated single-fiber compartments as well as a GM and CSF compartment, synthetic diffusion weighted signals can be constructed with:

$$S(\mathbf{b}, g, f_{FW}) = f_{FW}S_{FW}(\mathbf{b}) + (1 - f_{FW})S_{issue}(\mathbf{b}, g), \quad (1)$$

where \mathbf{b} designates the b-value, g describes the direction of the diffusion sensitizing gradients, and S_{issue} is modeled with up to three white matter fiber compartments and a GM compartment:

$$S_{tissue}(\mathbf{b}, g) = f_1 S_{gm}(\mathbf{b}) + \sum_{n=2}^4 f_n R_n(S_{wm}(\mathbf{b}, g)) \quad (2)$$

with random compartment fractions $0 \leq f_{FW} \leq 1$, $0 \leq f_n$, $f_1 + f_2 + f_3 + f_4 = 1$ and $R_n()$ a random rotation in $SO(3)$.

Finally, the constructed signal is distorted with Rician noise with an SNR of 20. Employing this model, an infinite amount of multi-tissue voxels with a known FW fraction can be generated.

Using our methodology, the only assumptions made about diffusive properties are that diffusion of single-fibers can be described with prolate tensors for a single b-value, and that the diffusion for GM and CSF is isotropic. As the diffusion properties are estimated independently for each shell, b-value dependent effects (e.g. kurtosis) are thus included in the synthetic data.

Note that it is implicitly assumed that the extracted single-fiber WM voxels contain no FW. In [1, 5], a FW volume fraction of less than 2% is reported for such tissue, i.e., this modeling error is less than 2%.

Neural network training A neural network is trained on the simulated raw diffusion data to predict the FW volume fraction f_{FW} . Different network architectures were tested, and an optimum performance network was achieved with 4 fully connected layers in combination with tanh activation functions. As input, the normalized signal attenuation is used. The size of the input is thus dependent on the acquisition scheme. As an example, 270 non-zero diffusion gradients were acquired in the HCP dataset, compared to 64 in the clinical dataset. The initial layer width is automatically adjusted to this data shape. It is halved for each subsequent layer, and the last layer finally has only one output, which is regressed against the FW volume fraction with an L2-loss. Thus, for the exemplary HCP data, the number of artificial neurons of the fully connected layers in this half-hourglass shape is 270-135-67-33-1.

Training time depends on the number of acquisition shells and the number of generated synthetic diffusion weighted signals. By default, we create 25,000 voxels, split into 80% training and 20% test set, use a batch size of 256 and an Adam optimizer with a learning rate of 0.005. A larger training- and test set of up to 1,000,000 voxels was evaluated, but the obtained accuracy did not improve. On a consumer-grade CPU and an implementation in PyTorch, convergence is achieved after 100 epochs in less than a minute for an HCP 3-shell acquisition.

Inference step The trained neural network can finally be used on the signal attenuation of the whole brain to predict the volume fraction of FW in all voxels. Finally, the predicted FW signal can be subtracted from the original signal. FW contaminated voxels, i.e., voxels at the border between WM and CSF, or voxels including a vasogenic edema in glioblastoma cases, can thus be corrected. Consequently, biomarkers (FA, MD) extracted from these voxels are better comparable to other areas in the same brain or to other subjects.

4 Experiments and Results

4.1 Evaluation on Healthy Subjects

Since FW contamination of healthy, normal-appearing WM without contact to CSF is marginal, one quality hallmark of a FW correction is that biomarkers remain stable in aforementioned regions. Only with such a property, FW correction algorithms can be used for clinical decision making. In order to obtain normal-appearing WM non-adjacent to CSF or GM, an eroded white matter mask was constructed. On this WM skeleton, the FW proportions (f_{FW}) as well as differences in FA before and after correction were analyzed. Results obtained with our methodology as well as those obtained with FWE-DTI [8], the probably most-used approach, and with the recent neural network based FW correction approach (ANN-Syn) [10], are compared in Table 1 for the 100 subjects in the HCP database. The free-water fraction estimated by multi-shell multi-tissue CSD (MSMT-CSD) is also given as a comparison. Different version of MSMT-CSD were initially analyzed, and a recent version of the algorithm that includes the S0-signal in the fitting process [3] showed the best results and was used for all experiments.

To further get an impression of b-value dependence, the experiment was replicated for extracted single-shell, two-shell and three-shell data. Implementations were taken from DIPY [4] (FWE-DTI), DMIPY [7] (MSMT-CSD) or from associated Github repositories (ANN-Syn) for all experiments.

Literature states around 1–2% of mean free-water volume fraction in normal-appearing white matter [1, 5]. In order to reliably extract clinically important biomarkers such as FA, free-water correction approaches should not strongly exceed this fraction. Note that FWE-DTI is not applicable to single-shell data, and that diffusion kurtosis effects are not taken into account [8].

In Fig. 1, exemplary results of our method on the corpus callosum and lateral ventricles of an HCP subject are shown. Biomarkers (FA, MD) of normal-appearing white matter are not affected by our proposed correction. Meanwhile, the border between CSF and white matter is much sharper—those voxels have been appropriately corrected for the FW compartment.

Table 1 Mean FW volume fraction (f_{FW}) and, where applicable, mean difference between FA before and after FW correction (Δ FA) on WM skeleton. HCP 100 unrelated subjects. Single-shell: $b = 1000$, Two-shell: $b = 1000$ and 2000 , Three-shell $b = 1000, 2000$ and 3000 s/mm²

	Single-shell		Two-shell		Three-shell	
	f_{FW}	Δ FA	f_{FW}	Δ FA	f_{FW}	Δ FA
FWE-DTI	–	–	0.255	0.111	0.309	0.096
ANN-Syn	0.083	0.052	0.196	0.089	0.289	0.097
MSMT-CSD	–	–	0.038	–	0.037	–
Proposed	0.011	0.005	0.011	0.003	0.019	0.004

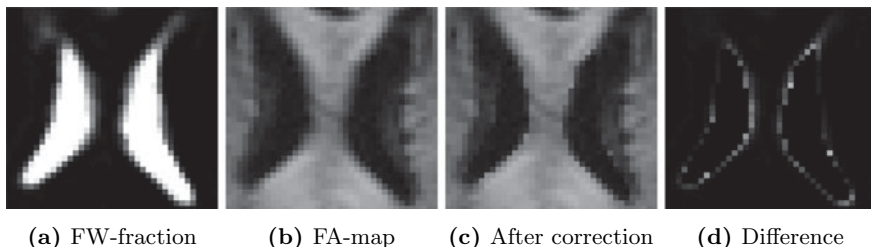


Fig. 1 Corpus callosum and lateral ventricles—showcase for FW correction

4.2 Synthetic Data Analysis

For human brains, a FW volume fraction groundtruth is not available. We thus evaluate the proposed method on the synthetic dataset comprising artificial voxels with multiple compartments.

In addition to previous FW correction approaches (FWE-DTI and ANN-Syn), we also analyze the FW compartment predicted by multi-shell multi-tissue CSD. In Table 2, the accuracy of these approaches is compared to our method, by using the coefficient of determination (R^2), the mean absolute error (MAE) and its standard deviation. In all approaches, the corresponding settings for tissue models were selected exactly as for the simulated data. As no segmentation mask is available for this synthetic data, in our model GM- and CSF diffusion properties are also matched to the simulation model, while single-fiber WM is extracted from all voxels with an $FA > 0.7$.

4.3 Application to Brain Tumor Patients

In order to show the clinical relevance of our approach, we applied the presented method on an in-house dataset containing MRI images of 28 brain tumor patients.

Table 2 Coefficient of determination (R^2) and mean absolute error (MAE) \pm mean standard deviation of f_{FW} for different water correction approaches on an artificial dataset with SNR=20

	Single-Shell		Two-Shell		Three-Shell	
	R^2	MAE	R^2	MAE	R^2	MAE
FWE-DTI	/	/	0.92	0.044\pm0.03	0.88	0.056 \pm 0.03
ANN-Syn	0.89	0.049 \pm 0.03	0.85	0.060 \pm 0.04	0.06	0.164 \pm 0.08
MSMT-CSD	/	/	0.80	0.074 \pm 0.03	0.78	0.077 \pm 0.03
Proposed	0.95	0.034\pm0.02	0.93	0.042\pm0.02	0.93	0.040\pm0.02

Figures 2 and 3 show the same patient, highlighting the results of our method. The area affected by edema can be identified as the hyperintense regions in the FLAIR image (Fig. 2a). In parts of the brain affected by this edema, the predicted water compartment is between 30% and 40% (Fig. 2b), in accordance with the FLAIR acquisition. Consequently, after FW correction, these areas now appear brighter in the FA-map (Fig. 3), i.e., our method determines the water fraction and exposes the tissue-only signal, thus enabling an improved assessment of this tissue. Further, the border between CSF and WM is much sharper after correction. Meanwhile, normal-appearing white matter, e.g. deep white matter on the contralateral side, is not altered. Compared to ANN-Syn, a recent method that is applicable to single-shell data, the proposed method shows less noise in healthy white matter areas.

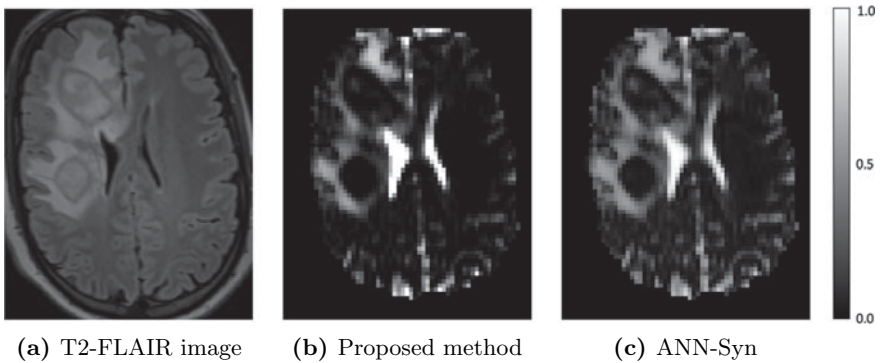


Fig. 2 Comparison of the water fraction as estimated by our method compared to the estimation of ANN-Syn, a recent method that is also applicable to single-shell acquisitions. Hyperintensities in the FLAIR image indicate the presence of edema

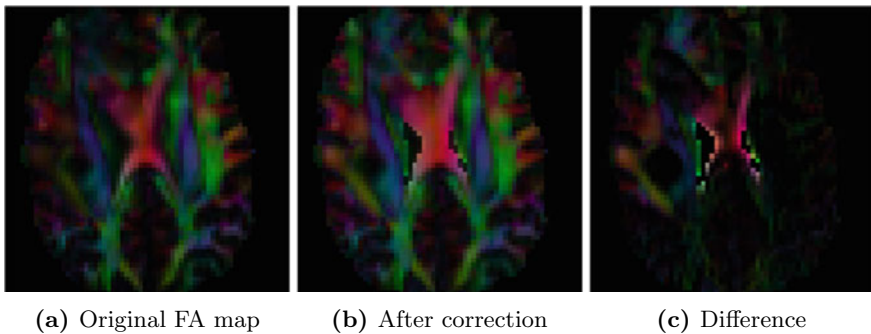


Fig. 3 Application showcase: Color-FA of a brain tumor patient DWI-acquisition before and after correction

5 Discussion

In healthy, normal-appearing WM, our methodology consistently predicts very low FW volume fractions. Here, the estimations of other tested approaches tend to be unreasonably high and fluctuate stronger.

FWE-DTI performs very well on the synthetic dataset, similar to MSMT-CSD. However, it fails for high b-values on the HCP data. This can be explained by the lack of including kurtosis effects, which are present in the real data for high b-values.

In contrast, ANN-Syn fails when including high b-values, both on the HCP data as well as on the synthetic dataset. For the single-shell low b-value case, the results are good. In effect, this method uses random uniform numbers to simulate diffusion data, a pragmatic approach useful for simulation of low b-value diffusion data. However, on the single-shell brain tumor dataset, the free-water estimation in healthy white matter is still noisy.

From the evaluated approaches, our method is the only one that is able to perform free-water correction consistently for different b-value settings. In contrast to FWE-DTI and MSMT-CSD, it takes noise into account, and in contrast to ANN-Syn our employed signal model is more realistic, especially for high b-values.

6 Conclusion

We present a novel, reliable and fast free-water partial volume correction method that is applicable to single- and multi-shell DWI-acquisitions.

Relying on data extracted from the subject, our method is the first that produces coherent and plausible results for different b-values. Subsequent steps, e.g. fiber tracking or biomarker extraction may strongly benefit from this correction, as water-contaminated WM-voxels no longer need to be omitted. Especially in clinical settings with relatively small resolution (e.g. 2.4 mm isotropic) such a correction can lead to more robust results.

In patients with brain tumors, our method may allow for a realistic tissue-only biomarker extraction of regions affected by vasogenic edema. Even for healthy subjects, our method supports a more robust extraction of FA values, as voxels at the border between CSF and WM are no longer biased due to free-water partial volume effects.

Acknowledgments Data were provided in part by the Human Connectome Project, WU-Minn Consortium (Principal Investigators: David Van Essen and Kamil Ugurbil; 1U54MH091657) funded by the 16 NIH Institutes and Centers that support the NIH Blueprint for Neuroscience Research; and by the McDonnell Center for Systems Neuroscience at Washington University.

References

1. Bender, B., Klose, U.: Cerebrospinal fluid and interstitial fluid volume measurements in the human brain at 3t with epi. *Magn. Reson. Med.* **61**(4), 834–841 (2009)
2. Collier, Q., Veraart, J., Jeurissen, B., Vanhevel, F., Pullens, P., Parizel, P.M., den Dekker, A.J., Sijbers, J.: Diffusion kurtosis imaging with free water elimination: a bayesian estimation approach. *Magn. Reson. Med.* **80**(2), 802–813 (2018)
3. Dhollander, T., Raffelt, D., Connelly, A.: Unsupervised 3-tissue response function estimation from single-shell or multi-shell diffusion mr data without a co-registered t1 image (2016)
4. Garyfallidis, Eleftherios., Brett, Matthew., et al.: Dipy, a library for the analysis of diffusion MRI data. *Frontiers Neuroinform.* **8**, 8 (2014)
5. Ernst, T., Kreis, R., Ross, B.: Absolute quantitation of water and metabolites in the human brain. i. compartments and water. *J. Magn. Reson. Ser. B* **102**(1), 1 – 8 (1993)
6. Essen, D.C.V., Smith, S.M., Barch, D.M., Behrens, T.E., Yacoub, E., Ugurbil, K.: The wu-minn human connectome project: an overview. *NeuroImage* **80**, 62 – 79 (2013). Mapping the Connectome
7. Fick, R.H., Wassermann, D., Deriche, R.: Mipy: An open-source framework to improve reproducibility in brain microstructure imaging. In: *OHBM 2018—Human Brain Mapping*, pp. 1–4. Singapore, Singapore (2018)
8. Hoy, A.R., Koay, C.G., Keckskemeti, S.R., Alexander, A.L.: Optimization of a free water elimination two-compartment model for diffusion tensor imaging. *NeuroImage* **103**, 323–333 (2014)
9. Jeurissen, B., Tournier, J.D., Dhollander, T., Connelly, A., Sijbers, J.: Multi-tissue constrained spherical deconvolution for improved analysis of multi-shell diffusion mri data. *NeuroImage* **103**, 411–426 (2014)
10. Molina-Romero, M., Wiestler, B., Gómez, P., Menzel, M.I., Menze, B.H.: Deep learning with synthetic diffusion MRI data for free-water elimination in glioblastoma cases. *MICCAI* (2018)
11. Pasternak, O., Sochen, N., Gur, Y., Intrator, N., Assaf, Y.: Free water elimination and mapping from diffusion MRI. *Magn. Reson. Med.* **62**(3), 717–730 (2009)
12. Scherrer, B., Schwartzman, A., Taquet, M., Sahin, M., Prabhu, S.P., Warfield, S.K.: Characterizing brain tissue by assessment of the distribution of anisotropic microstructural environments in diffusion-compartment imaging (diamond). *Magn. Reson. Med.* **76**(3), 963–977 (2016)
13. Schultz, T.: Learning a reliable estimate of the number of fiber directions in diffusion MRI. In: *Medical Image Computing and Computer-Assisted Intervention—MICCAI*, pp. 493–500 (2012)
14. Smith, S.M., Jenkinson, M., Woolrich, M.W., Beckmann, C.F., Behrens, T.E., Johansen-Berg, H., Bannister, P.R., Luca, M.D., Drobnjak, I., Flitney, D.E., Niazy, R.K., Saunders, J., Vickers, J., Zhang, Y., Stefano, N.D., Brady, J.M., Matthews, P.M.: Advances in functional and structural mr image analysis and implementation as fsl. *NeuroImage* **23**, S208 – S219 (2004). Mathematics in Brain Imaging
15. Tournier, J.D., Calamante, F., Connelly, A.: Robust determination of the fibre orientation distribution in diffusion mri: Non-negativity constrained super-resolved spherical deconvolution. *NeuroImage* **35**(4), 1459–1472 (2007)
16. Zhang, Y., Brady, M., Smith, S.: Segmentation of brain mr images through a hidden markov random field model and the expectation-maximization algorithm. *IEEE Trans. Med. Imaging* **20**(1), 45–57 (2001)

Convolutional Neural Networks for Fiber Orientation Distribution Enhancement to Improve Single-Shell Diffusion MRI Tractography



Oeslle Lucena, Sjoerd B. Vos, Vejay Vakharia, John Duncan, Sebastien Ourselin, and Rachel Sparks

Abstract Diffusion MRI (dMRI) tractography may help locate critical white matter (WM) tracts that should be preserved during neurosurgery. A key step in this process is estimating fiber orientation distribution (FOD), often done from a model such as constrained spherical deconvolution (CSD). Multi-shell (MS) multi-tissue CSD (M-CSD) provides a robust WM FOD by estimating the relative contribution to the dMRI signal from each tissue type (WM, grey matter, and cerebrospinal fluid), however, single-shell (SS) single tissue CSD (S-CSD) cannot independently estimate the signal contribution for each tissue type. S-CSD is therefore less accurate estimating FOD in voxels where multiple tissues are present. Due to that inaccuracy, tractography using S-CSD often generates more spurious WM streamlines compared to M-CSD. In this work, we present a framework to regress the M-CSD model coefficients from the S-CSD model coefficients using a convolutional neural network (CNN) in order to improve tractography. We construct a training dataset comprising acquired MS dMRI and paired synthetic SS dMRI, generated by selecting the outer shell from the MS dMRI. We select a High Resolution Network (HighResNet) as our choice of CNN to ensure subtle details of the CSD models are preserved during regression. The HighResNet is trained to perform patch-based regression from the S-CSD model coefficients and a co-registered T1-weighted MR (T1) to the M-CSD model coefficients. We evaluate the method on patients with epilepsy who appeared structurally normal on T1. Four WM tracts related to language are extracted using a ROI-based probabilistic tractography. For comparison, M-CSD is as a pseudo

O. Lucena (✉) · S. Ourselin · R. Sparks
School of Biomedical Engineering & Imaging Sciences, King's College London, London, UK
e-mail: oeslle.lucena@kcl.ac.uk

S. B. Vos
Centre for Medical Image Computing, University College London, London, UK

S. B. Vos · J. Duncan
Epilepsy Society MRI Unit, Chalfont St Peter, UK

V. Vakharia · J. Duncan
Department of Clinical and Experimental Epilepsy, University College London, London, UK

J. Duncan
National Hospital for Neurology and Neurosurgery, Queen Square, London, UK

ground truth. The original S-CSD generated tracts with Dice of 0.53–0.64, and the HighResNet regressed CSD models generated tracts with Dice of 0.73–0.77. We demonstrate HighResNet can regress M-CSD model coefficients from S-CSD model coefficients resulting in tracts more similar to the M-CSD generated tracts and with fewer spurious streamlines than S-CSD generated tracts.

1 Introduction

Diffusion magnetic resonance imaging (dMRI) tractography delineates white matter (WM) fibers by measuring the water diffusion within tissue and then modeling the direction of myelinated fibers from the dMRI signals [2, 11]. Accurate localization of WM tracts can aid presurgical planning by identifying the location of important eloquent structures, such as the motor sensory and language WM tracts [11]. Tractography is often preceded by a signal modeling of the dMRI to estimate the fibers orientation distribution (FOD) at the voxel level. However, signal modeling typically depends on the dMRI acquisition parameters such as signal-to-noise ratio, signal magnitude (b-values), and minimum number of diffusion-weighting gradients (b-vecs) [6, 19]. Usually, for more representative FOD models, more requirements regarding the dMRI signal acquisition are needed [19]. Nonetheless, in a clinical setting acquisition time is often limited, and the available commercial scanners may not provide the most robust state-of-the-art dMRI acquisitions.

Among many signal modeling methods that have been presented in the literature, constrained spherical deconvolution (CSD) uses spherical harmonics (SH) basis followed by a constraint (since it is poorly conditioned [8]) to estimate the FOD. CSD estimates the FOD SH components using a linear least-squares fitting where the original dMRI signal is approximated by a convolution of the FOD with a signal attenuation profile for a single fiber population, referred to as response function [8, 22].

For single-shell (SS) dMRI, where data is acquired for a single b-value, the volume contribution from isotropic tissues (grey matter (GM) and cerebrospinal fluid (CSF)) can not be taken into account when estimating the FOD. To compute an isotropic compartment, it is required either acquisition of multiple b-values (multiple shells) or the addition of stronger constraints, such as a finite number of fibers or known tissue diffusivities [7]. As a consequence, the single-shell single-tissue CSD (S-CSD) model produces unreliable and noisy FOD estimates for voxels containing mixtures of WM and CSF or GM, which is referred to as the partial volume effect (PVE) [7, 13].

In contrast, for multi-shell (MS) dMRI, where data is acquired for multiple b-values, the multi-shell multi-tissue CSD (M-CSD) is able to compute the relative dMRI signal contribution per tissue type by assuming two isotropic compartments for GM and CSF and an anisotropic compartment for WM [13]. M-CSD provides a more

precise and reliable FOD for voxels with PVE. Therefore, tractography performed on S-CSD contains more spurious WM streamlines (i.e., fibers at WM/GM boundaries) compared to M-CSD.

The overall aim of this work is to improve tractography for SS dMRI, which is routinely acquired in the clinic. We present a deep learning approach, using a convolutional neural network (CNN), to regress M-CSD model coefficients from S-CSD model coefficients. This regression will enable a more precise estimation of the WM FOD, by removing the dMRI signal contribution of non-WM tissue in voxels with PVE, and consequently more accurate WM tract delineation.

1.1 Related Works

Previous works have addressed solutions to reduce PVE in S-CSD [9]. Image quality transfer (IQT) for dMRI has been presented to transfer information from high-quality to lower spatial resolution data [1, 3]. As SS dMRI is often acquired due to timing constraints, [15] presented a data augmentation approach to estimate MS dMRI from SS dMRI by predicting SH coefficients. However, to our knowledge, no works have explicitly used machine learning to regress model coefficients for improving tractography.

In [9], an iterative approach to estimate the multi-tissue contribution for SS dMRI using pseudo multi-shell data is presented. The pseudo multi-shell data is generated combining the SS dMRI and the $b=0$ s/mm^2 to mimic a second shell. This initial study provides qualitative validation showing visualizations of the output CSD model coefficients.

In [1], IQT patch-based regression using a global linear regression models and random forest approaches are applied to (a) infer high-resolution from a lower spatial resolution dMRI signal and (b) dMRI parameter mapping between models. In (b), a low order diffusion tensor model is mapped to higher order models neurite orientation dispersion and density imaging [24] and spherical meaning technique [14].

The patch-based regression of IQT is expanded to be performed using a CNN with memory efficient backpropagation to infer high-resolution from a lower spatial resolution dMRI signal [3]. In this work, we also use patch-based regression between model parameters, however, we do not aim to improve the spatial resolution or mapping between parameters across different dMRI models. Rather, we aim to regress the individual tissue contributions to a multi-tissue model from a single-tissue model.

In [15], a multi-layer perceptron (MLP) to infer SH coefficients across dMRI shells is presented. One limitation of this approach is the MLP only use SH model coefficients from the same order obtained from a different shell or combination of shells with the restriction that all shells had the same number of acquired gradient directions. Furthermore, the MLP is only evaluated on pure WM voxels. Therefore, no improvements to multi-tissue modeling is evaluated in this study.

1.2 Our Approach

In this work, we present a patch-based CNN to learn a regression from S-CSD model coefficients to M-CSD model coefficients. The CNN framework we present can be generalized to other dMRI parameter mapping applications. We investigate the effect of using structural information obtained from T1-weighted MRI (T1) in the network to distinguish between tissue types. We also evaluate our method by its ability to generate appropriately four WM language related tracts on patients with epilepsy who appeared structurally normal on T1 performing a ROI-based probabilistic tractography. To our knowledge, no works have explicitly used machine learning to regress model coefficients for improving tractography generation.

2 Methods

2.1 Training Dataset Synthesis

All patients underwent a MRI protocol as part of the clinical procedures acquired on a 3T GE MR750 that included a T1 sequence (MPRAGE) and a MS dMRI with 2 mm isotropic resolution with the gradient directions 11, 8, 32, and 64 at $b = 0, 300, 700, \text{ and } 2500 \text{ s/mm}^2$, respectively and single $b = 0 \text{ s/mm}^2$ with reverse phase-encoding. DMRI was corrected for signal drift, geometric distortions and eddy-current induced distortions as in [17]. From the corrected MS dMRI, a paired SS dMRI was constructed by selecting the 64 images at $b = 2500 \text{ mm/s}^2$ from the MS dMRI similar to [21]. All dMRI were skull-stripped, then, CSD models with l_{max} order of 4, comprising 15 coefficients, were fit using the M-CSD [13] for the MS dMRI and the S-CSD [22] for the SS dMRI.

2.2 CNN Design

We implemented in PyTorch a High Resolution Network (HighResNet) [16] as depicted in Fig. 1 to regress the M-CSD model coefficients from the S-CSD model coefficients. HighResNet comprises of dilated convolutions and residual connections. Dilated convolutions can be used to produce accurate predictions and detailed probabilistic maps alongside object boundaries [16]. HighResNet can more accurately regress finer details compared to networks that use pooling operations such as U-Net [20] and V-Net [18] architectures. A parametric rectified linear unit (PReLU) activation function was used in place of a ReLU as it adaptively learns the parameters of the rectifiers, and it has been shown to improve CNNs accuracy in other applications [12]. The network was trained with an RMSprop optimizer to minimize the L_2

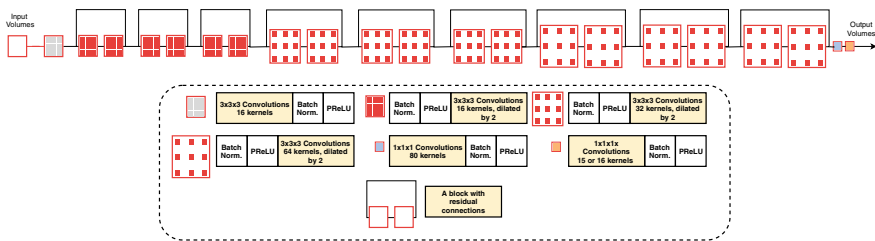


Fig. 1 HighResNet architecture [16]

loss function of the form $loss(y, \hat{y}) = \frac{\|y - \hat{y}\|_2^2}{2}$ where y is the ground truth M-CSD and \hat{y} is the output inferred from the model. In the training stage, HighResNet was initialized using He uniform function [12], and it was trained for 400 epochs, based on experimentally chosen convergence, with a weight decay of $1E - 6$. Training started with a learning rate of $3E - 2$, it was reduced by $1/2$ for every 50 epochs. The entire network is trained using patches sampled from the intracranial space, where for each subject, we used its binary skull-stripped mask as a prior to provide an intensity-based likelihood.

2.3 Training Setup

For each iteration in an epoch, a subject from the training set is randomly picked. Then, we performed whitening where each image is normalized to have a zero mean and unit standard deviation per channel. Subsequently, the subject data is augmented by randomly rotating orthogonal planes with an angle in the interval of $[-10^\circ, 10^\circ]$, scaling by a factor between 0.9 and 1.1, and random axis flipping. As a next step, 40 patches of size $32 \times 32 \times 32 \times c$ were sampled from the subject data, where c is the number of channels that could either be 15 or 16 comprising of only S-CSD or with an addition of the T1 image respectively. An epoch was finished when all subject data from the train set were used to optimize the loss function.

3 Experimental Design and Validation

Our dataset comprised 37 volumetric MS MRI datasets (acquisition described in Sect. 2.1) acquired from patients with epilepsy who appeared structurally normal on a T1. We performed five-fold random bootstrapped validation, where for each fold we split our data into 27 volumes for training, 5 volumes for validation, and 5 volumes for a hold-out test set. We trained our CNN model to regress M-CSD coefficients from: (a) S-CSD as input only *CNN (S-CSD)* and (b) S-CSD and T1 as input *CNN (S-CSD, T1)*. At the evaluation stage, we compute Dice between WM

tracts (Sect. 3.2), peak similarity for the output CSD models coefficients (Sect. 3.1), and the mean absolute error (MAE) per CSD model coefficients for each tissue type independently.

3.1 Peak Similarity Analysis

We conducted a peak similarity analysis per tissue type as followed. Firstly, we masked the CSD models using WM, GM or CSF masks from the geodesic-information flow (GIF) parcellation [5]. The peaks analysis are computed as follows: for the set of CSD model coefficients, we used MRtrix [23] *sh2peaks* to extract the two peaks with the largest amplitude. At the voxel level v , for M-CSD model coefficients, the major fiber directions are denoted as $G(v) = \{g_1, \dots, g_N\}$ containing N fiber directions. For the regressed CSD or S-CSD model coefficients, the major fiber directions are denoted as $P(v) = \{p_1, \dots, p_M\}$ containing M fiber directions, where $N, M \in \{0, 1, 2\}$. An angular difference (AD) matrix $\mathfrak{R}^{N \times M}$ is defined as follows:

$$AD(v)_{i,j} = \arccos\left(\frac{g_i \times p_j}{|g_i||p_j|}\right), \quad i \in N, j \in M \quad (1)$$

We then select matching directions by finding the two minimum angular differences between g_i and p_j fiber directions in the $AD(v)$ matrix. Once the matched directions are found, amplitude error is computed using $\frac{g_i \times p_j}{|g_i||p_j|}$.

3.2 Tracts Generation

We reconstructed the following four WM tracts: arcuate fasciculus (AF), inferior fronto-occipital fasciculus (IFOF), inferior longitudinal fasciculus (ILF), and uncinate fasciculus (UF) from the left side of the brain based on similar pipeline introduced in [17]. Briefly, WM tracts were reconstructed probabilistically with MRTrix3 using iFOD2 [23]. 1000 streamlines were estimated with a FOD amplitude cutoff of 0.05 by placing 10M seeds randomly at the WM/GM interface; determined from a GIF parcellation [5]. For each tract, a binary mask was generated by setting as foreground all voxels containing at least one WM streamline [4]. Dice was computed to measure tract overlap between the M-CSD and $CNN(\cdot)$ WM tract masks.

4 Results and Discussion

Figure 2 displays in each row, from left to right, the first CSD model coefficient, the corresponding MAE, a diffusion-encoded color (DEC) map calculated as in [10], and the four language tracts generated from each CSD model. From top to bottom in Fig. 2, the ground truth M-CSD, S-CSD, regressed approaches $CNN(S-CSD)$ and $CNN(S-CSD, T1)$ results are shown. The CSD model outputs from the CNN are more similar to the M-CSD than the S-CSD, and they generate tracts with fewer spurious streamlines when compared to tracts generated using S-CSD. As expected, the S-CSD has large differences with the M-CSD in gray matter and near intra-cortical boundaries. While $CNN(S-CSD)$ is more similar to the M-CSD compared to S-CSD, there are still some errors in intra-cranial boundary regions. For $CNN(S-CSD, T1)$, there is a further improvement near to tissue boundaries which is likely due to the addition of structural information to inform the regression. For $CNN(\cdot)$ the largest error reduction was in the in GM and CSF regions, where the S-CSD cannot properly capture differences between the tissue types (Table 1).

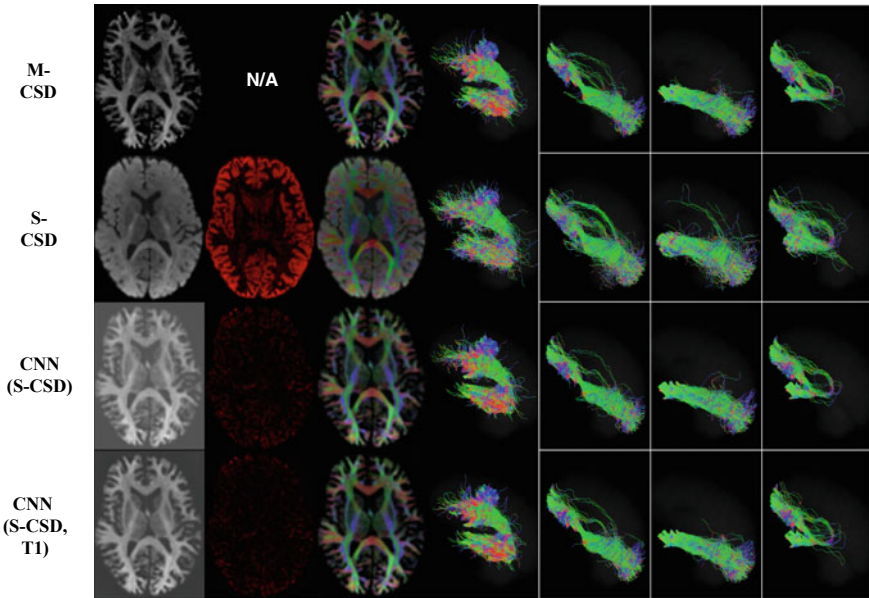


Fig. 2 From left to right: **1** the first coefficient in the CSD model, **2** the MAE between M-CSD model coefficients and the given model, **3** the DEC map, and **4–7** Left AF, IFOF, ILF, and UF for one patient from the test set. MAE shows colors between 0 (black) and 1 (red)

Table 1 MAE between M-CSD and CSD model coefficients for each tissue type. The minimum MAE appears in bold. BG indicates pixels outside of the intracranial space

Input type	MAE			
	WM	GM	CSF	BG
S-CSD	0.69 ± 0.05	0.67 ± 0.06	0.53 ± 0.06	0.01 ± 0.00
CNN(S-CSD)	0.19 ± 0.02	0.19 ± 0.02	0.08 ± 0.02	0.02 ± 0.01
CNN(S-CSD, T1)	0.20 ± 0.02	0.20 ± 0.03	0.10 ± 0.04	0.07 ± 0.04

Table 2 Dice between tracts generated from M-CSD and the input model. Maximum dice values per tract are in bold

Tract	Dice		
	S-CSD	CNN (S-CSD)	CNN (S-CSD, T1)
Left AF	0.64 ± 0.02	0.77 ± 0.01	0.77 ± 0.02
Left IFOF	0.61 ± 0.03	0.75 ± 0.01	0.76 ± 0.01
Left ILF	0.58 ± 0.03	0.74 ± 0.02	0.74 ± 0.02
Left UF	0.53 ± 0.04	0.73 ± 0.02	0.73 ± 0.02

As shown in Table 2, Dice between all WM tracts improved for the $CNN(\cdot)$ compared to S-CSD. $CNN(S-CSD, T1)$ was most similar to M-CSD for all WM tracts considered. The top two major fiber directions had a closer agreement between M-CSD and the $CNN(\cdot)$ than M-CSD and S-CSD (Fig. 3). Both $CNN(S-CSD)$ and $CNN(S-CSD, T1)$ had similar performance across all peaks considered. However, pronounced angular differences are still found in the GM and CSF. Nonetheless, peaks in CSF and GM regions are mainly dominated by noise that might have been amplified during the regression. This may be due to the per-channel normalization used in this approach.

Figure 4 displays an example of glyph representation of the FOD for highlighted regions in the brain. The voxel color is represented of tissue volume fraction, with red corresponding to CSF, green corresponding to GM, and blue corresponding to WM. Figure 4 demonstrates a reliable FOD for WM with less PVE resulting in higher Dice for tracts (Table 2).

Lastly, the training dataset was acquired from patients with epilepsy who appeared structurally normal on T1. However, white matter structures that appear normal on T1 may still be accompanied by micro-structural changes. Such changes might have affected WM FOD from the acquired dMRI and consequently our proposed method results.

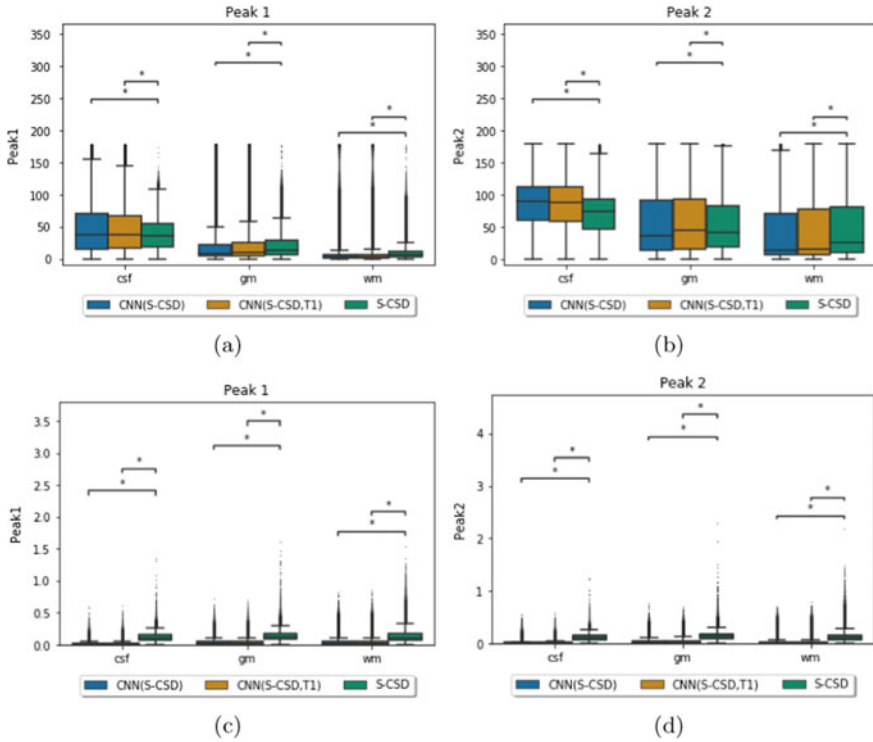


Fig. 3 Box plots for the first (Peak 1) and second (Peak 2) largest FOD peaks showing angular and amplitude differences per tissue type (WM, GM, and CSF) for the *CNN(S-CSD)* (blue), *CNN(S-CSD, T1)* (yellow), and *S-CSD* (green). The first row display angular differences while the second row displays amplitude differences for the Peak 1 and 2. Mann-Whitney-Wilcoxon test was carried out to assess statistical significance where * in the plots denotes p -value < 0.01

5 Conclusion

We present the use of a High Resolution Network to improve tractography by regressing multi-shell multi-tissue constrained spherical deconvolution (M-CSD) model coefficients from a single-shell single tissue (S-CSD) model coefficients. We demonstrate our method provides a reliable fiber orientation distribution and can generate white matter fiber tracts with fewer spurious streamlines than those generated from the original S-CSD. In this work, we evaluate our approach on a single dataset with the MS dMRI which from we synthetic generated SS dMRI using the outer shell. As the regression occurs in the CSD model space, this method is generalizable across acquisitions and datasets. Finally, a more extensive validation of our method on other datasets, including different dMRI acquisitions, addition of noise, and varying num-

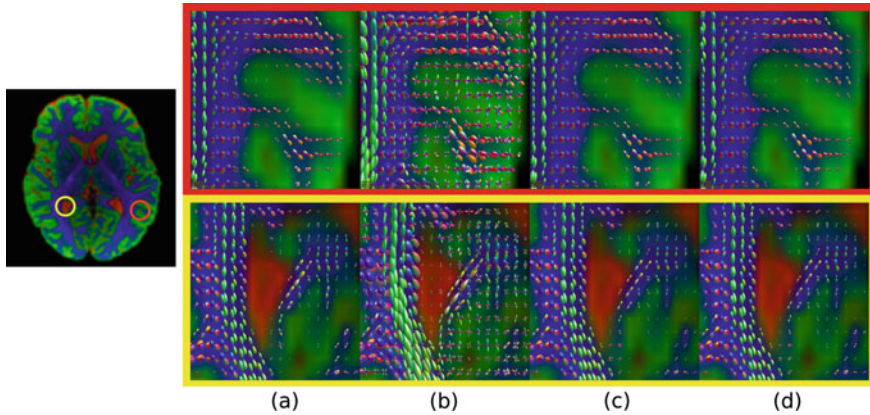


Fig. 4 A glyph representation of the FOD for the regions indicated by the red and yellow circles (magnified by $4\times$). Voxels are colored by estimated tissue contribution, where blue corresponds to WM, green corresponds to GM, and red corresponds to CSF. Models are shown for **a** M-CSD, **b** S-CSD, **c** CNN (*S-CSD*), and **d** CNN (*S-CSD, TI*)

ber of gradient directions which is necessary to prove the generalizability of this method. A limitation of the presented approach is the high angular differences in the FOD peaks for GM and CSF regions. In future work we will investigate other normalization and loss functions to minimize these errors.

Acknowledgments This research was funded/supported by the National Institute for Health Research (NIHR) Biomedical Research Centre based at Guy’s and St. Thomas’ NHS Foundation Trust and King’s College London and/or the NIHR Clinical Research Facility. Oeslle Lucena is funded by EPSRC Research Council (EPSRC DTP EP/R513064/1). Sjoerd B. Vos is funded by the National Institute for Health Research University College London Hospitals Biomedical Research Centre (NIHR BRC UCLH/UCL High Impact Initiative BW.mn.BRC10269). We also thank NVIDIA for the Titan V GPU used in this work. The views expressed are those of the author(s) and not necessarily those of the NHS, the NIHR or the Department of Health.

References

1. Alexander, D.C., Zikic, D., Ghosh, A., Tanno, R., Wottschel, V., Zhang, J., Kaden, E., Dyrby, T.B., Sotiropoulos, S.N., Zhang, H., et al.: Image quality transfer and applications in diffusion MRI. *NeuroImage* **152**, 283–298 (2017)
2. Berman, J.: Diffusion mr tractography as a tool for surgical planning. *Magn. Reson. Imaging Clin. North Am.* **17**(2), 205–214 (2009)
3. Blumberg, S.B., Tanno, R., Kokkinos, I., Alexander, D.C.: Deeper image quality transfer: training low-memory neural networks for 3d images. In: *International Conference on Medical Image Computing and Computer-Assisted Intervention*, pp. 118–125. Springer, Berlin (2018)
4. Calamante, F., Tournier, J.D., Jackson, G.D., Connelly, A.: Track-density imaging (tdi): super-resolution white matter imaging using whole-brain track-density mapping. *Neuroimage* **53**(4), 1233–1243 (2010)

5. Cardoso, M.J., Modat, M., Wolz, R., Melbourne, A., Cash, D., Rueckert, D., Ourselin, S.: Geodesic information flows: spatially-variant graphs and their application to segmentation and fusion. *IEEE Trans. Med. Imaging* **34**(9), 1976–1988 (2015)
6. Daducci, A., Canales-Rodri, E.J., Descoteaux, M., Garyfallidis, E., Gur, Y., Lin, Y.C., Mani, M., Merlet, S., Paquette, M., Ramirez-Manzanares, A., et al.: Quantitative comparison of reconstruction methods for intra-voxel fiber recovery from diffusion mri. *IEEE Trans. Med. Imaging* **33**(2), 384–399 (2013)
7. Dell’Acqua, F., Scifo, P., Rizzo, G., Catani, M., Simmons, A., Scotti, G., Fazio, F.: A modified damped richardson-lucy algorithm to reduce isotropic background effects in spherical deconvolution. *Neuroimage* **49**(2), 1446–1458 (2010)
8. Dell’Acqua, F., Tournier, J.D.: Modelling white matter with spherical deconvolution: How and why? In: *NMR in Biomedicine*, p. e3945 (2018)
9. Dhollander, T., Connelly, A.: A novel iterative approach to reap the benefits of multi-tissue csd from just single-shell ($+ b = 0$) diffusion MRI data. In: *Proceedings of ISMRM*. vol. 24, p. 3010 (2016)
10. Dhollander, T., Raffelt, D., Smith, R.E., Connelly, A.: Panchromatic sharpening of fod-based dec maps by structural t1 information. In: *Proceedings of the 23th Annual Meeting of the International Society of Magnetic Resonance in Medicine*, p. 566 (2015)
11. Essayed, W.I., Zhang, F., Unadkat, P., Cosgrove, G.R., Golby, A.J., O’Donnell, L.J.: White matter tractography for neurosurgical planning: a topography-based review of the current state of the art. *NeuroImage: Clin.* **15**, 659–672 (2017)
12. He, K., Zhang, X., Ren, S., Sun, J.: Delving deep into rectifiers: Surpassing human-level performance on imagenet classification. In: *Proceedings of the IEEE International Conference on Computer Vision*, pp. 1026–1034 (2015)
13. Jeurissen, B., Tournier, J.D., Dhollander, T., Connelly, A., Sijbers, J.: Multi-tissue constrained spherical deconvolution for improved analysis of multi-shell diffusion mri data. *NeuroImage* **103**, 411–426 (2014)
14. Kaden, E., Kruggel, F., Alexander, D.C.: Quantitative mapping of the per-axon diffusion coefficients in brain white matter. *Magn. Reson. Med.* **75**(4), 1752–1763 (2016)
15. Koppers, S., Haarbuerger, C., Merhof, D.: Diffusion mri signal augmentation: from single shell to multi shell with deep learning. In: *International Conference on Medical Image Computing and Computer-Assisted Intervention*, pp. 61–70. Springer, Berlin (2016)
16. Li, W., Wang, G., Fidon, L., Ourselin, S., Cardoso, M.J., Vercauteren, T.: On the compactness, efficiency, and representation of 3d convolutional networks: brain parcellation as a pretext task. In: *International Conference on Information Processing in Medical Imaging*, pp. 348–360. Springer, Berlin (2017)
17. Mancini, M., Vos, S.B., Vakharia, V.N., O’Keeffe, A.G., Trimmel, K., Barkhof, F., Dorfer, C., Soman, S., Winston, G.P., Wu, C., et al.: Automated fiber tract reconstruction for surgery planning: extensive validation in language-related white matter tracts. *NeuroImage: Clin.* 101883 (2019)
18. Milletari, F., Navab, N., Ahmadi, S.A.: V-net: Fully convolutional neural networks for volumetric medical image segmentation. In: *2016 Fourth International Conference on 3D Vision (3DV)*, pp. 565–571. IEEE (2016)
19. Neher, P.F., Cote, M.A., Houde, J.C., Descoteaux, M., Maier-Hein, K.H.: Fiber tractography using machine learning. *Neuroimage* **158**, 417–429 (2017)
20. Ronneberger, O., Fischer, P., Brox, T.: U-net: Convolutional networks for biomedical image segmentation. In: *International Conference on Medical Image Computing and Computer-assisted Intervention*, pp. 234–241. Springer, Berlin (2015)
21. Tong, Q., He, H., Gong, T., Li, C., Liang, P., Qian, T., Sun, Y., Ding, Q., Li, K., Zhong, J.: Reproducibility of multi-shell diffusion tractography on traveling subjects: a multicenter study prospective. *Magn. Reson. Imaging* (2019)
22. Tournier, J.D., Calamante, F., Gadian, D.G., Connelly, A.: Direct estimation of the fiber orientation density function from diffusion-weighted mri data using spherical deconvolution. *NeuroImage* **23**(3), 1176–1185 (2004)

23. Tournier, J.D., Smith, R.E., Raffelt, D.A., Tabbara, R., Dhollander, T., Pietsch, M., Christiaens, D., Jeurissen, B., Yeh, C.H., Connelly, A.: Mrtrix3: a fast, flexible and open software framework for medical image processing and visualisation. *BioRxiv* 551739 (2019)
24. Zhang, H., Schneider, T., Wheeler-Kingshott, C.A., Alexander, D.C.: Noddi: practical in vivo neurite orientation dispersion and density imaging of the human brain. *Neuroimage* **61**(4), 1000–1016 (2012)

q-Space Novelty Detection with Variational Autoencoders



Aleksei Vasilev, Vladimir Golkov, Marc Meissner, Ilona Lipp, Eleonora Sgarlata, Valentina Tomassini, Derek K. Jones, and Daniel Cremers

Abstract In machine learning, novelty detection is the task of identifying novel unseen data. During training, only samples from the normal class are available. Test samples are classified as normal or abnormal by assignment of a novelty score. The usage of deep neural networks for novelty detection remains an open challenge. Here we propose novelty detection methods based on training variational autoencoders (VAEs) on normal data. We apply these methods to magnetic resonance imaging, namely to the detection of diffusion-space (q-space) abnormalities in diffusion MRI scans of multiple sclerosis patients. q-Space novelty detection can reduce scan time duration and does not require any disease-specific prior knowledge, thus overcoming the disadvantages of other diffusion MRI processing methods. The methods proposed

A. Vasilev (✉) · V. Golkov · M. Meissner · D. Cremers
Computer Vision Group, Technical University of Munich, Munich, Germany
e-mail: alex.vasilev@tum.de

V. Golkov
e-mail: vladimir.golkov@tum.de

M. Meissner
e-mail: marc.meissner@tum.de

D. Cremers
e-mail: cremers@tum.de

I. Lipp · E. Sgarlata · V. Tomassini · D. K. Jones
CUBRIC, Cardiff University, Cardiff, UK
e-mail: lippi@cardiff.ac.uk

E. Sgarlata
e-mail: elesgarlata@hotmail.it

V. Tomassini
e-mail: tomassiniv@cardiff.ac.uk

D. K. Jones
e-mail: jonesd27@cardiff.ac.uk

E. Sgarlata
Department of Neurology and Psychiatry, Sapienza University of Rome, Rome, Italy

V. Tomassini
Division of Psychological Medicine and Clinical Neurosciences, Cardiff University, Cardiff, UK

© Springer Nature Switzerland AG 2020

E. Bonet-Carne et al. (eds.), *Computational Diffusion MRI*,

Mathematics and Visualization, https://doi.org/10.1007/978-3-030-52893-5_10

herein outperform the state of the art on q-space data in terms of quality and inference time. Our methods also outperform the state of the art on a standard novelty detection benchmark, and hence are also promising for non-MRI novelty detection.

1 Introduction

The purpose of novelty detection is to score how dissimilar each test sample is from a “normal” training set. Application domains include medical diagnostics, fraud and failure detection, and computer vision. The quality of novelty detection results depends on the algorithm and data distribution. Deep generative neural networks can reveal internal structure of the data and learn a better data representation. In this paper we design a set of novelty detection methods based on variational autoencoders (VAEs). We apply them to directly detect abnormalities such as multiple sclerosis lesions in diffusion magnetic resonance imaging (diffusion MRI).

1.1 Related Work on Novelty Detection with Generative Models

During the last years, several new methods for novelty detection were proposed. Variational autoencoders [9, 15], adversarial autoencoders [12], and generative adversarial networks (GANs) [2] are used by these methods to learn the normal patterns in the data. In [1], the reconstruction error of a VAE trained on the normal class only is used to detect abnormalities in the test data. A novelty score metric based on the adversarial autoencoder network is proposed in [11]. Another approach [20] uses a framework consisting of an autoencoder and a network that estimates a Gaussian mixture model of a normal class distribution in the latent space. In [16, 18], a GAN is trained to learn the distribution of the normal data. During test time a search over the latent space is performed to find the closest generated sample to the test sample. Another line of work [19] tries to unify classification and novelty detection into a single framework.

1.2 Diffusion MRI

Diffusion MRI is a magnetic resonance imaging (MRI) technique that uses the diffusion of water molecules to generate contrast in MR images. Since this diffusion is not free and affected by obstacles, it can reveal microstructural details about the tissue.

Classical diffusion MRI processing methods fit a handcrafted mathematical or physical model/representation to the measurements, and interpret the estimated model parameters. These approaches have several limitations: they require long scan times, partially discard information, and interpreting model parameters requires prior knowledge about how they are affected by disease.

Supervised and weakly-supervised deep learning in diffusion MRI can overcome said issues by learning a direct mapping between q-space measurements and diseases [3, 6]. In deep learning terminology, each diffusion-weighted 3D image corresponding to a certain q-space coordinate is treated as a “channel” of the overall multi-channel 3D volume. For *voxel-wise supervised learning*, for example to reconstruct missing q-space measurements from existing ones, or to predict handcrafted-model-based parameters more robustly and at a shorter scan time, or to directly estimate tissue types and properties, a “voxels-to-voxels” convolutional network can be used [3]. *Global supervised learning* (i.e. image-wise rather than voxel-wise prediction) and *voxel-wise weakly-supervised learning* are also possible [6] (see [17] for an overview). However, supervised and weakly-supervised disease detection requires disease-specific labels.

The aforementioned methods are complemented by **q-space novelty detection methods**, which do not require disease-related labels [4, 5] nor long scans [5]. In this line of work, each voxel is treated as a separate d -dimensional feature vector, where d is the number of measured diffusion directions. Voxels from scans of healthy volunteers are used as a reference dataset, and the Euclidean distance in feature space between the test datapoint and its nearest neighbor from the reference dataset is used as a novelty score. A high novelty score thus indicates that the voxel is lesioned. This novelty score coincides with multiple sclerosis lesions at AUC scores between 0.82 and 0.89 on various datasets, and we use this method as a baseline to compare our methods with.

Novelty detection methods are crucial for diffusion MRI because they work without handcrafted representations (whose usage and fitting cause information loss and long scan durations [3, 5] that are unacceptable in clinical practice), and *do not* require any labels for the lesion class, thus are applicable even when the influence of disease on diffusion properties is not entirely studied (which is often the case due to complex tissue microstructure).

1.3 Our Contributions

In this paper we show that the usage of a variational autoencoder can help to better understand the normal patterns in the data and thus improve the quality of novelty detection. We further explore the possibilities of applying novelty detection to diffusion MRI processing. The main contributions of the paper are:

- We propose several new novelty detection methods in the VAE original and latent feature spaces. These methods can be applied to different datasets. We evaluate

them on the MNIST handwritten digits dataset and show that some of them outperform the state of the art. Our code will be made publicly available.

- We adapt the VAE network to q-space novelty detection. We show that this solution can outperform the original q-space novelty detection algorithm in terms of quality and speed.

2 VAE-Based Novelty Detection Methods

A variational autoencoder [9, 15] is a deep neural network that models a relationship between a low-dimensional latent random variable z and a random variable x in the original data space. A VAE consists of an encoder and a decoder. The encoder is trained to approximate the posterior distribution $q_\phi(z|x)$, where ϕ are the network parameters, learned with backpropagation during training. The decoder performs the inverse task: it approximates the posterior distribution $p_\theta(x|z)$, where θ are learned parameters.

We decided to use the VAE for q-space novelty detection for multiple reasons:

- A VAE provides an explicit map into latent space, where features and novelty metrics are high-level.
- Diffusion-MRI voxels form a single unseparated “island” in feature space (with transitions between tissue classes due to voxel mixtures) and the VAE regularizer encourages appropriate treatment (non-separateness in latent space) of such data.
- The VAE regularizer encourages (similar) training samples to be close in latent space, so that distance-based methods do not consider normal samples as novel.

In our case we train the VAE model to capture normal data only. Thereby, the VAE learns distributions of the normal dataset in latent and original feature space. Both of these distributions as well as their combination can be used to define novelty score metrics, thus we split our methods into three main categories.

2.1 Novelty in the Latent Space

The trained VAE maps each sample x to a distribution z in some lower-dimensional latent space. This representation can be used to define several novelty metrics.

Novelty as VAE regularizer The VAE loss function includes the following regularizer term: $D_{\text{KL}}(q_\phi(z|x) \parallel \mathcal{N}(0, I))$. This term forces the model to map inputs closely to the unit Gaussian distribution $\mathcal{N}(0, I)$ in the latent space. Without this regularizer the model could learn to give each input a representation in a different region of the latent space. For the model trained on the normal class only, one could expect that abnormal samples will have distributions in the latent space that diverge more from

the unit Gaussian than normal samples. We thus can use this term as a novelty score for test sample x_{test} :

$$N_{\text{VAE-reg}}(x_{\text{test}}) = D_{\text{KL}}(q_{\phi}(z|x_{\text{test}}) \parallel \mathcal{N}(0, I)). \quad (1)$$

Distance-based approaches in latent space The latent space of a VAE trained on the normal class can be considered an effective representation of the distribution of normal data. Therefore, classical novelty detection approaches can be adapted to be used in this space. The algorithm here is to map normal (reference) data as well as test data into the learned latent space using the trained encoder. Then one can use nearest-neighbour analysis to find the closest sample from the reference dataset to each test sample x_{test} using some distance measure in the latent space. This distance to the closest normal sample is used as a novelty score. A VAE maps each input point to a distribution (rather than a point) in latent space. We propose two distance measures:

Euclidean distance between means of the distributions The first approach uses only information about the means of the approximated posterior in the latent space for normal and test datapoints. The novelty score is computed as the distance between the means of the latent-space distribution of the test datapoint and of the closest latent-space distribution of a normal sample:

$$N_{\bar{q}-\bar{q}_y}(x_{\text{test}}) = \min_{y \in Y} \|E[q_{\phi}(z|x_{\text{test}})] - E[q_{\phi}(z|y)]\|_2^2, \quad (2)$$

where the minimum is taken over all normal samples y from the normal dataset Y .

Bhattacharyya distance between distributions The Bhattacharyya distance is a symmetric measure of dissimilarity of two probability distributions p and q . It is defined as $D_B(p, q) = -\ln(\text{BC}(p, q))$, where $\text{BC}(p, q) = \int \sqrt{p(z)q(z)} dz$ is the Bhattacharyya coefficient of distributions p and q . This approach utilizes information about the full learned distributions, computing the amount of the overlap between them. A novelty score is defined as the Bhattacharyya distance between the latent-space distribution $q_{\phi}(z|x_{\text{test}})$ of the test sample and the most similar latent-space distribution $q_{\phi}(z|y)$ of a normal sample:

$$N_{q-q_y}(x_{\text{test}}) = \min_{y \in Y} D_B(q_{\phi}(z|x_{\text{test}}), q_{\phi}(z|y)). \quad (3)$$

Density-based approach in latent space Another approach to novelty detection is to estimate the density of normal data in the latent space. Each normal datapoint is represented as a Gaussian distribution in the VAE latent space. Thus the distribution of the whole normal dataset can be estimated as an average of these Gaussians: $q_Y(z) = \frac{1}{|Y|} \sum_{y \in Y} q_{\phi}(z|y)$. Then, the novelty score for the test sample can be computed from the density estimate q_Y of the normal dataset, evaluated at the mean of the latent distribution $q_{\phi}(z|x_{\text{test}})$ of the test sample (see also Fig. 1):

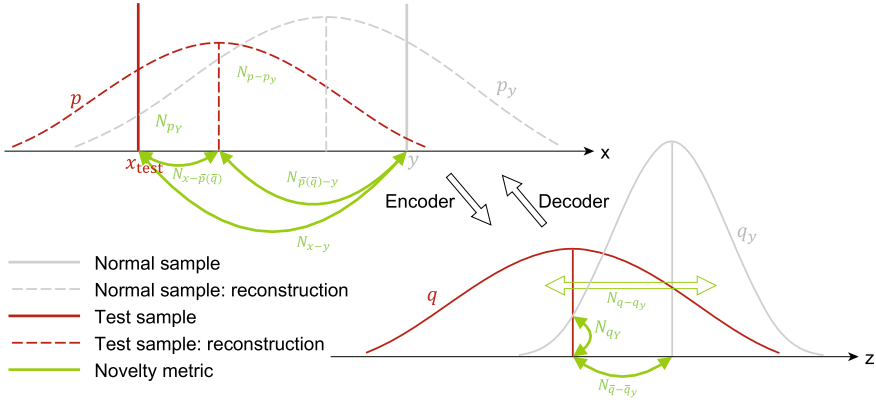


Fig. 1 Some of the proposed novelty detection methods, illustrated for the simplified case of 1D original space x and 1D latent space z of the VAE with only one normal sample y and one test sample x_{test} . Green arrows measure distances between points (\rightarrow) or distributions (\leftrightarrow). The score $N_{x-\bar{p}(\bar{q})}$ quantifies whether the VAE reconstructs x_{test} badly; N_{x-y} and $N_{\bar{p}(\bar{q})-y}$ measures how dissimilar x_{test} (or its reconstruction $\bar{p}(\bar{q})$) is from normal samples y ; N_{q-q_y} and $N_{\bar{q}-q_y}$ measure how dissimilar x_{test} is from y in latent space; N_{q_y} measures how likely x_{test} belongs to the modeled distribution of normal data

$$N_{q_y}(x_{\text{test}}) = -q_y(E[q_\phi(z|x_{\text{test}})]). \quad (4)$$

2.2 Novelty in the Original Feature Space

VAE reconstruction-based approaches Like a traditional autoencoder network, a VAE is trained to reconstruct the input. If a VAE is trained on the normal class only, one could expect that it learns how to reconstruct data from the normal class well, but may not be particularly good at reconstructing unseen data, so the reconstruction error for the unseen class should be higher. Thus, the reconstruction error can be used as a novelty score. The encoder and decoder are both stochastic. For each of them, we can either draw samples, or consider the mean. For the decoder it is also possible to consider the entire distribution and compute the density value of the test sample. For example, one can use means of both the encoder $q_\phi(z|x)$ and the decoder $p_\theta(x|z)$ to deterministically reconstruct the input and compute the reconstruction error:

$$N_{x-\bar{p}(\bar{q})}(x_{\text{test}}) = \|x_{\text{test}} - E[p_\theta(x|E[q_\phi(z|x_{\text{test}})])]\|_2^2. \quad (5)$$

Distance-based approaches In addition to reconstruction-based approaches, it is possible to apply distance-based approaches described in Sect. 2.1 to the distributions produced by the decoder of the VAE. It is also possible to apply the Euclidean-distance-based approach to the reconstructed test sample and original (not reconstructed) normal datapoints:

$$N_{\hat{p}(\bar{q})-y}(x_{\text{test}}) = \min_{y \in Y} \left\| E[p_{\theta}(x|E[q_{\phi}(z|x_{\text{test}}) - y])] \right\|_2^2. \quad (6)$$

Distance to the closest generated sample A VAE is a generative model. Trained on a normal class only, one could expect that it will not be able to generate the datapoints that do not belong to the normal class. Thus a novelty score can be computed as the distance between a test sample and the closest sample that the VAE decoder is able to produce from any latent vector z :

$$N_{x-\hat{p}}(x_{\text{test}}) = \min_z \|x_{\text{test}} - E[p_{\theta}(x|z)]\|_2^2. \quad (7)$$

This is an optimization problem over the latent space. It can be solved using a non-linear optimization method such as L-BFGS [13]. The encoder of the VAE with x_{test} as an input can be used to get an initial value for z for optimization.

If the bottleneck of the VAE is not narrow enough, the VAE may still be able to reconstruct abnormal data. However, the values of z for abnormal datapoints might be far from the unit Gaussian, since the VAE loss includes the term $D_{\text{KL}}(q_{\phi}(z|x) \parallel \mathcal{N}(0, I))$, and is trained on the normal data only. Thus the optimization can also be performed not over the whole latent space, but within some boundaries (we used $[-10, 10]^{\dim z}$), defining a new novelty score $N_{x-\hat{p}_b}$. During the experiments, we found that the best results are achieved with $[-10, 10]$ boundaries for each of the dimensions of the latent space.

2.3 Novelty as Full VAE Loss

If the VAE is trained on the “normal” class only, its loss function applied to a test sample can be considered as a novelty metric itself. The VAE loss function value from datapoint x_i is a reverse of the lower bound of the marginal probability $p(x_i)$ of this datapoint [9, 15]. Abnormal datapoints have a low probability according to a model that was trained on the normal class and thus high loss value. Thus we propose the following novelty metric:

$$N_{\text{-ELBO}}(x_{\text{test}}) = -E_{q_{\phi}(z|x_{\text{test}})}[\log p_{\theta}(x_{\text{test}}|z)] + D_{\text{KL}}(q_{\phi}(z|x_{\text{test}}) \parallel \mathcal{N}(0, I)). \quad (8)$$

Like in the original VAE training algorithm [9], the Monte Carlo estimate of $E_{q_{\phi}(z|x_{\text{test}})}$ should be computed. We also propose to use several samples from the probabilistic decoder $q_{\phi}(z|x_{\text{test}})$ to define a novelty metric:

$$N_{\widehat{\text{-ELBO}}}(x_{\text{test}}) = \min_{z \sim q_{\phi}(z|x_{\text{test}})} [\log p_{\theta}(x_{\text{test}}|z)] + D_{\text{KL}}(q_{\phi}(z|x_{\text{test}}) \parallel \mathcal{N}(0, I)). \quad (9)$$

3 Experiments

As the “normal” data to train the model for diffusion MRI, we used 26 diffusion MRI scans of healthy volunteers that were split into 20 training and (for hyperparameter tuning) 6 validation scans. Each scan has six $b = 0$ images and 40 uniformly distributed diffusion directions ($b_{\max} = 1200\text{s/mm}^2$, SE-EPI, voxel size $1.8\text{ mm} \times 1.8\text{ mm} \times 2.4\text{ mm}$, matrix 128×128 , 57 slices, $T_E = 94.5\text{ ms}$, $T_R = 16\text{ s}$, distortion-corrected with elastix [10] and upsampled to $256 \times 256 \times 172$). Using machine learning nomenclature, we refer to these 46 volumes (six $b = 0$ and 40 diffusion-weighted volumes) as *channels* or *voxel-wise features*. Test data consisted of three multiple sclerosis patients’ scans with the same scan parameters as for healthy volunteers. Note that every voxel (rather than every scan) is a sample. Hence, the test set contains more than 5 million samples (brain voxels) in total, 55 thousand of which are lesion voxels. To validate the results of proposed methods, we used multiple sclerosis lesion labels created by human raters using additional structural T_2 -weighted scans. We compared the performance of proposed novelty detection algorithms with the distance-based q-space novelty detection algorithm [4, 5] (described in Sect. 1.2).

In order to avoid potential discrepancies in image intensity across scans, each scan was divided by its mean intensity. In addition, to prevent some channels from dominating over others, feature scaling was performed, i.e. each channel was divided by the channel-wise mean taken across all scans. Each voxel was considered as a separate data sample. We ignore information from neighboring voxels because the goal is to discover unusual microstructure (using q-space channels) without any bias from unusual macrostructure.

We used the area under the curve (AUC) of the receiver operating characteristic (ROC) as the quality metric because it quantifies the sensitivity and specificity of novelty detection across all possible decision thresholds, is robust to class imbalance, and is the most common quality metric for novelty detection in literature. For each of the novelty metrics described in Sect. 2, we performed a hyperparameter search varying the dimensionality of the latent space, the depth of the architecture and the number of hidden layers to find the model that achieves the highest AUC score. The Adam optimizer [8] with learning rate 0.001, batch size of 32768 voxels and early stopping was used during training. Three different models with the following number of input/hidden/output features per layer were selected: $46 - 64 - 32 - 16 - \mathbf{8} - 16 - 32 - 64 - 46$; $46 - 128 - 64 - 32 - \mathbf{16} - 32 - 64 - 128 - 46$; $46 - 128 - 64 - 48 - \mathbf{24} - 48 - 64 - 128 - 46$. Here 46 is the number of input/output features of the autoencoder. Results are shown in Table 1; these three models can be distinguished by the ‘dim z ’ column (the dimensionality of the latent space). Moreover, fixing $\text{dim } z = \mathbf{12}$ in all models without individual tuning yielded almost the same performance (± 0.005 AUC).

As the baseline to compare the proposed methods with, we used the distance-based ND method [4, 5]. This method was already compared to the traditional ND methods (such 1-class SVM and kernel PCA) on multiple sclerosis q-space data and has shown the best results while performing much faster.

Table 1 AUC scores of multiple sclerosis lesion segmentation and approximate inference time in minutes per scan for different q-space novelty detection methods. Many of our methods outperform (marked in **bold**; statistically highly significant due to millions of samples used, p-value in most cases around 10^{-6}) the baseline method N_{x-y} [5] and provide considerable time gain

Method	dim z	AUC scan 1	AUC scan 2	AUC scan 3	Time (min)
Baseline	–	0.859	0.838	0.884	360
$N_{\text{VAE-reg}}$	16	0.803	0.773	0.812	1
$N_{\bar{q}-\bar{q}_y}$	16	0.893	0.831	0.890	120
N_{q-q_y}	16	0.888	0.835	0.893	360
N_{q_y}	24	0.860	0.815	0.880	360
$N_{x-\hat{p}(\bar{q})}$	24	0.857	0.841	0.882	2
$N_{\hat{p}(\bar{q})-y}$	16	0.893	0.852	0.897	360
$N_{x-\hat{p}}$	8	0.857	0.849	0.878	60
$N_{x-\hat{p}_b}$	8	0.859	0.849	0.879	60
$N_{\text{-ELBO}}$	16	0.895	0.856	0.852	4
$N_{\text{-}\widehat{\text{ELBO}}}$	16	0.897	0.867	0.873	20

Lesion segmentation results are shown in Fig. 2. AUC improvement over the baseline is highly significant due to millions of samples used. More specifically, AUC improvement of 2% (achieved by the majority of the proposed methods) has the p-value of about 0.0000005, which is statistically highly significant.

We also evaluated some of the proposed methods on the MNIST digits dataset using a convolutional VAE with the architecture C16-P-C32-FC64-FC196-C32-U16-C1, where numbers indicate channels, C is a 3×3 convolutional layer, P is 2×2 max-pooling, FC is a fully connected layer, U is a 2×2 upconvolutional layer. We consider one of the MNIST handwritten digits as novel and train on the remaining ones. Training data consist of 80% of the normal data. Test data consist of the remaining 20% of the normal data as well as all of the novel data. With 10 possible novelty classes/digits, this results in 10 different experiments. Results are shown in Table 2.

4 Discussion and Conclusions

Most of the proposed methods show a good performance. More specifically, latent-space distance-based methods (N_{q-q_y} and $N_{\bar{q}-\bar{q}_y}$) outperform the method based on Euclidean distance in the original data space [5] (N_{x-y} ; see also Fig. 2) despite the fact that the model was not trained on abnormal data. This happens on one hand due to the fact that the VAE has a regularizer that keeps the latent representation of the normal data tightly clustered around the unit Gaussian, while abnormal data that were not used during training can be mapped to a different region of the latent

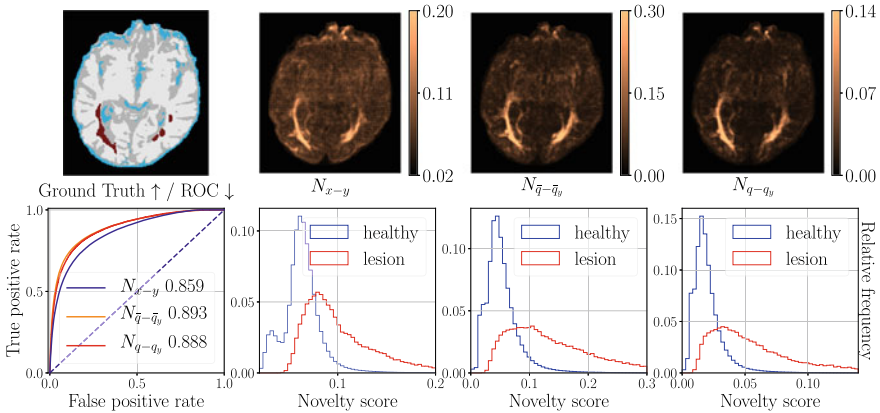


Fig. 2 Feasibility of q-space novelty detection for multiple sclerosis lesion segmentation. Top row: manual lesion segmentation (left) and novelty-score maps using the baseline method N_{x-y} [5] and two VAE latent space distance-based novelty detection methods $N_{\bar{q}-\bar{q}_y}$ and N_{q-q_y} . Bottom row: ROC for one scan measuring coincidence of novelty detection with human-marked labels (proposed methods outperform the baseline); normalized histogram of the novelty score for lesion and non-lesion voxels for the three methods above (many lesion voxels have considerably higher novelty scores than healthy voxels). In other words, disease-related microstructural tissue changes are detected in a data-driven way, without any prior knowledge about them

Table 2 AUC scores for selected novelty detection methods on the MNIST dataset for all novelty classes. Our methods outperform the state of the art

Method	dim z	AUC scores for novelty digits:									
		0	1	2	3	4	5	6	7	8	9
An&Cho [1]	200	0.917	0.136	0.921	0.781	0.808	0.862	0.848	0.596	0.895	0.545
$N_{\text{VAE-reg}}$	64	0.395	0.146	0.637	0.498	0.459	0.144	0.358	0.626	0.792	0.512
$N_{\bar{q}-\bar{q}_y}$	64	0.922	0.528	0.965	0.877	0.870	0.876	0.872	0.803	0.772	0.637
N_{q-q_y}	64	0.925	0.480	0.966	0.882	0.869	0.855	0.868	0.815	0.802	0.641

space (which is confirmed by the fact that the VAE regularizer itself also produces meaningful novelty scores); and on the other hand due to the fact that the trained VAE simply happens to map abnormal data to slightly different latent-space regions.

These results indicate that normal and abnormal data are better separated in latent space than in input space. This can be expected on one hand because latent representations usually highlight high-level features (in this case tissue properties) as opposed to unimportant low-level ones; and on the other hand because the aforementioned effects of the regularizer apply particularly to the latent space.

Reconstruction-based methods also perform well, since the reconstruction of abnormal data (of which the model has not seen any during training) can be very imprecise, thus yielding a high novelty score for reconstruction-based methods. However, in order to be able to reconstruct the normal data (and assign a low novelty score

to it), a VAE should have a sufficient number of latent dimensions to avoid substantial information loss. High AUC scores of $N_{x-\hat{p}_b}$ indicate that the VAE mostly generates the kind of samples it was trained on, namely normal ones. However, to achieve this ability, the bottleneck of the VAE (in contrast to reconstruction-based methods) should be narrow enough, otherwise the model may also be able to generate some “random” data that may be very close to the abnormal data in the original feature space.

Finally, the VAE loss itself as the inverse of the lower bound of the likelihood of the data sample is a good novelty metric: abnormal data (none of which were used during training) have low likelihood according to the model and thus high novelty score.

Note that the manual lesion labels are not perfect, and novelty detection is not specific to multiple sclerosis. It simply marks voxels that are unlike the normal dataset in some way. Thus it may also mark subtle disease-related microstructural changes that went undetected by manual labeling, or image artifacts that are too rare/diverse to be learned from the normal training dataset. However in practice high novelty scores coincide well with labeled lesions, as can be expected. Some of the proposed methods do not only outperform the baseline but also perform inference orders of magnitude faster (see Table 1). In general, there is a trade-off between accuracy and runtime of the proposed methods. Thus, a specific method should be selected based on the task requirements.

Results on a standard benchmark for novelty detection (Table 2) show that our methods can outperform Ref. [1], which is state of the art to the best of our knowledge. Thus, our novelty detection methods can be applied successfully to different datasets.

In this work, we presented a set of novelty detection algorithms that utilize the ability of variational autoencoders to reveal the internal structure of the normal-class data. We found that high novelty scores produced by our methods coincide with multiple sclerosis lesions in diffusion MRI data, and many of our methods outperform the baseline q-space novelty detection method. Additionally, we evaluated the methods on the MNIST dataset, where we were able to surpass state-of-the-art results.

References

1. An, J., Cho, S.: Variational Autoencoder based Anomaly Detection using Reconstruction Probability. Technical Report, SNU Data Mining Center (2015)
2. Goodfellow, I.J., et al.: Generative Adversarial Nets. NIPS 2672–2680 (2014)
3. Golkov, V., et al.: q-space deep learning: twelve-fold shorter and model-free diffusion MRI scans. *IEEE Trans. Med. Imaging* **35**(5), 1344–1351 (2016)
4. Golkov, V., et al.: Model-Free Novelty-Based Diffusion MRI (2016). ISBI 1233-1236
5. Golkov, V., et al.: q-Space Novelty Detection in Short Diffusion MRI Scans of Multiple Sclerosis. *ISMRM* 5378 (2018)
6. Golkov, V., et al.: q-Space Deep Learning for Alzheimer’s Disease Diagnosis: Global Prediction and Weakly-Supervised Localization. *ISMRM* 1580 (2018)
7. Hoffmann, H.: Kernel PCA for novelty detection. *Pattern Recognit.* **40**(3), 863–874 (2007)
8. Kingma, D.P., Adam, J.Ba.: A Method for Stochastic Optimization. *ICLR* (2014)

9. Kingma, D.P., Welling, M.: Auto-Encoding Variational Bayes. ICLR (2014)
10. Klein, S., et al.: Elastix: a toolbox for intensity-based medical image registration. *IEEE Trans. Med. Imaging* **29**(1), 196–205 (2010)
11. Leveau, V., Joly, A.: Adversarial Autoencoders for Novelty Detection. Research Report, Inria—Sophia Antipolis (2017)
12. Makhzani, A., et al.: Adversarial Autoencoders. ICLR (2016)
13. Nocedal, J.: Updating quasi-newton matrices with limited storage. *Math. Comput.* **35**(151), 773–782 (1980)
14. Pimentel, M.A.F., et al.: A review of novelty detection. *Signal Process.* **99**, 215–249 (2014)
15. Rezende, D.J., et al.: Stochastic backpropagation and approximate inference in deep generative models. *ICML* **32**(2), 1278–1286 (2014)
16. Schlegl, T., et al.: Unsupervised Anomaly Detection with Generative Adversarial Networks to Guide Marker Discovery. *IPMI* (2017)
17. Swazinna, P., et al.: Negative-Unlabeled Learning for Diffusion MRI. *ISMRM* 3480 (2019)
18. Wang, H., et al.: Generative adversarial network based novelty detection using minimized reconstruction error. *Frontiers Inf. Technol. Electron. Eng.* **19**, 116 (2018)
19. Wang, W., et al.: Safer Classification by Synthesis (2017). [arXiv:1711.08534](https://arxiv.org/abs/1711.08534)
20. Zong, B., et al.: Deep Autoencoding Gaussian Mixture Model for Unsupervised Anomaly Detection. ICLR (2018)

DWI Simulation-Assisted Machine Learning Models for Microstructure Estimation



Jonathan Rafael-Patino, Thomas Yu, Victor Delvigne, Muhamed Barakovic, Marco Pizzolato, Gabriel Girard, Derek K. Jones, Erick J. Canales-Rodríguez, and Jean-Philippe Thiran

Abstract Diffusion MRI (DW-MRI) allows for the detailed exploration of the brain white matter microstructure, with applications in both research and the clinic. However, state-of-the-art methods for microstructure estimation suffer from known limitations, such as the overestimation of the mean axon diameter, and the infeasibility of fitting diameter distributions. In this study, we propose to eschew current modeling-based approaches in favor of a novel, simulation-assisted machine learning approach. In particular, we train machine learning (ML) algorithms on a large dataset of simulated diffusion MRI signals from white matter regions with different axon diameter distributions and packing densities. We show, on synthetic data, that the trained models provide an accurate and efficient estimation of microstructural parameters

J. Rafael-Patino (✉) · T. Yu · M. Barakovic · M. Pizzolato · G. Girard · E. J. Canales-Rodríguez · J.-P. Thiran
Signal Processing Lab (LTS5), École Polytechnique Fédérale de Lausanne,
Lausanne, Switzerland
e-mail: j.rafael.patino@gmail.com

V. Delvigne
Université de Mons, Mons, Belgium

G. Girard · E. J. Canales-Rodríguez · J.-P. Thiran
Radiology Department, Centre Hospitalier Universitaire Vaudois, Lausanne, Switzerland

G. Girard
Centre d'Imagerie BioMédicale (CIBM), Lausanne, Switzerland

D. K. Jones
Cardiff University Brain Research Imaging Centre (CUBRIC), School of Psychology, Cardiff University, Cardiff, UK

Mary McKillop Institute for Health Research, Australian Catholic University, Melbourne, Australia

E. J. Canales-Rodríguez
FIDMAG Germanes Hospitalàries, Sant Boi de Llobregat, Barcelona, Spain

Mental Health Research Networking Center (CIBERSAM), Madrid, Spain

J.-P. Thiran
University of Lausanne, Lausanne, Switzerland

in-silico and from DW-MRI data with moderately high b-values (4000 s/mm^2). Further, we show, on in-vivo data, that the estimators trained from simulations can provide parameter estimates which are close to the values expected from histology.

1 Introduction/Related Work

Diffusion-Weighted MRI (DW-MRI) provides a non-invasive, in-vivo technique for investigating the micro-anatomy of brain tissue. As the DW-MRI signal depends on the self-diffusion process of water molecules within the intra- and extra-axonal spaces, it can be used to estimate the local, microstructural properties of cells via inverse modeling. A number of microstructure parameters of the white matter fibres such as the statistical distribution of axon diameters (mean and variance) and orientations, as well as the volume fraction occupied by axons (i.e., fibre density) can be inferred from DW-MRI signals through the inversion of complex, non-linear models that require time consuming optimization algorithms. Some examples of state-of-the-art models are AxCaliber [3] and ActiveAx [1], which are used to estimate the axon diameter distribution, and CHARMED [2] and NODDI [15] to estimate the fibre orientations and their volume fractions. To make the fitting more stable, previous models rely on different approximations that require different assumptions. One common assumption is to model the signal from the white matter by a sum of signals from two independent compartments: the intra- and extra-axonal spaces. Other assumptions include modeling axons as perfect, impermeable cylinders. There are some well-known issues with these model-based approaches, including difficulty in separating signals into compartments, model oversimplification, degeneracy, and instability during fitting [7, 14, 15].

In this study, we explored the feasibility of bypassing some of the limitations of the current inverse models by developing an emerging approach that is based on using DW-MRI simulations as a tool for performing forward modeling [9, 12]. In our approach, we first created a large and detailed dataset of numerical white matter phantoms with varying geometric properties of interest, such as the mean and standard deviation of axon diameters and the axon density. We then generated the DW-MRI signals of these phantoms using a DW-MRI Monte-Carlo simulator [11]. We trained two different machine learning algorithms, i.e., random forest and multi-layer perceptron, to map the simulated signals with and without handcrafted features, to the microstructural parameters. The learned models were then applied to both synthetic and in-vivo brain data.

2 Methods

2.1 Dataset Generation

Figure 1 shows the structure of our framework from the dataset generation to the accuracy evaluation. In generating the dataset, we express the DW-MRI signal in the brain white matter (WM) as the sum of the signals from the intra-axonal S_{int} and extra-axonal S_{ext} compartments, weighted by their relaxation-weighted volume fractions $icvf$ and $ecvf = 1 - icvf$, where $icvf + ecvf = 1$:

$$S = (icvf)S_{int} + (1 - icvf)S_{ext} \tag{1}$$

The intra-axonal space represents the axons which we model as straight and parallel cylinders, and the extra-axonal space corresponds to the space outside the axons, including the extra-axonal matrix, glial cells, and cerebrospinal fluid, etc. We further assume that within a bundle, the axon diameters follow a Gamma distribution [13], with different bundles having different means and standard deviations.

A large dataset of WM phantoms with different geometrical properties was generated by parameterising the intra-axonal space with the volume fraction $icvf$ as well as the mean μ and standard deviation σ of a Gamma distribution. These parameters were varied according to the realistic values reported in Table 1. A packing algorithm that generates axon geometries matching these predefined parameters was implemented similar to [6]. Then, simulated DW-MRI signals for each one of these phantoms were generated using a DW-MRI Monte-Carlo simulator [11] with a specific acquisition protocol consisting of 2 shells with b-values equals to 1000 s/mm^2

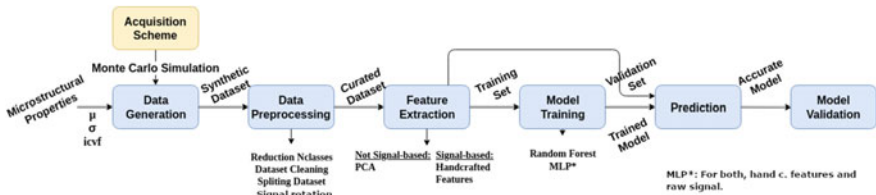


Fig. 1 Framework pipeline

Table 1 Table of values used to generate all the substrates for the mean radius (μ), the standard deviation of the distribution (σ), and the ICVF. A total of 1824 combinations were produced

Parameters	Values
μ	{0.2, 0.3, 0.5, 0.66, 0.81, 0.97, 1.12, 1.28, 1.44, 1.59, 1.75, 1.91, 2.06, 2.22, 2.34, 2.53, 2.69, 2.84, 3}
σ	{ 0.1, 0.3, 0.5, 1, 1.5, 2, 2.5, 3 }
$icvf$	{0.35, 0.4, 0.45, 0.5, 0.53, 0.57, 0.6, 0.63, 0.67, 0.7, 0.73, 0.75}

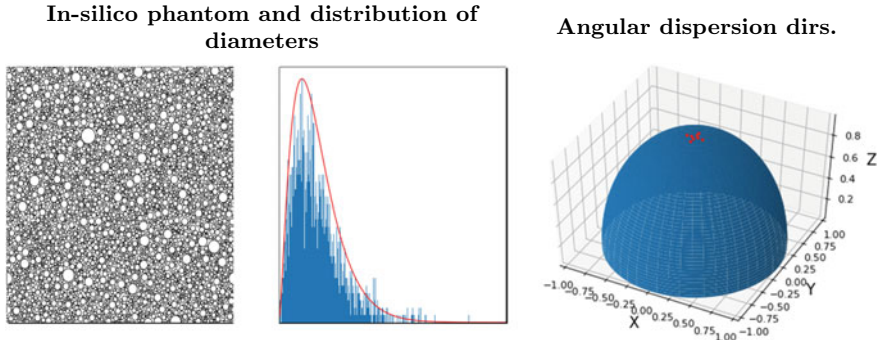


Fig. 2 From left to right, an example of a generated phantom, the resulting distribution of axons after fitting, and the directions used to rotate the main fiber direction to simulate minor angular dispersion

and 4000 s/mm^2 ; $\delta = 7 \text{ ms}$ and echo time (TE) = 80 ms , with an isotropic voxel resolution of 2 mm . For each shell, the Δ time was varied as follows, $\Delta = 17.3, 30, 42, 55 \text{ ms}$. A total of 30 uniformly sampled directions in the sphere were used per different Δ time for the shell with $b\text{-value} = 1000 \text{ s/mm}^2$ and 60 directions for the $b\text{-value} = 4000 \text{ s/mm}^2$. In addition, to include some uncertainty related to the main fiber orientation, 4 additional signals were generated for each phantom by rotating the original signal by 5 degrees in 4 directions around the mean fiber direction. We chose this dispersion by computing the variance of the main fiber direction in a region of interest in the CC from the in-vivo data. The resulting substrates were removed if the packed distribution were not close enough to the desired distribution of diameters, or couldn't reach the desired ICVF. Figure 2 shows an example of a generated distribution, as well as the directions used to rotate the phantom's main direction. In total, the final database consisted of 82,400 white matter phantoms and their DW-MRI signals, which were obtained after generating different realizations of each of the 1824 combinations of $icvf$, μ and σ (Table 1) after pruning.

The in-vivo data were acquired using a 3T Connectome scanner equipped with 300mT/m diffusion gradients and using the same imaging parameters employed to generate the synthetic dataset. The same healthy volunteer subject was scanned 5 times to test the robustness of the method to multiple repetitions.

2.2 Machine Learning

To learn the mapping from simulated signals to microstructural parameters, we implemented three different approaches, relying on either handcrafted features or the raw diffusion signal. To create the handcrafted features, the diffusion signal vector was separated into 8 parts, each one corresponding to a different shell with a specific

combination of the parameters of the imaging protocol used, i.e., Δ , δ and G . Then, for each of these, a Principal Component Analysis was carried out and the first 3 components were selected, which explained more than 98% of the signal variance. In addition, the fractional anisotropy (FA) and the mean diffusivity (MD) were computed and concatenated to the feature vector. The total feature vector signal consisted of $8 * 3 + 2 = 26$ normalized features.

First, we trained a random forest (RF) regressor using the handcrafted features described above. A total of 100 estimator trees with a maximum depth of 17 were used. The random forest parameters were optimized using the Bootstrap aggregation method.

Second, a multi-layer perceptron (MLP) was trained using the same handcrafted features with the following architecture: four dense hidden layers with 129, 32, 16 and 3 units respectively. We used a rectified linear unit (Relu) as the activation function for all layers, with dropout after the first and second layers with probability 0.01. The third layer was regularized using L_2 -based kernel and bias regularization with a coefficient of 0.01. We used the L_2 loss between the predicted and ground truth parameters as the cost function. Finally, Adam optimizer was employed to train the network for 100 epochs with a batch size of 10. We refer to this method as MLP-feat on the rest of the paper.

Third, we trained an MLP using the DW-MRI signal directly, with no feature extraction. The architecture consists of 6 hidden layers with 400, 200, 100, 56, 16 and 3 neurons respectively. The fifth layer is regularized as in the MLP above. Other training details are identical to those used in the MLP above. We refer to this method as MLP-raw to differentiate it from the previous one trained with handcrafted features.

In this study, 80% of the dataset was used for training and validation, while 20% was held-out for testing; 10-fold cross-validation to mitigate overfitting was performed. The three described approaches were tested on both, the held-out synthetic data and five in-vivo DW-MRI images masked into the CC. As a baseline for the in-vivo data, we compare these results with those of the AMICO [4] implementation of ActiveAx [1], using the default regularization parameters and dictionary.

3 Results and Discussion

Figure 3 shows the microstructure parameters estimated by the three ML algorithms from synthetic data. Our main finding is that they are able to accurately estimate both the mean and standard deviation of the axon diameter distributions even for diameters much smaller than those estimated in previous studies (i.e., 2 μm), and using an acquisition protocol employing b-values lower than the conventional ones used for diameter estimation [1, 4]. To explain why the proposed ML techniques can improve the estimation of axons with smaller diameters, it is important to remember that the model-based approaches determine the axon diameter entirely from an intra-axonal model, as the signal from the extra-axonal space is difficult to relate analytically to the underlying microstructure parameters. The limited diffusion contrast of the

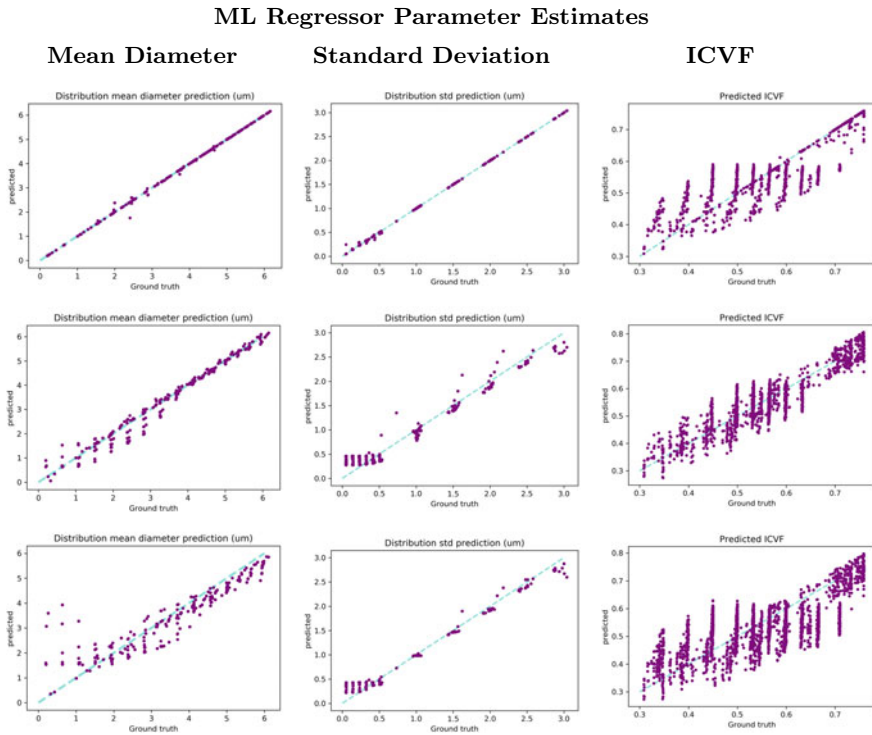


Fig. 3 Estimates of the trained regressors on the validation dataset. From top to bottom, results for the Random Forest (top), MLP trained with hand crafted features (middle row), and the MLP trained with the raw signal (bottom). From left to right, ground truth versus the estimated parameters on the validation dataset for the mean diameter, the standard deviation, and the ICVF respectively

DW-MRI signal from the intra-axonal space along the direction perpendicular to the fibers hampers the estimation of axons with small diameters. In contrast, applying ML techniques to the whole signal allows finding hidden non-trivial and nonlinear relationships between the microstructure parameters and the DW-MRI signal from both the intra- and the extra-axonal spaces. As the properties of the diffusion process in the extra-axonal space (i.e., mean displacement length, tortuosity, time-dependent diffusion) are highly influenced by the microstructure features of the intra-axonal space, the ML algorithms can exploit this additional information. Another important factor is that, by defining a specific distribution of axon diameters in our forward model, the ML algorithms could predict the full distribution using only the information from the right-tail of the distribution, which is not affected by the contrast/resolution problem mentioned before.

Table 2 shows the mean absolute error of the three parameters estimated on the noise-free test dataset. From Fig. 3 and Table 2, we can see that the RF regressor has the best accuracy for all three parameters, with ICVF the most difficult parameter to

Table 2 Mean absolute error (MAE) on the cross validation dataset for the three trained classifiers: RF, MLP trained with feature vectors, and MLP trained with the raw signal

Cross validation MAE		
RF feat.	MLP feat.	MLP raw
0.028	0.070	0.134

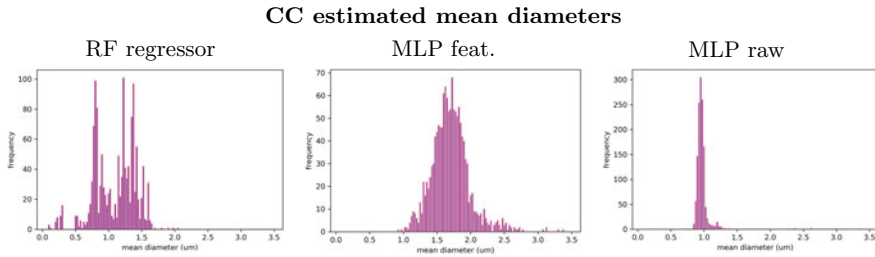


Fig. 4 Joint histogram of the estimated mean diameters in the segmented mask of the CC across 5 scans for (from left to right) the RF regressor, MLP-feat and the MLP-raw. Each histogram was computed using the combined estimates of the 5 in-vivo scans

estimate. Both MLP methods had good accuracy during training but lower accuracy on the test dataset than the RF regressor (Fig. 4).

Figure 5 shows the estimated mean diameter (mD) maps for two arbitrarily selected scans from the in-vivo data, in the same anatomical cross-section for the three methods. For each ML regressor, the parameter estimates are quite consistent over the five images used; that is, the values and the anatomical locations of small or large mean diameters are similar across scans. In addition, we show the axon’s diameter maps computed with AMICO-ActiveAx, which are notably higher than those from the ML methods. Is important to notice however that the used protocol is far from idoneous for the former method—which requires b-values as high as $b = 9,000 \text{ s/mm}^2$ in ex-vivo conditions [5] to estimate mean axon diameters below 2 um—and thus, such over-estimation is expected.

Figure 4 depicts the histograms of the estimated mean diameters. There is a noticeable variability between the parameter estimates of two different regressors. This is important as this lack of consensus between regressors implies that at least one must be biased and shows how three different estimators, with similar performance and accuracy in in-silico data, can estimate remarkably different distributions in in-vivo data. This is likely to be and effect of several compartments not included in our training data: axonal tortuosity and diameter changes, or even T2 relaxation or artifacts effects. Therefore, this study will benefit of including such effects during the training. Or the use of more advanced machine learning models [10]. Notably however, while all ML models predicted mean diameters with magnitudes close—

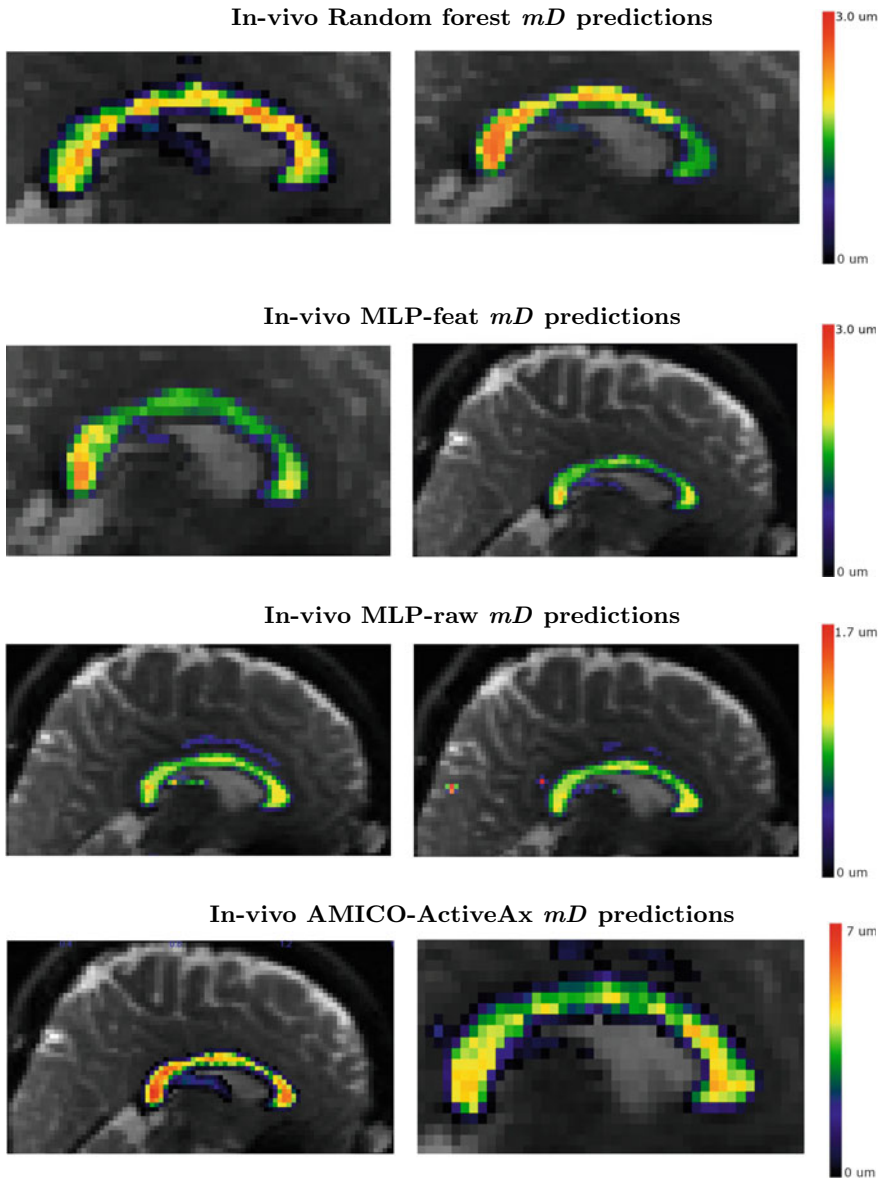


Fig. 5 Midsagittal plane of the estimation maps for two subjects (showed from posterior to anterior). The colorbars were adjusted per model to highlight the regions with higher and lower values. In one of the MLP-raw predictions it can be notice the presence of a notorious outlayer values in regions voxels outside the CC

but still higher—from the ones extracted from histology, the trend in mean diameter on the genu, truncus and splenium of the CC predicted by the RF regressor (i.e., the optimal one in synthetic data) matches that from a previous study on electron-microscopy for the distribution of axon diameters in cortical white matter [8].

4 Conclusions

The main focus of this work is the introduction of a emerging simulation-based technique for the microstructural parameter estimation; from the construction of a large dataset of realistic numerical phantoms to training machine learning algorithms on the corresponding simulated signals. A comprehensive dataset accounting for a wide variety of parameters characterizing axon packing and size, as well as small angular dispersion mimicking that which occurs in the CC was generated. We demonstrated that machine learning models with and without handcrafted features can accurately recover the mean and standard deviation of the axon diameter distribution on synthetic data and from DW-MRI data with moderately high b-values (4000 s/mm²). The proposed approach allowed us to estimate, for the first time, the number-weighted distribution of axon diameters, which cannot be estimated with previous DW-MRI modeling techniques. As this is the distribution conventionally reported in histological studies, this study may help to fill the gap between in-vivo DW-MRI and postmortem histology. Furthermore, once trained, machine learning models require a few seconds of computation time for estimating the microstructure parameters in the whole-brain white matter. Finally, the in-vivo results show consistent trends and values for all 5 subject scans with the same ML model, however, there are qualitative differences between the different models that should be explored in future studies. Our findings show that values reported in the CC for all ML models are close to those found in histology, with the RF regressor further replicating the expected spatial trend in mean diameter [8]. It is important to mention, however, that in this work a simplified model of the CC microstructure is employed by considering a 2 compartment model which assumes that axons are completely straight cylinders, without micro-dispersion along the axons. Nevertheless, since it is straightforward to generate more realistic phantoms (e.g. axons with undulations and angular dispersion) and simulate the corresponding DW-MRI signals using state-of-the-art MC simulators, both limitations can be addressed in the future by generating more complex axon configurations without significantly modifying the machine learning models and related parameters. Future in-silico validations will be conducted to evaluate the robustness of the method as a function of the signal-to-noise ratio and acquisition protocol.

Acknowledgments This work was supported by EPFL through the use of the facilities of its Scientific IT and Application Support Center. We gratefully acknowledge the support of NVIDIA Corporation with the donation of the Titan Xp GPU used for this research. This work is supported by the Swiss National Science Foundation under grant number CRSII5_170873 (Sinergia project).

References

1. Alexander, D.C., Hubbard, P.L., Hall, M.G., Moore, E.A., Ptito, M., Parker, G.J., Dyrby, T.B.: Orientationally invariant indices of axon diameter and density from diffusion MRI. *NeuroImage* (2010). <https://doi.org/10.1016/j.neuroimage.2010.05.043>
2. Assaf, Y., Basser, P.J.: Composite hindered and restricted model of diffusion (CHARMED) MR imaging of the human brain. *NeuroImage* (2005). <https://doi.org/10.1016/j.neuroimage.2005.03.042>
3. Assaf, Y., Blumenfeld-Katzir, T., Yovel, Y., Basser, P.J.: AxCaliber: a method for measuring axon diameter distribution from diffusion MRI. *Magn. Reson. Med.* (2008). <https://doi.org/10.1002/mrm.21577>
4. Daducci, A., Canales-Rodríguez, E.J., Zhang, H., Dyrby, T.B., Alexander, D.C., Thiran, J.P.: Accelerated Microstructure Imaging via Convex Optimization (AMICO) from diffusion MRI data. *NeuroImage* (2015). <https://doi.org/10.1016/j.neuroimage.2014.10.026>
5. Dyrby, T.B., Sagarad, L.V., Hall, M.G., Ptito, M., Alexander, D.C.: Contrast and stability of the axon diameter index from microstructure imaging with diffusion mri. *Magn. Reson. Med.* **70**(3), 711 (2013). <https://doi.org/10.1002/mrm.24501>
6. Hall, M.G., Alexander, D.C.: Convergence and parameter choice for monte-carlo simulations of diffusion mri. *IEEE Trans. Med. Imaging* **28**(9), 1354–1364 (Sep 2009). <https://doi.org/10.1109/TMI.2009.2015756>
7. Jelescu, I.O., Veraart, J., Fieremans, E., Novikov, D.S.: Degeneracy in model parameter estimation for multi-compartmental diffusion in neuronal tissue. *NMR Biomed.* **29**(1), 33–47 (2016). <https://doi.org/10.1002/nbm.3450>
8. Liewald, D., Miller, R., Logothetis, N., Wagner, H.J., Schüz, A.: Distribution of axon diameters in cortical white matter: an electron-microscopic study on three human brains and a macaque. *Biol. Cybern.* (2014). <https://doi.org/10.1007/s00422-014-0626-2>
9. Nedjati-Gilani, G.L., Schneider, T., Hall, M.G., Cawley, N., Hill, I., Ciccarelli, O., Drobnyak, I., Wheeler-Kingshott, C.A., Alexander, D.C.: Machine learning based compartment models with permeability for white matter microstructure imaging. *NeuroImage* **150**, 119–135 (2017). <https://doi.org/10.1016/j.neuroimage.2017.02.013>
10. Rafael-Patino, J., Barakovic, M., Girard, G., Daducci, A., Thiran, J.P.: Learning global brain microstructure maps using trainable sparse encoders (2019). <http://infoscience.epfl.ch/record/265398>
11. Rafael-Patino, J., Romascano, D., Ramirez-Manzanares, A., Canales-Rodríguez, E.J., Girard, G., Thiran, J.P.: Robust monte-carlo simulations in diffusion-MRI: effect of the substrate complexity and parameter choice on the reproducibility of results (2019). <https://doi.org/10.3389/fninf.2020.00008>, <https://www.frontiersin.org/articles/10.3389/fninf.2020.00008/full>
12. Rensonnet, G., Scherrer, B., Girard, G., Jankovski, A., Warfield, S.K., Macq, B., Thiran, J.P., Taquet, M.: Towards microstructure fingerprinting: estimation of tissue properties from a dictionary of monte carlo diffusion mri simulations. *NeuroImage* **184**, 964–980 (2019). <https://doi.org/10.1016/j.neuroimage.2018.09.076>, <http://www.sciencedirect.com/science/article/pii/S1053811918319487>
13. Seppehrband, F., Alexander, D.C., Clark, K.A., Kurniawan, N.D., Yang, Z., Reutens, D.C.: Parametric probability distribution functions for axon diameters of corpus callosum. *Frontiers Neuroanat.* (2016). <https://doi.org/10.3389/fnana.2016.00059>
14. Yu, T., Pizzolato, M., Girard, G., Rafael-Patino, J., Canales-Rodríguez, E.J., Thiran, J.P.: Robust biophysical parameter estimation with a neural network enhanced hamiltonian markov chain monte carlo sampler. In: Chung, A.C.S., Gee, J.C., Yushkevich, P.A., Bao, S. (eds.) *Information Processing in Medical Imaging*, pp. 818–829. Springer International Publishing, Cham (2019)
15. Zhang, H., Schneider, T., Wheeler-Kingshott, C.A., Alexander, D.C.: NODDI: Practical in vivo neurite orientation dispersion and density imaging of the human brain. *NeuroImage* **61**(4), 1000–1016 (2012)

Convolutional Neural Network on DTI Data for Sub-cortical Brain Structure Segmentation



G. R. Pinheiro, D. S. Carmo, C. Yasuda, R. A. Lotufo, and L. Rittner

Abstract Convolutional neural networks have become a powerful tool for MRI brain analysis and are the state-of-the-art in the matter of brain structure segmentation. Despite the deep learning power and advantages, most of the work is still done in classical methods, such as atlas based segmentation. The majority of those methods also uses only anatomical MRI sequences, e.g. T1- and T2-weighted images, however, other sequences of MRI could lead to much more interesting results. In this work, we are proposing the use of Convolutional Neural Networks, in a multitask approach, which is a tendency to the deep learning community, in order to segment a variety of brain structures. We used over 100 subjects with 32 directions diffusion data and manual annotation, drawn on T1 images, of 8 different brain structures. We have tested variations in the CNN architecture and input data configurations to ensure the best performance. Our results show the results of a particular CNN to segment sub-cortical structures such as Ventricle, Thalamus, Putamen, and Caudate Nucleus.

1 Introduction

Convolutional Neural Networks (CNNs) are the state-of-the-art in the field of brain structure segmentation. The current reported results, using anatomical Magnetic Resonance Images (MRI), are above 0.9 DICE similarity coefficient [6], while before the CNNs, in the same type of images, common values for DICE were around 0.8 [14].

Despite great advances in CNN-based brain structures segmentation, this task is still broadly done with classical methods, such as atlas-based, in public and commercial tools, for example in FreeSurfer [8]. Those tools have a good performance, however results could be as low as 0.65 DICE for some structures, e.g., accumbens, amygdala, and others, while taking many hours to process a single brain image.

G. R. Pinheiro (✉) · D. S. Carmo · C. Yasuda · R. A. Lotufo · L. Rittner
University of Campinas, Campinas, São Paulo, Brazil
e-mail: gustavo_r_p@hotmail.com; gustavorp@dca.fee.unicamp.br

Another advantage of the CNNs over other methods is the computational cost. Deep learning algorithms do require Graphic Cards, huge amounts of data, and so on during the training step. However, the prediction (or segmentation) on a trained model has lower requirements. For instance, a CNN model can segment a volume within seconds [2] even on a mobile system, such as tablets, while atlas-based segmentation could take hours on a server [15]. This advantage could be very helpful in the clinical environment as the image processing is done instantaneously after data acquisition.

In both approaches, classical and CNNs, the majority of the methods uses anatomical images, mainly T1-weighted and T2-weighted MRI [3, 14, 16, 26]. However, other MRI sequences such as diffusion sequences, that carry other than tissue contrast information, could lead to more interesting results.

Also, there are research and clinical applications that require only diffusion data, e.g. stroke early detection [21, 22]. In those cases, being able to segment structures exclusively on diffusion data could lead to shorter scan protocols by eliminating the acquisition of T1- or T2-weighted images, for example.

In this work, we are investigating the ability of a CNN of segmenting sub-cortical structure using only data derived from Diffusion MRI. We have chosen to use a U-Net like architecture [18] as it is the state-of-the-art in brain structures segmentation and can be customized to work with diffusion data.

This paper is organized as follows: the dataset and its properties are presented in Sect. 2. The methodology, including registration, DTI processing, training, and testing are presented in Sect. 3. The experimental setup and results are presented in Sect. 4 and discussed in Sect. 5. Our conclusions are presented in Sect. 6.

2 Dataset

The dataset was originally composed of 134 folders among controls, epilepsy patients, and postoperative epilepsy patients [25]. However, 13 of them were discarded due to failed registration. From the rest, 103 were used for the validations and training while 18 were used for the CNN models testing. Data acquisition was approved by the ethics committee and all patients and healthy controls provided written informed consent.

Each folder contained the T1 image, the structures segmentation (performed on the T1 image), and the Diffusion Weighted Images (DWI) with 32 gradient directions plus a $B0$ image. The DWI acquisition parameters were: Philips ACHIEVA 3T, 2 mm between slices, $1 \times 1 \times 2$ mm voxel, DwiSE sequence, and $b = 1000$ s/mm². The DWI volumes were also corrected to eddy currents and subject motion.

All images were registered to the MNI-152 [9] space with $1 \times 1 \times 1$ mm voxel size using the FSL registration tool [12]. After registration, they were visually inspected and 13 subjects were removed due to bad registration, caused mainly by artifacts and severe atrophy.

Each data was associated to segmentation of 16 structures, 8 from each hemisphere (Fig. 1): ventricle, caudate, putamen, thalamus, globus pallidus, hippocampus,

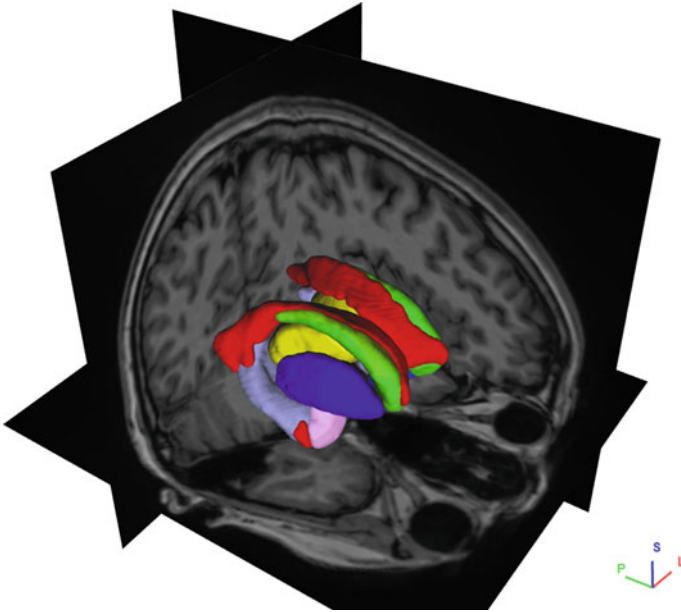


Fig. 1 Manual segmentation of ventricle, caudate, putamen, thalamus, globus pallidus, hippocampus, amygdala, and accumbens over T1-weighted image in the native space. Each color represents a different label

amygdala, and accumbens. Each pair was assigned with a single label, as they are symmetrical and indifferent to the CNN perspective. They were all manually segmented by a specialist in the T1 native space.

3 Methodology

3.1 Registration

In order to achieve the best results in the deep learning training, the ground-truth and the diffusion data must be very well positioned and scaled, since the ground-truth is generated in the T1 space. Therefore, there is a need for translating the diffusion images and the masks to a common space, aligning the manual structures annotations to the diffusion data. This procedure was done with a few steps.

The first step in the registration is the brain extraction (BET) for diffusion and the T1 images, also done in the FSL tool. After the BET step, all T1 images, and their respective structures segmentations were registered to the standard space MNI-152 ($1 \times 1 \times 1$ mm). The last step was to register the diffusion data to their respective T1 images that were previously registered to the standard space.

These steps might introduce propagating errors, and the resulting alignment is not perfect with the masks. However, they are necessary since the diffusion data has no associated manual annotations.

3.2 DTI Processing

Once we had the diffusion and the ground truth in the same space, we could compute the Diffusion Tensor Images (DTI), and then, the scalar maps derived from it. In this work, we used the Fractional anisotropy (FA), Mean Diffusivity (MD), mode of anisotropy (MO), and a non diffusion weighted volume (B0) [7].

After the computation of the scalar maps, each map was normalized (0–1) and used as a channel, forming a 4-channel volume input for the CNN.

3.3 Patch Selection

In order to increase the amount of data and also to balance the amount of each structure, we used patches (Fig. 2) in the training.

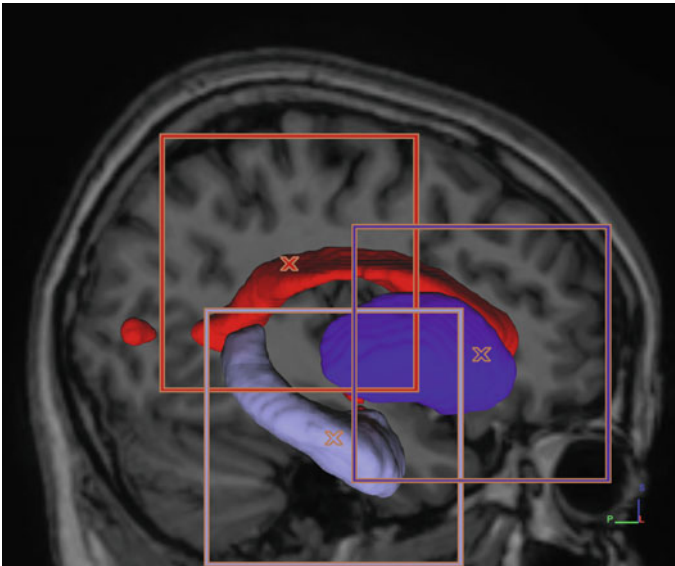


Fig. 2 Patch selection in the sagittal view: 64×64 voxels patches centered within the ventricle (red), putamen (blue), and hipocampus (gray)

To ensure that the same number of patches of each structure would be selected, the center of the patches were placed within the volume of the structure mask the same number of times for each structure. Furthermore, patches centered outside of all masks were taken to ensure that the model would learn what is not the target structures.

As an example, we could have a proportion of 3 patches centered in a non mask region, 5 patches centered in the putamen, 5 patches centered in the hippocampus, and so on. In this case we could call it as a 3/5 patch balance.

3.4 CNN Architecture

In this work, we built our CNN architecture based on the U-Net [18], which has been showing state-of-the-art results in brain structures segmentation [1, 4, 20].

Most of the works apply some modifications to the original 2015 architecture in order to achieve even better results. We also added a variety of improvements to the CNN creating a custom U-Net (Fig. 3).

Batch normalization has been shown to improve convergence and in some cases validation results [11], thus, we have added this feature to our U-Net. Leaky ReLU

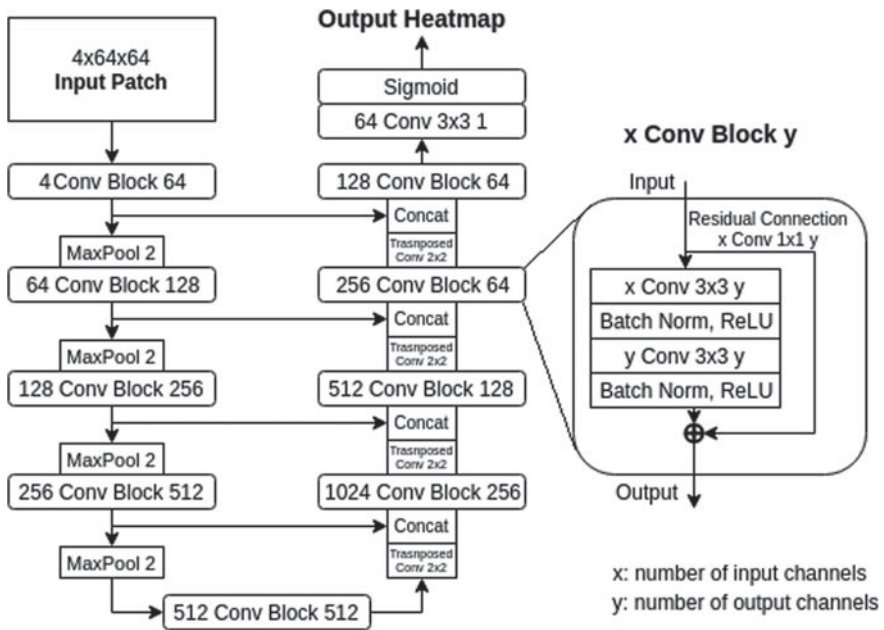


Fig. 3 Custom CNN architecture based on the U-Net. Main modifications were: residual connections, Leaky ReLU activations and batch normalization [2]

Table 1 Description of the applied data augmentations

Augmentation level	Description
0	No augmentation
1	Random intensity variation, random affine transformation
2	Same as 1, with more aggressive parameters

activations are also used in opposition to original ReLU. This new activation function uses a small negative slope for the negative values instead of only saturating in zero. This kind of activation can mainly improve performance and convergence in relation to the classic ReLU [24]. The last significant customization to the U-Net was the use of residual connection blocks, which was originally used in ResNet [10]. The use of residual or skip connections is useful, as, empirically speaking, they present a more linear “path” for the data, in cases where a shortcut improves the results.

3.5 Training

The training was done over mini batches of patches, and prediction over multi-channel 2D slices.

We also used data augmentation during the CNN training. The data augmentation was applied at 3 different levels (Table 1). In more details, augmentation 1 always applies a random intensity variation of -0.1 to $+0.1$, and the random affine performs a rotation by -20 to 20° and image scale of -20 to 20% . Augmentation 2 follows augmentation 1 but doubling every argument (0.2 intensity, and 40 rotation and scale).

Comparisons were performed between different optimizers and training parameters. After studying different parameters for patch extraction, we had access to 28 more volumes that were included for patch extraction.

The last consideration is that the training is performed in all structures included in the dataset or in only the 4 bigger structures, for comparison. This configures a multitask approach which has become a tendency in deep learning [19] as it improves the overall results and reduces overfitting.

3.6 Testing

The performance of each CNN model was tested in a specific test group of 18 subjects that was not used in the training phase to ensure the test is trustworthy.

The test was done in the complete MRI volumes as the U-Net is a Fully Convolutional Neural Network (FCNN) and can handle many input sizes. As we used a 2D version of the U-Net, the test volumes predictions are generated by stacking the

prediction of every slice and the DICE is computed over the resulting 3D predictions and the volume's masks.

It is important to notice that only the 4 biggest structures, Ventricle, caudate, putamen and thalamus, are considered to the model testing results.

4 Experiments and Results

In the experiments reported here, DICE is calculated accounting all channels, unless otherwise noted. Also note that they do not involve any post processing step, only the direct output of the CNN, as the interest is to study the response of the CNN to DTI data in this particular segmentation task.

Preliminary experiments with ADAM [13] and SGD as optimizers gave similar results, and SGD was chosen. With those experiments, the following training hyperparameters were fixed: maximum of 500 epochs; 0.01 initial learning rate (LR); LR is multiplied by a factor of 0.9 every 50 epochs; 50 epochs patience as a stop criteria. Another preliminary experiment was finding the best range for minmax voxel intensity normalization to use, $[0, 1]$ or $[-1, 1]$. $[0, 1]$ was chosen for the next experiments due to around 2% better validation results, evaluated over validation patches. After these experiments, network architecture, optimizer, and normalization parameters were kept unchanged for the next experiments.

In the next experiment, using 75 subjects, we have changed the hyperparameters related to training input data (Table 2): patch sizes of 32×32 or 64×64 ; different patch balances, as described in Sect. 3.3; different augmentation levels. The best combination is found to be 64×64 patches with 5/15 patch balance and augmentation level 2.

With those parameters fixed, and now with 28 more volumes (103 in total) generating patches for training, more tests were performed over different orientations (axial, sagittal and coronal), and with the inclusion of T1 data on input channels (Table 3). There is a notable performance improvement with the addition of more training data, going from 0.82 to 0.89 in DICE values. Also, it is clear that the sagittal is the best

Table 2 Test DICE over different patches sizes, patch balance, and augmentation parameters

Patch size	Patch balance	Augmentation level	DICE
32	5/10	2	0.6961
64	3/5	2	0.6614
64	5/10	2	0.8181
64	5/15	0	0.8142
64	5/15	1	0.8226
64	5/15	2	0.8237
64	5/15	3	0.8186

Table 3 DICE coefficient for different volume orientations

Slice orientation	Input	DICE
Axial	DTI	0.7779
Coronal	DTI	0.8829
Sagittal	DTI	0.8864
Sagittal	T1	0.9650
Sagittal	DTI and T1	0.9638

orientation for slice extraction following our methodology. We can also see that T1 exclusively, and DTI plus T1, presented the best DICE values, around 0.96.

Up to this point, training patches were centered on all 8 structures of the dataset, and test only performed on the 4 bigger structures. Smaller structures were not included in test evaluation due to early experiments showing no convergence to good segmentations on them. As a last experiment, training patches were only centered on the 4 bigger structures: putamen, ventricle, thalamus and caudate. The result of this experiment is that including only the bigger structures for patch selection resulted in around 2% worse performance, even though they are not included in the test evaluation. This shows that learning information about the smaller structures, even when their predictions are not good, contributes to the model as a whole (Fig. 4 and 5).

Another relevant result in the test data is the DICE value for each of the 4 tested structures (Fig. 6). Using our best CNN model with only DTI, we can see that the ventricle is the hardest structure and the thalamus is the easiest for the model to learn in this dataset with our methodology. Although that may seem counter-intuitive as the ventricle is the biggest segmented structure, it is caused by the complexity in the ventricle shape. The used protocol for manual segmentation makes the ventricle a

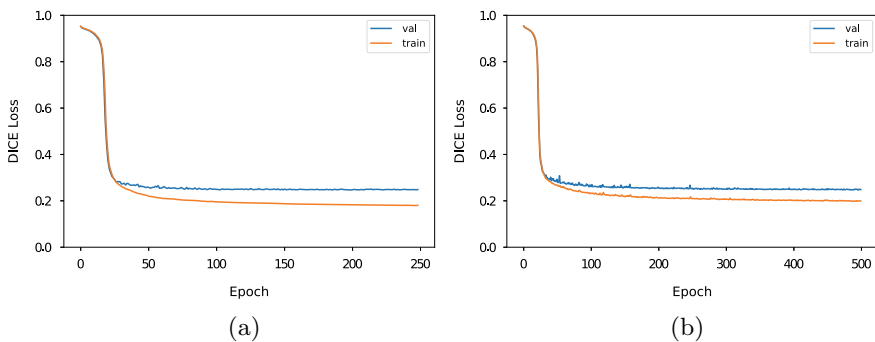


Fig. 4 Training loss curves for comparison of data augmentation levels: **a** No augmentation; **b** Augmentation level 2. The different number of epochs is due to the patience stop criteria ending the training earlier because of no validation improvement for 50 epochs

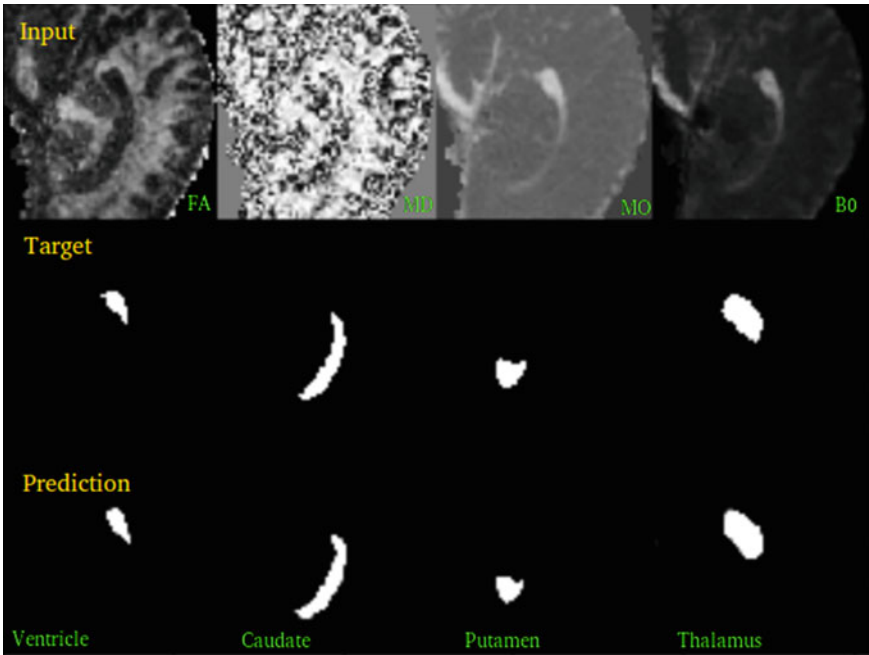


Fig. 5 Visual comparison between 2D targets and predictions, using our best DTI only model

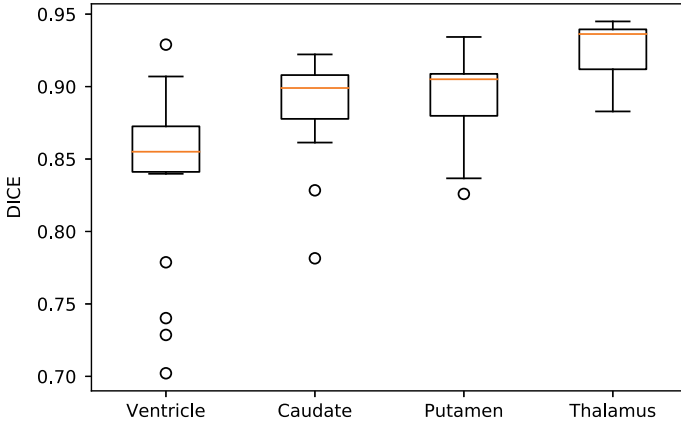


Fig. 6 DICE distribution per tested structure, over all test volumes, using the DTI only input model

disconnected volume of two sections, anterior (bigger portion) and posterior (smaller portion) (Figs. 1, 2, and 5), making it harder to segment when compared to the Thalamus that is mostly a round connected volume.

5 Discussion

Results show some interesting points of analysis for segmentation with DTI data. The improvements in training and in results are noticeable when using augmentation (Fig. 4), with slightly overfitting reduction, as in most machine learning applications.

Regarding patch sizes, 64×64 had better results than 32×32 . Empirically, we believe that this is because a bigger patch size includes more of the relatively big structures, especially because we are testing exclusively on them. Regarding patches balance, the inclusion of more patches centered in random points of the structures instead of random patches was positive to the results. Models with fewer patches around structures tended to undersegment.

One interesting characteristic of this work is learning from a total of 8 structure labels, but testing performance for only the four bigger structures (Fig. 5). It was verified that performance is worsened when training only in the four tested structures, under the same hyperparameters.

When T1 data are involved in the training, the results are improved (Table 3). This is expected due to it being the original source of the manual segmentation. Also, as hypothesized before, pre-disclosed registering of DTI data introduces an error that is being propagated to the final results. This leads to the conclusion that the registration among the different MRI sequences is very critical to this application, limiting the improvement of the algorithm.

As we are investigating the ability of CNNs on subcortical structures segmentation task using diffusion images, it is hard to compare to other segmentation methods on diffusion images since most of them are focused on white matter [5, 17] or on lesions [23]. In fact, this is one of the first works that segment multiple sub-cortical structures using deep learning on diffusion images only.

Finally, we can also see that the model has room for improvement if fed with more data, as the sagittal results improved significantly after the addition of more subjects.

6 Conclusion

We evaluated the segmentation of brain sub-cortical structures using a modified version of U-Net (CNN architecture). Diffusion data were registered to the same space as T1 masks and used as input channels. The network behavior was studied with different hyperparameters.

Although the obtained segmentation results using only DTI as input for the CNN were inferior to the results using also T1 images, the proposed CNN was able to learn the features from the diffusion data even with no clear visual distinction between the target structures and other tissues. Results were qualitatively and quantitatively good, with a mean DICE coefficient of 0,8864. In applications where the acquisition and processing times must be reduced, an approach as described in this paper is one of the most suitable choices.

There are also room for improvements since some poor results were due to registration problems. The manual segmentation used as ground truth to train the CNN was obtained in T1 native space and there are many sensitive steps to register all data to the same reference. Future work might investigate better registration methodologies and usage of different DTI maps.

Acknowledgments This project was supported by National Council for Scientific and Technological Development (CNPq 159829/2017-8 and 308311/2016-7) and Teaching, Research and Extension Support Fund (FAEPEX-UNICAMP). Diedre Carmo thanks FAPESP (2018/00186-0) for the scholarship.

References

1. Bui, T.D., Shin, J., Moon, T.: 3d densely convolutional networks for volumetric segmentation (2017). [arXiv:1709.03199](https://arxiv.org/abs/1709.03199)
2. Carmo, D., Silva, B., Yasuda, C., Rittner, L., Lotufo, R.: Extended 2d consensus hippocampus segmentation. In: International Conference on Medical Imaging with Deep Learning (2019)
3. Chang, H.H., Hsieh, C.C.: Brain segmentation in mr images using a texture-based classifier associated with mathematical morphology. In: 2017 39th Annual International Conference of the IEEE Engineering in Medicine and Biology Society (EMBC), pp. 3421–3424. IEEE (2017)
4. Çiçek, Ö., Abdulkadir, A., Lienkamp, S.S., Brox, T., Ronneberger, O.: 3d u-net: learning dense volumetric segmentation from sparse annotation. In: International Conference on Medical Image Computing and Computer-assisted Intervention, pp. 424–432. Springer, Berlin (2016)
5. Cover, G., Pereira, M., Bento, M., Appenzeller, S., Rittner, L.: Data-driven corpus callosum parcellation method through diffusion tensor imaging. *IEEE Access* **5**, 22421–22432 (2017). <https://doi.org/10.1109/ACCESS.2017.2761701>
6. Duarte, J.M., Santos, J.B.d., Melo, L.C.: Comparison of similarity coefficients based on rapid markers in the common bean. *Genet. Mol. Biol.* **22**(3), 427–432 (1999)
7. Ennis, D.B., Kindlmann, G.: Orthogonal tensor invariants and the analysis of diffusion tensor magnetic resonance images. *Magn. Reson. Med.* **55**(1), 136–146 (2006). <https://doi.org/10.1002/mrm.20741>
8. Fischl, B.: Freesurfer. *Neuroimage* **62**(2), 774–781 (2012). <https://doi.org/10.1016/j.neuroimage.2012.01.021>
9. Fonov, V., Evans, A.C., Botteron, K., Almlí, C.R., McKinstry, R.C., Collins, D.L., Group, B.D.C., et al.: Unbiased average age-appropriate atlases for pediatric studies. *Neuroimage* **54**(1), 313–327 (2011). <https://doi.org/10.1016/j.neuroimage.2010.07.033>
10. He, K., Zhang, X., Ren, S., Sun, J.: Deep residual learning for image recognition. In: Proceedings of the IEEE Conference on Computer Vision and Pattern Recognition, pp. 770–778 (2016)
11. Ioffe, S., Szegedy, C.: Batch normalization: Accelerating deep network training by reducing internal covariate shift (2015). [arXiv:1502.03167](https://arxiv.org/abs/1502.03167)
12. Jenkinson, M., Beckmann, C.F., Behrens, T.E., Woolrich, M.W., Smith, S.M.: Fsl. *Neuroimage* **62**(2), 782–790 (2012). <https://doi.org/10.1016/j.neuroimage.2011.09.015>
13. Kingma, D.P., Ba, J.: Adam: A method for optimization (2014). [arXiv:1412.6980](https://arxiv.org/abs/1412.6980)
14. Kushibar, K., Valverde, S., González-Villà, S., Bernal, J., Cabezas, M., Oliver, A., Lladó, X.: Automated sub-cortical brain structure segmentation combining spatial and deep convolutional features. *Med. Image Anal.* **48**, 177–186 (2018). <https://doi.org/10.1016/j.media.2018.06.006>
15. Manj, J.V., Coup, P.: volbrain: An online mri brain volumetry system. *Frontiers Neuroinform.* **10**, 30 (2016). <https://doi.org/10.3389/fninf.2016.00030>

16. Mehta, R., Sivaswamy, J.: M-net: a convolutional neural network for deep brain structure segmentation. In: 2017 IEEE 14th International Symposium on Biomedical Imaging (ISBI 2017), pp. 437–440. IEEE (2017)
17. Pomiecko, K., et al.: 3d convolutional neural network segmentation of white matter tract masks from mr diffusion anisotropy maps. In: 2019 IEEE 16th International Symposium on Biomedical Imaging (ISBI 2019), pp. 1–5 (2019). <https://doi.org/10.1109/ISBI.2019.8759575>
18. Ronneberger, O., Fischer, P., Brox, T.: U-net: Convolutional networks for biomedical image segmentation. In: International Conference on Medical Image Computing and Computer-Assisted Intervention, pp. 234–241. Springer, Berlin (2015)
19. Wachinger, C., Reuter, M., Klein, T.: Deepnat: deep convolutional neural network for segmenting neuroanatomy. *NeuroImage* **170**, 434–445 (2018)
20. Wang, G., Li, W., Ourselin, S., Vercauteren, T.: Automatic brain tumor segmentation using convolutional neural networks with test-time augmentation. In: International MICCAI Brainlesion Workshop, pp. 61–72. Springer, Berlin (2018)
21. Warach, S., Chien, D., Li, W., Ronthal, M., Edelman, R.R.: Fast magnetic resonance diffusion-weighted imaging of acute human stroke. *Neurology* **42**(9), 1717–1717 (1992). <https://doi.org/10.1212/WNL.42.9.1717>
22. Warach, S., Gaa, J., Siewert, B., Wielopolski, P., Edelman, R.R.: Acute human stroke studied by whole brain echo planar diffusion-weighted magnetic resonance imaging. *Ann. Neurol.* **37**(2), 231–241 (1995). <https://doi.org/10.1002/ana.410370214>
23. Winzeck, S., et al.: Ensemble of convolutional neural networks improves automated segmentation of acute ischemic lesions using multiparametric diffusion-weighted mri. *Am. J. Neuro-radiol.* (2019). <https://doi.org/10.3174/ajnr.A6077>
24. Xu, B., Wang, N., Chen, T., Li, M.: Empirical evaluation of rectified activations in convolutional network (2015). [arXiv:1505.00853](https://arxiv.org/abs/1505.00853)
25. Yasuda, C., et al.: Dynamic changes in white and gray matter volume are associated with outcome of surgical treatment in temporal lobe epilepsy. *Neuroimage* **49**(1), 71–79 (2010)
26. Van der Lijn, F., et al.: Automated brain structure segmentation based on atlas registration and appearance models. *IEEE Trans. Med. Imaging* **31**(2), 276–286 (2011). <https://doi.org/10.1109/TMI.2011.2168420>

Diffusion MRI Outside the Brain and Clinical Applications

A Framework to Construct a Longitudinal DW-MRI Infant Atlas Based on Mixed Effects Modeling of dODF Coefficients



Heejong Kim, Martin Styner, Joseph Piven, and Guido Gerig

Abstract Building of atlases plays a crucial role in the analysis of brain images. In scenarios where early growth, aging or disease trajectories are of key importance, longitudinal atlases become necessary as references, most often created from cross-sectional data. New opportunities will be offered by creating longitudinal brain atlases from longitudinal subject-specific image data, where explicit modeling of subject's variability in slope and intercept leads to a more robust estimation of average trajectories but also to estimates of confidence bounds. This work focuses on a framework to build a continuous 4D atlas from longitudinal high angular resolution diffusion images (HARDI) where, unlike atlases of derived scalar diffusion indices such as FA, statistics on dODFs is preserved. Multi-scalar images obtained from DW images are used for geometric alignment, and linear mixed-effects modeling from longitudinal diffusion orientation distribution functions (dODF) leads to estimation of continuous dODF changes. The proposed method is applied to a longitudinal dataset of HARDI images from healthy developing infants in the age range of 3 to 36 months. Verification of mixed-effects modeling is obtained by voxel-wise goodness of fit calculations. To demonstrate the potential of our method, we display changes of longitudinal atlas using dODF and derived generalized fractional anisotropy (GFA) of dODF. We also investigate white matter maturation patterns in genu, body, and splenium of the corpus callosum. The framework can be used to build an average dODF atlas from HARDI data and to derive subject-specific and population-based longitudinal change trajectories.

H. Kim (✉) · G. Gerig

Department of Computer Science and Engineering, New York University, NY, USA
e-mail: heejong.kim@nyu.edu

M. Styner · J. Piven

Department of Psychiatry, University of North Carolina, Chapel Hill, NC, USA

M. Styner

Department of Computer Science, University of North Carolina, Chapel Hill, NC, USA

© Springer Nature Switzerland AG 2020

E. Bonet-Carne et al. (eds.), *Computational Diffusion MRI*,

Mathematics and Visualization, https://doi.org/10.1007/978-3-030-52893-5_13

1 Introduction

Statistical brain atlases have become important models to provide standards to measure structural variations in anatomy, to define a common coordinate system for spatial correspondence between subjects, and as priors to segment brain structures. As diffusion weighted (DW) imaging yields micro-structural information, several studies have been proposed to construct DW atlases [2, 4, 8, 9, 12, 14, 15]. Atlas building in DW imaging is challenging in that we need to consider diffusivity represented by multiple directional volumes rather than scalar images. Previous studies used diffusion tensor modeling [15] and high order diffusion distribution for high angular resolution diffusion imaging (HARDI) data [2, 4, 12, 14] to construct atlases using DW images. In a longitudinal DW atlas based on subject-specific longitudinal data, atlas building is more challenging as one faces temporal changes in addition to structural variability of sets of directional volumes. There are recently published works to build atlases with longitudinal HARDI images using fractional anisotropy (FA) maps and patch fusion to provide an early brain development atlas of infants [8] or considering multi-tissue time- and orientation-resolved group average atlases [9]. These studies, however, focus on building a template which reflects temporal differences of different age groups but not on building a fully continuous longitudinal atlas.

In this article, we introduce a new framework to construct a continuous longitudinal DW infant atlas based on linear mixed effects (LME) modeling of diffusion orientation distribution function (dODF) coefficients. The framework starts with building a multivariate HARDI template using FA and baseline images. We transform HARDI series to the template space with a reorientation step [13]. Spherical harmonics (SH) coefficients are used to represent dODFs and for LME modeling of HARDI image time series. Considering repeated image data from longitudinal subject image series, we need to take into account the inherent correlation of repeated data and possibly unbalanced image time points which favor the use of mixed effects models. We applied our framework to a longitudinal dataset of HARDI images from healthy developing infants with ages between 3 to 36 months. We show the resulting longitudinal atlas with the time changes of dODF and its derived generalized fractional anisotropy (GFA). The following sections discuss our framework, experiments, and results.

2 Method

2.1 Multivariate Atlas Building

We use unbiased atlas building to create an anatomical average of the given population and time points. Construction of multivariate atlas is preferable in that the optimization satisfies both shape and appearance. We employed the symmetric group-wise

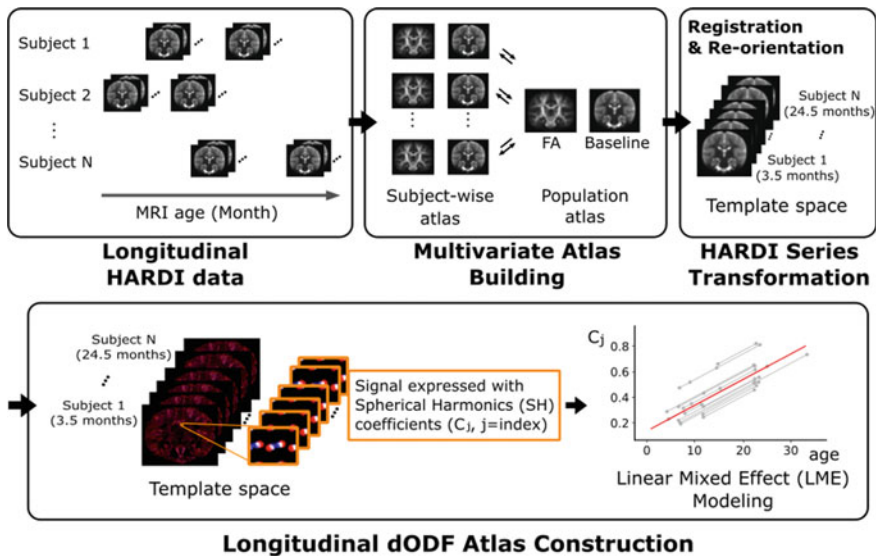


Fig. 1 Overview of longitudinal DW-MRI infant atlas building based on linear mixed effects modeling of diffusion orientation distribution function (dODF) coefficients

normalization algorithm, which is a part of the open source toolkit Advanced Normalization Tools [1]. Given N sets of the K multi-modality images, $\mathbf{I} = \{I_1, \dots, I_K\}$, multivariate template construction computes the set of diffeomorphic transforms, $\{(\phi_1, \phi_1^{-1}), \dots, (\phi_N, \phi_N^{-1})\}$, and the optimal multivariate template, $\mathbf{J} = \{J_1, \dots, J_K\}$, with the coordinate system $\psi(x)$ minimizing the cost function:

$$\sum_{n=1}^N \left[D(\psi(\mathbf{x}), \phi_n^n(\mathbf{x}, 1)) + \sum_{k=1}^K \Pi_k(I_k^n, J_k(\phi_n^{-1}(\mathbf{x}, 1))) \right] \quad (1)$$

where D is the diffeomorphic shape distance, $D(\phi(\mathbf{x}, 0), \phi(\mathbf{x}, 1)) = \int_0^1 \|v(\mathbf{x}, t)\|_L dt$ which depends on the linear operator, L , v is the velocity field $v(\phi(\mathbf{x}, t)) = d\phi(\mathbf{x}, t)/dt$, $\phi(\mathbf{x}, 0) = \mathbf{x}$, and Π_k is the similarity metric. We use baseline images and FA maps to construct the multivariate atlas so that $K = 2$ in Eq. 1. The normalized cross-correlation similarity metric has been suggested previously for multi-modality registration problems [1].

2.2 Registration of HARDI Series to Atlas

Diffeomorphic transforms from the multivariate atlas building are used to transform HARDI series to a common coordinate system. In HARDI, we need an additional step which correctly reorients the diffusion profile for angular alignment in addition to

transforming image series for structural alignment. This reorientation step is applied at each voxel in each HARDI series using a DW spatial warping algorithm [13] as follows: Weighted diffusion basis functions are (1) computed by decomposition; (2) reoriented based on a local affine transformation; and (3) recomposed to the reoriented HARDI signal. The main advantage of using this warping algorithm is that it works directly on the signal so that we can make use of the reoriented HARDI signal for further processing.

2.3 Longitudinal Atlas Building from dODFs

We calculate dODFs for each voxel from HARDI data sets from all subjects and time points. HARDI signals can be represented by functions on the unit sphere where we can express the signal $S(\theta, \phi) = \sum_{l=0}^L \sum_{m=-l}^l c_{l,m} Y_{l,m}$. The basis functions Y_l^m are given by:

$$Y_l^m(\theta, \phi) = \sqrt{\frac{(2l+1)(l-m)!}{4\pi(l+m)!}} P_l^m(\cos \theta) e^{im\phi} \quad (2)$$

where P_l^m is the associated Legendre polynomial, l is the order, and $m \in [-l, l]$ is a phase factor. We calculated dODFs using a symmetric, real, orthonormal SH basis based on an analytical Q-ball imaging reconstruction method [3]. With the modified SH basis, we can write the set of equations as a linear system to solve for the coefficients c_j , where j represents the index of coefficients, $j \in [1, (l^2 + l + 2)/2 + m]$.

Continuous longitudinal modeling is obtained by applying LME modeling to the sets of SH coefficients of ODFs measured at discrete time points. The LME model is preferable over linear regression as it takes into account the variability between subjects, the correlation of repeated data, and unbalanced data points. For each SH coefficient value, we evaluated longitudinal trajectories. Subject-wise intercepts are considered to have random effects and the group-wise slope is considered as the fixed effect representing estimated trends. The model for SH coefficients for the population of subjects and repeated measures over time can be formulated as follows,

$$c_j \sim X\beta + Z\alpha + \epsilon, \quad (3)$$

where $\sim \mathcal{N}(0, \delta^2 I)$, $X = [1, t]$, Z is a design matrix and ϵ is an error term. β is a fixed effects vector and α is a random effects vector. In our work, t is MRI age and subjects are random effects factors. The LME formulation Eq. 3, therefore, estimates group-wise slopes and intercepts as an average of subject-wise slopes and intercepts in the groups. From the estimated slopes of c_j coefficients, we calculate the group-wise dODF trend at each voxel which results in a continuous longitudinal dODF atlas. The subject-wise dODF trends from the random effects represent individual subject-specific variability.

3 Experiments and Results

3.1 Subjects

Image data is selected from a population of 3- to 36-month-old children scanned on 3-T Siemens TIM Trio scanners on four different sites as part of an ongoing autism infant imaging study (ACE-IBIS). In this paper, thirty-three preprocessed HARDI scans from healthy developing infants with scans at more than one time-point are included to build atlas. The preprocessing pipeline includes quality control and correction techniques which are DTIPrep¹ and Q-space resampling for correction [5]. DWI datasets were acquired with FoV = 209 mm, 76 transversal slices, voxel size = $2 \times 2 \times 2$ mm³ voxel resolution, matrix size = 106×106 , TR = 11100 ms, TE = 103 ms, one baseline image with zero b-value and 64 directional DWI volumes sampled on the half sphere with b-value at 2000 s/mm², with a total scan time of 12.5 min.

3.2 Multivariate Atlas Building and HARDI Series Registration

We use multivariate atlas building to obtain an anatomical average of the given population and time points. Fractional anisotropy (FA), the degree of anisotropy derived from the eigenvalues of diffusion tensor, has been used in building DW atlases for spatial alignment [2, 6, 7]. Despite the advantage of representing locations of strong white matter tracts, FA maps do not fully represent boundaries of anatomical and fluid structures. There are different diffusivity indices representing different microstructure properties such as mean diffusivity (MD), radial diffusivity (RD), and axial diffusivity (AD). The diffusivity indices, which are FA, MD, RD and AD maps, are calculated measures from eigenvalues of the diffusion tensor. The DW baseline image, which is a T2-weighted image, depicts structural properties not explained by FA maps. To decide which scalar values to be used for the multivariate atlas building, we compared a similarity between FA and the other scalar images by calculating normalized cross-correlation coefficient for all image pairs. Baseline and FA are the least correlated result in our infant dataset (Mean:0.62, std:0.05). The correlation coefficient values from combination pairs of MD, RD, AD, and baseline are higher than 0.95 in average meaning that they represent similar structures. Thus, FA map and baseline were used to build multivariate atlas.

The atlas building approach includes two steps, building of subject-specific atlases, and of a population atlas. The initial subject-wise atlas building step copes with much lower within-subject variability as compared to across subject deformations. We compared our resulting atlas to an alternative atlas building without

¹<https://github.com/NIRALUser/DTIPrep>.

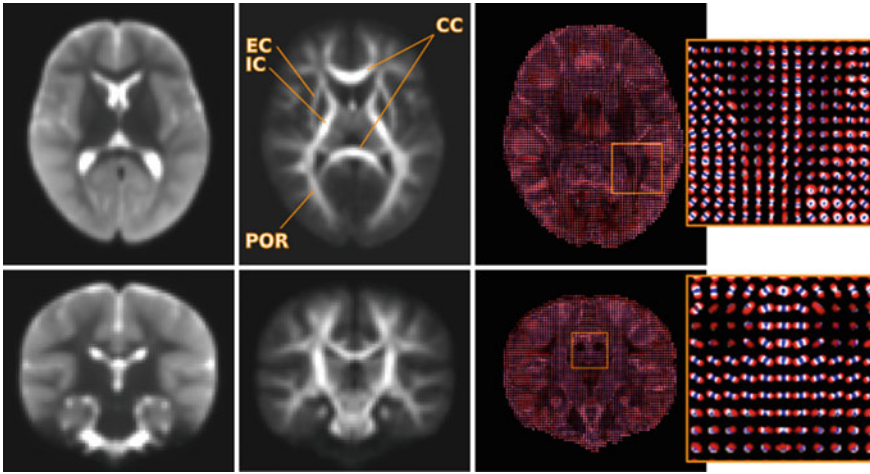


Fig. 2 Multivariate atlas construction result of baseline of DW image (Left) and fractional anisotropy (FA) (Middle). Visualization of dODFs calculated by averaging Spherical Harmonics (SH) coefficients across all HARDI series registered and reoriented into the template space (Right)

subject-wise atlas construction step. For each subject, the variance of normalized cross-correlation between the subject's scans and template was calculated. 12 out of 14 subjects showed lower variance in the atlas building with subject-wise step, justifying our choice.

Results of multivariate atlas building are shown in Fig. 2 with the resulting baseline atlas is in the first and FA atlas is in the middle column. The images in the third column illustrate the dODF visualization from averaged spherical harmonics (SH) coefficients of all infant HARDI images registered and reoriented to the template space. At each voxel, the average dODF is calculated from averaged coefficients. The known white matter tracts in the central part of brain including corpus callosum (CC), internal capsule (IC), external capsule (EC), and posterior optic radiation (POR) are clearly noticeable. We obtained whole brain tractography of the average dODF in the template space as additional visualization method (Fig. 3). We used the deterministic tracking algorithm using `Dipy`² package (version 0.16.0.0). We set a maximum 30° angle threshold and used generalized fractional anisotropy (GFA) from the dODF model to classify white matter.

3.3 Longitudinal dODF Atlas

To calculate a longitudinal dODF atlas, we first estimate ODFs from transformed HARDI images. The SH basis of order 6 ($l = 6$), which makes 28 SH coeffi-

²<https://dipy.org/>.

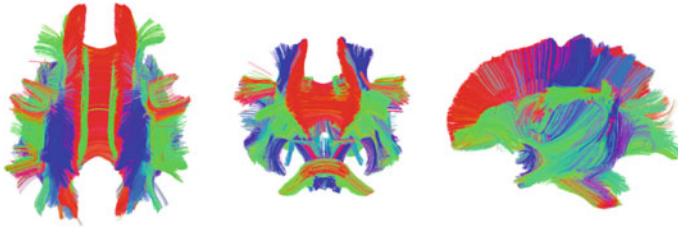


Fig. 3 Whole brain tractography from the average dODFs (Fig. 2) in the template space: Axial (Left), coronal (Middle), sagittal (Right) view. We used generalized fractional anisotropy (GFA) from the dODF model to classify white matter. Deterministic fiber tracking with 30° maximum angle threshold is used to obtain the tractography image. Tractography color shows the directions: red for left/right, blue for dorsal/ventral, and green for anterior/posterior

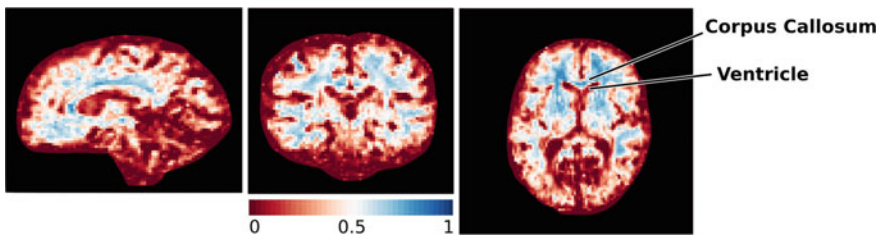


Fig. 4 Goodness of fit for the linear mixed effect (LME) result on the voxel-wise spherical harmonics (SH) coefficients. R^2 is calculated using the Frobenius norm for each voxel. Left: Sagittal view, Middle: Coronal, Right: Axial view

icients ($j = 1, \dots, 28$), with $\lambda = 0.006$ has been selected following suggestions from Descoteaux's paper [3]. The order-6 terms consider up to 3 crossing directions in the orientation estimation. We adopted an LME modeling to obtain a continuous longitudinal dODF atlas. The model is applied to dODF coefficients for each voxel to estimate the group trends. To assess the goodness of fit, we calculated the R^2 on the voxel-wise SH coefficients \mathbf{c} using the Frobenius norm (Fig. 4). R^2 will be near zero if the difference between estimated values and data is small due to the absence of longitudinal changes. For voxels located in regions having small diffusion signal changes such as cerebrospinal fluid, we get near zero R^2 values. Figure 4 shows the clear boundary of existing white matter structures, for example, corpus callosum and ventricle area, which can display the LME model has fitted well in voxels with white matter structures. We illustrate the estimated dODF and the generalized fractional anisotropy (GFA) of the resulting continuous longitudinal dODF atlas at different time points. We followed the GFA that Tuch proposed which can be interpreted as FA value but being able to be calculated from dODF [11]. We show the dODF and the GFA (Fig. 5) changes in the age range from 6 to 24 months. Figure 5 illustrates how the white matter structures change in the developing infant brains. The structure, for example, cingulum which is a red circle in the Fig. 5, has a more clear directional shape in dODF as development continues.

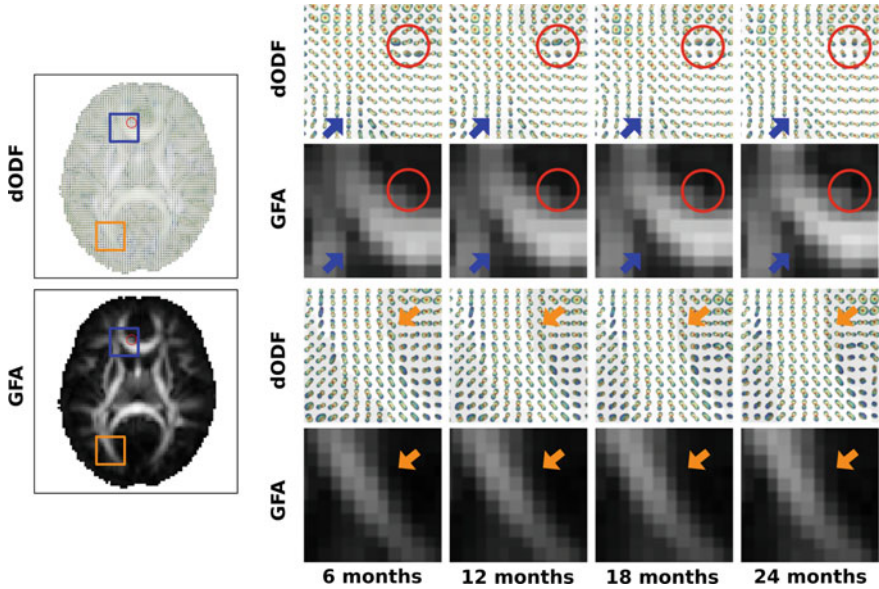


Fig. 5 Visualization of the 4D atlas result of longitudinal continuous diffusion orientation distribution functions (dODF) shown for cingulum (red circle), corpus callosum (blue arrow), posterior optic radiation (orange arrow). Each column on the right shows estimated dODFs and calculated generalized fractional anisotropy (GFA) at different time points

3.4 Evaluation Based on Longitudinal GFA Changes

In order to show the potential use of a longitudinal dODF atlas, we evaluate the GFA values calculated from dODFs in the corpus callosum (CC). In Fig. 6, the colored lines describe the population trends and the gray lines are the subject-wise trends. We analyzed three parts of the CC, genu, body, and splenium. The positive slope plots imply that the diffusivity of those area becomes more anisotropic as the brain develops. In addition, the splenium of CC starts with higher GFA which may indicate that the maturation of the splenium begins earlier compared to the body and the genu. This result is in line with the findings in a previous white matter tract-based study on DTI atlas, reporting that in neonates, the splenium shows highest FA, followed by genu and then the body of the CC [6]. However, the study showed that changes in the first year were larger than the second year which could not be found with our framework since we assumed linear changes in dODF coefficients. Figure 6 also illustrates the subject-specific variability in the GFA changes (gray lines). Developing statistics for individual trends to express confidence bounds will be subject of future work to develop methods such as age prediction will be our future work.

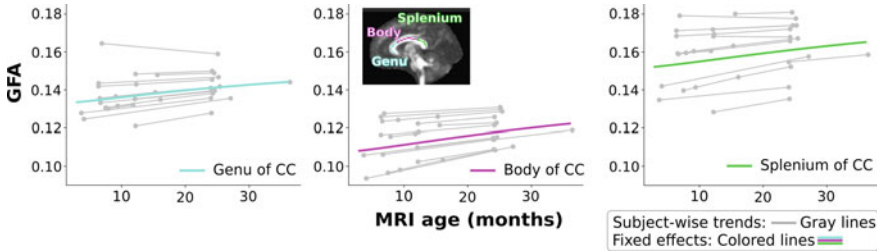


Fig. 6 Generalized fractional anisotropy (GFA) calculated from the longitudinal diffusion orientation distribution functions (dODF) infant atlas for genu, body, and splenium of the corpus callosum

4 Discussion and Conclusion

We introduce a framework to build a continuous longitudinal HARDI brain atlas based on statistics of dODF SH coefficients, applied to longitudinal data of healthy developing infants. The framework is generic and can be applied to any longitudinal study using DWI data, for example aging, disease progression or monitoring of therapeutic outcome. New concepts presented here are the use of longitudinal data for 4D atlas building which allowed the use of mixed effects modeling versus conventional regression, and continuous temporal modeling of dODFs from HARDI data, resulting in a 4D HARDI atlas where common scalar indices and variabilities can be derived. Geometric variability across subjects and age is normalized by unbiased atlas building, here using multi-modal image data to provide correspondences at anatomical boundaries as well as within interior white matter. We model continuous longitudinal dODFs by mixed effects modeling from longitudinal HARDI data, where fixed effects represent average and random effects variability as a function of age, a concept not shown before. Using the new framework, we will be able to not only to build average dODF atlases and derived scalar indices such as GFA at different time points, but also estimates of confidence intervals and thus variability as a function of time. Feasibility is shown with visualization of dODFs and derived GFA maps at multiple time points, demonstrating the ability to model maturation trajectories. Here, we could compare dODF atlas building and comparison of GFA with atlas-building directly from GFA maps, but the latter would only represent an atlas for one derived indices versus the rich set of measures to be derived from ODFs, and would lack the capability to apply fiber tractography from the atlas. The voxel-wise goodness of fit serves as validation of longitudinal modeling. As a potential use of the 4D atlas, we demonstrate GFA analysis of genu, body, and splenium of the corpus callosum which replicates previous findings [6] based on DTI.

The presented work still has limitations. First, the unbalanced age points and the relatively small sample size may not allow to fully explain development between 3- to 36-month-old infants. This may lead to the result that the developmental effect is smaller than the inter-subject variability. Second, we assumed a linear change in time. The linear model may not be able to fully reflect non-linear age-dependent changes.

In future work, we will quantify the expected robustness of LME modeling versus cross-sectional atlas building and thus compare our concept to previously proposed atlas construction schemes. Future efforts will test improved geometric normalization via longitudinal regression, explore alternative mixed effects models for dODF coefficient modeling and further direct modeling method for diffusion MRI signals, examine higher order or nonlinear temporal models, and include a statistical framework for estimation of confidence bounds [10]. We will also extend the framework for longitudinal tract-based analysis of HARDI image data following concepts based on DTI [7].

Acknowledgments This work was supported by the NIH grants R01-HD055741-12, 1R01HD089390-01A1, 1R01DA038215-01A1 and 1R01HD08812501A1. We are thankful for research discussions with Dr. Ragini Verma.

Conflict of Interest Statement The authors declare that there are no conflicts or commercial interest related to this article.

References

1. Avants, B.B., Tustison, N.J., Song, G., Cook, P.A., Klein, A., Gee, J.C.: A reproducible evaluation of ants similarity metric performance in brain image registration. *Neuroimage* **54**(3), 2033–2044 (2011)
2. Bouix, S., Rathi, Y., Sabuncu, M.: Building an average population hardi atlas. In: MICCAI Workshop on Computational Diffusion MRI (2010)
3. Descoteaux, M., Angelino, E., Fitzgibbons, S., Deriche, R.: Regularized, fast, and robust analytical q-ball imaging. *Magn. Reson. Med. Official J. Inter. Soc. MR Med.* **58**(3), 497–510 (2007)
4. Du, J., Goh, A., Kushnarev, S., Qiu, A.: Geodesic regression on orientation distribution functions with its application to an aging study. *NeuroImage* **87**, 416–426 (2014)
5. Elhabian, S., Vachet, C., Piven, J., Styner, M., Gerig, G.: Compressive sensing based q-space resampling for handling fast bulk motion in hardi acquisitions. In: 2016 IEEE 13th ISBI. IEEE (2016)
6. Geng, X., Gouttard, S., Sharma, A., Gu, H., Styner, M., Lin, W., Gerig, G., Gilmore, J.H.: Quantitative tract-based white matter development from birth to age 2 years. *Neuroimage* **61**(3), 542–557 (2012)
7. Goodlett, C.B., Fletcher, P.T., Gilmore, J.H., Gerig, G.: Group analysis of dti fiber tract statistics with application to neurodevelopment. *Neuroimage* **45**(1), S133–S142 (2009)
8. Kim, J., Chen, G., Lin, W., Yap, P.T., Shen, D.: Graph-constrained sparse construction of longitudinal diffusion-weighted infant atlases. In: MICCAI. Springer, Berlin (2017)
9. Pietsch, M., Christiaens, D., Hutter, J., Cordero-Grande, L., Price, A.N., Hughes, E., Edwards, A.D., Hajnal, J.V., Counsell, S.J., Tournier, J.D.: A framework for multi-component analysis of diffusion mri data over the neonatal period. *NeuroImage* (2018)
10. Sadeghi, N., Prastawa, M., Fletcher, P.T., Vachet, C., Wang, B., Gilmore, J., Gerig, G.: Multi-variate modeling of longitudinal mri in early brain development with confidence measures. In: 2013 IEEE 10th ISBI. IEEE (2013)
11. Tuch, D.S.: Q-ball imaging. *Magn. Reson. Med.* **52**(6), 1358–1372 (2004)
12. Yang, Z., Chen, G., Shen, D., Yap, P.T.: Robust fusion of diffusion mri data for template construction. *Scientific reports* **7**(1), 12950 (2017)
13. Yap, P.T., Shen, D.: Spatial transformation of dwi data using non-negative sparse representation. *IEEE Trans. Med. Imaging* **31**(11), 2035–2049 (2012)

14. Yeh, F.C., Tseng, W.Y.I.: Ntu-90: a high angular resolution brain atlas constructed by q-space diffeomorphic reconstruction. *Neuroimage* **58**(1), 91–99 (2011)
15. Zhang, H., Yushkevich, P.A., Rueckert, D., Gee, J.C.: Unbiased white matter atlas construction using diffusion tensor images. In: *MICCAI*. Springer, Berlin (2007)

Investigation of Changes in Anomalous Diffusion Parameters in a Mouse Model of Brain Tumour



Qianqian Yang , Simon Puttick , Zara C. Bruce, Bryan W. Day, and Viktor Vegh 

Abstract In this paper, we investigate anomalous diffusion models in a mouse model of glioblastoma, a grade IV brain tumour, and study how the anomalous diffusion model parameters reflect the change in tumour tissue microstructure. Diffusion-weighted MRI data with multiple b -values at 9.4 T was acquired from mice bearing U87 brain tumour cells at four time points. Voxel-level fitting of the MRI data was performed on the classical mono-exponential model, and four anomalous diffusion models, namely, the stretched exponential model, the sub-diffusion model, the continuous time random walk model and the fractional Bloch-Torrey equation. The performance of the anomalous diffusion parameters for differentiating the three-concentric layers of tumour tissue (i.e., core; intermediate zone; peripheral and hyper-vascularised tumour layer) was evaluated with multinomial logistic regression and multi-class classification analysis. We found that parameter α from the stretched exponential model, parameter β from the sub-diffusion model and parameter β from the continuous time random walk model provide a clear delineation of the three layers of tumour tissue. The analysis revealed that the combination of diffusion coefficient D

Q. Yang (✉)

School of Mathematical Sciences, Queensland University of Technology,
Brisbane QLD4001, Australia
e-mail: q.yang@qut.edu.au

S. Puttick

Australian Institute for Bioengineering and Nanotechnology,
The University of Queensland, Brisbane QLD4072, Australia
e-mail: s.puttick@uq.edu.au

Z. C. Bruce · B. W. Day

Sid Faithfull Brain Cancer Laboratory, QIMR Berghofer Medical Research Institute,
Brisbane QLD4006, Australia
e-mail: zara.bruce@qimrberghofer.edu.au

B. W. Day

e-mail: bryan.day@qimrberghofer.edu.au

V. Vegh

Centre for Advanced Imaging, The University of Queensland,
Brisbane QLD4072, Australia
e-mail: viktor.vegh@cai.uq.edu.au

© Springer Nature Switzerland AG 2020

E. Bonet-Carne et al. (eds.), *Computational Diffusion MRI*,

Mathematics and Visualization, https://doi.org/10.1007/978-3-030-52893-5_14

and anomalous diffusion parameter (α and/or β) greatly improved the classification power in terms of F1-scores compared with the current approach in clinics, in which D is used alone. Hence, our mouse brain tumour study demonstrated that anomalous diffusion model parameters are useful for differentiating different tumour layers and normal brain tissue.

1 Introduction

In MRI an inherent mismatch exists between the scale at which water diffusion occurs and the scale at which measurements are taken. This mismatch makes the interpretation of changes in tissue microstructure challenging which is further complicated by water diffusion in a hindered and restricted tissue micro-environment. In this paper, we attempt to address this issue by studying the potential role of anomalous diffusion models (a subset of non-Gaussian diffusion models) in linking tissue microstructure differences with changes in anomalous diffusion model parameters. Our investigations are performed in the context of glioblastoma, a grade IV glioma in the brain, as increasing evidence suggests that proper mapping of the tissue micro-environment in this disease can lead to improved treatment planning [8], better surgical intervention with positive outcomes [19] and the development of drugs targeting specific tissue micro-environment features such as angiogenesis [27].

Studies in diffusion-weighted MRI (DWI) involve a parameter called the b -value (units of s/mm^2) which is a function of diffusion gradient amplitude and its duration, and the amount of time water is allowed to diffuse in tissue. It is widely observed that the DWI signal decay at high b -values ($>1000 \text{ s}/\text{mm}^2$) does not follow the classical mono-exponential model which assumes diffusing spins are undergoing Brownian motion in tissue [26], and hence a simple ADC value obtained from the mono-exponential model may not be able to adequately capture tissue heterogeneity. Due to the limitation of ADC, several research groups have developed a number of more sophisticated diffusion models to extract structure tissue information beyond what ADC can provide (eg. [7, 14–18, 20]). In this study, we focus on several anomalous diffusion models developed using theory in fractional calculus. These models incorporate a broad and continuous distribution of diffusion compartments, and describe water molecule transport processes influenced by the multiple length and time scales through a heterogeneous medium at sub-voxel resolution [5, 24]. Anomalous diffusion models considered in this study include

- stretched exponential model (also known as super-diffusion model) which allows for deviation from mono-exponential decay by assuming diffusing spins are more likely to take long jumps, ie. undergoing Lévy walks rather than Brownian motion [3, 9, 10];
- sub-diffusion model which assumes the waiting times between jumps for diffusing spins follow a long-tailed probability distribution (ie. long waiting times) [5, 9];

- continuous time random walk model which incorporates assumptions for both super- and sub-diffusions, i.e. diffusing spins are more likely to take long jumps and have long waiting times between jumps [9, 12, 13]; and
- fractional Bloch-Torrey equation which generalises the Bloch-Torrey equation through fractional order differential operators [20];

Each of these models yields a new set of parameters to describe the anomalous diffusion in complex biological tissue, which provide useful information not only on the diffusion coefficient (D) but also on the tissue structures (α and/or β) through which water molecules diffuse. For example, researchers used anomalous diffusion models to differentiate low- and high- grade pediatric brain tumours [13, 14, 25], to characterise white matter tissue microstructure [28, 29], to study healthy fixed rat brain tissue [12], and to characterise myocardial microstructure in cardiac tissue [5].

Previous studies [21, 22] reported that there are often three concentric layers observed in the glioma tumour mass (core/necrotic, intermediate layer and peripheral/hyper-vascularised layer). The formation of such layered structure is driven by the extent of hypoxia within the tumour region. The goal of this study is to investigate the utility of anomalous diffusion model parameters in differentiating the three tumour layers in a mouse model of glioma.

2 Methods

2.1 Anomalous Diffusion Models in MRI

Based on the Bloch-Torrey equation for the magnetisation of water protons and in conjunction with the Stejskal-Tanner diffusion protocol, the amplitude of the acquired diffusion weighted signal follows a mono-exponential decay

$$S/S_0 = \exp(-bD), \quad (1)$$

where S_0 is the baseline signal intensity, D is the diffusion coefficient of water in tissue (typically, 2×10^{-3} mm²/s for water at room temperature), $b = (\gamma G \delta)^2 (\Delta - \delta/3)$ is the degree of sensitisation to diffusion of the MRI pulse sequence, γ is the gyromagnetic ratio (42.58 MHz/T for protons) and the diffusion-weighting is applied with a pair of unipolar gradient waveforms of duration δ , separation Δ , and amplitude G . As a generalisation of this mono-exponential decay, a stretched exponential model

$$S/S_0 = \exp(-(bD)^\alpha), \quad 0 < \alpha \leq 1, \quad (2)$$

has been proposed in a few previous studies [2, 3, 10], which becomes (1) when $\alpha = 1$. The model parameter α is the so-called heterogeneity index and can be used to infer microscopic tissue structure [3].

Alternatively, the mono-exponential model can be generalised to a sub-diffusion model [5, 9]

$$S/S_0 = E_\beta(-bD), \quad 0 < \beta \leq 1 \quad (3)$$

where $E_\beta(z) = \sum_{k=0}^{\infty} \frac{z^k}{\Gamma(1+\beta k)}$ and $\Gamma(\cdot)$ are the Mittag-Leffler and Gamma functions, respectively [23]. When $\beta = 1$, $\Gamma(1+k) = k!$, and $E_1(z)$ by definition is the exponential function.

A further generalisation of the stretched exponential model (2) and the sub-diffusion model (3) gives the continuous-time random walk (CTRW) model (demonstrated on healthy fixed rat ventricles [5], healthy fixed rat brain tissue [12] and paediatric brain tumours [13])

$$S/S_0 = E_\beta(-(bD)^\alpha), \quad 0 < \alpha, \beta \leq 1. \quad (4)$$

Finally, using first principles and by adopting the fractional calculus in the derivation, a solution to the fractional Bloch-Torrey equation (FBTE) [20] is obtained,

$$S/S_0 = \exp \left[-D\mu^{2(\alpha-1)}(\gamma G\delta)^{2\alpha} \left(\Delta - \frac{2\alpha-1}{2\alpha+1}\delta \right) \right], \quad (5)$$

where $\mu^{2(\alpha-1)}$ is fractional order space constant needed to preserve units.

2.2 Mouse Preparation and Data Acquisition

All animal experiments were approved by the University of Queensland animal ethics committee. To form intracranial tumours, 1×10^5 U87 cells were injected into the right striatum of six-week old NOD/SCID mice, +0.6 mm anterior-posterior, +1.2 mm mediolateral from bregma and at a depth of 3 mm from the dural surface using a stereotactic device. MR images were acquired at 7, 14, 19 and 21 days post injection. The MRI examination included T2-weighted and multiple b -value DWI data acquisitions using a Bruker Biospin 9.4 T large bore MRI animal scanner. T2-weighted images were acquired using the fast spin echo MRI sequence with TR/TE = 2500/33 ms, echo train length = 8, matrix size = 256 by 256, field of view (FOV) = 2 cm by 2 cm, spatial resolution = 78.125 μm by 78.125 μm , slice thickness = 0.7 mm. The multiple b -value DWI data was acquired using an echo planar imaging (EPI) sequence with b -values = 0, 500, 1000, 1500, 2000, 2500, 3000, 3500, 4000 s/mm^2 . Three $b = 0$ images were acquired. At each nonzero b -value, trace-weighted images were generated from the 30 direction Stejskal-Tanner DWI data. The key data acquisition parameters were: TR/TE = 5000/30 ms, separation between the Stejskal-Tanner gradient lobes $\Delta = 20$ ms, diffusion gradient duration $\delta = 3$ ms, matrix size = 108 by 96, field of view (FOV) = 2.16 cm by 1.92 cm, spatial resolution = 0.2 mm by 0.2 mm, slice thickness = 0.2 mm. The acquisition time was

approximately 10 min per mouse. Following the final MRI acquisition, mice were euthanised and the brain drop fixed in 4% paraformaldehyde. Paraffin-embedded brains were sectioned by microtome at room temperature using a section thickness of 12 μm and hematoxylin and eosin (H&E) staining was performed. Slides were scanned using an Aperio CS2 digital slide scanner and the images were processed using ImageScope.

2.3 Image Analysis

Multi b -value diffusion images were fitted to the anomalous diffusion models (2)–(5) on a voxel-by-voxel basis. Firstly, D was calculated using the mono-exponential decay model (1) for the subset of acquired data up to $b = 1000 \text{ s/mm}^2$. Secondly, the full range of b -values was used to fit the parameters using the trust-region-reflective algorithm [4, 6] with prescribed tolerance of 10^{-6} . Parameter bounds were taken as $0 < \alpha, \beta \leq 1$, with initial guesses $\alpha = 1$ and $\beta = 1$, representative of the case of diffusion governed by the mono-exponential model. Parameter fittings were implemented in MATLAB. Evaluation of the Mittag-Leffler function was performed using Garrappa's optimal parabolic contour algorithm, which is available in MATLAB central (file exchange number 48154). We found fitting results to be insensitive to the choice of initial values.

Regions of interest (ROIs) were carefully selected, guided by the histological sections (H&E), to represent each layer of tumour tissue (core, intermediate and peripheral) and the contralateral normal-appearing tissue. The ROIs were placed on the diffusion images first and then propagated to the corresponding model parameters for statistical analysis: (D, α) for the stretched exponential model, (D, β) for the sub-diffusion model, (D, α, β) for the CTRW model and (D, α, μ) for the FBTE model.

2.4 Statistical Analysis

For each anomalous diffusion model, mean values and standard deviations of model parameters were calculated from the tumour and the normal-appearing ROIs. A two-sided Wilcoxon rank sum test with significance set at $p < 0.05$ was performed for comparing parameter values in each pair of ROIs, i.e., core-versus-intermediate, core-versus-peripheral, core-versus-normal, intermediate-versus-peripheral, intermediate-versus-normal, and peripheral-versus-normal.

Since anomalous diffusion models have at least two parameters, multinomial logistic regression was used in two ways: (i) to determine the significance of each model parameter and (ii) to evaluate the set of model parameters in differentiating three tumour regions as well as normal brain tissue region. In statistics or machine learning, this is called a multi-class classification problem. Quality of the overall classification is assessed by precision, recall(also known as sensitivity) and F1-score

in the macro-averaging sense. Precision-recall curves were also generated to assess the performance of the set of parameters from each anomalous diffusion model. All statistical analyses were carried out in MATLAB.

3 Results

Figure 1 presents the progression of gliomas in the right hemisphere of mouse brains as observed in longitudinal T2-weighted MRI scans. These images show the level of temporal and spatial heterogeneity in tumour development.

To capture additional information on tumour structure apart from water diffusivity D , the anomalous diffusion models (2)–(5) were fitted to the acquired diffusion data to yield a new set of parameters. Representative spatially resolved maps of the diffusion coefficient (D), the anomalous diffusion parameters and the relative fitting errors for each model are shown in Fig. 2. The D map was computed using the mono-exponential model with lower b values (≤ 1000 s/mm²) as outlined in the methods section, and it is not model dependent. This parameter was also comparable to the ADC value, which is typically obtained with $b = 0$ and $b = 1000$ s/mm². The relative fitting error was calculated by $\text{norm}(\text{signal values} - \text{fitted values}) / \text{norm}(\text{signal values})$. The relative error maps corresponding to each model fit have a level of similarity between them, whilst the contrast of the spatially resolved parameter maps varies with method.

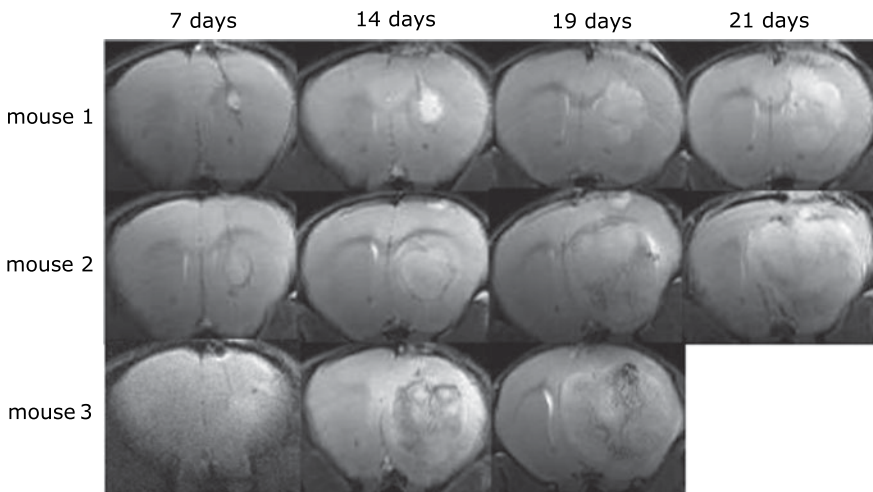


Fig. 1 T2-weighted MRI scans at 7, 14, 19 and 21 days showing glioblastoma progression in three different mice. Tumour cells were injected on day 0, and mouse 3 was euthanised after the day 19 imaging session. All other mice were euthanised after the day 21 imaging session

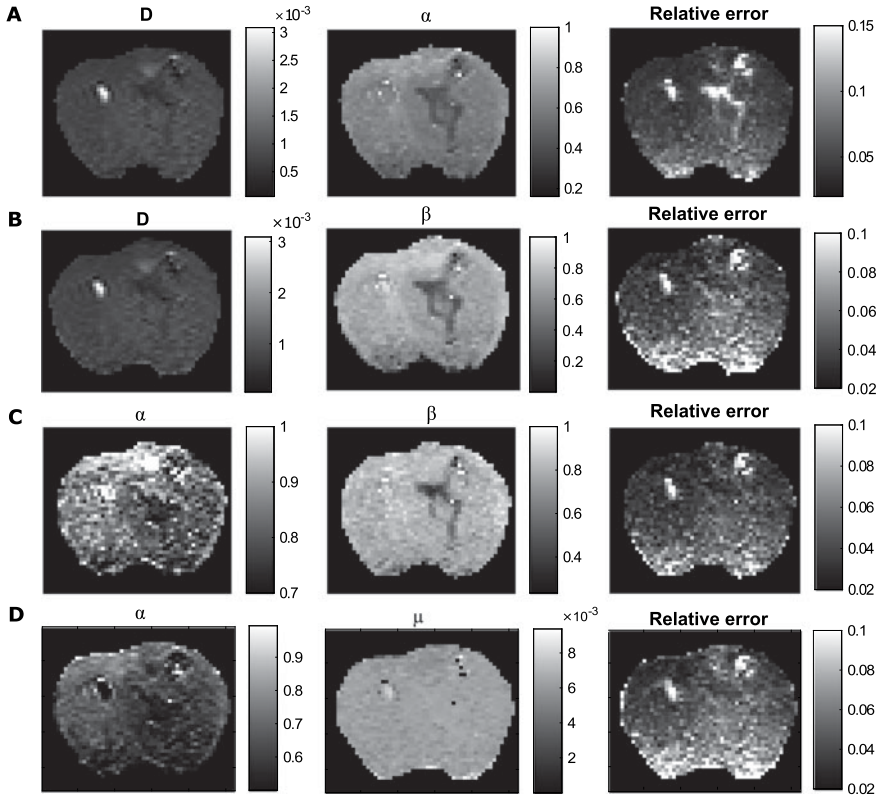


Fig. 2 Representative parameter maps and errors from fitting anomalous diffusion models. **A** D and α maps for stretched exponential model; **B** D and β maps for sub-diffusion model **c** α and β maps for continuous time random walk model (CTRW); **D** D and μ maps for fractional Bloch-Torrey equation (FBTE). Note D map is obtained from fitting the mono-exponential model for $b \leq 1000$ s/mm² and remains the same for the anomalous diffusion models

Our key observations from these images are: (i) α from the stretched exponential model (Fig. 2A), β from the sub-diffusion model (Fig. 2B) and β from CTRW (Fig. 2C) provide a clear delineation of the three layers of tumour tissue; (ii) Both α s from the CTRW (Fig. 2C) and FBTE (Fig. 2D) show a darker core layer of the tumour, but they cannot differentiate the intermediate and peripheral layers of tumour; (iii) μ values from the FBTE (Fig. 2D) seem very similar across the whole brain region and hence not very sensitive to brain and tumour tissue structure. Since μ is used to preserve units, so its interpretation may not be meaningful.

These observations were further confirmed by the box plots analysis in Fig. 3. Regions of interest (Fig. 3A) have been selected based on H&E section of the tumour-bearing right hemisphere of mouse brain (Fig. 3B). In Fig. 3C–F, separation of notches ($>$ $<$) implies the medians are significantly different across ROIs at the 95%

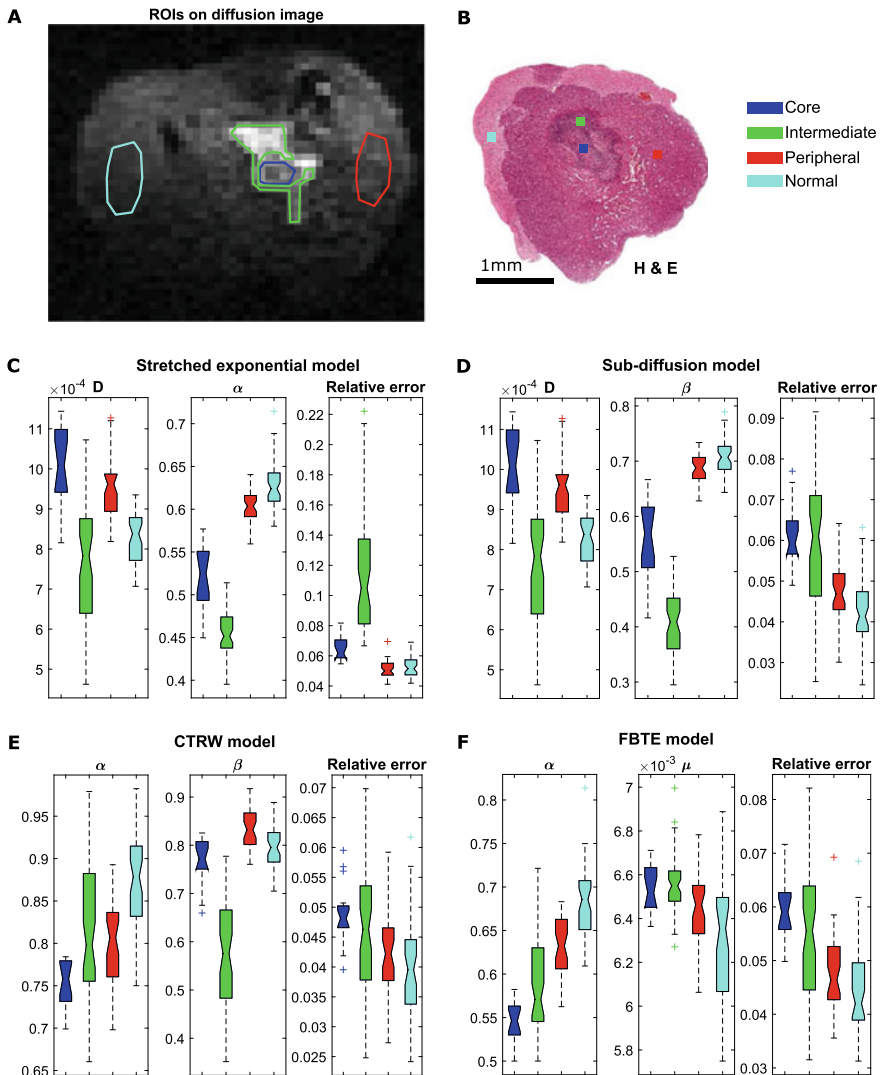
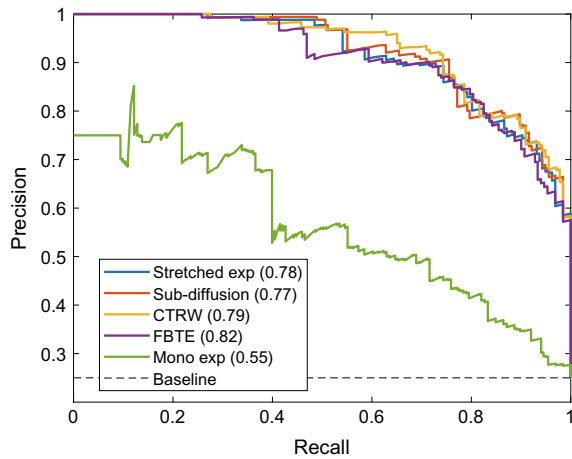


Fig. 3 Behaviour of model parameters for representative specific regions of interest inside and around the tumour. Shown are **A** selected regions of interest marked on the diffusion image; **B** Histological section (H&E staining) of the right hemisphere of a mouse brain; **C–F** notched box plots of parameters based on the stretched exponential, sub-diffusion, CTRW and FBTE models, respectively. Note, if the notches ($>$ $<$) of the two box plots do not overlap, it indicates that the medians of two regions are significantly different at the 95% confidence level

Table 1 Statistics of the anomalous diffusion parameters in tumour and normal tissue ROIs

	Stretched exp		CTRW	
	$D \times 10^{-3} \text{ mm}^2/\text{s}$	α	α	β
Core	1.00 ± 0.10	0.52 ± 0.04	0.75 ± 0.03	0.77 ± 0.05
Intermediate	0.76 ± 0.16	0.45 ± 0.03	0.81 ± 0.08	0.58 ± 0.12
Peripheral	0.95 ± 0.08	0.60 ± 0.02	0.80 ± 0.05	0.83 ± 0.04
Normal	0.83 ± 0.06	0.63 ± 0.03	0.88 ± 0.05	0.80 ± 0.04
	Sub-diffusion		FBTE	
	$D \times 10^{-3} \text{ mm}^2/\text{s}$	β	α	$\mu (\mu\text{m})$
Core	1.00 ± 0.10	0.56 ± 0.07	0.55 ± 0.02	6.5 ± 0.11
Intermediate	0.76 ± 0.16	0.41 ± 0.06	0.58 ± 0.06	6.6 ± 0.15
Peripheral	0.95 ± 0.08	0.69 ± 0.03	0.63 ± 0.04	6.4 ± 0.18
Normal	0.83 ± 0.06	0.71 ± 0.03	0.68 ± 0.04	6.3 ± 0.30

Fig. 4 Precision-Recall curves and F1-scores (shown in brackets) for evaluating the performance of model parameters on differentiating different tumour tissue layers and normal tissue



confidence level. This hypothesis was confirmed by the Wilcoxon rank sum test as described in the methods section. A statistical summary of the parameter values for each ROI is presented in Table 1.

Multivariate logistic regression analysis showed that all the anomalous diffusion model parameters were significant with $p < 0.01$. Figure 4 shows the precision-recall curves and F1-scores (in brackets) for each set of model parameters to differentiate three tumour layers and normal tissue. The curves for anomalous diffusion models behaved similarly, bowing towards the corner (1, 1), and well above the curve for mono-exponential model. F1-scores for each anomalous model were very similar (around 0.8), and again outperformed the mono-exponential model with F1-score 0.55. These metrics indicate that anomalous diffusion models preformed very well in differentiating tumour layers and normal tissue.

4 Discussion

We set out to investigate the role of anomalous diffusion models in the characterisation of the tissue microenvironment in a mouse model of glioblastoma, a grade IV brain cancer. We acquired 9.4T DWI mouse brain data with multiple b -values at fixed diffusion time over four time points. Whilst several other anomalous diffusion models have been described in the literature (e.g. [7, 14–18, 20]), only a subset of them are applicable in the fixed diffusion time regime considered herein. Moreover, different models behave differently based on the diffusion time set in the experiment. With this in mind, we investigated the utility of four anomalous diffusion models in characterising the tumour tissue layers through spatial variations in model parameters (see Figs. 2 and 3). After applying the stretched exponential, sub-diffusion, continuous time random walk and fractional Bloch-Torrey equation models to the data, we found the anomalous diffusion model parameters are very sensitive to tissue changes in the presence of a tumour. In particular, α from the stretched exponential model (Fig. 2A), β from the sub-diffusion model (Fig. 2B) and β from CTRW (Fig. 2C) provide a clear delineation of the three layers (core, intermediate layer and peripheral/hyper-vascularised layer) of tumour tissue.

We found the three-parameter models (CTRW and FBTE) to marginally better fit and classify the data than the two-parameter models (stretched exponential and sub-diffusion models) in terms of relative fitting errors and F1-scores from the multinomial logistic regression and multi-class classification analysis. However, both α s of the CTRW and FBTE models were not able to differentiate regions within the tissue micro-environment to the same extent as α and β from the stretched exponential and sub-diffusion models. We may attribute this finding with a potential of data over-fitting using the three-parameter models. For example, the AIC (Akaike Information Criteria) for model selection involves a term representative of fitting error which is penalised by an increase in models parameters [1]. Since our relative fitting errors are somewhat similar across the different models (see Figs. 2 and 3), we may argue that insufficient gain in fitting quality is achieved through an increase in the degrees of freedom within the model. As such, a change in one parameter can counteract a change in another parameter, which make the underlying effects on the model parameters less distinguishable (comparing Fig. 3E, F with Fig. 3C, D).

In the box plots for α from the stretched exponential model (Fig. 3C) and β from the sub-diffusion model (Fig. 3C), the notches on selected regions of interest inside tumour do not overlap, which means the medians of any regions are significantly different at the 95% confidence level. Hence, the anomalous diffusion parameters from the stretched exponential model and the sub-diffusion model have the ability to differentiate tissue types in tumour, whereas such detailed information on tumour structure can not be observed in vivo usually [11]. In addition, the α and β values are higher in the normal-appearing brain tissue and lower in the tumour tissue region. This can be explained through fractional calculus theory; i.e. if α is closer to 1 then the diffusion process is closer to Gaussian diffusion (free diffusion) and if less than

1 then the diffusion process is more anomalous and indicating the diffusion medium is more heterogeneous and complex (such as tumour tissue) [2, 20].

Moreover, multinomial logistic regression and multi-class classification analysis revealed that the combination of D and anomalous diffusion parameter (α and/or β) greatly improved the classification power in terms of F1-scores compared with the current approach in clinics, in which the diffusion coefficient D is used alone.

With these results, our mouse brain glioma study demonstrates the ability of using anomalous diffusion models to differentiate tumour layers and normal brain tissue. Future work will be to apply such analysis to patient data.

Acknowledgments Qianqian Yang acknowledges the Australian Research Council for the Discovery Early Career Researcher Award (DE150101842). Simon Puttick acknowledges the Cure Brain Cancer Foundation Innovation Grant (R14/2173).

References

1. Akaike, H.: Akaike's information criterion. In: Lovric, M. (ed.) International Encyclopedia of Statistical Science. Springer, Heidelberg (2011). https://doi.org/10.1007/978-3-642-04898-2_110
2. Bennett, K., Hyde, J., Schmainda, K.: Water diffusion heterogeneity index in the human brain is insensitive to the orientation of applied magnetic field gradients. *Magn. Reson. Med.* **56**(2), 235–239 (2006). <https://doi.org/10.1002/mrm.20960>
3. Bennett, K., Schmainda, K., Bennett, R., Rowe, D., Lu, H., Hyde, J.: Characterization of continuously distributed cortical water diffusion rates with a stretched-exponential model. *Magn. Reson. Med.* **50**(4), 727–734 (2003). <https://doi.org/10.1002/mrm.10581>
4. Branch, M., Coleman, T., Li, Y.: A subspace, interior, and conjugate gradient method for large-scale bound-constrained minimization problems. *SIAM J. Sci. Comput.* **21**(1), 1–23 (1999). <https://doi.org/10.1137/s1064827595289108>
5. Bueno-Orovio, A., Teh, I., Schneider, J.E., Burrage, K., Grau, V.: Anomalous diffusion in cardiac tissue as an index of myocardial microstructure. *IEEE Trans. Med. Imaging* **35**(9), 2200–2207 (2016). <https://doi.org/10.1109/TMI.2016.2548503>
6. Coleman, T., Li, Y.: An interior trust region approach for nonlinear minimization subject to bounds. *SIAM J. Optim.* **6**, 418–445 (1996). <https://doi.org/10.1137/0806023>
7. Eliazar, I., Shlesinger, M.: Fractional motions. *Phys. Rep.* **527**(2), 101–129 (2013). <https://doi.org/10.1016/j.physrep.2013.01.004>
8. Fritz, L., Dirven, L., Reijneveld, J., Koekkoek, J., Stiggelbout, A., Pasman, H., Taphoorn, M.: Advance care planning in glioblastoma patients. *Cancers* **8**(11), 102 (2016). <https://doi.org/10.3390/cancers8110102>
9. Hall, M.: Continuity, the Bloch-Torrey equation, and diffusion MRI (2016). [arXiv:1608.02859](https://arxiv.org/abs/1608.02859)
10. Hall, M., Barrick, T.: From diffusion-weighted mri to anomalous diffusion imaging. *Magn. Reson. Med.* **59**, 447–455 (2008). <https://doi.org/10.1002/mrm.21453>
11. Iima, M., Reynaud, O., Tsurugizawa, T., Ciobanu, L., Li, J., et al.: Characterization of glioma microcirculation and tissue features using intravoxel incoherent motion magnetic resonance imaging in a rat brain model. *Invest. Radiol.* **49**(7), 485–490 (2014). <https://doi.org/10.1097/rli.0000000000000040>
12. Ingo, C., Magin, R., Colon-Perez, L., Triplett, W., Mareci, T.: On random walks and entropy in diffusion-weighted magnetic resonance imaging studies of neural tissue. *Magn. Reson. Med.* **71**(2), 617–627 (2014). <https://doi.org/10.1002/mrm.25153>

13. Karaman, M., Sui, Y., Wang, H., Magin, R., Li, Y., Zhou, X.: Differentiating low- and high-grade pediatric brain tumors using a continuous-time random-walk diffusion model at high b-values. *Magn. Reson. Med.* **76**(4), 1149–1157 (2016). <https://doi.org/10.1002/mrm.26012>
14. Karaman, M., Wang, H., Sui, Y., Engelhard, H., Li, Y., Zhou, X.: A fractional motion diffusion model for grading pediatric brain tumors. *NeuroImage: Clin.* **12**, 707–714 (2016). <https://doi.org/10.1016/j.nicl.2016.10.003>
15. Lin, G.: An effective phase shift diffusion equation method for analysis of PFG normal and fractional diffusions. *J. Magn. Reson.* **259**, 232–240 (2015). <https://doi.org/10.1016/j.jmr.2015.08.014>
16. Lin, G.: Analyzing signal attenuation in PFG anomalous diffusion via a non-Gaussian phase distribution approximation approach by fractional derivatives. *J. Chem. Phys.* **145**(19), 194202 (2016). <https://doi.org/10.1063/1.4967403>
17. Lin, G.: The exact PFG signal attenuation expression based on a fractional integral modified-Bloch equation (2017). [arXiv:1706.02026](https://arxiv.org/abs/1706.02026)
18. Lin, G.: Fractional differential and fractional integral modified-Bloch equations for PFG anomalous diffusion and their general solutions (2017). [arXiv:1702.07116](https://arxiv.org/abs/1702.07116)
19. Madsen, H., Hellwinkel, J., Graner, M.: Clinical trials in glioblastoma—designs and challenges. In: Lichtor, T. (ed.) *Molecular Considerations and Evolving Surgical Management Issues in the Treatment of Patients with a Brain Tumor*, Chap. 13. IntechOpen (2015). <https://doi.org/10.5772/58973>
20. Magin, R., Abdullah, O., Baleanu, D., Zhou, X.: Anomalous diffusion expressed through fractional order differential operators in the Bloch-Torrey equation. *J. Magn. Reson.* **190**(2), 255–270 (2008). <https://doi.org/10.1016/j.jmr.2007.11.007>
21. Persano, L., Rampazzo, E., Della Puppa, A., Pistollato, F., Basso, G.: The three-layer concentric model of glioblastoma: cancer stem cells, microenvironmental regulation, and therapeutic implications. *Sci. World J.* **11**, 1829–1841 (2011). <https://doi.org/10.1100/2011/736480>
22. Pistollato, F., Abbadi, S., Rampazzo, E., Persano, L., Della Puppa, A., Frasson, C., Sarto, E., Scienza, R., D'avella, D., Basso, G.: Intratumoral hypoxic gradient drives stem cells distribution and mgmt expression in glioblastoma. *Stem cells* **28**(5), 851–862 (2010). <https://doi.org/10.1002/stem.415>
23. Podlubny, I.: *Fractional Differential Equations*. Academic Press (1998)
24. Reiter, D., Magin, R., Li, W., Trujillo, J., Velasco, M., Spencer, R.: Anomalous T2 relaxation in normal and degraded cartilage. *Magn. Reson. Med.* **76**(3), 953–962 (2016). <https://doi.org/10.1002/mrm.25913>
25. Sui, Y., Wang, H., Liu, G., Damen, F.W., Wanamaker, C., Li, Y., Zhou, X.J.: Differentiation of low-and high-grade pediatric brain tumors with high b-value diffusion-weighted mr imaging and a fractional order calculus model. *Radiology* **277**(2), 489–496 (2015). <https://doi.org/10.1148/radiol.2015142156>
26. Torrey, H.: Bloch equations with diffusion terms. *Phys. Rev.* **104**(3), 563–565 (1956). <https://doi.org/10.1103/physrev.104.563>
27. Wang, Z., Dabrosin, C., Yin, X., Fuster, M., Arreola, A., et al.: Broad targeting of angiogenesis for cancer prevention and therapy. *Semin. Cancer Biol.* **35**, S224–S243 (2015). <https://doi.org/10.1016/j.semcancer.2015.01.001>
28. Yu, Q., Reutens, D., O'Brien, K., Vegh, V.: Tissue microstructure features derived from anomalous diffusion measurements in magnetic resonance imaging. *Hum. Brain Mapp.* **38**(2), 1068–1081 (2017). <https://doi.org/10.1002/hbm.23441>
29. Yu, Q., Reutens, D., Vegh, V.: Can anomalous diffusion models in magnetic resonance imaging be used to characterise white matter tissue microstructure? *NeuroImage* **175**, 122–137 (2018). <https://doi.org/10.1016/j.neuroimage.2018.03.052>

A Network-Based Analysis of the Preterm Adolescent Brain Using PCA and Graph Theory



Hassna Irzan, Michael Hütel, Carla Semedo, Helen O'Reilly, Manisha Sahota, Sebastien Ourselin, Neil Marlow, and Andrew Melbourne

Abstract The global increase in the rate of premature birth is of great concern since it is associated with an increase in a wide spectrum of neurologic and cognitive disorders. Neuroimaging analyses have been focused on white matter alterations in preterm subjects and findings have linked neurodevelopment impairment to white matter damage linked to premature birth. However, the trajectory of brain development into childhood and adolescence is less well described. Neuroimaging studies of extremely preterm born subjects in their adulthood are now available to investigate the long-term structural alterations of disrupted neurodevelopment. In this paper, we examine white matter pathways in the preterm adolescent brain by combining state-of-the-art diffusion techniques with graph theory and principal component analysis (PCA). Our results suggest that the pattern of connectivity is altered and differences in connectivity patterns result in more vulnerable premature brain network.

1 Introduction

Neonatal care has transformed our ability to treat babies born at the lowest gestational ages, although increased survival has not been associated with as strong a decrease in neonatal morbidity [7]. Emerging evidence suggests that the preterm infant brain endures anatomical, microstructural and functional disruption, it is less clear, however, how these alterations extend into adulthood. This is of great concern, since the number of subjects with a wide spectrum of neurologic and cognitive disorders is increasing. This has an associated burden for society, health care systems and education. Neuroimaging studies have documented brain volume alteration [8]

H. Irzan (✉) · C. Semedo · S. Ourselin · A. Melbourne
Department Medical Physics and Biomedical Engineering,
University College London, London, UK
e-mail: hassna.irzan.17@ucl.ac.uk

H. Irzan · M. Hütel · C. Semedo · M. Sahota · S. Ourselin · A. Melbourne
Biomedical Engineering and Imaging Sciences, Kings College London, London, UK

H. O'Reilly · N. Marlow
Institute for Women's Health, University College London, London, UK

© Springer Nature Switzerland AG 2020
E. Bonet-Carne et al. (eds.), *Computational Diffusion MRI*,
Mathematics and Visualization, https://doi.org/10.1007/978-3-030-52893-5_15

and impaired white matter (WM) connectivity and correlated this with low cognitive performance following preterm birth [1]. Recent studies have analysed the structural integrity of WM in adult preterm brain; the findings revealed preservation of the global connectivity at the expense of peripheral connectivity in infants [6] and adults [2].

The primary aim of this study is to identify brain sub-networks in which term and preterm are separable and to examine the properties of such sub-networks and how critical they are to the overall functioning of the brain. The role of such sub-networks can be estimated by examining the impact on the global efficiency when inflicting damage to these sub-networks. We hypothesise that extremely premature birth affects the structure of the adolescent preterm brain and that this structural alteration negatively influences measures of brain communication efficiency and network vulnerability to attack. Generally, the WM tract architecture has been characterised by diffusion tensor imaging (DTI); more robust models are now available, which overcome some of the inherent limitations of the diffusion tensor. For example fiber tracking with constraints has improved the biological plausibility of reconstructed WM bundles [5]. Comparing all the WM pathways without an a priori hypothesis destroys the statistical power of the analysis because of multiple comparison. We use PCA to reduce the redundancy of the data, which produces deterministic and reproducible low-dimensional representations of the data in which variance is preserved. The resulting networks are amenable to graph theory analysis [9], which can be used to summarise complex networks and aid interpretation. Specifically, we use PCA to detect the network properties in which term and preterm are distinguishable. We further examine the networks by investigating network vulnerability to attack. The outline of the analysis is presented in Fig. 1.

2 Methods

We perform data preprocessing and estimate WM tracts in Sect. 2.1. We analyse the effect of the confounding variables on the global efficiency of the networks in Sect. 2.2 and identify the tracts with highest variance between term born and preterm born subjects in Sect. 2.3. To investigate the role of the sub-networks derived from PCA analysis we examine the vulnerability to attack of term and preterm brain in Sect. 2.4.

2.1 Data

Data acquisition: T1-weighted (T1w) MRI acquisitions are acquired for a cohort of adolescents born extremely preterm (<26 weeks gestation): 39/12 females/males, term born: 20/12 females/males on a 3T Philips Achieva at TR = 6.93 ms, TE = 3.14 ms and 1 mm isotropic resolution. Diffusion weighted MRI (dWMRI) volumes

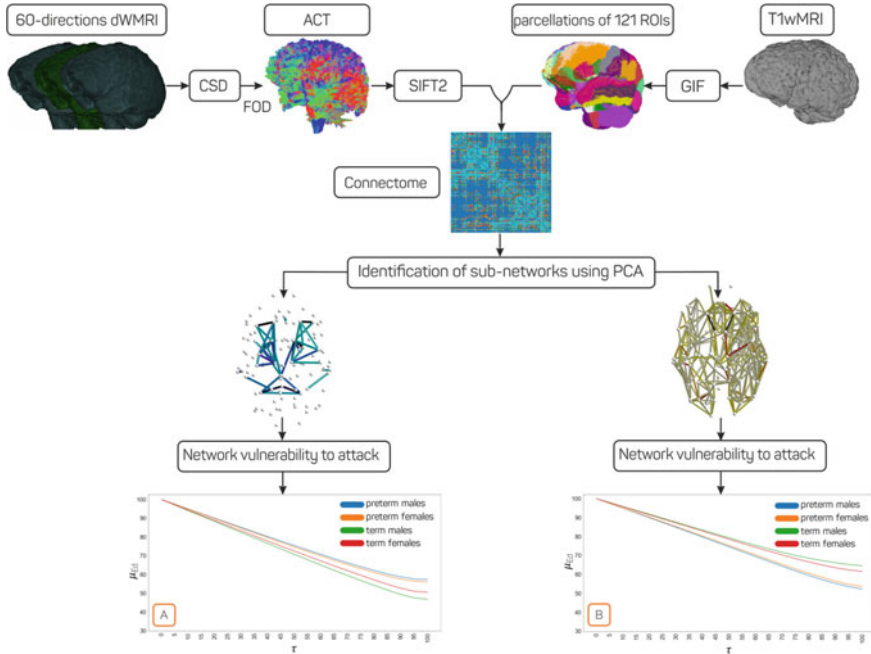


Fig. 1 The presented analysis is organised in three main steps. Top: for each individual subject a structural brain network is computed. We applied Constrained Spherical Deconvolution (CSD) algorithm to estimate the Fiber Orientation Distribution (FOD) in each voxel and performed Anatomically Constrained Tractography (ACT). From Geodesic Information Flow template we consider 121 unique regions as nodes of each connectome. The connection between each node region is quantified after applying Spherical-Deconvolution Informed Filtering of Tracks (SIFT2). Middle: Principal Component Analysis (PCA) is applied and discriminative sub-networks between preterm and term subjects are identified. Bottom: network vulnerability analysis is conducted by causing damage to the identified networks and quantifying the change in network global efficiency

are acquired at $2.5 \times 2.5 \times 3$ mm resolution across b -values of (0, 300, 700, 2000) s/mm^2 , $n = 4, 8, 16, 32$ directions and $TE = 70$ ms. On average preterm subjects were born at 24.9 ± 0.8 weeks of gestation and their average birth weight is 728.4 ± 126.3 g. The age at scan of all subjects is 19 years of age.

Data preprocessing: We apply N4ITK algorithm for bias field correction of T1-weighted images. Subject motion in the dWMI volumes is addressed by affinely registering them to the mean- b_0 volume.

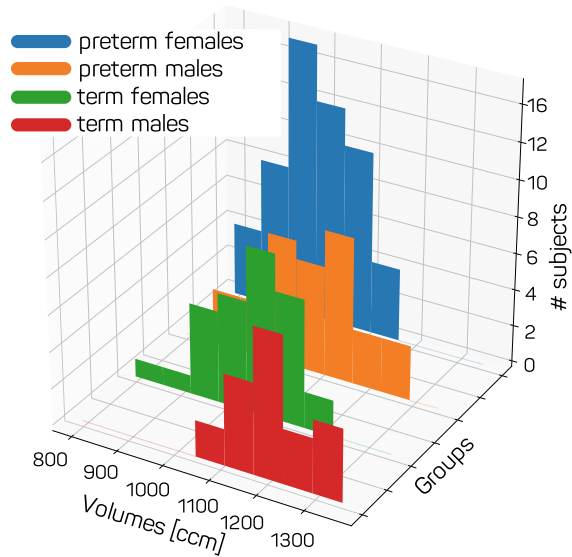
Tractography and networks extraction: All analysis is performed in the original anatomical space of each subject to minimise anatomical bias in the subsequent analysis. Brain parcellations are obtained using Geodesic Information Flow (GIF) [3]. Fibre orientation distribution (FOD) is derived by means of constrained spherical deconvolution (CSD) [12]. We normalise the FODs intensity such that they are comparable across subjects and perform anatomically constrained tractography (ACT) [10] on multi-shell data [5]. We consider 121 regions-of-interest (ROIs) of

a parcellation that include: neocortex, subcortical structures, cerebellum, pons and brainstem. For each subject i , we define a network G_i , in which J nodes are the individual ROIs and K edges are connections between each pair of ROIs equivalent to streamline count weighted by the cross-sectional area of the fibre (SIFT2) [11]. We remove the effect of network strength on global efficiency by normalising each network G_i by its total strength.

2.2 Statistical Analysis

Group, gender and brain size may present a confounding effect in the analysis. There is correlation between brain efficiency and weeks of gestation [2]. In addition, as illustrated in Fig. 2, there is difference in brain size between females and males as well as between preterm and term born subjects [4]. As such, to establish the influence of brain size, gender and group in the analysis, we test their statistical influence in the network efficiency. The statistical model is $E = \beta_0 X_0 + \beta_1 X_1 + \beta_2 X_2 + \beta_3 X_3 + \epsilon$, where β_0 is the intercept, X_1 , X_2 are regressors encoding for group and gender membership respectively, X_3 the brain size values and E the network global efficiency.

Fig. 2 Brain volume distribution for preterm born females, preterm born males, term born females and term born males



2.3 Identification of Sub-networks Using PCA

We apply PCA to the set of edges of N subjects networks $\{G_i, i = 1 \dots N\}$ to obtain the first C eigenvectors $\mathbf{E} \in R^{K \times C}$ that approximate 90% of the variance in all edges $\mathbf{X} \in R^{N \times K}$. \mathbf{X} is projected onto the C eigenvectors to obtain the reduced data $\mathbf{X}_{\text{red}} = \mathbf{X}\mathbf{E}$. We then investigate the capability of each eigenvector E_c to separate term from preterm subjects. We test the statistical significance of this by running the Kruskal-Wallis test because it has no assumptions about the distribution of the data. To compensate for multiple comparisons, we test each individual null hypothesis at a significance level of α/C (Bonferroni correction), with $\alpha = 0.05$.

2.4 Network Vulnerability to Attack

We investigate how damaging some nodes or edges impacts the appropriate functioning of a network, which we model as the capacity of information transfer. We associate the network performance with its global efficiency E_G . We define the efficiency decay as $E_d = E_{G_d}/E_G$ with E_G and E_{G_d} the global efficiency of the intact and damaged network, respectively. The damage to network G_d is carried out by setting the weights of the targeted connection w_{ij} to $w_{ij}^d = w_{ij} \times (1 - \tau/100)$ [13], where τ is the inflicted damage ranging from a minimum of 0 (no damage) to a maximum of 100 (full damage). We test the brain network vulnerability by performing targeted attacks to the sub-network that best separates preterm from term subjects. We carry vulnerability analysis for each network G_i and evaluate the mean E_d (μ_{E_d}) value for each group. The main aim of these tests is not only to identify the most critical structures or connections for the network performance, but to investigate if the preterm born network is more or less vulnerable to attack and which brain regions or network are more critically impacted.

3 Results

3.1 Statistical Analysis

With respect to the network global efficiency E , the statistical analysis indicated that there was not significant statistical influence of gender ($p = 0.253$) and brain size ($p = 0.064$). The group membership was statistically significant ($p = 0.010$).

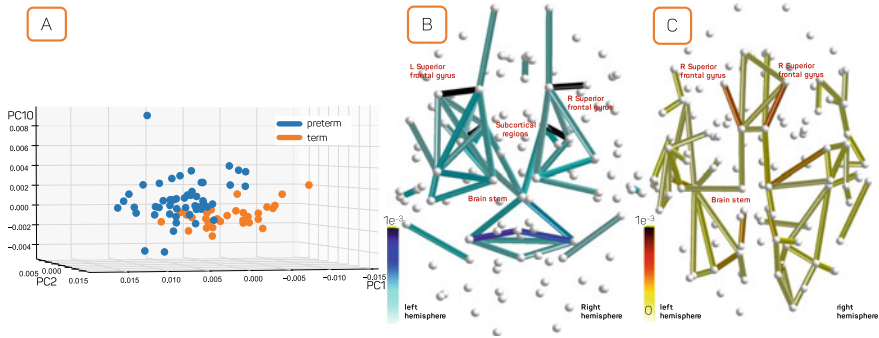


Fig. 3 **A** The three PCs with discriminatory power between term born (females and males) and preterm born (females and males) subjects. The corresponding eigenvectors reveal the underlying sub-networks: **B** sub-network from the lowest 25% values shows connections from the fronto-parietal areas to the deep grey matter regions and **C** sub-network from the highest 25% values displays a widespread connectivity

3.2 Identification of Sub-networks Using PCA

Forty principal components (PCs) explained 90% of the variation in the dataset. The PCs with discriminatory power between term and preterm were 1st ($p = 2.02e^{-6}$), 2nd ($p = 5.82e^{-4}$) and 10th ($p = 2.93e^{-5}$). All PCs are statistically significant after Bonferroni correction. Figure 3A captures the separation between term and preterm born subjects along these PCs. The discriminatory sub-network between the preterm and term group is obtained as $\lambda_1 v_1 + \lambda_2 v_2 + \lambda_{10} v_{10}$. Where, the linear combination of the eigenvectors (v_1, v_2, v_{10}) corresponding to the 1st, 2nd, and 10th PCs is weighted by the mean contribution of the preterm subjects in each PC ($\lambda_1, \lambda_2, \lambda_{10}$). Figure 3B illustrates the top 25% negative values and Fig. 3C the top 25% positive values. The highest weights are found in connections of bilateral middle and superior frontal gyrus, bilateral precentral gyrus, bilateral thalamus and putamen, bilateral caudate, right supplementary motor cortex. The connectivity strength in the sub-network Fig. 3B is significantly reduced ($p = 4.68e^{-5}$) in the preterm subjects ($\mu = 2.14e^{-2} \pm 5.9e^{-3}$) compared to term subjects ($\mu = 2.80e^{-2} \pm 5.7e^{-3}$). Preterm group ($\mu = 2.33e^{-2} \pm 5.41e^{-3}$) have a comparable ($p = 0.11$) connectivity strength in the sub-network in Fig. 3C with term born group ($\mu = 2.15e^{-2} \pm 5.0e^{-3}$).

3.3 Network Vulnerability to Attack

The effect of targeted attack to the sub-networks in Fig. 3B, C is shown in Fig. 4A, B respectively from null (0) to full (100) damage. Figure 4A shows that targeted attack to the connections in sub-network in Fig. 3B results in a slight reduction of

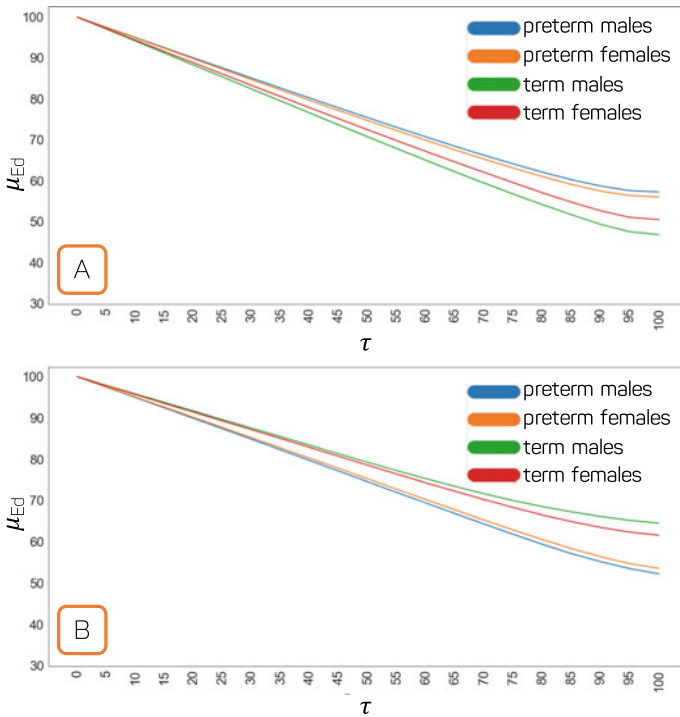


Fig. 4 The effect on the brain of progressively increasing the inflicted damage from a minimum of no damage $\tau = 0$ to a maximum of full damage $\tau = 100$: **A** The effect on the brain network of damaging sub-network in Fig. 3B and **B** sub-network in Fig. 3C

global efficiency for the full term groups more than the preterm groups; this is more pronounced in the full term males. The decay of global efficiency when damaging the sub-network in Fig. 3C shows higher vulnerability in the preterm groups (males and females) with respect to the control group (about 12.8% less).

4 Discussion

This study investigates differences in structural connectivity between 19 year-old adolescents born extremely preterm (born before 26 weeks completed gestation) and their socio-economically matched term-born peers.

The main finding is that the connectivity in the preterm brain is altered leading to a more vulnerable network. The strength is reduced in the network in Fig. 3B, while it is preserved in the connections in Fig. 3C. Furthermore, the vulnerability analysis suggests that the full term subjects are relatively more vulnerable in the sub-network in between fronto-parietal and subcortical structures (Fig. 3B). In this respect, it is

more plausible that this sub-network is preserved in preterm subjects. However, when damaging the network in Fig. 3C, the preterm subjects showed higher vulnerability regardless of gender. This supports the hypothesis of a widespread vulnerability to attack in the preterm brain network suggesting an overall fragile network.

Brain connectivity is affected by brain volume, however the functional relationship between brain size and streamline count is not known [4]. In our cohort, there are differences in average brain volume between groups (Fig. 2). Therefore, we analysed the influence of gender, group and brain size on the brain global efficiency; the results showed that only prematurity condition affects the global efficiency ($p = 0.010$). Hence, we compared term born (females and males) and preterm born (females and male) subjects in the analysis.

The interpretation of graph metrics makes assumptions about the network. For example, the network global efficiency definition assumes that the signals propagate in the network along the shortest paths between network elements. Although this assumption is sensible for artificial networks, there is no tangible evidence that such hypothesis holds for the human brain which may have different optimisation criteria. Graph theory analysis of networks is also sensitive to the parcellation scheme; a more detailed analysis could result from a higher resolution network. Here, the PCA analysis is biased towards the average preterm network as there are more preterm born subjects. To mitigate this effect we ran the same analysis with matched sample size of term and preterm born subjects and observed the same results.

This work has shown differences in the connectivity of the adolescent brain network after preterm birth; such abnormalities resulted in a network more vulnerable to network damage. Future work will aim to detect the nature of such alterations by analysing white matter microstructure at the voxel level and within individual brain regions linked to the sub-networks we have identified (hubs and peripheral regions). In addition, we aim to investigate the neuropsychological correlates of the sub-networks that we have established.

Acknowledgments We acknowledge the EPSRC-funded UCL Centre for Doctoral Training in Medical Imaging (EP/L016478/1), the National Institute for Health Research (NIHR) and the MRC (MR/J01107X/1).

References

1. Ball, G., et al.: Thalamocortical connectivity predicts cognition in children born preterm. *Cereb. Cortex* (New York, N.Y.: 1991) **25**(11), 4310–4318, 11 (2015)
2. Batalle, Dafnis., et al.: Early development of structural networks and the impact of prematurity on brain connectivity. *NeuroImage* **149**, 379–392 (2017)
3. Cardoso, M.J., et al.: Geodesic information flows: spatially-variant graphs and their application to segmentation and fusion. *IEEE Trans. Med. Imaging* **34**(9), 1976–1988 (2015)
4. Hänggi, J., et al.: The hypothesis of neuronal interconnectivity as a function of brain size—a general organization principle of the human connectome. *Frontiers Hum. Neurosci.* **8**, 915, 11 (2014)

5. Jeurissen, Ben., et al.: Multi-tissue constrained spherical deconvolution for improved analysis of multi-shell diffusion mri data. *NeuroImage* **103**, 411–426 (2014)
6. Karolis, V.R., et al.: Reinforcement of the brain's rich-club architecture following early neurodevelopmental disruption caused by very preterm birth. *Cereb. Cortex (New York, N.Y.: 1991)* **26**(3), 1322–1335, 03 (2016)
7. Moore, T., et al.: Neurological and developmental outcome in extremely preterm children born in england in 1995 and 2006: the epicure studies. *BMJ: British Med. J.* **345**, e7961, 12 (2012)
8. Nosarti, C., et al.: Adolescents who were born very preterm have decreased brain volumes. *Brain* **125**(7), 1616–1623, 07 (2002)
9. Rubinov, Mikail., et al.: Complex network measures of brain connectivity: uses and interpretations. *NeuroImage* **52**, 1059–1069 (2010)
10. Smith, Robert E., et al.: Anatomically-constrained tractography: improved diffusion mri streamlines tractography through effective use of anatomical information. *NeuroImage* **62**(3), 1924–1938 (2012)
11. Smith, Robert E., et al.: Sift2: enabling dense quantitative assessment of brain white matter connectivity using streamlines tractography. *NeuroImage* **119**, 338–351 (2015)
12. Tournier, J.-D., et al.: Robust determination of the fibre orientation distribution in diffusion mri: Non-negativity constrained super-resolved spherical deconvolution. *NeuroImage* **35**(4), 1459 – 1472 (2007)
13. van den Heuvel, M.P., et al.: Aberrant frontal and temporal complex network structure in schizophrenia: a graph theoretical analysis. *J. Neurosci.* **30**(47), 15915, 11 (2010)

Diffusion MRI Fiber Tractography by Flow Field Formation with Extended Physarum Solver: A Pilot Study with 2D Phantoms



Yoshitaka Masutani

Abstract Information of the brain white matter fiber bundle structures is obtained by diffusion MRI (dMRI) analysis and is already indispensable for medical science and clinical medicine. Since the fundamental technique for tractography was presented about twenty years ago, various methodologies have been developed and reported. However, this problem leaves room for technical improvement, especially for application in clinical dMRI data of limited quality. In this study, a novel approach based on the physarum solver was investigated. Through the experiments on synthetic and real data sets, potentials and limitations of the approach were displayed and discussed.

1 Introduction

The fiber tractography based on diffusion MRI (dMRI) data is widely used in both clinical purpose and brain science research [1]. The detail information brought by tractography including the connectivity within the brain white matter opened a new horizon of the brain science. In addition, it is almost indispensable for navigation of minimally invasive neurosurgery, in which the important fiber structures must not be damaged.

Since the original FACT algorithm by Mori et al. [2] has been proposed, various algorithms have been investigated based on various theories and approaches. One of the important categorizations is deterministic or probabilistic. The term; deterministic tractography is a kind of retronym, which was given when the probabilistic approach [3] was newly proposed. Similarly, local approach is also defined for distinguishing the new approach of global tractography [4]. In those approaches, reliable information of local fiber orientation(s) within a voxel, i.e. assuming cases of crossing, kissing, and fanning fibers, is the key for tractography. In that sense, the family of approaches by spherical deconvolution [5] is promising for the purpose when higher angular resolution is available. In addition, recent updates include machine-learning

Y. Masutani (✉)
Hiroshima City University, Hiroshima, Japan
e-mail: masutani@hiroshima-cu.ac.jp

© Springer Nature Switzerland AG 2020
E. Bonet-Carne et al. (eds.), *Computational Diffusion MRI*,
Mathematics and Visualization, https://doi.org/10.1007/978-3-030-52893-5_16

approaches [6, 7] for empirical determination of local fiber orientation, which seem to have potentials to cope with clinical data of limited quality.

In the current situations, the problems of fiber tractography leave rooms for technical improvement [1], and it is worth considering new approaches based on various theories and methodologies. On that standpoint, a novel approach based on the physarum solver [8] was investigated in this study. It is a computational simulation of the amoeboid organism behavior to form an optimal network [9], and is applied to maze-solving for the shortest route finding on graphs. This tractography approach by using the physarum solver has certain similarity with the existing methodologies, which are described later in the discussion section. When applying the physarum solver, it is necessary to extend the theory in several aspects since tractography is not a simple problem of optimal path finding. Therefore, a few extensions of the physarum solver dedicated to dMRI fiber tractography are proposed in this study.

In this paper, the basics and the extension of the physarum solver are described first. Then, feasibility studies by using 2D phantoms are performed and their results are shown. Finally, potentials and limitations of the approach were discussed with referring to the existing similar approaches.

2 Methods

2.1 Physarum Solver Basics

The physarum solver [8] is adapted to an undirected graph to find optimal path from a node to a node. For an undirected graph consisting of nodes; $N_i (i = 1, 2, \dots, n)$, and edges; $M_{i,j} (i \neq j)$ connecting nodes N_i and N_j with a single source; N_1 and a single sink; N_2 are given with total flux I_0 from the source. By assuming Poiseuille flow on the graph as network of pipes, we get the flux Q_{ij} at an edge $M_{i,j}$ as a pipe is defined as;

$$Q_{ij} = \frac{\pi a_{ij}^4}{8\kappa} \frac{p_i - p_j}{L_{ij}} \quad (1)$$

where a_{ij} is the radius of the pipe, κ is the viscosity coefficient, p_i and p_j are the pressures at the nodes N_i and N_j respectively, and L_{ij} is the length of the pipe. When we define conductivity D_{ij} at $M_{i,j}$ as;

$$D_{ij} = \frac{\pi a_{ij}^4}{8\kappa}, \quad (2)$$

The Eq. (1) is rewritten as below.

$$Q_{ij} = \frac{D_{ij}}{L_{ij}} (p_i - p_j) \quad (3)$$

By the conservation law of the flow material, we obtain a linear equation for each node; N_i below.

$$\sum_j Q_{ij} = \begin{cases} I_0 & (i = 1) \\ -I_0 & (i = 2) \\ 0 & (i \neq 1, 2) \end{cases} \quad (4)$$

When the conductivities are regarded as constant, we get a unique combination of pressures as a set of solution and consequently flux values for all edges. In addition, by simulating the network behavior of physarum, conductivity is dynamically changed as;

$$\frac{d}{dt} D_{ij} = f(|Q_{ij}|) - D_{ij} \quad (5)$$

where $f(\cdot)$ is a monotonically increasing and continuous function to update conductivity with satisfying $f(0) = 0$. For example, $f(x) = x$ was used in this study. By discretizing (5), we get the update equation;

$$D_{ij}^{t+1} = (1 - \alpha)D_{ij}^t + \alpha f(|Q_{ij}^t|) \quad (6)$$

where t is a time parameter for generation of update and α is an update rate. Also after the conductivities are dynamically changed, pressure values are updated by solving (4) iteratively. The linear equations contain only sparse non-zero components due to that inter-node connections are limited to their neighbors. Therefore, the solution is effectively obtained via the ICCG (Incomplete Cholesky factorization for Conjugate Gradient) solver [8, 10]. After certain generations of updates, limited numbers of edges have high flux values, which indicate the optimal path from the source to the sink. Otherwise, flux converges to virtually zero. Thus, the network is adapted to find the optimal path from the source to the sink. An example of maze-solving by physarum solver is shown in Fig. 1.

2.2 Extending Physarum Solver for Diffusion MRI Fiber Tractography

In this study, the physarum solver is applied to the pixel/voxel graphs of dMRI data on a regular grid for fiber tractography. Due to two potential problems of tractography become critical then, the physarum solver is extended for the purpose. One is uncertainty of tracking termination point. That is, when an explicit seed point to start tracking is defined, the corresponding target (or goal) point to terminate tracking cannot be specified in advance. This is not a suitable situation for the solver in which explicit source and sink nodes must be defined. The other is a problem regarding size of seed/target ROI configuration. It is very hard to define the ROIs in just enough sizes for the fiber tract expected to be extracted before tracking. Therefore, larger

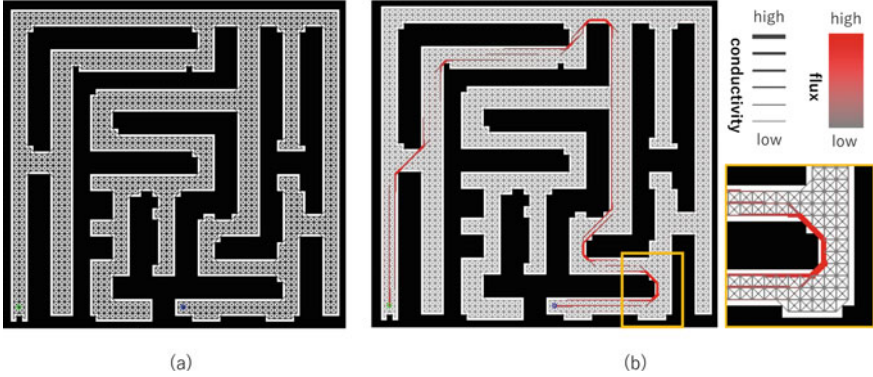


Fig. 1 Maze-Solving Example (Shortest-Path Finding) by Physarum Solver. **a** Undirected graph network with a source node (green) and a sink node (blue). **b** Solution display after 250 generations of update. Note that the optimal path is highlighted with red thick lines indicating high conductivity and high flux including several parallel routes due to their identical path length

ROIs are often used initially and are iteratively adjusted until the expected tract is obtained. In addition, it is necessary to consider the shortest path not in the Euclid distance but in the direction of high fiber tract probabilities. Also avoiding zig-zag trajectories resulting from graph edge patterns, smoothing of the extracted path must be considered.

To overcome these problems, the physarum solver is extended in this study. The main components of the extension are three-fold; (1) addition of virtual nodes, (2) modulation of edge length by local property deriving from anisotropic diffusion, and (3) conversion of graph to flow field. The extensions are described below.

Virtual Nodes. First of all, multi-source and multi-sink nodes are allowed to be defined for tractography with certain size of seed and target ROIs. In addition, a virtual source and a virtual sink are introduced, which are connected to multi-source nodes and multi-sink nodes respectively. This yields selectivity of nodes among multi-source/sink during network adaptation. The placement of these nodes are inspired by the graph configuration for image segmentation by GraphCuts [11].

Edge Length Modulation by Anisotropic Diffusion. For emphasizing flux in orientation of high diffusion probability, edge length is modulated based on diffusion properties at the two nodes at the ends of the edge. In this study, diffusion tensor is employed for the modulation. For the original edge length; $L_{ij} = (1, \sqrt{2}, \text{ or } \sqrt{3})$ as inter-pixel/voxel distance, modulated edge length; L'_{ij} is defined instead as;

$$L'_{ij} = L_{ij} \cdot \phi(\mathbf{T}_i, \mathbf{T}_j) \quad (7)$$

where \mathbf{T}_i denotes diffusion tensor at the node N_i , $\phi(\cdot)$ is a modulation function. The function should be designed to shorten the length of edges directed to similar

orientations of high diffusion probability. The function below was employed in this study.

$$\phi(\mathbf{T}_i, \mathbf{T}_j) = \max\{(1 - |\mathbf{v}_i \cdot \mathbf{m}_{ij}|)^{FA_i}, (1 - |\mathbf{v}_j \cdot \mathbf{m}_{ij}|)^{FA_j}\} \quad (8)$$

where \mathbf{m}_{ij} denotes the normalized orientation vector of the edge $M_{i,j}$ from N_i to N_j , \mathbf{v}_i represents the principal eigenvector of D_i , and FA_i is fractional anisotropy (FA) value of \mathbf{T}_i . By this modulation, high flux is yielded on edges in direction of high diffusivity with considering diffusion anisotropy. Natural extension of the modulation can be realized by use of ODF (Orientation Distribution Function) [1] instead of the diffusion tensor.

Converting Graph to Flow Field. After certain updates of the graph by the extended physarum solver described above, global flux from sources to sinks is formed, which are consistent with local anisotropic diffusion. When fiber tracking is performed from a node with in the sources, the path toward the sinks is obtained as a group of edges in a zig-zag shape. To smooth the fiber trajectory, the graph with flux is converted to a flow field. That is, flow vector; \mathbf{F}_i at each node; N_i on the regular grid is given by a flux-weighted average of outflow vector from the node as;

$$\mathbf{F}_i = \sum_j W_{ij} \mathbf{n}_{ij} \quad (9)$$

where W_{ij} is a weighting factor for the edge; $M_{i,j}$ as shown below.

$$W_{ij} = \left\{ R(Q_{ij}) / \sum_j R(Q_{ij}) \right\}^\beta \quad (10)$$

$R(\cdot)$ is the ramp function to omit inflow and $\beta (\geq 0)$ represents a factor to emphasize directivity. When β is zero, flux quantity; Q_{ij} is never considered, and larger β yields higher directivity based on directional distribution of Q_{ij} . Note that the flow vectors obtained above only define directions of fiber tracking, and are not used to tracking termination criteria. In this study, sum of outflow; $\sum_j R(Q_{ij})$ was used in addition to the standard criteria such as FA values and path length.

2.3 Tractography as Streamlines in Flow Field

After the vector field formation, fiber tracking is performed by a standard stream-line method [12]. For each start point within the given seed area, tracking is iterated until reaching to the target area, or is terminated when several conditions are satisfied. As the tracking termination criteria, lower bound for FA, sum of out-flow, and maximum number of iteration are employed in this study.

3 Results

3.1 Synthetic Data Experiments

For confirming the effect of virtual nodes, synthetic data set in 40×40 matrix size with uniform isotropic diffusion tensors was used (Fig. 2a). Among the pixel graph of fully-connected 8 neighbors, simple vertical flow field only in the center part of the data is expected between multiple sources and sinks at the upper and lower ends. Without virtual nodes, input and output flux was equally distributed among the multi-source and sink, and non-negligible amount of flux was yielded (Fig. 2b, c), and consequently diagonal streamlines were yielded (Fig. 2d). With virtual nodes (Fig. 2e, f), selectivity avoiding flux from/to unnecessary nodes was observed and most of streamlines were vertical (Fig. 2g, h). In addition, it is interesting that certain concentration of flux was observed at the border with unnecessary nodes (Fig. 2f). In Fig. 3, the effect of edge length modulation and the parameters is shown with another synthetic data set with a simple configuration of fully connected pixel graph with a single source and a single (Fig. 3a). In addition, the anisotropic tensor field showing radial directions of principal vectors centered at the upper left corner (Fig. 3b) was used for edge length modulation. As shown in Fig. 3c, d without the modulation, simple diagonal flow and streamline were observed. With the modulation, depending on the parameters, the streamlines were bent along the radial flow of the tensor field.

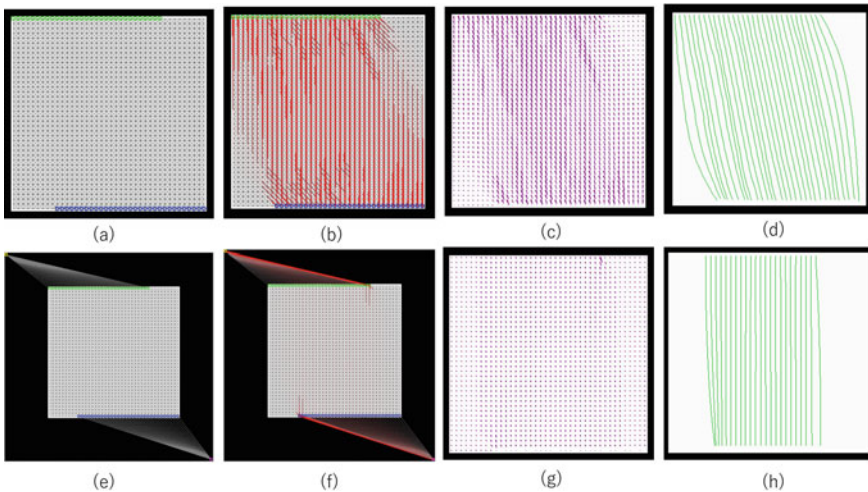


Fig. 2 Effect of Virtual Nodes in Synthetic Data. **a–d** Without virtual nodes. **e–h** With virtual nodes. **a** and **e** graph setting with multi-source (green) and multi-sink (blue). In **e**, a virtual source (yellow) shown at the upper left corner is connected to all the source nodes, and identically a virtual sink (magenta) at the bottom right is also for all the real sinks. **b** and **f** after 200 iterations. **c** and **g** flow field. **d** and **h** streamlines

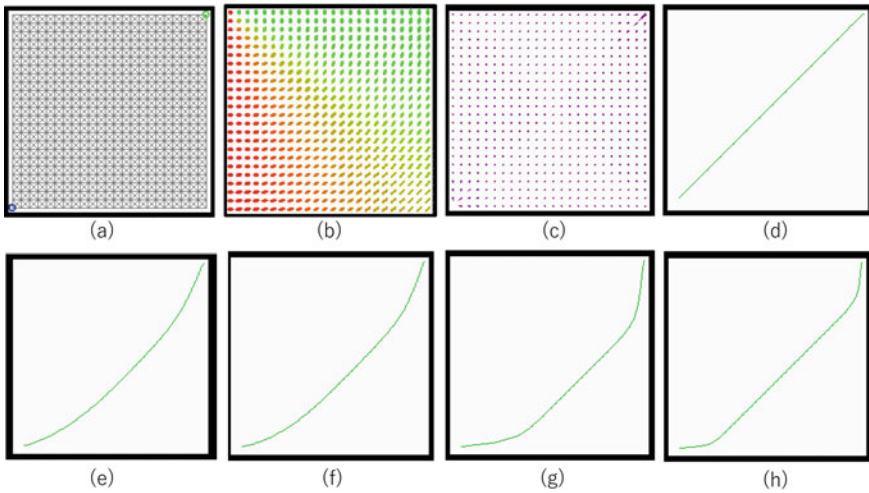


Fig. 3 Effect of Edge Length Modulation by Diffusion Tensor Field and the Parameters. **a** Pixel-graph configuration with single source and single sink. **b** Anisotropic tensor field with orientation color-coding for edge length modulation. **c** Flow field formation result without the modulation. **d** Streamline for **d** with a seed point at the source node. **e–h** streamline results with the modulation. **e** $\beta = 0.8$ and 100 iterations. **f** $\beta = 1.0$ and 100 iterations. **g** $\beta = 4.0$ and 100 iterations. **h** $\beta = 1.0$ and 400 iterations

As seen in higher directivities; β and more iteration of updates, the path shape is quantized to small variations of orientation to show that there exists significant dependency on those parameters.

3.2 FiberCup Data Experiment

Figure 4 shows the results for the FiberCup data [13, 14], which contains fiber-crossing (e.g. yellow frame in Fig. 4a) where conventional algorithms fail to track. A smooth fiber tracts were obtained beyond two crossing area (Fig. 4g). In the graph, 1,000 nodes and 3,173 edges were yielded. With a standard laptop PC (Apple Macbook Pro), the computation time was 25 s for the whole process including 100 iteration of conductivity updates, flow field formation and fiber tracking.

4 Discussion

In this study, the physarum solver was extended for the purpose of applying to dMRI fiber tractography. The experimental results revealed basic characteristics of the approach including its potentials. As shown in the result, one of the most important

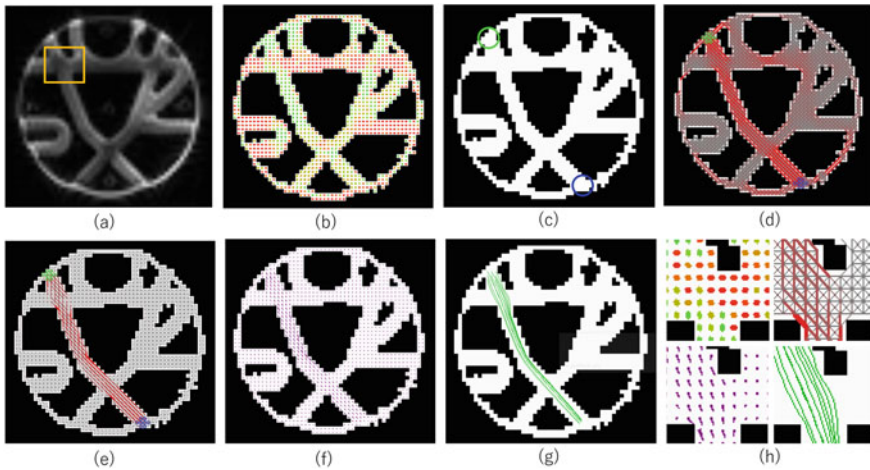


Fig. 4 Fiber Tractography by Extended Physarum Solver in FiberCup Data. **a** Original dMRI data ($b = 0$ image). **b** diffusion tensor field with binary mask given by thresholding the $b = 0$ image. **c** Tractography ROI setting for seed (green) and target (blue), also used for source and sink node configuration in physarum solver. **d** Initial solution by physarum solver with of multi-source/sink graph. **e** After 100 iterations. **f** Flow field converted from (e). **g** Streamlines from seed points given in seed ROI. **h** Zoomed images of (b), (e), (f) and (g) within the frame shown in (a)

feature is that it can consider global structure of extracted fiber tract similarly to the global approach [4], which is indispensable with solving the crossing fiber problem. That is, global smooth stream from sources to sinks takes priority over the local fiber orientation information with uncertainty, while considering the local consistency of diffusion anisotropy to adjustable extent. This feature is commonly observed among the existing tractography approaches of wide spectrum aimed at solving the problem. Those approaches are categorized in three groups and are discussed in comparison with the proposed method.

First of all, shortest-path approaches have been proposed and discussed in the past decade [15–18], which shares similar concept with the physarum solver. The former two approaches [15, 16] perform the shortest-path finding on the graph, and therefore suffer from path direction quantization and yield zig-zag trajectories. In the proposed method, however, streamline within vector field converted from graph fixed the problem and can yield smooth trajectories. The latter two approaches [17, 18] from the same group use no graph structure and are combined with the probabilistic approach. The most important problem of the shortest-path approaches is that it basically requires two explicit endpoints of the path, which are hard to determine in advance. On the other hand, the proposed method can avoid this issue by using multiple source and sink and conversion to vector field.

The next category is family of the space-warping and geodesic approaches [19–21]. O’Donnell et al. [19] defined tensor-warped space, which is almost equivalent to the tensor-based edge length modulation in this study. Tractography by fast-marching

method of level set [20] is also similar to the space-warping by controlling the speed function. The recent report of utilizing adjugate diffusion tensor [21] is on the basis of a similar concept. The uniqueness of the proposed method in comparison with them can be that these concept is performed on the graph structure.

In the sense of forming flow vector field, there found certain similarity with the fluid mechanics approach by Hageman et al. [22]. However, fluid simulation can be categorized in local approaches have little essence of the optimization to form path as global shape. Thus, the proposed approach based on the extended physarum solver has similarity and uniqueness in comparison with the existing approaches and detailed comparison is planned.

An important limitation of the proposed approach is the cost for computation. Even in the simple 2D datasets, thousands of nodes and edges are yielded for the graph. When this approach is extended to 3D data, it is necessary to take a measure to reduce graph size based on diffusion properties such as anisotropy and anatomical information. Also, the dependency on the parameters such as iteration number of graph updates and directivity emphasizing factor increases complexity and may prevent from practical use of the approach. Further investigations including tuning for optimal setting are also required as the future work.

5 Summary

In this paper, preliminary results of dMRI fiber tractography with the extended physarum solver was presented. Through the experiments by using the 2D datasets of synthetic and real phantoms, certain potentials for solving the crossing fiber problems were shown with dependency to various parameters included in the methodologies as a limitation. Further investigation and modification of the algorithm are planned including 3D extension of the approach for tractography in clinical dMRI data, use of ODF of the edge length modulation, and optimal parameter tuning.

Acknowledgments The author is grateful to Prof. Atsushi Tero in Kyushu University, Japan and his group for the valuable discussion and advice on the physarum solver. This research was partially supported by JST CREST Grant Number JPMJCR15D1.

References

1. Jeurissen, B., Descoteaux, M., Mori, S., Leemans, A.: Diffusion MRI fiber tractography of the brain. *NMR Biomed.* **32**(4), e3785 (2019)
2. Mori, S., Crain, B.J., Chacko, V.P., van Zijl, P.C.: Three-dimensional tracking of axonal projections in the brain by magnetic resonance imaging. *Ann. Neurol.* **45**(2), 265–269 (1999)
3. Behrens, T.E.J., Berg, H.J., Jbabdi, S., Rushworth, M.F.S., Woolrich, M.W.: Probabilistic diffusion tractography with multiple fibre orientations: what can we gain? *Neuroimage* **34**(1), 144–155 (2007)

4. Reisert, M., Mader, I., Anastasopoulos, C., Weigel, M., Schnell, S., Kiselev, V.: Global fiber reconstruction becomes practical. *Neuroimage* **54**(2), 955–962 (2011)
5. Tournier, J.D., Calamante, F., Gadian, D.G., Connelly, A.: Direct estimation of the fiber orientation density function from diffusion-weighted MRI data using spherical deconvolution. *Neuroimage* **23**(3), 1176–1185 (2004)
6. Neher, P.F., Götz, M., Norajitra, T., Weber, C., Maier-Hein, K.H.: A machine learning based approach to fiber tractography using classifier voting. In: Navab, N., Hornegger, J., Wells, W.M., Frangi, A. (eds.) *MICCAI 2015 (Part I)*, LNCS, vol. 9349, pp. 45–52. Springer, Cham (2015)
7. Koppers, S., Merhof, D.: Direct estimation of fiber orientations using deep learning in diffusion imaging. In: Wang, L., Adeli, E., Wang, Q., Shi, Y., Suk, H.I. (eds.) *MLMI 2016*, LNCS, vol. 10019, pp. 53–60. Springer, Cham (2016)
8. Tero, A., Kobayashi, R., Nakagaki, T.: Physarum solver: a biologically inspired method of road-network navigation. *Phys. Stat. Mech. Appl.* **363**(1), 115–119 (2006)
9. Nakagaki, T., Yamada, H., Toth, A.: Maze-solving by an amoeboid organism. *Nature* **407**, 470 (2000)
10. Kershaw, D.S.: The incomplete Cholesky-conjugate gradient method for the iterative solution of systems of linear equations. *J. Comput. Phys.* **26**(1), 43–65 (1978)
11. Boykov, Y., Funka-Lea, G.: Graph cuts and efficient N-D image segmentation. *Int. J. Comput. Vis.* **70**(2), 109–131 (2006)
12. Faber, T.E.: *Fluid Dynamics for Physicists*. Cambridge University Press, Cambridge (1995)
13. Poupon, C., Rieul, B., Kezele, I., Perrin, M., Poupon, F., Mangin, J.F.: New diffusion phantoms dedicated to the study and validation of HARDI models. *Magn. Reson. Med.* **60**, 1276–1283 (2008)
14. Original Fibercup—Data. http://www.tractometer.org/original_fibercup/data/. Last accessed 29 Aug 2019
15. Sotiropoulos, S.N., Bai, L., Morgan, P.S., Constantinescu, C.S., Tench, C.R.: Brain tractography using Q-Ball imaging and graph theory: improved connectivities through fibre crossings via a model-based approach. *Neuroimage* **49**(3), 2444–2456 (2010)
16. Brown, C.J., Booth, B.G., Hamarneh, G.: K-confidence: assessing uncertainty in tractography using K optimal paths. In: *Proceedings IEEE 10th International Symposium on Biomedical Imaging*, pp. 250–253 (2013)
17. Schober, M., Kasenburg, N., Feragen, A., Hennig, P., Hauberg, S.: Probabilistic shortest path tractography in DTI using gaussian process ODE solvers. In: Golland, P., Hata, N., Barillot, C., Hornegger, J., Howe, R. (eds.) *MICCAI 2014 (Part III)*, LNCS, vol. 8675, pp. 265–272. Springer, Cham (2014)
18. Hauberg, S., Schober, M., Liptrot, M., Hennig, P., Feragen, A.: A random riemannian metric for probabilistic shortest-path tractography. In: Navab, N., Hornegger, J., Wells, W., Frangi, A. (eds.) *MICCAI 2015 (Part I)*, LNCS, vol. 9349, pp. 597–604. Springer, Cham (2015)
19. O’Donnell, L., Haker, S., Westin, C.F.: New approaches to estimation of white matter connectivity in diffusion tensor MRI: Elliptic PDEs and geodesics in a tensor-warped space. In: Dohi, T., Kikinis, R. (eds.) *MICCAI 2002 (Part I)*, LNCS, vol. 2488, pp. 459–466. Springer, Heidelberg (2002)
20. Parker, G.J.M., Wheeler-Kingshott, C.A.M., Barker, G.J.: Estimating distributed anatomical connectivity using fast marching methods and diffusion tensor imaging. *IEEE Trans. Med. Imaging* **21**(5), 505–512 (2002)
21. Fuster, A., Dela Haije, T., Tristán-Vega, A., Plantinga, B., Westin, C.F., Florack, L.: Adjugate diffusion tensors for geodesic tractography in white matter. *J. Math. Imaging Vis.* **54**, 1–14 (2016)
22. Hageman, N.S., Toga, A.W., Narr, K., Shattuck, D.W.: A diffusion tensor imaging tractography algorithm based on Navier-Stokes fluid mechanics. *IEEE Trans. Med. Imaging* **28**(3), 348–360 (2010)

CDMRI'19 MUDI Challenge

Acquiring and Predicting Multidimensional Diffusion (MUDI) Data: An Open Challenge



Marco Pizzolato, Marco Palombo, Elisenda Bonet-Carne, Chantal M. W. Tax, Francesco Grussu, Andrada Ianus, Fabian Bogusz, Tomasz Pieciak, Lipeng Ning, Hugo Larochelle, Maxime Descoteaux, Maxime Chamberland, Stefano B. Blumberg, Thomy Mertzaniidou, Daniel C. Alexander, Maryam Afzali, Santiago Aja-Fernández, Derek K. Jones, Carl-Fredrik Westin, Yogesh Rathi, Steven H. Baete, Lucilio Cordero-Grande, Thilo Ladner, Paddy J. Slator, Joseph V Hajnal, Jean-Philippe Thiran, Anthony N. Price, Farshid Sepehrband, Fan Zhang, and Jana Hutter

Abstract In magnetic resonance imaging (MRI), the image contrast is the result of the subtle interaction between the physicochemical properties of the imaged living tissue and the parameters used for image acquisition. By varying parameters such

M. Pizzolato

Department of Applied Mathematics and Computer Science, Technical University of Denmark, Kongens Lyngby, Denmark

M. Pizzolato (✉) · J.-P. Thiran

Signal Processing Lab (LTS5), École Polytechnique Fédérale de Lausanne (EPFL), Lausanne, Switzerland

e-mail: marco.pizzolato@epfl.ch

M. Palombo · E. Bonet-Carne · F. Grussu · S. B. Blumberg · T. Mertzaniidou · D. C. Alexander · P. J. Slator

Centre for Medical Image Computing, Department of Computer Science, University College London, London, UK

E. Bonet-Carne

BCNatal Fetal Medicine Research Center, Barcelona, Spain

C. M. W. Tax

Cardiff University Brain Research Imaging Centre (CUBRIC), School of Physics and Astronomy, Cardiff University, Cardiff, UK

University Medical Center Utrecht, Utrecht, The Netherlands

F. Grussu

Queen Square MS Centre, UCL Queen Square Institute of Neurology, Faculty of Brain Sciences, University College London, London, UK

A. Ianus

Champalimaud Research, Champalimaud Centre for the Unknown, Lisbon, Portugal

F. Bogusz · T. Pieciak

AGH University of Science and Technology, Kraków, Poland

as the echo time (TE) and the inversion time (TI), it is possible to collect images that capture different expressions of this sophisticated interaction. Sensitization to diffusion—summarized by the b-value—constitutes yet another explorable “dimension” to modify the image contrast, which reflects the degree of dispersion of water in various directions within the tissue microstructure. The full exploration of this multidimensional acquisition parameter space offers the promise of a more comprehensive description of the living tissue but at the expense of lengthy MRI acquisitions, often unfeasible in clinical practice. The harnessing of multidimensional information passes through the use of intelligent sampling strategies for reducing the amount of images to acquire, and the design of methods for exploiting the redundancy in such information. This chapter reports the results of the MUDI challenge, comparing different strategies for predicting the acquired densely sampled multidimensional data from sub-sampled versions of it.

T. Pieciak · S. Aja-Fernández

Laboratorio de Procesado de Imagen (LPI), Universidad de Valladolid, Valladolid, Spain

L. Ning · C.-F. Westin · Y. Rathi · F. Zhang

Brigham and Women’s Hospital, Harvard Medical School, Boston, MA, USA

H. Larochelle

Google Brain, Montréal, Canada

M. Descoteaux

SCIL, Université de Sherbrooke, Sherbrooke, Canada

M. Chamberland · M. Afzali · D. K. Jones

Cardiff University Brain Research Imaging Center (CUBRIC), School of Psychology, Cardiff University, Cardiff, UK

D. K. Jones

Faculty of Health Sciences, Mary MacKillop Institute for Health Research, Australian Catholic University, Melbourne, Australia

S. H. Baete

Center for Biomedical Imaging, Department of Radiology, New York University School of Medicine, New York, NY, USA

Center for Advanced Imaging, Innovation and Research, New York University School of Medicine, New York, NY, USA

L. Cordero-Grande · J. V. Hajnal · A. N. Price · J. Hutter

Centre for Medical Engineering, Centre for the Developing Brain, King’s College London, London, UK

T. Ladner

Department of Chemistry and Applied Biosciences, ETH Zurich, Zurich, Switzerland

J.-P. Thiran

Radiology Department, Centre Hospitalier Universitaire Vaudois and University of Lausanne, Lausanne, Switzerland

1 The Multi-contrast Nature of MRI Images

The abundance of acquisition parameters available in magnetic resonance imaging (MRI), and the focus on the b-value (b) and gradient directions (dir) when performing a typical diffusion acquisition—for example a pulsed gradient spin-echo experiment [1]—may lead one to consider parameters such as the echo time (TE) and the inversion time (TI) merely as indispensable yet irrelevant for the outcome of the acquisition. On the contrary, the choice of TE and TI is delicate as it attains to what physicochemical environment of the living tissue one would like to be the most dominant in the measured signal. Indeed, when the complexity of the tissue is summarized at the scale of an MRI voxel, the contributions from the different physicochemical environments add up in a distribution of longitudinal and transverse relaxation times T_1 and T_2 . Indicating with $\phi(TI, TE|T_1, T_2)$ the functional form of the contribution to the overall measured signal intensity, $S(TI, TE)$, then

$$S(TI, TE) \propto \int_0^\infty \int_0^\infty P(T_1, T_2) \phi(TI, TE|T_1, T_2) dT_1 dT_2 \quad (1)$$

where $P(T_1, T_2)$ is the joint distribution of the T_1 and T_2 expressed within the voxel. From the equation it appears clear that the nature of the functional form ϕ determines the contribution of a specific (T_1, T_2) population in the overall measured signal $S(TI, TE)$. For instance, focusing only on the dependency between TE and T_2 for the sake of simplification, in first approximation

$$\phi(TI, TE|T_1, T_2) \propto \exp(-TE/T_2) \quad (2)$$

which indicates that for a specific echo time TE a population having higher T_2 will have more contribution to the overall signal compared to an equivalently abundant population having a lower T_2 value, the latter being effectively less *represented*. This relaxation-weighted relative contribution is at the origin of an *observability* challenge in MRI: for instance, in order to acquire a signal that contains the contribution of water trapped within myelin sheaths in the nervous system, characterized by a short T_2 [2], it would be necessary to use a short echo time, according to Eq. 2, which can pose technical challenges. Beyond observability, which attains to the technical issue of collecting data using the required values of the acquisition parameters for observing a particular population, the need for representing all the observable populations leads to a *sampling* problem. A viable strategy consists in collecting data with many different combinations of acquisition parameters, where a large coverage and dense sampling of the multidimensional parameter space is desirable. Following the example above, a naive implementation of such strategy would lead to a combinatorial explosion of all the possible feasible pairs (TI, TE) according to a convenient discretization

F. Sepéhrband

Laboratory of Neuro Imaging (LONI), USC Stevens Neuroimaging and Informatics Institute, University of Southern California, Los Angeles, CA, USA

of the corresponding bi-dimensional parameter space. However, as the number of dimensions increases a similar strategy is no longer a reasonable option for practical purposes related to the lengthening of the time required for acquiring the MRI data, and to the increasing capacity required for its storage. Additional dimensions come, for instance, from the use of diffusion sensitization in the acquisition—summarized here by the b-value and the gradient directions [1, 7]—leading to a parameter space defined by the space of (TI, TE, b, dir) .

The design of an efficient sampling/sub-sampling strategy entails the adoption of two complementary approaches. The first one consists in developing accelerated MRI acquisition methods to reduce the overall acquisition time for a fixed sampling. These methods exploit acceleration opportunities on the engineering and physics side. They include a plurality of approaches like k-space sub-sampling, multi-band/multi-slice acquisition, parallel imaging, and others. Examples of particular relevance for the parameter space (TI, TE, b, dir) are those techniques combining different contrasts in the same acquisition - thus effectively reducing the waiting time inserted into the sequence to achieve specific contrasts. One method among these is ZEBRA [3], which leverages ideas such as slice-shuffling [4] and multi-echo read-outs and adds diffusion-preparation changes on a slice level in order to efficiently acquire information related to the interplay of the diffusion process and the T_1 and T_2^* relaxation. Here, the usage of multiple gradient-echos leads to T_2^* weighting (the observed transverse relaxation time affected by the presence of magnetic field inhomogeneities). The second approach consists of designing a sampling strategy that allows the shortening of the acquisition time by reducing the required number of samples. Typically, a sampling strategy is associated with a corresponding reconstruction method that is capable of exploiting the information from the acquired samples. As different sampling and reconstruction designs have different performance it is important to rank them. This chapter reports the description of the MULTIdimensional Diffusion (MUDI) challenge, organized within the MICCAI 2019 conference, with the purpose of evaluating the sampling and reconstruction designs on acquired in vivo data.

2 The Challenge

In order to evaluate the performance of a particular design, comprising of sampling and reconstruction, it would be necessary to know *a priori* the underlying information of interest. This is however impossible in the case of acquired experimental data. This would indeed require knowing the biophysical properties of interest—the T_1 , T_2 , and the diffusion properties of each population—which would only be known through the use of the very reconstruction techniques to be ranked. Therefore, a viable paradigm for quantifying the performance of the various methods consists in assessing the power that each tested design has in predicting unseen data samples for which an actual ground truth is available. Indeed, if a design is capable of predicting acquired signal samples from only a subset of these then it fulfills a necessary condition for

performing an efficient sampling and reconstruction. Following this criterion, designs can be ranked based on the capability of retrieving missing samples from a specified number of available ones.

2.1 Data

Five datasets were acquired from healthy human volunteers (3 f, 2 m, age = 19–46 years), after informed consent was obtained (REC 12/LO/1247), on a clinical 3T Philips Achieva scanner (Best, Netherlands) with a 32-channel adult head coil. Each dataset includes 1344 volumes (Fig. 1) distributed over four b-shells, $b \in \{500, 1000, 2000, 3000\}$ s/mm², with 106 uniformly spread directions [5], three echo times $TE \in \{80, 105, 130\}$ ms, and 28 inversion times $TI \in [20, 7322]$ ms. Single-shot PGSE EPI with the modifications proposed in ZEBRA [3] sequence was employed. Other parameters include TR = 7.5 s, resolution = 2.5 mm isotropic, FOV = 220 × 230 × 140 mm, SENSE = 1.9, halfscan = 0.7, multiband factor 2, total acquisition time 52 min (including preparation time).

Data was reconstructed and denoised in the complex domain [6]. *Ad hoc* affine volume registration was performed: collinear magnitude diffusion-weighted images (DWIs) acquired with different pairs (TI, TE) were first co-registered together using the highest TI and lowest TE volume as reference; the 106 reference volumes were then registered together based on a mutual information metric using Dipy [8], and the registrations were then propagated across the corresponding collinear DWIs. Data was collected with reversed phase-encode blips to allow for susceptibility-induced distortion correction using FSL [9, 10].

2.2 Tasks

Three fully-sampled datasets (1344 samples) were given to participants as training data, such that they could use them to propose a sub-sampling strategy based on 500 samples/volumes. In a second phase, participants were asked to provide the indexes

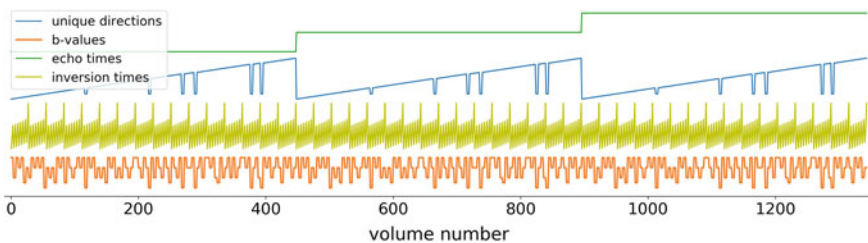


Fig. 1 The organization of the data. The lines report the variation of the parameters (with arbitrary scale units) as a function of the volume number

of the desired 500 volumes, where each volume had a different set (TI, TE, b, dir) . Then, only those selected 500 volumes of the two unseen test subjects were provided to each participant. Finally, participants were asked to submit their prediction of the remaining 1344–500 volumes. Additionally, participants were asked to select $X = 250, 100,$ and 50 volumes as subsets of the previously chosen 500 volumes subset, and again predict the 1344– X remaining samples.

2.3 Evaluation

The capability of retrieving missing samples from each specified subset of available samples—of the test subjects—was ranked using the mean squared error (MSE) between the predicted volumes and the corresponding acquired ones that were unknown to the participant. A comparative analysis of the MSE on the whole brain (WB), white matter (WM), gray matter (GM), and cerebrospinal fluid (CSF) masks was also performed in order to characterize the behavior of the various designs. Tissue segmentation was performed using SPM12 [11] on the T_1 -weighted image. The output included three probabilistic segmentation maps—WM, GM, and CSF—each subsequently down-sampled to match the resolution of the MUDI data. Only voxels with a probability over 0.9 were included. Although a ranking for each tissue type could be performed, the overall ranking accounts for the MSE results over the whole brain.

3 Proposed Methods

This report evaluates five submissions from different groups. Figure 2 reports charts illustrating the characteristics of the submitted sub-sampling strategies with respect to those of the fully-sampled datasets. A description of the designs follows.

1. S1. The best subset of 500 samples was identified using an autoencoder neural network having a ‘concrete selector layer’ as first layer [12, 13]. A temperature associated to such layer was minimized during training [14] for 800 epochs; a linear decoder was employed to reconstruct the features (samples) from the selected ones; the procedure was used recursively for the other tasks i.e. selecting 250, 100, and 50 samples from the subset of 500 while every time predicting all 1344 features. After the selection process, five networks were trained to predict the full set of 1344 features based on leave-one-out cross-validation over the five training subjects. Each network had two hidden layers of 800 and 1000 nodes respectively, and Leaky ReLu as activation function, using a MSE loss. The average prediction from these networks was used for the test subjects.
2. S2. This is a multilayer, feedforward, fully-connected deep neural network that analyzes MRI data on a voxel-by-voxel basis. Two separate and sequential sub-

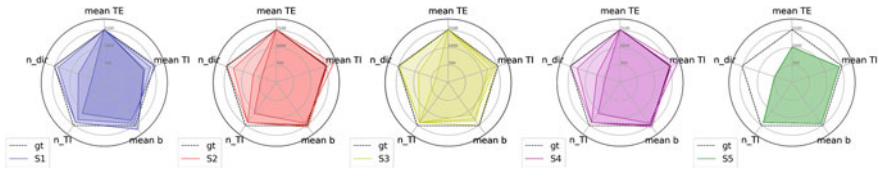


Fig. 2 The sub-sampling strategies adopted in the five different submissions for the different number of samples used to make predictions. Each radar chart (except the last one on the right) reports four polygons each corresponding to the 500 (polygon with largest area), 250, 100, and 50 (polygon with smallest area) samples cases. Polygons are overlapped using transparency, therefore the most opaque region represents the intersection between the four cases. The charts report the mean TI , b , and TE , the number of different directions “ n_dir ” and of TIs “ n_TI ” used in the sub-sampling. The dashed, black line pentagon “ gt ” (ground truth) reports the values of the fully-sampled dataset

networks, a selector and a predictor, work together to find the optimal subset of 500 samples and predict the remaining ones; as for S1, the 250, 100, and 50 samples tasks are managed recursively and samples extracted from the previously selected 500-measurement set. During training [14], the loss function was the MSE between the predicted and ground truth signals. 20% of the training data’s voxels were used for validation, with the remaining 80% used for the actual learning via backpropagation.

3. S3. The submission is based on a representation of the diffusion and relaxation signal. For the relaxation part a single compartment was considered, i.e. a single pair (T_1, T_2) . Diffusion was represented through an analytical distribution of diffusivities leading to the inclusion of a Kurtosis term [15]. T_1, T_2 , proton density, inversion efficiency, diffusivity, and Kurtosis were estimated with a non-linear method. The prediction was based on extrapolating the relevant signal from the estimated parameters, the signal along different gradient directions being predicted with interpolation. Samples were selected by maximizing the number of included TIs while eventually penalizing the number of directions considered.
4. S4. This submission is based on a signal representation similarly to S3. In this case, however, the diffusion part has been represented using DTI [7]. In this case, the inversion efficiency was set to 2. The samples selection was based on the results of S2.
5. S5. This is a signal representation approach based on modeling the moments of the joint relaxation and diffusion probability distribution [16]. The 500 samples were selected to include 20 volumes with $b = 0$ and different values of TI and TE , plus 480 volumes along 30 gradient directions with $b \in \{1000, 3000\} \text{ s/mm}^2$. The directional signal for a given set (TI, TE, b) was represented using the spherical ridgelet functions [17]. No submissions to the 250, 100, and 50 samples cases were provided.

4 Preliminary Results

Figure 3 reports the MSE maps obtained by calculating the MSE values voxel-by-voxel for the four prediction cases and for all of the submissions. The contrast of the images is therefore informative of the local performance of each proposed design, where a bright color indicates a larger error. It is therefore possible from these images to deduce that the submissions have different regional performance trends. Submissions 2 and 3, for instance, visually perform better in GM than in WM, whereas the opposite is true for submission 4. Submission 5 instead, reveals a substantially uniform performance across these two tissue types. A structured MSE map is visible also for submission 1 although less noticeable.

The differences across the different participant groups are attributed to both the proposed sub-sampling strategy and the reconstruction method. Regarding to the sub-sampling, all groups favored exploiting the redundancy in the diffusion gradient directions as illustrated in Fig. 2. Indeed, in the progressive reduction of the available samples illustrated by the reduced area of the radar charts (from more to less transparent due to the overlap), the “n_dir” entry corresponds to that displaying the largest decrease compared to the original sampling (dashed black line). In submissions 2 to 4 the signal is sub-sampled such that the mean TI in the dataset is kept substantially unaltered compared to the original sampling (this is marginally true for submission 1). However, submissions 1, 2, and 4 reduced of about one third the total number of unique TIs in the sub-sampling - perhaps exploiting the redundancy of such a parameter space - whereas submission 3 included almost all available TIs . To compensate for this, in submission 3 the mean b-value was much lower and slightly fewer gradient directions were selected. All these submissions kept the mean TE unaltered compared to the original sampling. Submission 5, on the other hand, reduced the mean TE in the sampling as well as the number of directions. This was likely a requirement due to the fitting procedure and signal representation they employed.

The MSE values increased with the reduced number of samples used for the prediction, with submissions 1, 2, and 3 having overall the best three rankings. This is illustrated in the images of Fig. 5 and better quantified in the summary results reported in the bar plots of Fig. 4. These results are calculated for the two test subjects and for the various regions of interest. From these, it is possible to observe that submissions 3 and 4 suffered more the extreme reduction of available samples from 250 to 100 compared to submissions 1 and 2 (submission 5 was only applied to the 500 samples case). Indeed, the submissions based on machine learning report a superior stability and an overall lower MSE in all the regions and sub-sampling configurations. All methods revealed a performance loss, with different degrees, in CSF and cerebellar regions. A summary of the results is reported in Table 1.

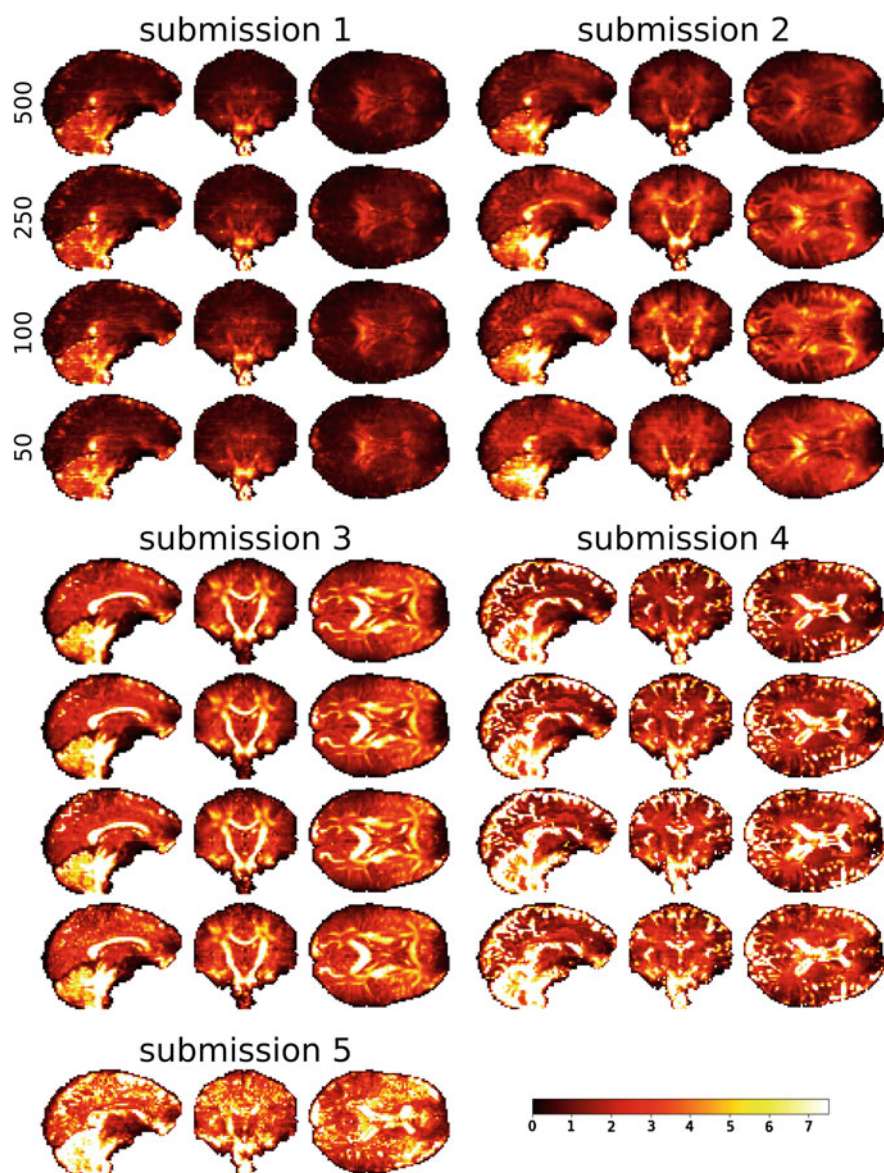


Fig. 3 Voxel-wise MSE values for testsbj0002

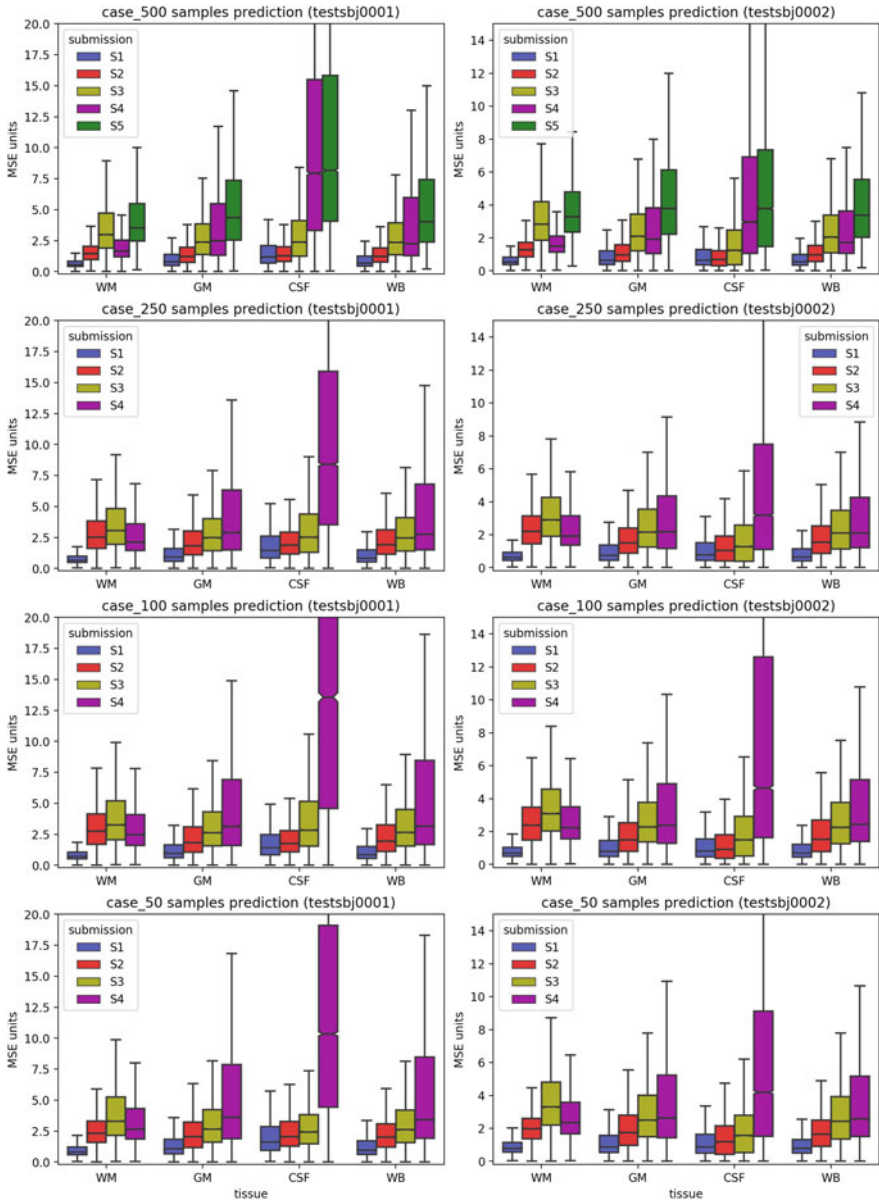


Fig. 4 Mean MSE per region of interest: white matter (WM), gray matter (GM), cerebrospinal fluid (CSF), and for the whole brain (WB). Rows report results for the 500, 250, 100, and 50 samples cases

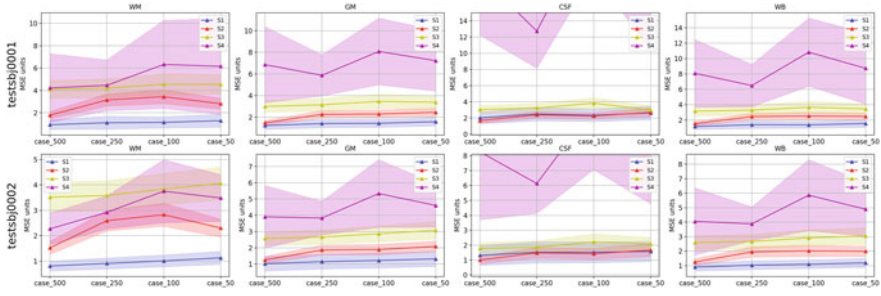


Fig. 5 Progression of the MSE as the number of samples available for prediction decreases. Lines report the trend of the average MSE in the corresponding region (WM, GM, CSF, WB). Shaded areas are proportional to the standard deviation

Table 1 Mean, median, and 85th percentile of the MSE for each submission. For each sub-sampling case (500, 250, 100, and 50) the first row corresponds to testsbj0001 and the second to testsbj0002

		S1	S2	S3	S4	S5
WM	500	0.94, 0.56, 1.26	1.79, 1.45, 2.48	4.10, 2.98, 6.22	4.23, 1.67, 3.85	5.74, 3.54, 7.38
		0.81, 0.53, 1.14	1.52, 1.28, 2.02	3.52, 2.83, 5.24	2.27, 1.5, 3.06	4.23, 3.28, 6.12
	250	1.12, 0.65, 1.46	3.15, 2.52, 4.72	4.2, 3.05, 6.36	4.46, 2.13, 5.24	–
		0.91, 0.61, 1.25	2.59, 2.20, 3.74	3.58, 2.90, 5.33	2.92, 1.92, 4.32	–
	100	1.15, 0.71, 1.53	3.44, 2.76, 5.15	4.56, 3.26, 6.88	6.32, 2.47, 5.93	–
		1.01, 0.68, 1.40	2.83, 2.39, 4.16	3.83, 3.09, 5.71	3.75, 2.23, 4.87	–
	50	1.3, 0.81, 1.74	2.81, 2.33, 4.04	4.55, 3.3, 6.88	6.16, 2.67, 6.41	–
		1.12, 0.78, 1.52	2.30, 1.98, 3.08	4.05, 3.3, 5.99	3.48, 2.35, 4.94	–
GM	500	1.22, 0.79, 1.96	1.48, 1.21, 2.49	2.99, 2.38, 4.92	6.86, 2.49, 9.69	6.8, 4.35, 10.44
		1.02, 0.64, 1.69	1.26, 0.97, 2.19	2.57, 2.09, 4.42	3.91, 1.91, 5.88	5.13, 3.78, 8.01
	250	1.41, 0.92, 2.28	2.26, 1.83, 3.91	3.14, 2.48, 5.12	5.87, 2.91, 10.71	–
		1.15, 0.74, 1.90	1.86, 1.50, 3.20	2.66, 2.16, 4.55	3.83, 2.18, 6.61	–
	100	1.43, 0.97, 2.29	2.29, 1.83, 3.95	3.46, 2.63, 5.55	8.08, 3.14, 12.96	–
		1.22, 0.80, 2.03	1.89, 1.49, 3.36	2.86, 2.28, 4.85	5.34, 2.37, 8.06	–
	50	1.58, 1.07, 2.54	2.44, 2.05, 4.07	3.38, 2.67, 5.40	7.23, 3.62, 12.69	–
		1.32, 0.87, 2.20	2.08, 1.74, 3.66	3.07, 2.5, 5.10	4.61, 2.63, 7.8	–
CSF	500	2.02, 1.17, 2.98	1.66, 1.28, 2.59	3.04, 2.38, 5.36	19.57, 7.93, 22.91	14.95, 8.17, 24.07
		1.31, 0.64, 1.88	1.00, 0.68, 1.70	1.78, 1.23, 3.31	8.26, 2.97, 10.26	6.82, 3.78, 10.81
	250	2.48, 1.46, 3.6	2.38, 1.88, 3.75	3.23, 2.52, 5.75	12.72, 8.4, 21.56	–
		1.52, 0.80, 2.17	1.48, 1.04, 2.62	1.86, 1.28, 3.46	6.13, 3.19, 10.93	–
	100	2.33, 1.42, 3.46	2.24, 1.77, 3.62	3.82, 2.84, 6.93	26.33, 13.57, 55.04	–
		1.52, 0.81, 2.21	1.42, 0.90, 2.54	2.22, 1.49, 4.1	11.23, 4.65, 19.94	–
	50	2.62, 1.63, 3.88	2.69, 2.05, 4.29	2.99, 2.44, 4.92	18.04, 10.34, 26.41	–
		1.58, 0.87, 2.33	1.67, 1.18, 2.9	2.07, 1.56, 3.71	8.34, 4.19, 13.39	–
WB	500	1.15, 0.69, 1.81	1.54, 1.23, 2.40	3.15, 2.37, 5.14	8.07, 2.26, 10.94	7.53, 4.03, 11.06
		0.89, 0.55, 1.44	1.24, 0.97, 1.96	2.58, 2.04, 4.37	4.05, 1.72, 5.81	4.88, 3.38, 7.43
	250	1.39, 0.82, 2.17	2.44, 1.92, 4.01	3.28, 2.47, 5.36	6.48, 2.75, 11.75	–
		1.02, 0.64, 1.64	1.94, 1.54, 3.24	2.66, 2.1, 4.48	3.88, 2.09, 6.62	–
	100	1.37, 0.85, 2.15	2.52, 1.94, 4.17	3.66, 2.65, 6.00	10.82, 3.15, 17.76	–
		1.09, 0.70, 1.74	2.01, 1.53, 3.49	2.91, 2.26, 4.86	5.86, 2.43, 9.03	–
	50	1.55, 0.96, 2.44	2.47, 2.02, 3.92	3.45, 2.61, 5.48	8.73, 3.43, 14.01	–
		1.18, 0.78, 1.88	1.98, 1.65, 3.19	3.04, 2.43, 5.00	4.89, 2.57, 7.91	–

5 Discussion

Results indicate that submission 1, based on machine learning, shows the highest prediction accuracy and stability among those submitted, followed by the other machine learning method submission 2. The challenge was deliberately designed in order for participants to be free in the choice of the samples such that this can best couple in synergy with the proposed reconstruction method. Because of this, however, it is impossible to separate the influence of the sampling strategy from the reconstruction method used. Nevertheless, it is possible that the proposed modeling-based reconstruction methods, which are primarily designed to enable more explicit descriptions of the physical phenomenon rather than signal reconstruction, might be affected by the difficulty of balancing model complexity and prediction performance. For instance, assuming one relaxation compartment (submissions 3 and 4) can oversimplify the fit while including more variability (submission 5) can destabilize it. Submissions 1 and 2, on the other hand, do not aim at an explicit representation of the physical parameters and for this reason they can rely on more flexible mathematical relationships to predict the signal. These reasons might contribute to an advantage of machine learning methods for tasks such as signal prediction. Moreover, a similar method can learn highly non-linear relationships between the reconstructions obtained from the different sub-sampling tasks thus obtaining a higher stability as the number of available samples (for the prediction) decreases: the proposed architectures in submissions 1 and 2 were flexible enough to interpret the 250, 100, and 50 samples predictions recursively. Among the modeling-based reconstruction methods, submissions 3 and 4 perform similarly when considering the whole brain. However, while submission 3—modeling the diffusion kurtosis—seems more suitable for gray matter, submission 4—based on DTI—outperforms it in white matter. Submission 5, although being the most comprehensive from a point of view of modeling as it describes the distribution of the parameters space (TI , TE , b , dir) within each voxel, has the highest MSE. This, however, could be mainly related to the chosen sub-sampling strategy which stands apart from the others.

Interestingly, the regional dependency of the performance of each submission suggests that some brain regions are more difficult to predict than others. While this might seem obvious, less intuitive is to grasp the reason behind such a regional trend. The cause of such regional performance differences is most likely connected with the reconstruction method, i.e. to the chosen type of modeling, although different brain regions might also require different sampling. With this regard, however, it is surprising to note similar regional trends also with submissions 1 and 2 as they do not involve an explicit modeling of the voxel' signal. Nevertheless, these regional performance differences underline the need for better descriptions of the MRI signal.

6 Conclusion

The MUDI challenge aimed at prompting the community to propose methods for exploiting the richness of information of multidimensional MRI acquisitions while at the same time suggesting sub-sampling strategies to allow for future clinical use. In this challenge, the sub-sampling and prediction tasks proposed were decoupled from the physical considerations connected to the MRI acquisition; indeed, every sample was considered to have the same weight in terms of acquisition time. Nevertheless, the results clearly point towards the direction to explore for future studies where the goal is to achieve MUDI data analysis within clinically feasible times. The machine learning methods indeed seem to provide greater prediction power and stability to sub-sampling compared to the signal representations. Perhaps the future will see the synergy between these two worlds where the former methods will provide the data redundancy necessary for using the latter methods as powerful and physically-informed tools for data analysis.

Acknowledgments MPiz acknowledges support from European Union's Horizon 2020 research and innovation programme under the Marie Skłodowska-Curie grant agreement No 754462. EB-C is partially supported by the Cerebra Foundation for the Brain Injured Child (Carmarthen, Wales, UK). CMWT is supported by a Veni grant (17331) from the Dutch Research Council (NWO) and a Sir Henry Wellcome Fellowship (215944/Z/19/Z). FB and TP acknowledge AGH Science and Technology, Kraków, Poland (16.16.120.773). MA and DKJ were supported by a Wellcome Trust Investigator Award (096646/Z/11/Z) and a Wellcome Trust Strategic Award (104943/Z/14/Z). SHB is supported in part by the National Institutes of Health (NIH, R01-CA111996, R01-NS082436, R01-MH00380 and P41EB017183). MPal, FG, DCA, TM and SBB acknowledge support from the UK EPSRC (EP/M020533/1, EP/N018702/1, EP/R006032/1), EU Horizon 2020 (ID 634541), NIH (Placenta imaging Project); Grant number: 1U01HD087202-01. AI acknowledges support from the Champalimaud Centre for the Unknown. LN is supported in part by NIH grants R21MH116352, R21MH115280, K01MH11 7346. SA-F's work was supported by Ministerio de Ciencia e Innovación of Spain with research grant RTI2018-094569-B-I00; FZ is supported by the following NIH grants: P41EB015898, R01MH108574, P41EB015902, R01MH 119222. JH was supported by the Wellcome Trust (Sir Henry Wellcome Fellowship, [201374/Z/16/Z] [201374/Z/16/B]), and the Wellcome/EPSCRC Centre for Medical Engineering [WT 203148/Z/16/Z].

References

1. Stejskal, E.O., Tanner, J.E.: Spin diffusion measurements: spin echoes in the presence of a time-dependent field gradient. *J. Chem. Phys.* **42**(1), 288–292 (1965)
2. MacKay, A.L., Laule, C.: Magnetic resonance of myelin water: an in vivo marker for myelin. *Brain Plast.* **2**(1), 71–91 (2016)
3. Hutter, J., Slator, P.J., Christiaens, D., Teixeira, R.P.A., Roberts, T., Jackson, L., Price, A.N., Malik, S., Hajnal, J.V.: Integrated and efficient diffusion-relaxometry using ZEBRA. *Sci. Rep.* **8**(1), 1–13 (2018)
4. Ordidge, R.J., Gibbs, P., Chapman, B., Stehling, M.K., Mansfield, P.: Highspeed multislice T1 mapping using inversionrecovery echo-planar imaging. *Magn. Reson. Med.* **16**(2), 238–245 (1990)

5. Jones, D.K., Horsfield, M.A., Simmons, A.: Optimal strategies for measuring diffusion in anisotropic systems by magnetic resonance imaging. *Magn. Reson. Med. Official J. Int. Soc. Magn. Reson. Med.* **42**(3), 515–525 (1999)
6. Cordero-Grande, L., Christiaens, D., Hutter, J., Price, A.N., Hajnal, J.V.: Complex diffusion-weighted image estimation via matrix recovery under general noise models. *NeuroImage* **200**, 391–404 (2019)
7. Basser, P.J., Mattiello, J., LeBihan, D.: MR diffusion tensor spectroscopy and imaging. *Biophys. J.* **66**(1), 259–267 (1994)
8. Garyfallidis, E., Brett, M., Amirbekian, B., Rokem, A., Van Der Walt, S., Descoteaux, M., Nimmo-Smith, I.: Dipy, a library for the analysis of diffusion MRI data. *Frontiers Neuroinform.* **8**, 8 (2014)
9. Andersson, J.L., Skare, S., Ashburner, J.: How to correct susceptibility distortions in spin-echo echo-planar images: application to diffusion tensor imaging. *Neuroimage* **20**(2), 870–888 (2003)
10. Smith, S.M., Jenkinson, M., Woolrich, M.W., Beckmann, C.F., Behrens, T.E., Johansen-Berg, H., Bannister, P.R., De Luca, M., Drobnjak, I., Flitney, D.E., Niazy, R.K., Saunders, J., Vickers, J., Zhang, Y., De Sefano, N., Brady, J.M., Matthews, P.M.: Advances in functional and structural MR image analysis and implementation as FSL. *Neuroimage* **23**, S208–S219 (2004)
11. Ashburner, J., Friston, K.J.: Voxel-based morphometry—the methods. *Neuroimage* **11**(6), 805–821 (2000)
12. Abid, A., Balin, M.F., Zou, J.: Concrete autoencoders for differentiable feature selection and reconstruction (2019). [arXiv:1901.09346](https://arxiv.org/abs/1901.09346)
13. Maddison, C.J., Mnih, A., Teh, Y.W.: The concrete distribution: a continuous relaxation of discrete random variables (2016). [arXiv:1611.00712](https://arxiv.org/abs/1611.00712)
14. Kingma, D.P., Ba, J.L.: Adam: a method for stochastic optimization, in: 3rd International Conference on Learning Representations. In: ICLR 2015—Conference Track Proceedings. International Conference on Learning Representations, ICLR (2015)
15. Jensen, J.H., Helpert, J.A.: MRI quantification of nonGaussian water diffusion by kurtosis analysis. *NMR Biomed.* **23**(7), 698–710 (2010)
16. Ning, L., Gagoski, B., Szczepankiewicz, F., Westin, C.F., Rathi, Y.: Joint RELaxation-Diffusion Imaging Moments (REDIM) to probe neurite microstructure. *IEEE Trans. Med. Imaging* (2019)
17. Michailovich, O., Rathi, Y., Dolui, S.: Spatially regularized compressed sensing for high angular resolution diffusion imaging. *IEEE Trans. Med. Imaging* **30**(5), 1100–1115 (2011)

Index

A

Adaptive group-patches, 80
Alignment, 26
Anatomically Constrained Tractography (ACT), 175
Atlas building, 150, 151, 153, 154, 157, 158

B

Brain tumor, 93

C

Cerebrospinal fluid, 91
Consistent estimator, 28
Constrained Spherical Deconvolution (CSD), 25, 101–109, 175
Convolutional Neural Network (CNN), 101, 103–108

D

Deep ADMM network, 79
Deep learning, 102, 103
Diffusion MRI (dMRI), 101–104, 109

E

Edema, 97

F

Fiber direction distribution, 79
Fiber Orientation Distribution Functions (FODFs), 25, 101–103, 106, 108, 109, 110, 175
Free-water correction, 92

G

Global efficiency, 177

H

Human Connectome Project, 92

L

Longitudinal atlas, 149, 150

M

Multi-shell, 101–103, 109

N

Network, 176
Neural network, 92

P

Principal Component Analysis (PCA), 177
Preterm, 173

R

Recursive calibration, 26
Response function, 25
Rotational invariant, 26

S

SIFT2, 176
Single fiber voxel, 26
Single-shell, 101, 102, 109
Sparse priors, 80
Sparse regularization, 80

Spatial continuity, [79](#), [80](#)
Spatial sparse FOD estimation, [79](#)
Spherical harmonic, [26](#)
Synthetic dataset, [92](#)

T

Tissue microstructure, [92](#)
Tractography, [101–104](#), [109](#)

U

Unbiased estimator, [28](#)

W

Wigner 3- j symbols, [28](#)